Hyperon production in p–Pb collisions with ALICE at the LHC.

Didier Alexandre

Thesis submitted for the degree of
Doctor of Philosophy

Nuclear Physics Group
School of Physics and Astronomy
University of Birmingham
June 2016

Abstract

This thesis discusses the production of the multi-strange, charged Ξ and Ω baryons in proton–lead (p–Pb) collisions at a centre-of-mass energy of 5.02 TeV. The transverse momentum, p_{T}, distributions are analysed as a function of event multiplicity. A hydrodynamical model based on statistical physics reproduces the shapes of the multi-strange p_{T} spectra, in conjunction with the spectra of lighter hadrons, in high multiplicity data. The good agreement is an indication of collective behaviour by all particles inside a system in thermal equilibrium, consistent with the picture of the build–up of a radially outward expansion due to an initially dense medium. These results are reminiscent of the observations made in lead–lead (Pb–Pb) collisions, which are explained by the formation of a Quark-Gluon Plasma. In addition, the p_{T}–integrated yields of the hyperons are reported on, revealing a steady increase as a function of multiplicity. An enhancement with respect to non-strange hadrons is observed, and the Ξ/π and Ω/π ratios in high multiplicity p–Pb data approach those measured in central Pb–Pb collisions. The Ξ/π ratio is comparable with the calculations from a thermal model for strangeness saturation, whereas the Ω/π ratio deviates from that value by 2σ.

Author's contributions

During the course of my degree, I have been a member of the ALICE collaboration. Therefore, my results cannot be solely attributed to my work. Instead, I benefited from the input of several other members. I made use of existing code written by David Dobrigkeit Chinellato, Michele Floris and Roberto Preghenella.

I started my physics analysis work on strangeness, by working on the production rates of Λ and K^0_S. I made use of a macro written by David, in order to read Event Summary Data (ESD) files and extract the p_{T}-distributions of these particles. Later, I adapted the existing code into one for the analysis of the doubly-strange Ξ hadrons, and then extended it to work for the triply-strange Ω, too. These particles became the focus of my main analysis project. David independently developed a code for the measurement of the multi-strange particles himself, which was very helpful to perform cross-checks on my results. I performed the analysis that led to the final decision on the selection cuts and analysis settings for the multi-strange hadrons, extracted all p_{T}-spectra and calculated their uncertainties. My results were approved by the collaboration to be presented in the Quark Matter conference in Darmstadt, in May 2014. I gave the corresponding talk in a parallel session and wrote the proceedings on my contribution [1]. In addition, I led the efforts towards the publication of the results in the Physics Letters B journal, shown in Appendix C [2], by taking the role of chair of the paper committee. I am grateful for all the discussions and advice provided to me by my supervisor Roman Lietava, by Lee Barnby and by David during this long process. I also have to thank Michele for introducing me to the thermal model code, with which I performed several fits and extracted model descriptions for the discussion of the results in the paper and in this thesis.

During my stay at CERN, I was also involved in several projects with the Central Trigger Processor (CTP) of ALICE. My main project consisted in performing tests on the firmware of the Local Trigger Unit (LTU), the interface between the CTP and the ALICE sub-detectors. I developed a C-written programme to run tests on

the trigger protocol. This work is the subject of the last section of Chapter 3. I also helped in running trigger simulations with the LTU and test, together with the experts of several sub-detectors, that these were received correctly by their systems. In addition, I wrote a Python script to manage the trigger configuration file. All this work was supervised by Anton Jusko and Roman. During the beginning of the Run 2 of the LHC, I also did several CTP on-call shifts. Finally, I completed a course on the operation of the Experiment Control System, and served 72 hours in shifts in the ALICE run control room.

To Marlene

Acknowledgements

I owe the completion of this degree to many people, who in their own way, helped me bring it to its end. I am especially grateful to my supervisor Roman Lietava, who has always been available to discuss my work, give good advice, but most importantly, to teach me. I am also grateful to David Evans for the great opportunity to do this degree with the ALICE group of Birmingham, and for all his help during it. Special thanks go also to Lee Barnby for the many invaluable interactions we had, in particular, but not only, in the paper committe we were part of. I also thank all other members of our group, with whom it was always a pleasure to work: Katie Graham, Luke Hanratty, Peter Jones, Anton Jusko, Marian Krivda, Graham Lee, Arvinder Palaha, Plamen Petrov, Patrick Scott, Orlando Villalobos-Baillie and Nima Zardoshti.

From the ALICE collaboration, I thank especially my friend David D. Chinellato. It was a privilege to be able to collaborate with him for the greater part of my degree. I am indebted to him for all that he taught me. I also thank him for the opportunity to work with him in Campinas, for a period of three months, during which I enjoyed all the discussions we had during the process of writing our paper. I also extend my gratitude to his colleagues Jun Takahashi and Giorgio Torrieri. I thank other members of the ALICE collaboration with whom I had the chance to have several helpful exchanges on the topic of strangeness, especially Domenico Colella, Michele Floris and Roberto Preghenella.

At this stage, it feels important to remember the beginning of this journey. I am grateful to Fabrizio Salvatore for introducing me to the field of High Energy Physics six years ago.

I enjoyed the company of my friends Pete Griffith, Luca Pescatore and Mark Levy, during our time spent at CERN, as well as during the summer schools we attended. I thank them for all the fun we had. I can also not forget the friends I made outside the field of physics during this time. There are several, however special thanks go to Deni, Fernanda and Luis from Brazil, for teaching me many things that cannot be expressed in equations.

On a more personal level, I thank my father, who over the last eight years must have broken all records in phone calls to me. I also thank my late mother, who contributed a lot to who I am today.
Finally, I thank Marlene, for her unconditional love and support through all these years.

It is the Land of Truth (enchanted name!), surrounded by a wide and stormy ocean, the true home of illusion, where many a fog bank and ice, that soon melts away, tempt us to believe in new lands, while constantly deceiving the adventurous mariner with vain hopes, and involving him in adventures which he can never leave, yet never bring to an end.

Immanuel Kant

Contents

Chapter 1

Introduction

Matter at its most fundamental level is made up of electrons and nucleons - protons and neutrons - which themselves are bound by the interactions of elementary quarks and gluons. These interactions take place via the strongest of the four forces of nature: the strong nuclear force. At CERN in Geneva, Switzerland, ALICE [3], A Large Ion Collider Experiment of the Large Hadron Collider (LHC) [4] was designed and constructed in order to study the properties of that force. Heavy nuclei, such as lead (Pb) ions are collided at ultra-relativistic speeds in order to create the densest and hottest conditions of matter ever attempted in a laboratory. In fact, temperatures as high as 10^5 times the temperature at the centre of the sun can be achieved in such collisions, and this within a small volume with a radius of the order of only ten femtometres (fm). There is conclusive evidence that under such extreme conditions, matter exists in a state of a Quark-Gluon Plasma (QGP), in which the temperature and density are so large that quarks and gluons can no longer be perceived as being bound to one particular hadron [5]. In fact, the notion of a hadron is meaningless in such a plasma. The study of such plasmas has some importance for cosmology, too. During the very first microseconds after the Big Bang, the universe is thought to have borne the extreme density and temperature conditions of a QGP, before a phase transition to a hadron gas took place, analogous to the phase transition of an electromagnetic plasma - in which nucleons and electrons were unable to form - to a

state of bound atoms some 300-400 thousand years later. It has also been suggested that QGPs may exist at the core of the densest visible objects in the universe: neutron stars [6].

The study of QGP properties with the ALICE experiment is the subject of this thesis. It concerns the measurement of the production of particles containing one particular quark: the *strange* quark. As will be discussed later, the production of this quark is very sensitive to the presence of a QGP, making this type of measurement an important probe of the plasma. The measurements reported here were performed in collisions between protons and Pb ions (p–Pb collisions) and are useful in comparative studies with measurements of the same observables in proton–proton (pp) and Pb–Pb collisions. Before discussing the concepts of heavy-ion physics, it is important to introduce essential concepts of quantum chromodynamics (QCD), the most successful theory in describing the strong nuclear force, and which makes predictions for the conditions of a QGP.

1.1 Quantum Chromodynamics

QCD is the theory that describes the strong nuclear force, responsible for the interactions between quarks, the particles that were proposed by Gell-Mann [7] and Zweig [8] independently in 1964 in a theoretical framework that could explain the existence of the hadronic states discovered over the preceding decades. Today, there are six known quarks, ranging from lightest to heaviest, the *up*(u), *down*(d), *strange*(s), *charm*(c), *bottom*(b) and the *top*(t) quark. Several parallels can be drawn between QCD and the successful theory for electromagnetism - quantum electrodynamics (QED). For instance, in QED the photon is a massless boson of spin-1, which mediates the force between two electric charges. In the strong force, the analogy of the electric charge, is the so-called *colour* charge. The boson which mediates the interaction between two colour-charged quarks q (and antiquarks $\overline{q}$) is the gluon, also a massless spin-1

boson. The exchange of gluons ensures that quarks are bound together in hadronic states, which may be mesons - composed out of a $q\overline{q}$ pair - or baryons - made up of three quarks. As such, quarks must carry partial electric charges: the up, charm and top quarks carry 2/3 of one unit of an electric charge (e), and the down, strange and bottom quarks carry -1/3e.

1.1.1 Colour charge

Quarks, with spin 1/2, are fermions, i.e. particles with half-integer spin, and as such obey the Pauli exclusion principle, which states that no two fermions can occupy the same quantum state. The same must therefore be true for baryons. It can be shown that fermionic states must be described by antisymmetric wavefunctions if they are to follow the Pauli principle [9]. It becomes clear, that for baryons such as the Δ^{++}(uuu) or the Ω^{-}(sss), this condition can only be satisfied if there is an additional quantum number inherent to the constituent quarks, since the spin, spatial and flavour wavefunctions of these baryonic states are symmetric under quark exchange. To solve this, Oscar W. Greenberg postulated the existence of a *colour* charge for quarks and gluons in 1964 [10]. This property is analogous to the electric charge in QED, with the difference that also the force mediators, gluons, carry colour, unlike photons in QED. There are three colour charges - called red, green and blue - and all hadrons must be colour neutral, or colour singlets. Colourless particles are defined as (rgb) or ($\overline{r}\overline{g}\overline{b}$) combinations for baryons or colour-anticolour pairs for mesons. This condition keeps quarks confined inside their hadrons. Gluons, on the other hand, carry colour charge, in one of eight possible combinations:

$$r\bar{b}, b\bar{r}, r\bar{g}, b\bar{g}, \bar{r}g, \bar{b}g, \frac{1}{\sqrt{2}}(b\bar{b} - r\bar{r}), \frac{1}{\sqrt{6}}(r\bar{r} + b\bar{b} - 2g\bar{g}) \quad . \tag{1.1}$$

Colour can thus be exchanged between quarks and gluons, which is one of the main differences with QED, where photons do not carry electric charge.

The number of three colour charges has been backed experimentally, for instance in measurements of the ratio of hadronic to leptonic production cross–section in e^+e^- interactions, a value which is dependent on the total number of degrees of freedom available to each process, and hence to the number of colour charges [11].

1.1.2 Confinement

In contrast to the electromagnetic force, which decreases with increasing separation between two charged particles, the potential energy of the strong force increases linearly with distance. As a result, the further one tries to separate two quarks, the stronger they are pulled back together to their hadronic state. This is why the strong nuclear force is short-range, as opposed to the electromagnetic force. In fact, free quarks cannot be observed experimentally. The energy one would need to supply to separate two quarks would be sufficient to create a new quark-antiquark pair. This characteristic of QCD, called *confinement*, is manifested experimentally in back-to-back di-jet observations in high energy physics detectors. A jet is a shower of a group of roughly collimated hadrons, supposedly originating from one quark (or gluon). A di-jet forms when two quarks are separated sufficiently by the energy released in a high-energy collision, that new quarks would emerge as a result of it, giving rise to the formation of a bunch of hadrons in the detector.

1.1.3 Asymptotic freedom

In QED, an electric field generated by a static charge, such as an electron, is subject to a smearing effect as the charge is screened by the presence of a cloud of electron-positron pairs generated by the vacuum fluctuations according to the Heisenberg uncertainty principle. The electric field polarises those pairs, such that the positron of one pair is always closer to the static electron. As a result, the field experienced by a second charge is reduced the further away it is from the source. The electromagnetic coupling constant α decreases with increasing distance to reach the asymptotic value

of 1/137 at infinity.

In QCD, this effect is cancelled due to the fact that gluons, unlike photons, carry charge, and thus actually increase the field at larger distances. The gluons carry away colour charge from the source quark, and as a result the coupling constant (α_s) is reduced for short-range interactions. Due to this screening and anti-screening effects, α and α_s are *running* coupling constant. In leading order perturbative QCD, the strong coupling constant is be expressed as:

$$\alpha_s = \frac{12\pi}{(33 - 2n_f)log\Big(\frac{Q^2}{\Lambda^2_{QCD}}\Big)} \quad , \tag{1.2}$$

where n_f is the number of quark flavours in nature [12]. Q is the momentum transferred between the two particles engaging in a strong interaction, which is inversely related to the distance between the two. In a strongly interacting medium, while the momentum transfer is linked to the temperature of the system, the quark separation can be associated to its density. The Λ_{QCD} term is called the QCD scaling constant, and determines the threshold above which the above equation for the coupling constant is applicable. Indeed, α_s diverges to infinity for small values of Q.

Through the cross-sections of several processes in high-energy collisions, the running coupling constant can be measured experimentally as a function of Q^2. Figure 1.1 shows a summary of several measurements performed in different experiments for a large range of momentum transfer. From such data, it is possible to extract a value for the Λ_{QCD} constant, which is found to lie around 0.2 GeV [13], corresponding to a distance of the order of 1 fm. For large momentum transfers ($Q^2 >> \Lambda^2$), α_s decreases and eventually vanishes, as can be deduced from equation 1.2 and observed in Figure 1.1. This vanishing of the coupling constant is referred to as *asymptotic freedom*.

The reduction of the strong coupling constant to the asymptotic freedom limit indicates, that in a hot medium, the strong force between two quarks will eventually

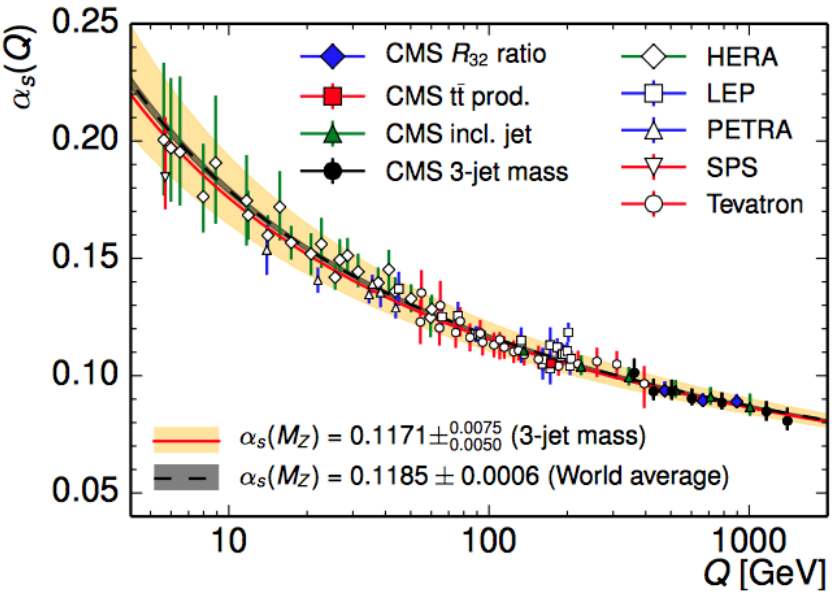

Figure 1.1: The strong coupling constant as a function of momentum transfer as measured by the CMS experiment [14] and by several previous experiments [15].

be so weak that quarks and gluons become free and do not belong to a hadron in particular any more. Hadrons cannot form under such extreme conditions, and the system finds itself in a Quark-Gluon Plasma.

1.1.4 The strong force potential

According to the above considerations of the strong nuclear force, the behaviour of the QCD potential (V_{QCD}) is dependent on the range of the interaction concerned. At large quark separations, the potential of the strong force is described by non-perturbative calculations, such as *lattice QCD* (see the coming section 1.1.5). At distances beyond ∼1 fm, V_{QCD} can be observed to follow a linear behaviour as a function of r:

$$V_{QCD} = kr \quad , \tag{1.3}$$

where the constant k is roughly equal to 1 GeV/fm [16]. This tension reflects the confined nature of hadrons which causes the attractive force to increase the further apart quarks are from each other, thus keeping them bound together. For very low

quark distances (below 0.1 fm), the strong potential is described in a Coulomb-like form as follows:

$$V_{QCD} = -\frac{4\alpha_S}{3r} \quad . \tag{1.4}$$

This equation suggests that the potential gets stronger as colour charges approach. However, since this description is valid in the perturbative regime of approaching asymptotic freedom, the running coupling constant will weaken the strong interactions. Therefore in a system of strongly interacting particles, de-confinement can take place at temperatures lower than required to reach asymptotic freedom. In a sufficiently hot and dense medium, the close proximity of polarised colour charges in a QGP causes a so-called *Debye screening* to the field of one point charge. The QCD potential can be rewritten as follows, in order to take into account that effect:

$$V_{QCD} = -\frac{4\alpha_S}{3r} e^{-r/\lambda_D} \quad , \tag{1.5}$$

where λ_D is the Debye screening length. This length decreases with increasing temperature, and as it becomes comparable to the size of a particular hadronic radius, the binding force between the quarks that would hold that hadron together, is smeared by the presence of a large number of nearby colour charges to the point that the hadron ceases to be able to form [17]. The partons - quarks and gluons - continue to interact strongly but do not belong to one particular hadronic state.

1.1.5 Lattice QCD

Lattice QCD is an approach to make calculations of strong processes [18, 19], based on a 4D discretisation of the QCD Lagrangian, the formula which expresses the dynamics of quarks and gluons, onto a grid of three spatial dimensions (N_S^3) and one time dimension (N_t). The volume (V) and temperature (T) quantities are directly linked to the lattice point separation a:

$$V = (N_s a)^3 \quad and \quad T^{-1} = N_t a \quad . \tag{1.6}$$

A baryon chemical potential μ_B is also introduced, in order to make predictions for heavy-ion collision experiments, where the Quark-Gluon Plasma differs from that of the early universe by the fact that μ_B is non-zero, since the initial baryon quantum number in a collision between two ions is finite. However, at the LHC, μ_B is approximately zero for particles in the central rapidity region, characterised by small longitudinal momenta.

Figure 1.2 shows the energy density (ϵ) divided by T^4 as a function of temperature as calculated by lattice QCD for three different quark mass assumptions: 2 and 3 massless quarks, and 2 massless plus 1 massive quark. A sharp increase on the energy density can be observed at a critical temperature of about $T_{cr} = 170$ MeV. This value is the predicted temperature for a QCD phase transition from hadronic matter to a medium of de-confined quarks and gluons. Lattice calculations predict the QGP to behave like an ideal gas in the high-temperature, or asymptotic, limit [20]. The value of the energy density at that limit, also indicated in the figure, is not reached for temperatures of up to 700 MeV.

Figure 1.3 is an illustration of the QCD phase diagram [19], plotted as temperature versus baryon chemical potential, according to phenomenological theoretical models and lattice QCD. At zero μ_B, the phase transition from a hadron gas to a QGP occurs at the critical value of 170 MeV. As μ_B increases, the temperature for the phase transition drops, following a curve of constant energy density of around 1 GeV/fm^3. The diagram also shows the phase transition of cold nuclear matter, such as is found at the core of atomic nuclei, from a liquid to a gaseous state at μ_B just under 1 and at a temperature of 7.5 MeV ($\sim 8.7 \times 10^{10}$K). Near the hadron gas–QGP transition, lattice QCD calculations are applicable for $\mu_b < 1$. These calculations indicate that the transition, in the early universe, as well as in heavy-ion collision experiments, is a progressive crossover, not characterised by a latent heat, such as in the case of the

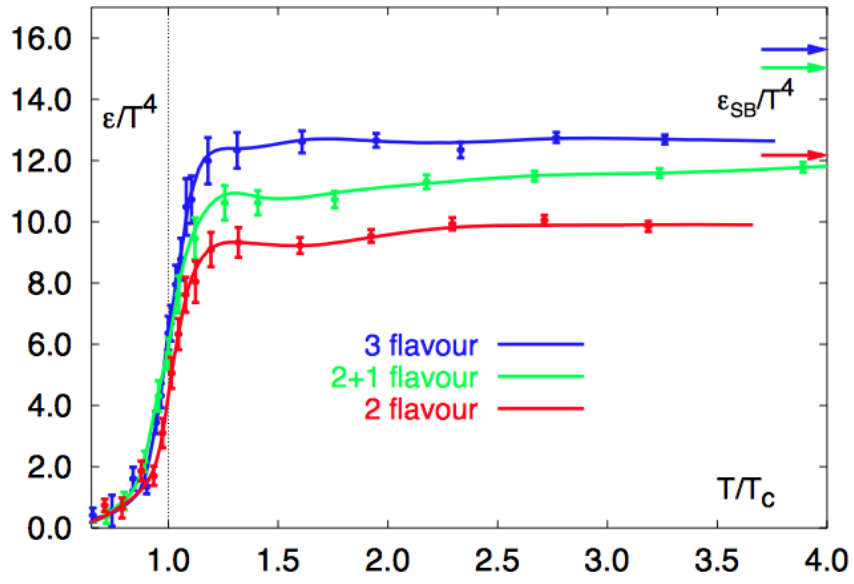

Figure 1.2: The energy density-temperature relation according to lattice QCD calculations. A critical temperature for a phase transition occurs at T_{cr}=170 MeV. The ideal gas ϵ_{SB}/T^4 at the high-temperature limit is also indicated [21]

solid-to-liquid transition, nor by a sharp transition with a critical temperature, such as the loss of permanent magnetisation in a ferromagnet.

1.1.6 Chiral symmetry

In a Quark-Gluon Plasma, the masses of the de-confined quarks are reduced as they take the values of their bare masses as opposed to their constituent masses they have when bound to a hadron. This decrease in mass represents roughly a hundred-fold drop in mass for up and down quarks and a five-fold decrease for the strange quark. In QCD, this drop in mass is associated to the existence of a so-called chiral symmetry, which is held at the limit of massless quarks [22]. Since it is known that quarks have non-zero masses, this symmetry is only partially restored in a plasma. This partial restoration of the chiral symmetry favours the production of second generation quarks (strange and charm) in high energy experiments, due to a considerable lowering of the energy threshold for thermal quark production in a hot medium [23].

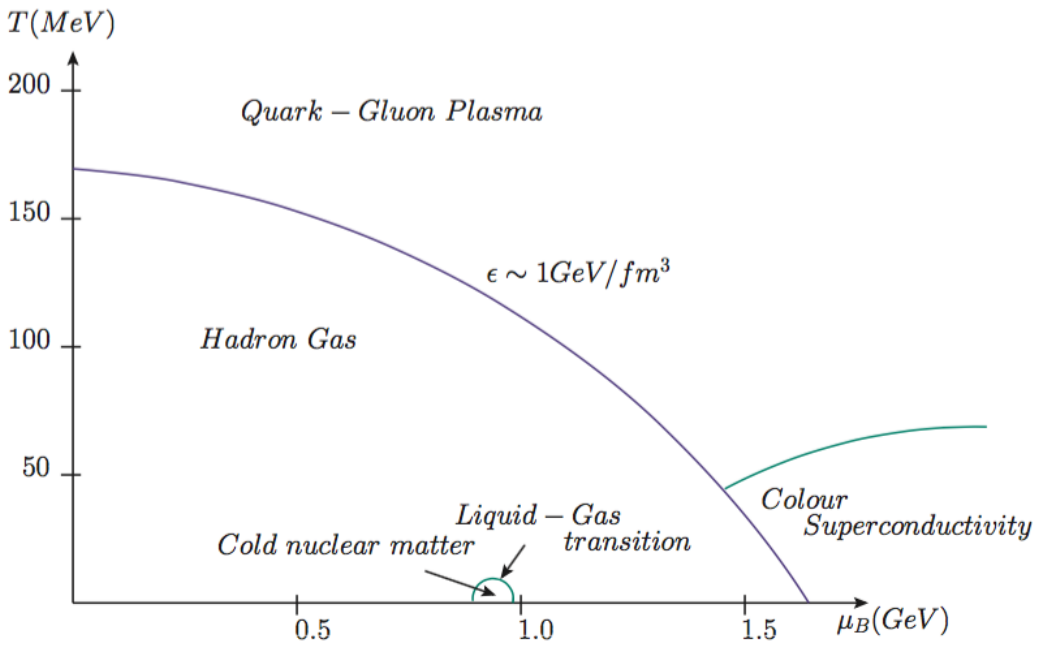

Figure 1.3: The QCD phase diagram.

Structure of the thesis

Having introduced some key concepts of the theory of the strong nuclear force, the remainder of this thesis is structured as follows: Chapter 2 will focus on the main experimental notions in heavy-ion physics, and provide an introduction to the Statistical Hadronisation Model for the description of the hadron distributions in high energy collisions. Strangeness production, being the scope of later chapters, will be given the main attention. Chapter 3 introduces the ALICE experiment of the Large Hadron Collider, describing some of the most relevant detector components for the physics analysis which leads to the measurement of the charged Ξ and Ω hadrons in p–Pb collisions as a function of event charged-particle multiplicity. This is the focus of Chapter 4, while Chapter 5 provides a detailed discussion of these measurements, comparing it to statistical models and to previous measurements in other collision systems (pp and Pb–Pb). Finally, a summary of that discussion is given in Chapter 6.

Chapter 2

Heavy Ion Physics

This chapter outlines the key concepts of heavy-ion physics in high energy collision experiments. Such collisions provide the necessary conditions for the formation of a Quark-Gluon Plasma (QGP). Several experimental observables, sensitive to the evolution of the system after the nuclear collisions, reveal important information about the properties of the QGP. An overview of these will be given in the first part of the chapter. Among such observables is the production rate of strange hadrons. Owing to the high temperatures of the QGP and the accessible mass of the bare strange quark, thermal production of such quarks is favoured, resulting in an overall enhancement of strangeness. This effect is the subject of the analysis presented in later chapters. Therefore, the second part of this chapter will provide a theoretical background of models based on statistical physics that attempt to predict the relative production rates of strange particles. Finally, proton–lead collisions are put into context, given that the study of strangeness of this thesis was conducted on such data.

2.1 Space-time evolution of a heavy-ion collision

The study of the Quark-Gluon Plasma in the laboratory can be achieved in collisions between heavy ions (A–A), where heavy nuclei (Au or Pb) are smashed against each

other at relativistic speeds. The interaction between such heavy nuclei causes hundreds of nucleon–nucleon interactions, resulting in a large amount of energy release in a very small time scale. The emerging partons thermalise within a time interval (τ_0) of less than 1 fm/c and a plasma is formed if the energy density of the system is above the critical density of about 1 GeV/fm^3. The strongly interacting partons cause large pressure gradients against the surrounding vacuum, causing the system to expand and cool in the process. After a time period no longer than around 15 fm/c, the critical temperature T_c for a phase transition to a hadron gas is reached. At this time, partons stop being de-confined and hadronisation takes place. Soon after, inelastic collisions between the hadrons also cease and a chemical freeze-out occurs. The relative abundances of the different hadrons will remain unaltered until they reach the surrounding detector. During that stage, elastic collisions can still take place while the hadronic gas continues to expand and cool. Finally, the mean free path of the hadrons becomes too large and the system reaches kinetic freeze-out. The particle momenta suffer no more modifications and are eventually measured by the detector. The evolution of heavy-ion collisions just described is sketched in the diagram of Figure 2.1 [19].

2.2 Experimental observables

The previous section introduced the presumed succeeding stages in heavy-ion collisions. This evolution can be studied and characterised by the measurement of several experimental observables, which this section gives an overview of. These observables can be grouped into two categories, one related to *soft*, low-momentum processes, which constitute the bulk of the system and allow the study of thermodynamic properties, and another concerning the *hard* processes, originating in jets, high-momentum partons that produce a shower of hadrons in the detector.

The measurement of strangeness production in high energy collisions, the subject of the work presented in this thesis, counts as one of the so-called *QGP signatures*.

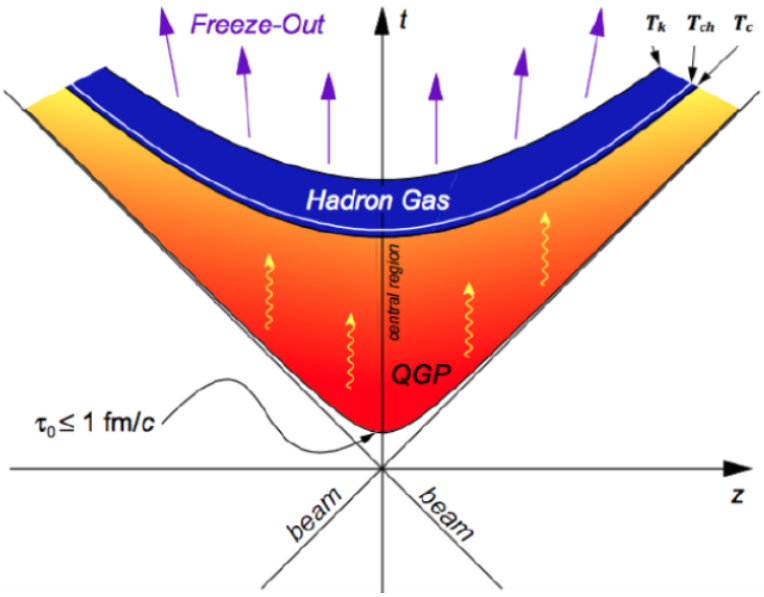

Figure 2.1: Space and time evolution of a heavy ion collision. The critical T_c, chemical freeze-out T_{ch} and kinetic freeze-out temperatures T_k are annotated. (Figure taken from [24])

Based on the relative hadron yields, theoretical models can be used to infer the presence of a partonic de-confined phase in thermal equilibrium in heavy-ion collisions. It falls under the category of soft physics. The observation of hard processes also plays an important role in determining the properties of the QGP. Theoretical predictions are made on how high-momentum particles are suppressed by the interaction with the plasma medium, with respect to a system where no de-confined phase occurs. Therefore, for these observables, as indeed for all other QGP observables, it is essential to make comparative studies between measurements made in different collision systems. Such studies search for differences between observations in heavy-ion collisions, e.g. Pb–Pb, and non-nuclear collisions, e.g. pp, which may suggest the presence of a QGP. Traditionally, pp collisions are used as a reference, in which no plasma is expected to be created, although as will be seen later, the formation of plasmas are not excluded and may even be likely in systems of particle multiplicities above average.

The following is a review of several of the experimental observables dealt with in heavy-ion physics. First, attention is given to the experimental concepts related to

strangeness production, before hydrodynamic observables, such as collective radial and elliptic *flow* are described. Then, this section turns to the relevance of the measurements of suppression of jets, before addressing the phenomenon of suppression of charmonium states in heavy-ion collisions. Finally, it is also explained how resonance measurements can provide information about the hadronic phase of the system after hadronisation has taken place. In each case, references are made to the already conducted experimental measurements.

2.2.1 Strangeness Enhancement

The production of strange particles in high energy collisions is one of the important observables for the characterisation of the QGP medium. The idea that strange hadrons will be produced in different abundances depending on whether they originate from a de-confined state or not, was first discussed by Johann Rafelski and Berndt Müller in [25]. Using QCD principles, they showed that if there is a Quark-Gluon Plasma formation, strangeness production in experimental collisions will be enhanced with respect to the cases where no de-confined state of matter occurs.

In order to understand the effect of a plasma on strangeness production, it is useful to consider the production of strange hadrons in a non-QGP environment. Such systems are most likely present in pp collisions, especially in low-multiplicity events. In such interactions no net strangeness is present in the colliding particles. As a result, strange particles have to be produced only from secondary partonic interactions. The energy threshold is raised by the strangeness conservation law, due to which hyperons and anti-hyperons must be created in equal amounts. The lowest energy threshold for strange hadron production is around $E_{th} = 3.4$ GeV, for the pp$\rightarrow$ppK^+K^- process. Lighter hadrons, composed of u and d quarks, need lower thresholds and are consequently produced more abundantly.

This picture changes with the presence of a state of de-confined quarks and gluons, such as in central Pb–Pb collisions. Due to the partial restoration of the chiral symme-

try, the strange quark acquires its bare mass of 95±5 MeV [26] in the plasma, instead of the much higher constituent value, which phenomenological calculations place at 483 MeV [27]. The energy threshold for the production of $s\bar{s}$ pairs is therefore only around 100 MeV. In case this value is attained in the plasma, thermal production of $s\bar{s}$ pairs is uninhibited. Figure 2.2 shows lowest order Feynman diagrams for the thermal generation of s-quark pairs, through quark fusion $q\bar{q} \rightarrow s\bar{s}$ and gluon fusion $gg \rightarrow s\bar{s}$. Calculations show that the latter reaction dominates by up to a factor of 10 [28].

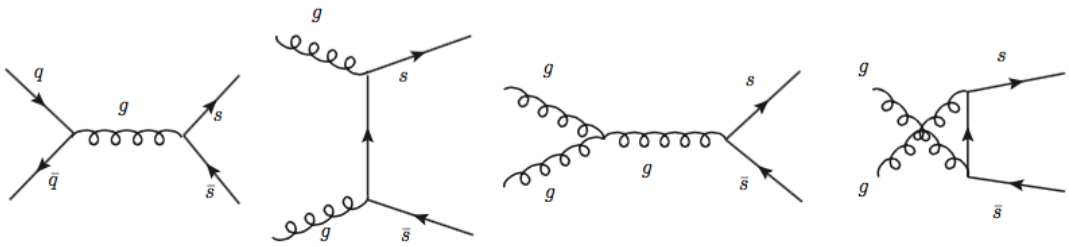

Figure 2.2: Lowest order Feynman diagrams showing the thermal production processes of $s\bar{s}$ pairs, via quark (left) and gluon fusion (middle and right).

Johann Rafelski and Berndt Muller were the first to predict this behaviour [25]. In their work, they also calculated the timescale for the saturation (τ_s) of strangeness production in a QGP, a state of equilibrium established when the production and annihilation rates of strange quark pairs match each other. It is not exactly known how hot the QGP medium gets at the LHC, although experimental measurements of direct photons, to be discussed in section 2.2.5, suggest that the QGP temperature is, on average, above 300 MeV. According to perturbative calculations of the relaxation time as a function of the temperature of the QGP, shown in Figure 2.3, the τ_s lies at around 3 fm/c for that temperature. The bigger the volume of the plasma, the longer-lived it is and therefore the more likely it is to equilibrate strangeness.

Experimentally, the enhancement of strangeness production is measured by comparing the relative production of hyperons in A–A, where QGPs form, relative to pp collisions

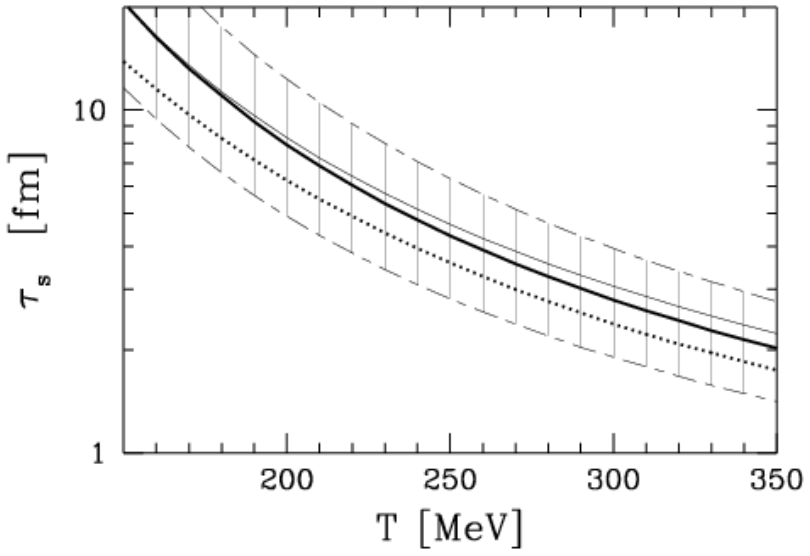

Figure 2.3: The relaxation time for strangeness saturation in a Quark-Gluon Plasma as a function of temperature. This is obtained from the ratio of the equilibrium density to the rate of the thermal production of strangeness [29]. The two solid lines [25] and the dashed line were obtained for different assumptions on the strong coupling constant α_s. The vertical lines represent the uncertainties, which are mainly due to the uncertainty on the mass of the strange quark.

and by normalising by the average number of participating nucleons (N_{part}) in the former collisions:

$$E = \frac{Y_h^{AA}}{< N_{part} > Y_h^{pp}} \quad , \tag{2.1}$$

where Y_h is the yield of the hyperon defined as the number of particles produced. From the equation above, it can be expected that in the case where no strangeness enhancement occurs (E=1), the production of strangeness in nucleus–nucleus collisions scales with N_{part}. As the collisions between the nuclei become more central, thereby involving more nucleons, the system is expected to be bigger and more conducive to the formation of a QGP, in which case the strange particle yields should go up considerably. A different way of expressing this enhancement is by comparing the yields of strange hadrons to those of pions (Y_π^{AA}), in other words by measuring the hyperon-to-pion ratio. This is a equivalent to equation 2.1, assuming the pion yield

scales with N_{part}:

$$E = \frac{Y_h^{AA}/Y_\pi^{AA}}{Y_h^{pp}/Y_\pi^{pp}} \quad . \tag{2.2}$$

In the case of strangeness having fully equilibrated with the system, presumably in a partonic phase of de-confinement, the hyperon-to-pion ratio takes a maximum value. That value can be predicted using a statistical physics approach for the hadronic yields, as will be discussed in the theoretical part of this chapter.

The enhancement of strange particles is particle-dependent. In environments of low strange quark density, it is for instance easier to form a Λ, than it is to form a Ξ^- or even a Ω^-, as the former only has one constituent strange quark. Hence, the yield of the Λ will deviate less from its equilibrium value, and its enhancement is smaller, as the strange quark density goes up. Strangeness enhancement therefore follows a hierarchy dependent on the strangeness quantum number of the hyperon:

$$E(\Lambda_{(uds)}) < E(\Xi^-_{(dss)}) < E(\Omega^-_{(sss)}) \quad . \tag{2.3}$$

2.2.1.1 Experimental review

Measurements of enhanced strangeness production in heavy-ion collisions were reported by the fixed-target WA85, WA94 and WA97 experiments at the CERN Super Proton Synchrotron (SPS) in sulphur-tungsten (S–W), sulphur-sulphur (S–S) at 200 A GeV/c and Pb–Pb collisions at 158 A GeV/c per beam [30, 31, 32]. The results from these collaborations showed that the production of Λ, $\bar{\Lambda}$, $\Xi^\pm$ and $\Omega^\pm$ in heavy ion collisions was larger than in p–W, p–S and p–Pb collisions, more so than if the production scaled simply with $\langle N_{\rm part}\rangle$. The Ω^- hyperon, which experienced the largest increase in production, were found to be enhanced by about ten times more than with $\langle N_{\rm part}\rangle$ scaling, and the first observations of a hierarchy of this phenomenon dependent on the strange quantum number of the particle was made. At the same

momentum per beam nucleon, the NA49 experiment observed the same phenomenon for Λ, $\bar{\Lambda}$[33] and $\Xi^{\pm}$[34].

The STAR (Solenoid Tracker at RHIC) experiment at the Relativistic Heavy-Ion Collider (RHIC) in Brookhaven observed a relative increase in the production of strangeness in Au–Au collisions with respect to pp at $\sqrt{s_{NN}}$=200 GeV of a factor of around 3, 5, and 10 for Λ, Ξ^{-} and $(\Omega^{-} + \overline{\Omega}^{+})$ hyperons, respectively [35]. Finally, in 2013, ALICE published its own measurements of the multi-strange hadrons in Pb-Pb collisions at $\sqrt{s_{\mathrm{NN}}} = 2.76$ TeV [35]. As can be seen in Figure 2.4, the relative increase of the hyperon-to-pion ratio from pp to Pb–Pb collisions is of 1.5–1.6 for Ξ^{-} and of about a factor 3 for Ω^{-}. Furthermore, the ratios obtained in the 60% most central Pb–Pb collisions (four data points with highest $\langle N_{part} \rangle$) appear to be constant for both $\Xi^{\pm}$ and $\Omega^{\pm}$, in agreement with indications from RHIC of the presence of an onset of the strangeness saturation being reached already in non-central A–A collisions, starting at $\langle N_{\mathrm{part}} \rangle \sim 150$.

2.2.2 Hydrodynamic flow

The large energy densities created in heavy-ion collisions, which lead to the formation of a thermalised plasma, build up radially outward pressure gradients against the surrounding vacuum. As a result, the particles composing the system experience a common radial boost which shifts their momenta to higher values. This effect, known as collective flow, can be observed through various observables:

- A *hardening* of the spectra of measured hadrons, characterised by an increase in the $\langle p_{\mathrm{T}} \rangle$ in systems undergoing collective flow. The shape of the p_{T} spectra become flatter at high momenta.

- A mass-dependent hierarchy of the increase in $\langle p_{\mathrm{T}} \rangle$ As the collective boost provides equal velocities to every particle, more massive particles gain more momentum.

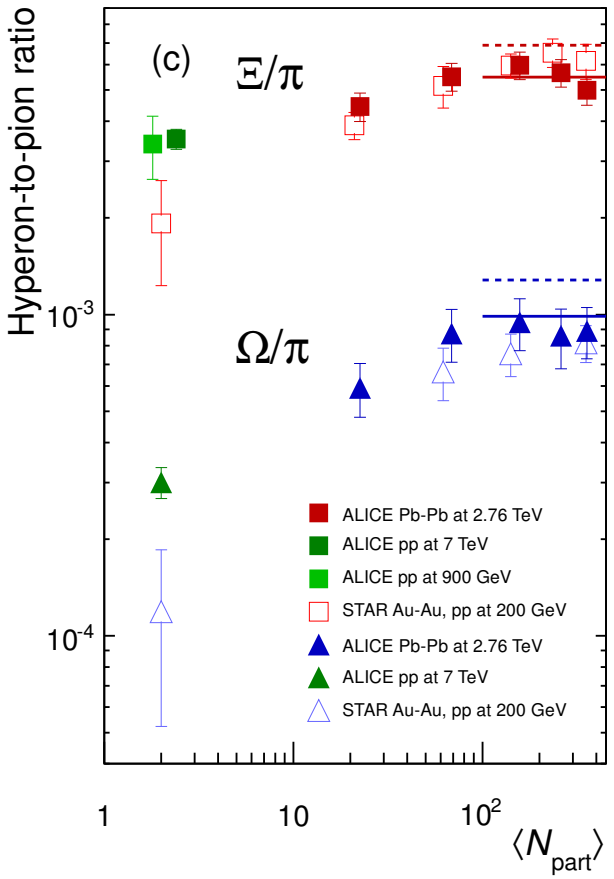

Figure 2.4: Ξ/π and Ω/π ratios as a function of $\langle N_{\rm part}\rangle$ in ALICE pp and Pb–Pb collisions as well as in STAR Au–Au interactions at 200 GeV [35]. The most central A-A results are compared with thermal model predictions for a chemical freeze-out temperature of 164 MeV (full line) and 170 MeV (dashed line).

- Spatial structure in two-particle correlations, observed when studying the correlation between particles separated in azimuthal angle φ and in the pseudorapidity η defined as:

$$\eta = \ln\left(tan\frac{\theta}{2}\right) = \frac{1}{2}ln\left(\frac{p+p_L}{p-p_L}\right) \quad , \tag{2.4}$$

where p is the magnitude of the particle three-momentum and p_L its longitudinal component with respect to the beam axis. The angle θ is the angle defined by the momentum vector of the particle and the beam axis. [1]

[1]Pseudorapidity is a relativistic approximation of *rapidity*, expressed as $y = \frac{1}{2}ln\left(\frac{E+p_L}{E-p_L}\right)$, where E is the energy of the particle

Strong peaks are observed for $\Delta\varphi \sim 0$ and $\Delta\varphi \sim \pi$ between particles, and those peaks are elongated across the measured pseudorapidity range [36, 37]. This *double-ridge* observation is suggestive of a collective behaviour between all hadrons of the system, and will be discussed later in section 2.4.

Statistical models incorporate a hydrodynamical expansion to describe the transverse momentum distributions of the hadrons that participate in collective flow effect. Such models will be introduced later in the theory sections of this chapter.

2.2.2.1 Elliptic flow

If the nucleus-nucleus collision is perfectly central, with zero impact parameter (b=0)[2], and there are no initial nucleus deformations, then the radial expansion is isotropic, and the fireball expands equally in both x and y directions. However, in the vast majority of events, this is not the case and the overlapping area of the collision takes an elliptic shape. Consequently, the initial geometry of the fireball is not spherical and pressure gradients of different magnitudes in different directions build up (see Figure 2.5).

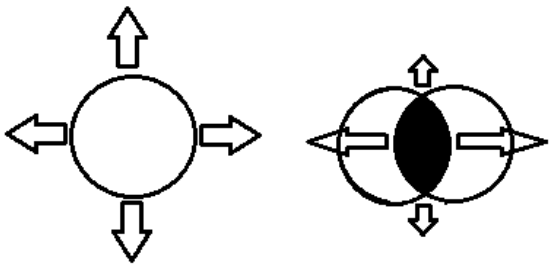

Figure 2.5: Sketch illustrating radial (left) and elliptic (right) flow in the transverse plane with respect to the beam axis. Note the unequal size of the pressure gradients in the latter case, represented by the arrows.

The spatial eccentricity translates into the momentum space as the produced par-

[2]Impact parameter is defined as the distance between the centres of the 2 colliding nuclei in the transverse plane; see section 4.1.

ticles undergo scattering processes. The momentum anisotropy reaches a maximum when the expansion becomes isotropic. Studying the momentum distributions of the produced particles is therefore a good approach to obtain information about the anisotropy of the collective flow. The elliptic flow coefficient (v_2) associated to a given particle is defined as the second Fourier coefficient of the expanded transverse momentum (p_T) spectrum as a function of the azimuthal angle φ with respect to the impact parameter vector ($\vec{b}$) [38]:

$$\frac{\mathrm{d}^3N}{\mathrm{d}yp_T\mathrm{d}p_T\mathrm{d}\varphi}(b) = \frac{1}{2\pi}\frac{\mathrm{d}^2N}{\mathrm{d}yp_T\mathrm{d}p_T}(b) \times \left(1 + 2\sum_{n=1}^{\infty} v_n cos(n\varphi)\right) \quad . \tag{2.5}$$

Thus:

$$v_2 = \langle \cos(2\varphi) \rangle \mid_{p_T,b} \quad . \tag{2.6}$$

The v_2 coefficient is largest for more *peripheral* collisions, in which the nuclei interact least with each other (larger impact parameter b), and decreases towards more head-on (central) collisions, as was measured in ALICE for identified hadrons in Pb–Pb events [39].

As equation 2.5 demonstrates, radial flow can be studied when neglecting the φ dependence of the momentum distributions, normalising the p_{T} spectrum by 2π.

2.2.3 Jet suppression

High momentum partons, which give rise to jets upon hadronisation, are produced in hard scatterings. In the presence of a QGP, the p_{T} of such partons is expected to soften due to the interaction with the medium. This energy loss can happen either through inelastic processes of gluon radiation [40] as the partons traverse the medium, or as a result of elastic collisional processes. The effect is illustrated in Figure 2.6.

The main experimental observable for this suppression effect is the nuclear modifica-

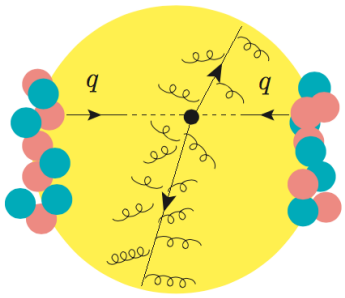

Figure 2.6: An illustration of two back-to-back jets created in heavy-ion collisions, and their energy loss in the medium.

tion factor R_{AA} as a function of p_{T} , which is defined as the ratio of the p_{T} –differential particle yield in A–A collisions (dN^{AA}/dp_T) to the yield in pp events (dN^{pp}/dp_T) in a given rapidity window [41]:

$$R_{AA}(p_T) = \frac{1}{\langle N_{coll} \rangle} \frac{1/N_{AA} \;\; \mathrm{d}N^{AA}/\mathrm{d}p_T}{1/N_{pp} \;\; \mathrm{d}N^{pp}/\mathrm{d}p_T}. \tag{2.7}$$

The yield in pp collisions is scaled by the average number of partonic interactions (N_{coll}) in the A–A interactions, which can be obtained from calculations with the Glauber model, as will be explained in chapter 4. The R_{AA} factor is calculated for particles expected to undergo a suppression in heavy-ion collisions. For an R_{AA} smaller than one, a suppression of the measured particles in the medium is observed. A measurement of $R_{AA} = 1$ indicates that there is no suppression, as if the nuclear collisions were a superposition of individual pp interactions.

The R_{AA} for charged hadrons is shown in Figure 2.7 as a function of p_{T} [41], measured in Pb–Pb collisions by the ALICE experiment. The ratio is smaller than unity, more so in central collisions (the 0-5% centrality class) than in peripheral collisions (the 70-80% class). At low p_{T}, the behaviour of the R_{AA} is a combination of the contributions from the soft and the hard processes, resulting in a peak at ∼2 GeV/c. As the p_{T} increases, jet suppression starts to dominate, and the nuclear modification factor reaches a minimum of smaller than 0.2 at a p_{T} of ∼6.5 GeV/c. For larger values of

p_{T}, the suppression is slowly reduced as harder jets are more resistent to the medium. On the right side of the figure, the R_{AA} of central collisions measured with ALICE is compared to measurements from earlier experiments which operated at smaller energies. The ALICE results show the strongest suppression of charged hadrons, indicating a denser, longer-lived plasma in higher centre-of-mass collisions.

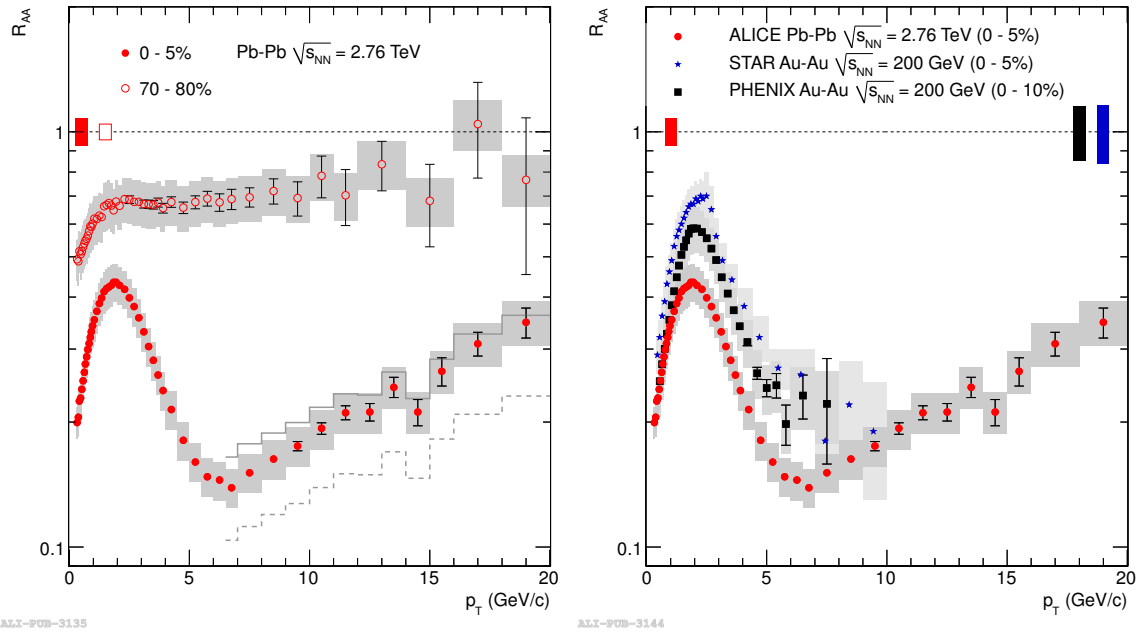

Figure 2.7: The R_{AA} of charged particles measured with ALICE (left) in central (0-5%)) and peripheral (70-80%) Pb–Pb collisions (left). The results from central collisions are compared to measurements performed at RHIC (right). [41]

A different method to observe the suppression of jets is by searching for a momentum imbalance in back-to-back jets [42, 43, 44, 45]. Such measurements are based on the idea that if one jet is closer to the edge of the medium, it may traverse less of the plasma and experience a smaller suppression than its counterpart (see Figure 2.6).

2.2.4 Charmonium suppression

In chapter 1, Debye screening was introduced as an effective description for quark-gluon de-confinement. Hadrons fail to form when the Debye length λ_D is smaller than their radius, which for $J/\psi(c\bar{c})$ mesons is of the order of 0.2-0.3 fm [46]. When a

QGP medium is formed in heavy-ion collisions, a c and $\bar{c}$ pair will not form a bound charmonium state. Instead the two quarks are separated by the interaction with other partons in the medium, until they finally hadronise with other more abundant quarks into open charm hadrons. The suppression of charmonium states in A–A collisions with respect to pp is therefore a key signature of the QGP.

While such a suppression has been observed in previous heavy-ion collision experiments, the degree to which J/ψ particles are suppressed depends on the centre-of-mass energy of the collisions studied. In fact, the suppression is seen to decrease from SPS to RHIC and LHC experiments. The favoured interpretation has been an increase of (re)combination processes at hadronisation between c and $\bar{c}$ quarks, due to an increased production of heavier quarks as a function of the centre-of-mass energy in the original nucleon–nucleon collisions [47].

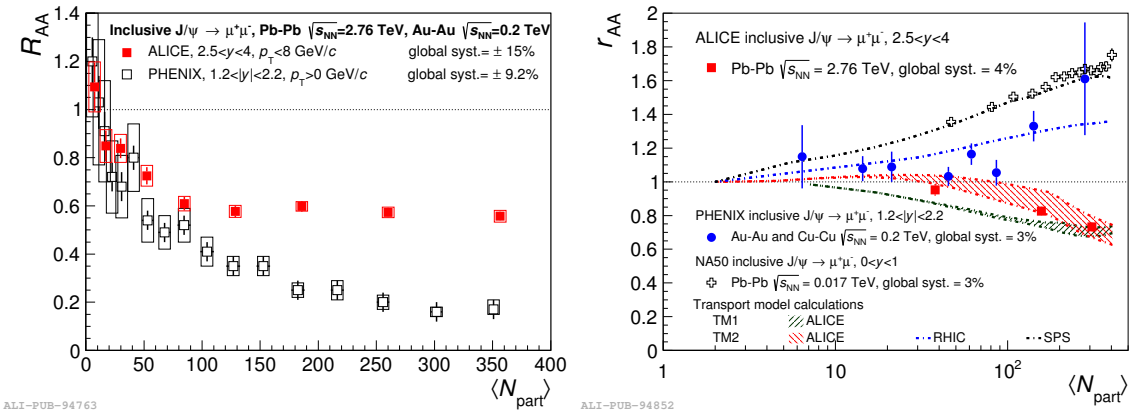

Figure 2.8: The J/ψ integrated R_{AA} as measured with ALICE [48] and PHENIX [49] in forward rapidity ranges as a function of the number of participating nucleons in the Pb–Pb (Au–Au) collisions (left). In addition, a comparison of the measured $r_{AA}(N_{part})$ distributions of the charmonium state with NA50 at $\sqrt{s}$ =0.017 TeV [50], the PHENIX experiment at $\sqrt{s}$ =0.2 TeV [49][51] and the ALICE detector at $\sqrt{s}$ =2.76 TeV [52] (right).

Indications of charmonium (re)combination are seen in Figure 2.8, which compares the R_{AA} and the ratio of the squared J/ψ transverse momentum in A–A relative to

pp collisions ($\mathrm{r}_{AA} = \langle p_T^2 \rangle_{AA} \,/\, \langle p_T^2 \rangle_{pp}$), measured in different experiments conducted at different collision energies. While the R_{AA} measured with the ALICE experiment indicates a suppression, the PHENIX experiment at RHIC measured a stronger effect, for a centre-of-mass energy smaller by a factor ten. When charmonia get suppressed, the population of their p_{T}-distribution experiences a shift toward higher values, as the suppression affects the low-p_{T} region more. This is reflected by an increasing r_{AA} as a function of N_{part}, which was measured by the NA50 experiment at $\sqrt{s} = 17$ GeV. This increase is less pronounced at RHIC energies, while at the LHC r_{AA} is measured to be smaller than unity (see Figure 2.8).

2.2.5 Direct photons

An important characteristic of the Quark-Gluon Plasma is its temperature. This value is for instance relevant in order to assess whether strange quarks can equilibrate with lighter quarks in the medium, since the thermal production of s-quarks is favoured the higher the temperature of the medium (see section 2.2.1).

Determining the temperature of the QGP in A–A collisions experimentally is not straightforward. However an estimate can be extracted from the measurement of direct photons, which are those photons that do not arise from the decays of hadrons and, therefore, are the result of prompt production in the original nucleon–nucleon collisions, as well as of thermal production in the QGP. The thermally emitted photons are expected to appear as an excess in the p_{T} spectrum of the direct photons. That excess can be described by an exponential decay function with temperature as an inverse slope parameter. Since thermal photons are emitted throughout the whole expansion of the de-confined medium, the value of that parameter reflects in fact the average temperature of the QGP during its lifetime. In Pb–Pb collisions, ALICE measured an effective temperature of 297±42 MeV in the 20% most central collisions (collisions with largest number of nucleon–nucleon interactions) [53], which exceeds

the 239±26 MeV measured in the less energetic Au–Au collisions at RHIC recorded with the PHENIX experiment [54].

2.2.6 Short-lived resonances

In addition to the experimental observations related to the Quark-Gluon Plasma, it is also of relevance to study the hadronic phase that follows. Resonances with sufficiently short lifetimes are good probes of the period between hadronisation and kinetic freeze-out, i.e. the moment elastic interactions cease. In energetic head-on heavy-ion collisions, the number of hadrons after the QCD phase transition can be large enough that they exchange momentum with each other before the final spectra are established. Very short-lived particles may decay during that period. The production of $K^{\star 0}$ resonance, which has a mean lifetime of 4.16 ± 0.05 fm/c [26], has been observed to decrease in very central Pb–Pb collisions with respect to the longer-lived K^{-}, indicating that they might indeed decay before kinetic freeze-out [55]. $K^{\star 0}$ predominantly decay into a charged π and K pair. The π daughter meson is then more likely to interact with another π than to engage with a K and regenerate the original resonance. In that case the resonance cannot be reconstructed through its decay products, which reduces its measured yield. Such studies help estimate a lower-limit for the duration of the interactive hadronic phase before freeze-out. Similar studies can be performed with other resonances of short lifetime, such as the ρ meson with a mean lifetime of around 1.4 fm/c [26].

2.3 Theoretical models

2.3.1 The Statistical Hadronisation Model

As was discussed earlier, the production rates of strange particles relative to non-strange hadrons in high-energy collisions play a very important role in revealing information about the evolution of the created system. In this section, the Statistical Hadronisation Model (SHM) is introduced and placed in the context of strangeness production. The SHM [56, 57, 58, 59] assumes a common source for all hadrons in thermal equilibrium, which originates at the moment of hadronisation, thus ignoring the conditions in the partonic phase preceding hadronisation. Relative particle yields can be predicted assuming a state of chemical equilibrium following a statistical description that depends on the temperature at chemical freeze-out, the volume of the hadronic system, and the chemical potential in it. As will be seen, this model has been able to reproduce, with some success, the particle yields, yield ratios and momentum spectra observed both in elementary and heavy-ion collision experiments. Canonical and grand canonical approaches are taken to describe systems of different sizes and particle multiplicities. The two cases will be described in the following sections.

The principles behind the SHM originated from the work of Fermi [60], and later Hagedorn in [61], where particles produced in a collision experiment were modelled as originating from a thermally equilibrated massive source, which is here called *cluster* or *fireball*. This cluster decays into hadrons according to the laws of statistical physics. Such a description was considered appropriate for heavy-ion collisions where it is assumed that the hadronisation occurs in a state of established thermal equilibrium due to an earlier formation of a Quark-Gluon Plasma, but has surprisingly also been found to exhibit good agreement with the data in smaller collision systems. Not only is the extracted hadronisation temperature in elementary collisions similar to that obtained in A-A collisions, but it is also close to the QCD critical temperature T_{cr}. It

is not yet understood why small systems with very low numbers of produced particles seem to be compatible with a thermal description.

2.3.1.1 Heavy-ion collisions as grand canonical ensembles

Large systems, such as those produced in heavy-ion collisions can be treated as Grand Canonical (GC) ensembles. In such a system, the conservation of the strangeness S, baryon B and electric charge Q quantum numbers is applied on average. This means that small event fluctuations on these quantities are permitted, since they are negligible with respect to the large number of particles present in the system. Chemical potentials for these quantities are thus introduced in the partition function, from which the event-averaged particle multiplicities are derived:

$$\begin{aligned} < N_j^{GC} > &= \gamma_S^{N_j^s} \frac{g_i V}{2\pi^2} \sum_{n=1}^{\infty} (\pm 1)^{n+1} \frac{m_j^2 T}{n} K(\frac{n m_j}{T}) e^{n\beta \boldsymbol{\mu_j}} \\ &= \gamma_S^{N_j^s} \sum_{n=1}^{\infty} W(m_j, V, T) e^{n\beta \boldsymbol{\mu_j}} \\ &= \gamma_S^{N_j^s} \sum_{n=1}^{\infty} W(m_j, V, T) \lambda_j(\boldsymbol{\mu_j}, T) \quad . \end{aligned} \tag{2.8}$$

In the equation above, $< N_j^{GC} >$ is the mean multiplicity density of particle species j, m_j its mass, $\beta = 1/T$ is the inverse of the hadronisation temperature T of the system, V its mean volume, and K is the modified Bessel function. The chemical potential parameter in the *fugacity* λ_j:

$$\boldsymbol{\mu_j} = B_j \mu_B + Q_j \mu_Q + S_j \mu_S \tag{2.9}$$

keeps the system in equilibrium on average. Each of the three components of the chemical potential is related to the net baryon (B), electric charge (Q) or strangeness (S) number densities, respectively.

For the production of strange particles, an additional parameter γ_s is introduced in the particle multiplicity expression, defined between 0 and 1. It is a non-derived, ad

hoc parameter, referred to as the *strangeness undersaturation factor*, which is implemented in order to account for the deviations from strangeness saturation observed in the data. Its exponent N_j^s is the number of strange valence quarks of hadron j. When the extracted γ_s parameter is found to be unity from data fits, strangeness is interpreted as being in equilibrium with the system. This allows one to infer the likely existence of a preceding partonic QCD phase of de-confined matter favourable for strangeness to equilibrate with the system. As γ_s goes up, the increase in the multiplicity of a strange hadron depends on the number of strange quarks of that hyperon. This hierarchy (see equation 2.3) is accounted for by the exponent S on the γ_S factor.

2.3.1.2 Strangeness suppression in small collision systems

In collisions between elementary hadrons or leptons, the conservation laws can no longer be applied on average, as, due to the small number of particles produced, fluctuations are comparable to the mean event multiplicities. Thus one has to resort to a Canonical (C) treatment, in which exact local conservation of S, B and Q is implemented. In this case, the fugacity term in the mean number of particles in the system is replaced by so-called *chemical factors* C^j_{BSQ} :

$$\begin{aligned} < N_j^C > &= \gamma_S^{N_j^s} \sum_{n=1}^{\infty} W(m_j, V, T) \frac{Z(B - B_j, S - S_j, Q - Q_j)}{Z(B, S, Q)} \\ &= \gamma_S^{N_j^s} \sum_{n=1}^{\infty} W(m_j, V, T) C^j_{BSQ} \quad , \end{aligned} \tag{2.10}$$

which can be written as:

$$< N_j^C >= C^j_{BSQ} < N_j^{GC} > |_{\boldsymbol{\mu_j}=0} \quad . \tag{2.11}$$

In equation 2.10, Z is the canonical partition function. The chemical factors are never bigger than unity and decrease with a reduction in the phase-space of the system.

This results in a decrease of the number of particles in the system as a function of its size. Therefore, while the production of strange particles in large systems is said to be enhanced with respect to small collision systems, according to the experimental enhancement concept introduced in 2.2.1, in the SHM it can be interpreted as being suppressed with respect to the Grand Canonical equilibrium value. This suppression may be driven by C^j_{BSQ} and by γ_S. For sufficiently large volumes, $C^j_{BSQ} \to \lambda j$ and the system is described by the GC formalism, in which the γ_S factor drives the suppression of strange particles.

The resonance $\phi(s\bar{s})$, being a hidden strange particle with strangeness quantum number equal to zero, does not undergo canonical strangeness suppression, i.e. suppression according to the restrictions of the available phase-space, with respect to non-strange quarks. This meson can however deviate from its grand canonical limit by a γ_S^2 factor.

2.3.1.3 Comparisons with data

Fits to hadronic yields from high energy collisions have been performed over the last decades, covering collisions of a wide range of centre-of-mass energies, and revealing good compatibility between data and model in heavy-ion collisions as well as in smaller systems. As an example, figure 2.9 shows the results of a Grand Canonical fit to central Pb–Pb collisions in ALICE [62]. The extracted parameters and the corresponding calculated particle yields are compared to the data. For an extracted freeze-out temperature of around 156 MeV and a zero chemical potential, all measured yields are consistent with the model within 2 standard deviations (σ), except for the $K*^0$ resonance and the protons, which deviate by up to 3σ. The thermal model fit has a χ^2_{red}/ndf ratio of 2.4 [3].

Figure 2.10 summarises a large set of thermal model fits to data from experiments

[3] ndf: number of degrees of freedom

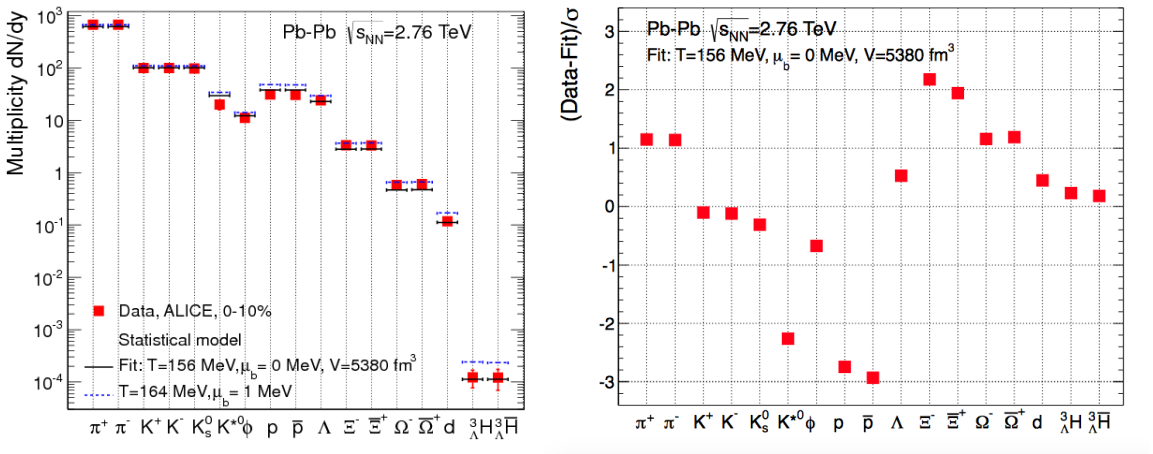

Figure 2.9: Left: Results of SHM fits to ALICE Pb–Pb data, and comparison with calculations with parameter values from a thermal model fit to data from heavy-ion collisions at RHIC (T=164 MeV). Right: Data-model difference for the various hadron yields normalised to the respective experimental uncertainty (σ) [62].

conducted in the AGS, SPS, RHIC and LEP synchrotrons. The chemical freeze-out temperature and baryon chemical potential are plotted as a function of the centre-of-mass energy. While, the temperature is seen to increase to a limit of around 160 MeV, μ_b approaches zero with increasing energy. These observations combine studies of elementary (e^+e^-) with those of heavy-ion collisions.

With regard to the SHM, the measurements presented in chapter 4 provide a good opportunity to obtain new insights into the onset of the lifting of canonical suppression on one side, and possibly the onset of strangeness enhancement on the high-multiplicity side. This is because they probe a multiplicity range intermediate between the Pb–Pb, where the enhancement of strangeness has been observed as shown earlier in this chapter, and pp data.

2.3.1.4 The core-corona superposition of A-A collisions

A possible interpretation of the γ_s <1 observations in non-central heavy-ion collisions is given by the core-corona superposition model [73, 74]. This model treats heavy-ion collisions as a superposition of i) a fully thermally equilibrated core and ii) an outer region of single nucleon–nucleon (N–N) collisions. In this picture, the

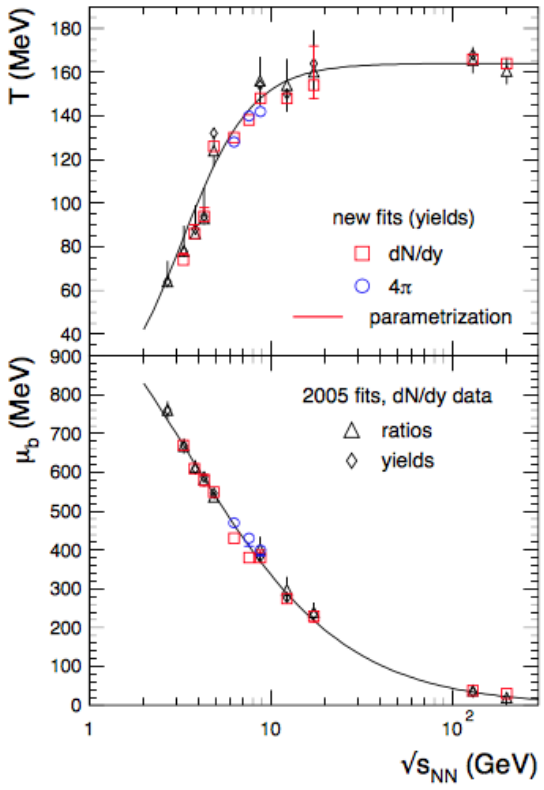

Figure 2.10: The chemical freeze-out temperature and baryon chemical potential as a function of the centre-of-mass energy of high energy collisions. The data were obtained from SHM fits to measurements in heavy-ion collisions at AGS [63, 64], SPS [65, 66, 67], and RHIC [68, 69] experiments. In addition, fits to data from elementary e^+e^- collisions at LEP, the Large Electron-Positron collider of CERN at different energies (including the highest 130 and 200 GeV) are also on the figure [70, 71]. (Figure taken from [72])

core is modelled as a grand canonical ensemble, whereas the individual N–N interactions give rise to canonical systems. As a result, the yields of strange particles are affected both by the enhancement associated with the thermalised source at the centre and the canonical suppression effect due to the hadron-hadron interactions in the corona region. The latter effect becomes more dominant in more peripheral A–A collisions, whereas head-on collisions produce one fully equilibrated system only.

This model was proposed as a result of the observations that the canonical formalism is not able to describe the centrality dependence of hyperon yields in heavy-ion collisions. In STAR, with Au-Au collisions at $\sqrt{s_{\rm NN}}$= 200 GeV, a continuing increase of

hyperons with centrality was measured, even in the region $\langle N_{\text{part}} \rangle > 100$, where the canonical description would predict a saturation [75]. Similarly, the ϕ/π meson ratio is found to increase with centrality, while in a canonical ensemble this ratio would remain constant. Figure 2.11 shows this enhancement as measured by the STAR experiment [76]. These observations cannot be due to canonical conservation laws, and must be accounted for by the γ_S parameter in the GC formalism.

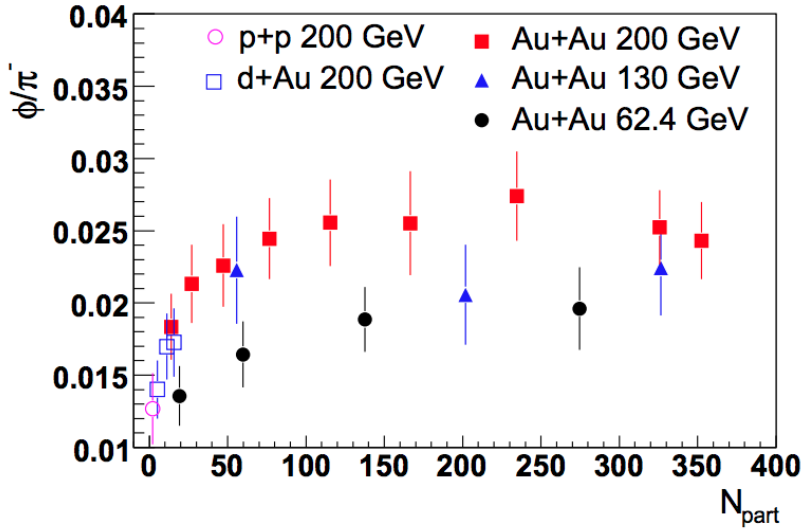

Figure 2.11: The ϕ enhancement normalised to the π yield as a function of $\langle N_{\text{part}} \rangle$ in Au–Au collisions as measured by STAR at centre-of-mass energies of 62.4, 130 and 200 GeV compared to pp and d–Au measurements at $\sqrt{s_{\text{NN}}} = 200$ GeV [76].

The presence of a fully equilibrated central region for every centrality in heavy-ion collisions in the core-corona interpretation, is motivated by the finding that SHM fits to data reveal a constant chemical freeze-out temperature across all centralities. An example is the extracted T parameter around 165 MeV in all five centrality classes of Au–Au collisions at $\sqrt{s_{\text{NN}}}$= 200 GeV in the STAR experiment at RHIC [77], while γ_S increases with increasing centrality. Instead of γ_S, it is proposed that the enhancement of strange particle production towards equilibrium is due to the change in the weight of contributions from the core and the corona effects. Calculations show that this model obtains a hierarchy of the increased production of hyperons, including

the ϕ meson, in accordance with measurements at RHIC [76] and at the LHC [78]. This model was also shown to reveal good agreement with the centrality dependence of hyperon yields measured at SPS and RHIC [79]. Figure 2.12 shows the relative contributing fractions of the core and corona regions according to the model.

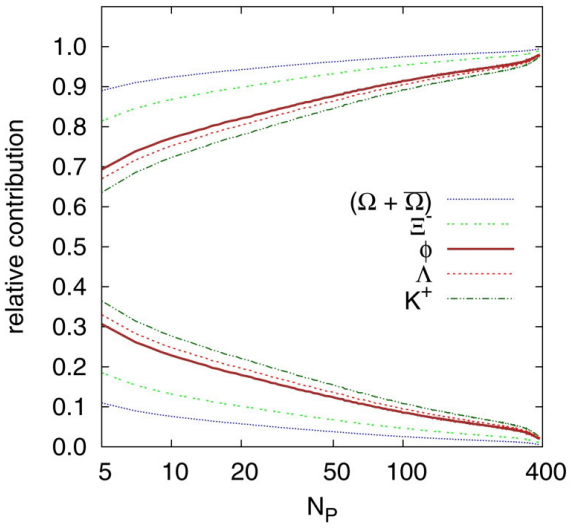

Figure 2.12: The relative contributions of the core (upper curves) and the corona (lower curves) in A–A collisions as a function of the number of participant nucleons N_p [74].

2.3.2 Transverse momentum distribution of hadrons

In this section, two statistical models are introduced, which describe the transverse momentum distributions of hadrons. As will be discussed, the Boltzmann-Gibbs *Blast-Wave* [80] introduces a boost in the transverse momentum in order to account for the collective flow experienced by the particles, an effect which was the subject of section 2.2.2. The *Lévy-Tsallis* [81] approach is a generalisation of the Boltzmann-Gibbs description, which can also reproduce particle spectra at high-p_{T}, where contributions from hard processes are relevant. The functions obtained for the momentum distributions are of importance for the analysis presented later, as their validity can be tested by the measured spectra, and in addition they can serve as useful fits in order to extract the p_{T}-integrated yields.

For the scope of the work reported in this thesis only radial flow is considered, which means that any azimuthal dependence of the outward expansion is ignored in the transverse momentum distribution of hadrons:

$$\frac{\mathrm{d}^3N}{\mathrm{d}y\mathrm{d}p_T\mathrm{d}\phi} = \frac{1}{2\pi}\frac{\mathrm{d}^2N}{\mathrm{d}y\mathrm{d}p_T} \quad . \tag{2.12}$$

It should also be noted that in addition, at LHC energies, the rapidity distribution of strange hadrons at mid-rapidity is expected - i.e. for small values of rapidity, $y \sim 0$ - to be flat [80], so in the later analysis the rapidity-differential component will be factored out, too.

2.3.2.1 The Boltzmann-Gibbs Blast-Wave model

The statistical distribution of the transverse momentum of a particular hadron originating from a thermalised source can be expressed by the Cooper-Frye formula [82]:

$$\frac{\mathrm{d}N}{\mathrm{d}y\mathrm{d}p_T} = \frac{gV}{2\pi^3}\sum_{n=1}^{\infty}(\pm 1)^{n+1}Ee^{-n(E-\mu)/T_k} \quad . \tag{2.13}$$

The temperature T_k is the instantaneous kinetic freeze-out temperature, i.e. the temperature of the system at which all hadronic scattering stops, and E is the energy carried by the hadron. In order to incorporate radial flow, a transverse boost is applied to the above p_T formulation. The transverse expansion velocity of that boost divided by the speed of light is defined as a function of the radius (r) from the explosive source as:

$$\beta_T = \left(\frac{r}{R}\right)^n \beta_S \quad , \tag{2.14}$$

where β_S is the velocity at the surface of the fireball, i.e. at radius R, and n is an exponent. From the above equations, it can be shown [80] that the shape of the p_T distribution at mid-rapidity in a system in thermal equilibrium undergoing a radial

expansion, can be described as:

$$\frac{1}{p_{\mathrm{T}}}\frac{dN}{dp_{\mathrm{T}}} \propto \int_0^R rdr\ m_T I_0\Big(\frac{p_{\mathrm{T}}\sinh\rho}{T_k}\Big) K_1\Big(\frac{m_T\cosh\rho}{T_k}\Big) \quad , \tag{2.15}$$

where

$$\rho = tan^{-1}(\beta_T) \quad . \tag{2.16}$$

I_0 and K_1 are the modified Bessel functions, $m_T = \sqrt{(p_T)^2 + m^2}$ is the transverse mass and m the rest mass of the particle.

This equation, known as the Blast-Wave function, predicts the p_{T} spectra of particles undergoing collective radial flow in heavy-ion collisions. Its free parameters are T_{kin}, the velocity β_T and the exponent n. At STAR [83, 84] and ALICE [85] it was found that a common set of parameters reproduces the p_{T} distributions of π, K, p, K^0_S and Λ. However, the multi-strange baryon p_{T} spectra were not in agreement with the curves obtained from those parameters. At RHIC [83], the Ξ and Ω were found to yield a common, hotter, kinetic freeze-out temperature and a smaller transverse flow velocity than the lighter particle species. This could be suggestive of an earlier freeze-out of the multi-strange particles due to their lower hadronic interaction cross-sections.

2.3.2.2 The Lévy-Tsallis function

In addition to the Blast-Wave function, a different approach based on Tsallis statistics [81] can be taken to attempt to describe the transverse momentum distribution of hadrons originating from a thermally equilibrated source. The Lévy-Tsallis function expresses the p_{T} distribution of hadrons as:

$$\frac{\mathrm{d}^2N}{\mathrm{d}y\mathrm{d}p_T} = \frac{(n-1)(n-2)}{nT_k[nT_k + m(n-2)]}\ \frac{\mathrm{d}N}{\mathrm{d}y}\ p_T\ \left(1 + \frac{m_T - m}{nT_k}\right)^{-n} \quad , \tag{2.17}$$

This equation assumes a Boltzmann-Gibbs–type exponential ($\propto e^{-p_T/T}$) at small p_T and a power-law at large p_{T} ($\propto T/np_T)^n$, and thus can describe the soft, thermal,

bulk of a hadronic system, and the particles from hard processes at large momenta.

2.4 Proton–lead collisions

The experimental observables introduced in the first part of this chapter have traditionally been the subject of efforts in analyses of collisions between heavy ions. In such collisions, a large number of particles originate from an initially small volume, fulfilling the large energy density conditions needed for plasma formation. Collisions between elementary leptons (electrons) or hadrons (protons), have served as a reference for comparisons, where in most cases, if not all, the latter conditions are not expected to be satisfied. Thus, many comparative studies, in which the same observables are measured in A–A and pp events have been made, and the observations lead to the conclusion of the existence of Quark-Gluon Plasmas in heavy-ion experiments.

Nevertheless, proton–proton collisions can be quite variable in nature. In ALICE, the average charged particle multiplicities in pp interactions at mid-rapidity at $\sqrt{s} = 7$ TeV have been measured to be around six, however, when the data were divided up into different multiplicity bins, it was found that the 5% highest multiplicity events recorded on average over 20 particles in the central rapidity region. According to the Bjorken formula [86] , the energy density (ϵ) in a high energy collision is proportional to the transverse energy (E_T) produced in the interaction per unit rapidity and inversely proportional to the thermalisation time, or the time it takes for the QGP to form τ_0:

$$\epsilon = \frac{1}{\tau_0 S}\frac{\mathrm{d}E_T}{\mathrm{d}y} \quad , \tag{2.18}$$

where S is the overlapping cross-sectional area between the two colliding particles. It is conceivable from the measured dE_T/dy carried by the produced particles, that energy densities as large as a few tens of GeV/fm^3 could have been reached already at

SPS energies [87]. For that reason, Bjorken predicted that QGPs could be formed in high multiplicity pp collisions, if the system thermalises at a timescale smaller than 1 fm.

Proton–lead (p–Pb) collisions produce numbers of charged particles intermediate between those achieved in pp and peripheral A–A. For the data analysis presented in this thesis, such data were, for the first time, sub-divided into different multiplicity bins, allowing the QGP observables to be studied in that intermediate range as a function of multiplicity.

Intriguing observations were made at the LHC with observations of a double-ridge structure (see section 2.2.2.1) in two-particle correlation studies, both in high multiplicity pp [88] and p–Pb [89, 90]. Figure 2.13 shows both the ridges (left) as measured by ALICE in the $\Delta\varphi\Delta\eta$ space and the peaks in $\Delta\varphi$ when integrated over pseudo-rapidity. This effect, suggestive of collective behaviour in the system, had previously only been observed in Pb–Pb collisions. These results were obtained in the 20 % most central p–Pb collisions (those with highest recorded multiplicity) after subtraction of more peripheral (low multiplicity) events, in order to remove correlations from jet contributions.

Furthermore, the Blast-Wave model, which assumes collectivity between all particles, was found to be compatible with the measured p_{T} distributions of π, K, and protons in high multiplicity pp events [91]. It has been argued by Shuryak et al in [92] that radial flow would be present in small collision systems too, and that in such a case, the effect would be more explosive due to larger pressure gradients per unit surface area, as was indeed observed. In recent ALICE measurements of the π, K, protons, K^0_S and Λ in p–Pb data have confirmed that in high-multiplicity data, the Blast-Wave model is compatible with the data, as the observed p_{T} shapes can be described by one

common set of free parameter values [91]. For similar charged-particle multiplicities, similar kinetic freeze-out temperatures were obtained from the simultaneous fits to the various p_{T} spectra in p–Pb and Pb–Pb data. However, the average transverse expansion velocity parameter $\langle \beta_T \rangle$ was found to be significantly larger in p–Pb, consistent with the picture of a more explosive system.

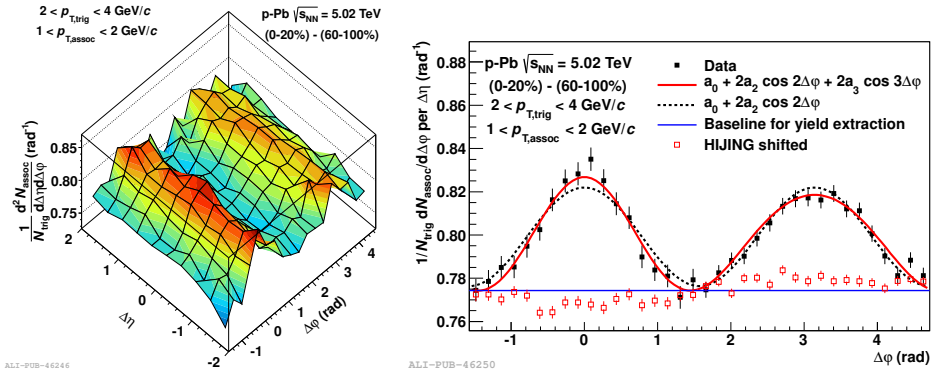

Figure 2.13: The double-ridge structure observed in two-particle correlations in the $\Delta\varphi\Delta\eta$ space (left), and projected onto $\Delta\eta$ (right). These observations were made in high multiplicity collisions in p–Pb collisions taken with the ALICE experiment [89]

Nuclear modification factors have also been measured in p–Pb collisions (R_{pPb}), and were found to be consistent with unity for hadrons, as for instance reported in [93] for D-meson production measurements. This suggests that suppression of high momentum particles is very weak as it must lie within the experimental uncertainty for each measurement. These measurements stand in contrast to what has been observed in A–A data, where a QGP medium is long-lived and composed of thousands of strongly interacting particles.

The measurement of strangeness production is an important observable for the search for QGPs in high multiplicity pp and p–Pb events. It can provide hints as to whether such plasmas may form in systems much smaller than those of central heavy-ion collisions, and whether the lifetime of that plasma is sufficiently long for strangeness to reach chemical saturation. The results of this work attempt to provide answers to

these questions.

In addition, non-QGP theories can be put to test. Theoretical models based on the concept that colour fields can be described by strings connecting partons, interpret the hadronisation process as the fragmentation of such strings [94]. Various predictions are made for the production of strange particles and the establishment of collective behaviour for different collision systems. These models will be introduced and discussed in the final chapter of this thesis.

Chapter 3

The ALICE Experiment at the LHC

In this chapter, the different systems that compose the complex ALICE experiment are described. Focus is given to the sub-detectors relevant to the work of the following chapters. In addition, the Central Trigger Processor of the experiment is also introduced in some detail.

3.1 The Large Hadron Collider

The Large Hadron Collider (LHC) is a circular proton and heavy ion accelerator and collider, located at CERN, through the border of Switzerland with France, near Geneva. Figure 3.1 depicts the LHC accelerator complex. It has a circumference of 26.7 km and is placed about 100 m underground. There are four major detectors at the LHC, at the centre of which bunches of protons or heavy ions travelling in opposite direction are aligned in order to produce a large number of high energy collisions. The ATLAS [95] and CMS [14] experiments are mainly dedicated in the searches for new particles predicted by the Standard Model (SM) and by theories beyond the SM. LHCb [96] focuses its efforts on understanding the matter-antimatter asymmetry in the early universe by observing the decays of b-hadrons, and ALICE [3] studies

the physics of strongly interacting matter in a QGP created in heavy-ion collisions. However, the physics programmes of each experiment are very extensive, and thus are complementary to or serve as cross-checks for the other experiments.

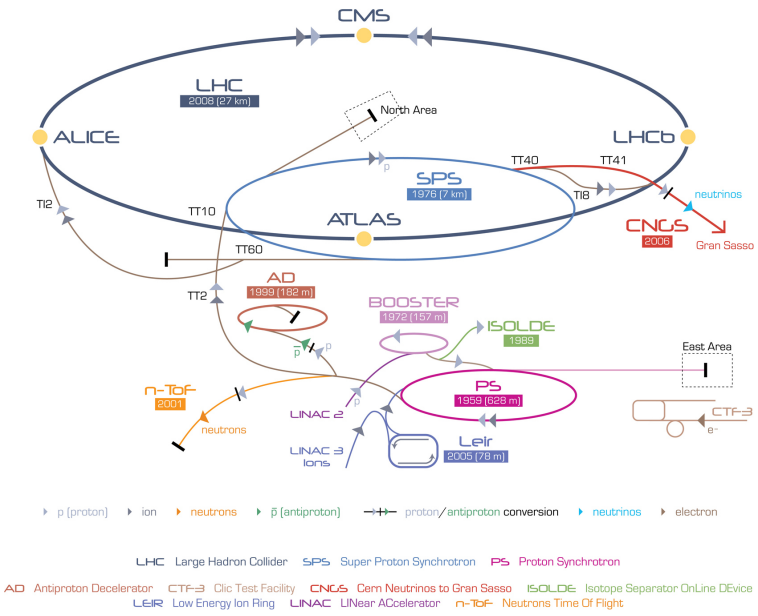

Figure 3.1: The CERN accelerator complex.[97]

The luminosities delivered to each of the four LHC experiments during the first p–Pb run conducted in 2013 are shown in Figure 3.2. The instantaneous luminosity captured by the ALICE experiment

$$\mathrm{d}\mathscr{L} = \frac{1}{\sigma_{pPb}} \frac{\mathrm{d}N_{ev}}{\mathrm{d}t} \quad , \tag{3.1}$$

where $\mathrm{d}N_{ev}/\mathrm{d}t$ is the interaction rate and σ_{pPb} the cross-section, is shown to have reached the nominal value of 10^{29} cm^{-2}s^{-1} for p–Pb collisions for the majority of the data collection period. The time-integrated luminosity reached around 32 nb^{-1}, similar to the values for the CMS and ATLAS experiments.

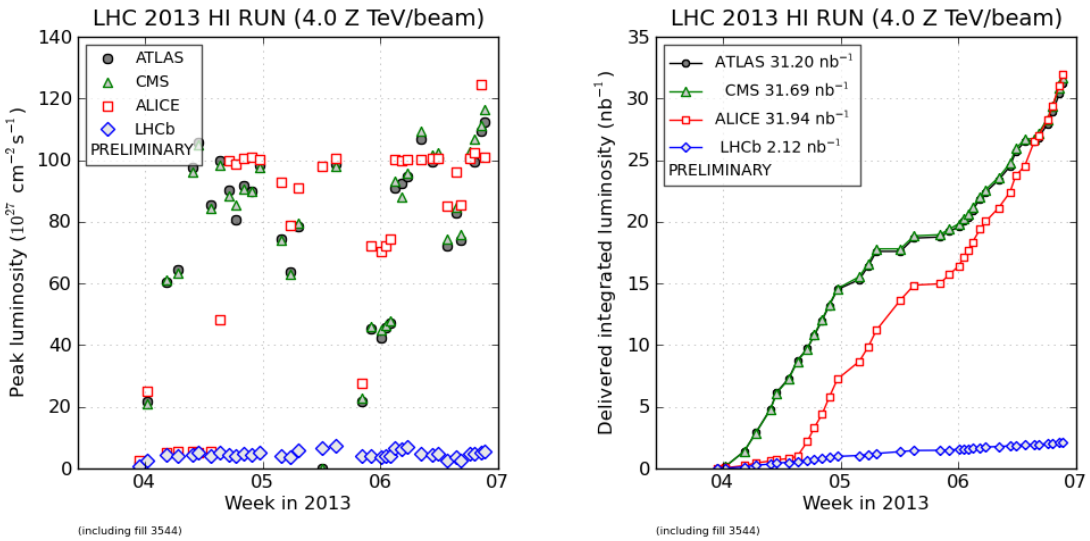

Figure 3.2: The instantaneous (left) and integrated (right) luminosities in the 2013 p–Pb collisions run at the LHC. [98].

3.2 The ALICE detector

The ALICE detector is located around 60 metres underground in St-Genis-Pouilly, near the French–Swiss border. This experiment is mainly dedicated to a heavy-ion physics programme, with a large number of studies based on collisions between Pb ions. Collisions between protons are also important, mainly serving as a reference for comparative studies. In addition, the intermediate p–Pb collisions are a suitable system in order to disentangle possible nuclear effects from the QGP effects observed in heavy-ion data.

ALICE is a complex detector, 26 m long, 16 m high and 16 m wide, and composed of 18 sub-systems shown in Figure 3.3. Its Cartesian coordinates are defined as follows: the beam axis is along the z-axis, being positive on the A-side of the detector, and negative on the C-side, the closest side to the CERN main site. The positive x-direction points towards the centre of the LHC ring and the positive y-direction points vertically upwards. A large solenoid houses the sub-detectors of the central

barrel of the ALICE experiment, placing them inside a uniform magnetic field of 0.5 T. Charged particles travel along curved trajectories under the influence of the field, and the curvature allows the measurement of their momenta.

The innermost barrel detectors are an Inner Tracking System (ITS) and a large Time Projection Chamber (TPC), which allow for most of the track reconstruction and - by measuring the energy loss in the active material of the detector - the identification of charged particles. The Transition Radiation Detector surrounds the TPC. It makes use of the radiative energy loss of charged particles as they traverse materials with a varying dielectric constant. The Time-Of-Flight detector (TOF) is a large set of gaseous multi-gap resistive plate chambers, sandwiched between two cathode pad plates and divided in two sections by a central anode plate. Five resistive plates placed parallel to each other within a length of less than 4 mm, attenuate the electron avalanche originated by the ionisation of the gas in the gaps produced by an incident charged particle. From the pulses received in the read-out pads from all the gaps, the TOF detector can determine the time at which the particle hits the detector with a resolution of 50 ps. Using momentum information from the TPC, the mass of the particle can be estimated, which is a very useful method for determining its identity, especially in momentum ranges where the TPC energy loss method - which will be discussed in section 3.2.2 - can least resolve between different particle masses. The High Multiplicity Particle Identification (HMPID) detector makes use of Cherenkov radiation to improve further the particle identification at high momentum. Two electromagnetic calorimeters, the EMCAL detector, based on Pb-scintillators, and the PHOS system, a scintillator detector based on lead tungstate crystals fill the remainder of the central barrel. They covering the restricted mid-rapidity gaps of $|\eta| < 0.7$ $|\eta| < 0.12$, respectively, and 110 and 100 degrees in azimuthal angle φ. Both detectors are applied in jet physics and direct photon analyses. On the positive y-side of the barrel, a cosmic ray detector (ACORDE) is placed on top of the ALICE magnet.

In the forward region, the T0 detector, a series of 12 quartz Cherenkov radiators coupled to photomultiplier tubes placed on both sides of the interaction point, with a timing resolution of 50 ps, determines the location of the primary vertex within 1.5 cm and provides a rough estimate for the event multiplicity. The Forward Multiplicity Detector (FMD), based on silicon strips and the V0 scintillators, also take measurements of the particle multiplicity in the forward region. A Photon Multiplicity Detector (PMD) is placed on the A-side of the detector at 361.5 cm from the interaction point. A 5 m long muon spectrometer is placed on the opposite side 7 m from the interaction vertex. The muon arm, covering the pseudorapidity range of -4.0< η <-2.5 uses a dipole magnet on its own of 0.67 T to measure the momenta of muons from charmonium and bottonium decays.

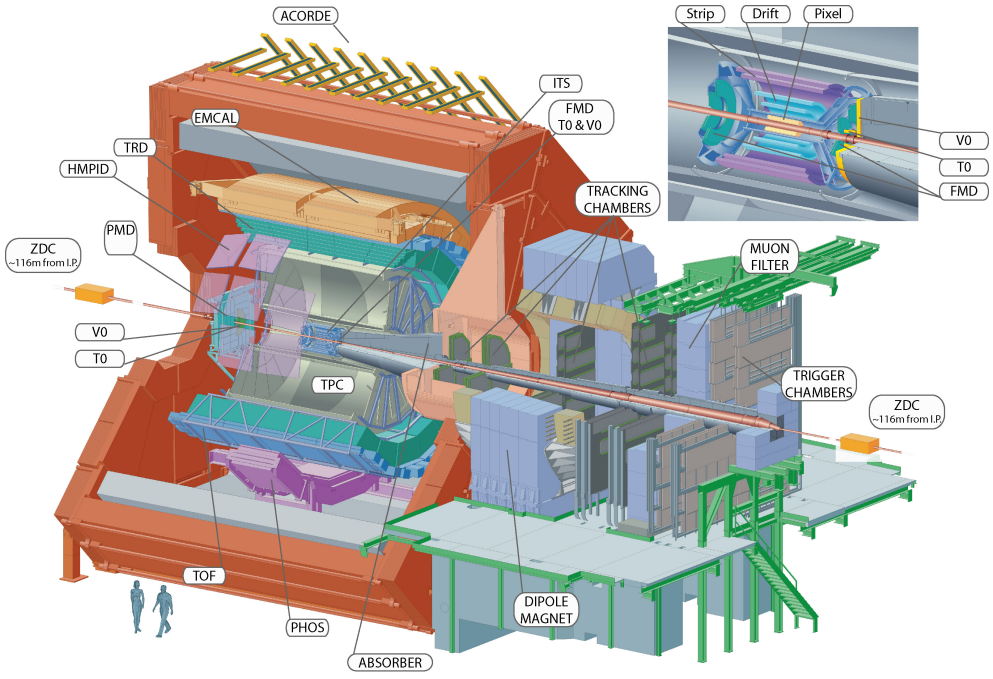

Figure 3.3: Schematics of the ALICE detector, with annotated subsystems. The ITS, TPC, TRD and TOF are the only detectors in the central barrel with a full 2π coverage of the azimuthal angle.

The ITS, TPC and V0 detectors, which were directly applied for the analysis discussed

in later chapters are now described in more detail.

3.2.1 Inner Tracking System

This section introduces the different layers of the Inner Tracking system (ITS). This detector is composed of six layers, that use different silicon detection techniques in order to meet the large track and momentum resolution requirements. Closest to the beam pipe, there are two silicon pixel layers, which are followed by two drift layers and two layers of silicon strips. The innermost layers are characterised by a very fine granularity, capable of dealing with thousands of charged particles that emerge in head–on Pb–Pb collisions.

3.2.1.1 The Silicon Pixel Detector

The innermost subsystem of ALICE is the Silicon Pixel Detector (SPD) [99, 100], which is composed of two layers of pixels containing 10^7 detector diodes, or *cells*. The layers are placed at radial distances of 3.9 cm and 7.6 cm away from the beam axis, are about 28 cm long and cover a pseudo-rapidity range of up to $|\eta| = 2.0$. The finest detector elements of the SPD are reverse-biased silicon diodes, which are bump-bonded onto pixel chips. Each such chip contains 256×160 cells. *Ladders*, made of a conjunction of 5 chips, are paired and connected to a multichip module (MCM) and powered by a *pixel bus*. Two coupled ladders build a stave that is placed parallel to the beam axis. At each end, the attached MCMs are responsible for transmitting signals to the SPD read-out system. The SPD is composed of 10 *sectors* made out of a carbon fibre structure, each supporting two staves in the innermost layer and four staves in the outer layer. This means that there are 60 staves, and 120 signals sent in parallel to the read-out system via optical cables. In Figure 3.4 an illustration of the different detector components is given.

The fine granularity achieved by the large number of microscopic pixels on the sil-

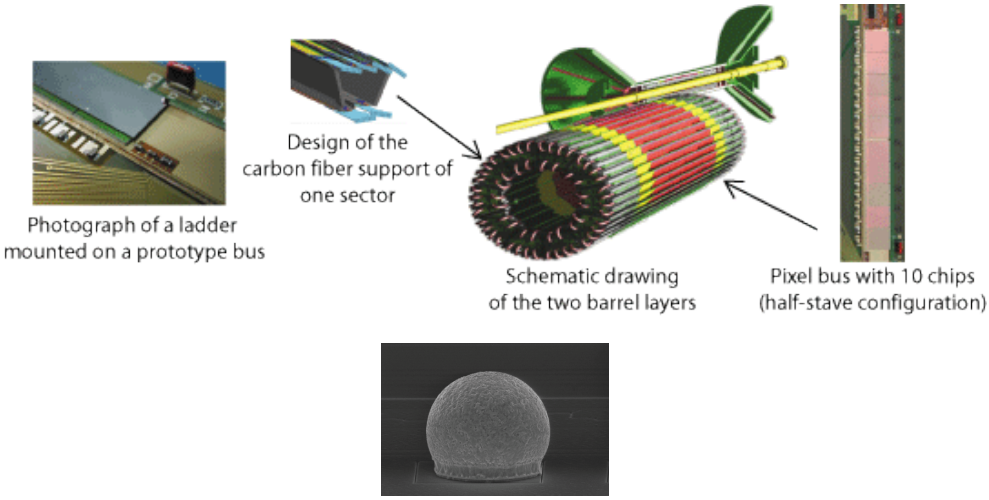

Figure 3.4: Annotated drawings of components of the Silicon Pixel Detector layers (top), and a microscopic photograph of a bump, which connects the diodes to the chip (bottom) [101].

icon chips - each measuring 50 μm in $r\varphi$ and 425 μm in z coordinates, allowing a spatial precision of 12 μm and 100 μm, respectively - is required in order to cope with particle densities of up to 8000 per unit rapidity in head-on Pb–Pb collisions. It also provides very good tracking for low momentum particles, with p_{T} lower than 200 MeV/c, which is essential for physics analyses that study the soft processes. In order to separate tracks that low in momentum the detector material must be kept to a very low minimum. An overall thickness of about 200 μm of the pixel chips helps keep the total material at about 2% of a radiation length. As a result, the SPD is also capable of determining the position of the primary vertex (PV) with a resolution better than 100 μm. Furthermore, it measures secondary vertices and their impact parameters (distance to the PV in the transverse plane), with good accuracy. This is essential to provide important topological information of weakly-decaying hyperons, which have mean decay lengths comparable to the radial distances of the pixel layers.

The read-out system processes the incoming signals within 256 μs. A separate trigger processor must send a signal to the ALICE Central Trigger Processor (CTP), introduced later in this chapter, in less than 800 ns. The pixel chips send fast-OR signals

to the SPD readout-out system, which fire if at least one pixel in the 2D matrix recorded a hit. The larger the number of chips firing, the larger the event multiplicity. Algorithms can therefore define multiplicity triggers by setting a threshold on the number of fast-OR signals.

3.2.1.2 The Silicon Drift Detector

The third and fourth layer of the ITS are equipped with silicon drift detectors [99, 102, 103]. In total, 260 silicon drift modules with a sensitive area of 7.02×7.53 cm^2 each, are mounted onto ladders placed parallel to the beam axis. The active area, accounted by a total of 202×294 μm^2 cells, is around 85% of the total detector area. Just as the pixel layers, the SDD is characterised by its high spatial resolution, measuring 12 μm and 100 μm in the $r\varphi$ and z coordinates, respectively. The layers, with a length of 59.5 cm and 67.0 cm in the z-direction, are placed at average radii of 14.9 cm and 24.8 cm. The left-hand side of Figure 3.5 depicts the side-view of half of the two layers.

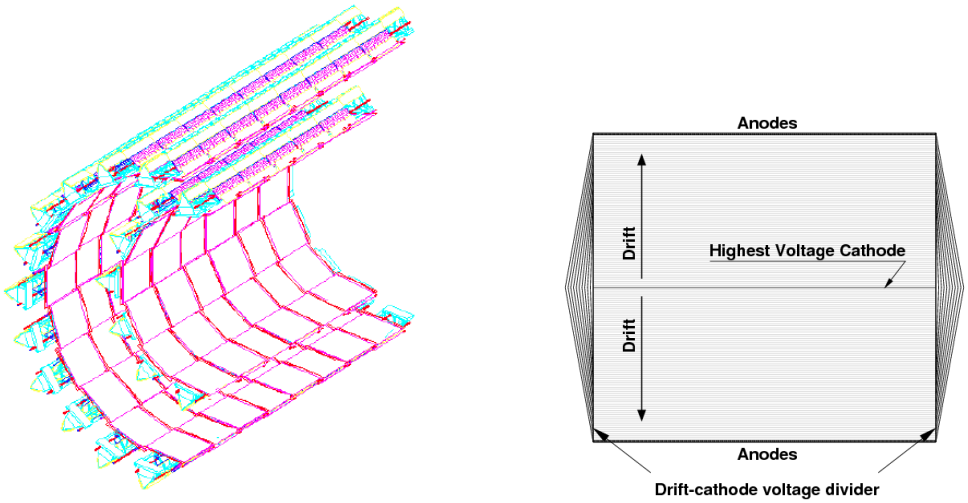

Figure 3.5: Drawing showing half of the two silicon drift detector layers (left) [99] and an annotated diagram of a silicon drift module (right) [104].

Figure 3.5 also shows a diagram of one of the detector modules. Electrons produced

by ionisation of charged particles traversing the silicon detector, drift towards one of the detector ends containing 256 anodes each under the influence of an applied external field with a potential difference of 8V between the central cathode and the anodes. The drift velocity is proportional to the electron mobility coefficient (μ_e) in the material and the electric field, $v_e = \mu_e E$. Measuring the drift time thus allows the position with respect to the anode end to be determined. The spatial coordinate on the beam axis is determined by the peak of the charge distribution deposited on the anodes.

In total the SDD counts 133,000 read-out channels. In addition to the high two-track resolutions necessary for the particle densities created in Pb–Pb collisions, the SDD also measures energy losses by the ionising particles as they interact with the detector, which helps provide information about the identity of low-momentum charged particles.

3.2.1.3 The Silicon Strip Detector

Silicon strips occupy the fifth and sixth layers of the ITS, in 1770 individual modules. Each module, with an area of 75×42 mm^2, contains 768 sensitive strips on both its sides. The strips alone constitute the active area of the SSD system. These strips are tilted by 17.5 mrad with respect to the short side of the module, but in different directions depending on the side. Thus, as two strips on opposite sides fire, the position in which a charged particle passed through is located near the place in which the two strips cross (see Figure 3.6). The total number of cells of the SSD amounts to 95×40000, and its spatial resolutions are of 20 μm in the $r\varphi$ and of 830 μm in the z coordinate. This resolution is worse than that for the inner tracking layers, as the tracks have dispersed further at average radii of 38 cm and 43 cm, at which the SSD layers are placed. These detectors cover a length along the z-direction of 90.2 cm and 101.6 cm in the fifth and outermost layer, respectively [105, 99].

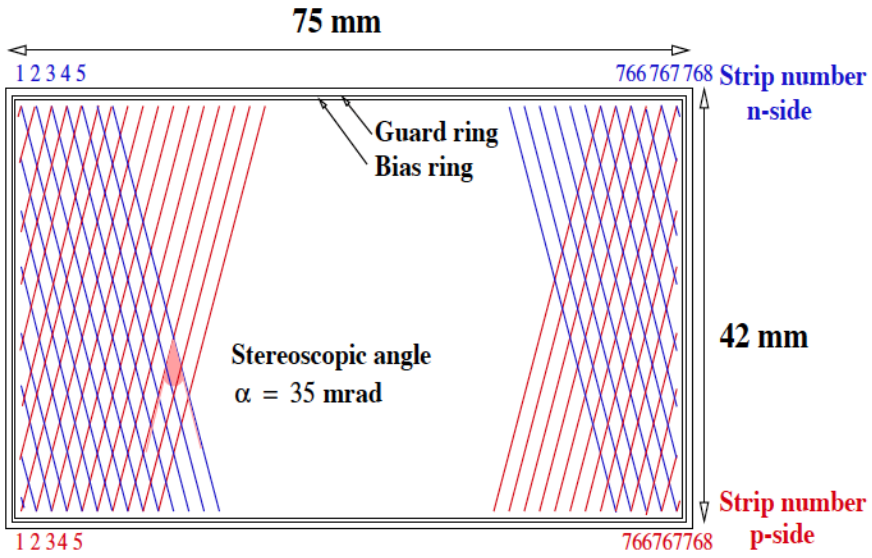

Figure 3.6: Annotated diagram of a silicon strip module [99]

3.2.2 The Time Projection Chamber

Surrounding the Inner Tracking System is a large Time Projection Chamber (TPC) [106]. This cylindrical chamber is 5 m long, and covers a volume of 88 m^3 from an inner radius of 0.8 m to an outer radius of 2.5 m. Its pseudo-rapidity range is $|\eta| < 0.9$. A $Ne/CO_2/N_2$ gas mixture with 90:10:5 relative ratios permeates the detector, which is divided in two parts by a central electrode. Charged particles traversing the chamber ionise the gas and produce electrons in the process, which drift towards cathodes placed at both ends of the detector due to a uniform electric field of 400 V/cm created along the z-axis between the electrode and each end plate. Multi-wire proportional chambers are placed at the end plates in order to amplify the signal from the receiving electrons, before the latter is forwarded to the front-end electronics. The drift time of the electrons is also measured, thus enabling a reconstruction of the passing tracks in three spatial dimensions. An annotated diagram of the TPC is shown in Figure 3.7.

As well as providing optimal conditions for good track reconstruction, the TPC measures the energy loss $(-\mathrm{d}E/\mathrm{d}x)$ of particles that travel through the gaseous material

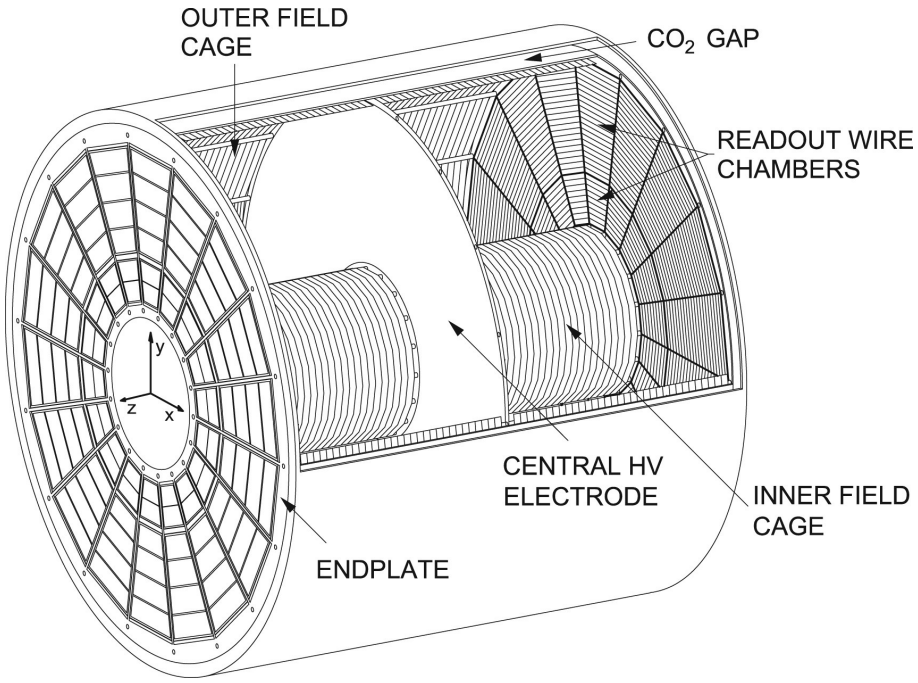

Figure 3.7: A three-dimensional view of the ALICE Time Projection Chamber [107].

of the chamber. The stopping power of the material for a charged particle can be parameterised according to the Bethe–Bloch formula [108], which is expressed as:

$$-\frac{\mathrm{d}E}{\mathrm{d}x} \propto \frac{Z}{A\beta^2}\left(\frac{1}{2}\,ln\left(\frac{2m_e c^2\gamma^2\beta^2}{I}\right) - \beta^2\right) \quad , \tag{3.2}$$

where Z is the atomic number, A the atomic mass number and I the mean excitation energy of the absorbing gas, m_e is the mass of the electron, $\gamma = 1/\sqrt{1-\beta^2}$ is the relativistic velocity factor and $\beta = v/c$ is the velocity of the charged particle divided by the speed of light c. Additional corrections must be applied to take into account the fact that electrons are not stationary inside the atoms (important for low momentum particles) and to consider polarisation effects in the medium which shield the electric field (important for high momentum particles). The right-hand side of equation 3.2 can be rewritten in terms of the mass and momentum of the charged particle. Since both the energy loss and the momentum (p) of a charged particle can be measured with the TPC, the only free parameter in that equation then remains the particle mass. When energy loss is plotted against momentum for accumulating

events, distinct patterns start to appear dependent on the particle masses. These entries can be shown to follow the curves of the Bethe–Bloch parameterisation, as Figure 3.8 illustrates for p–Pb collisions. A charged particle is attributed an identity according to its position on the (dE/dx vs p) graph, by requiring the measurement to lie within a chosen number of σ from a given Bethe–Bloch curve. The selection criteria used on the energy losses of the decay particles of multi-strange hadrons in the TPC will be discussed in the next chapter.

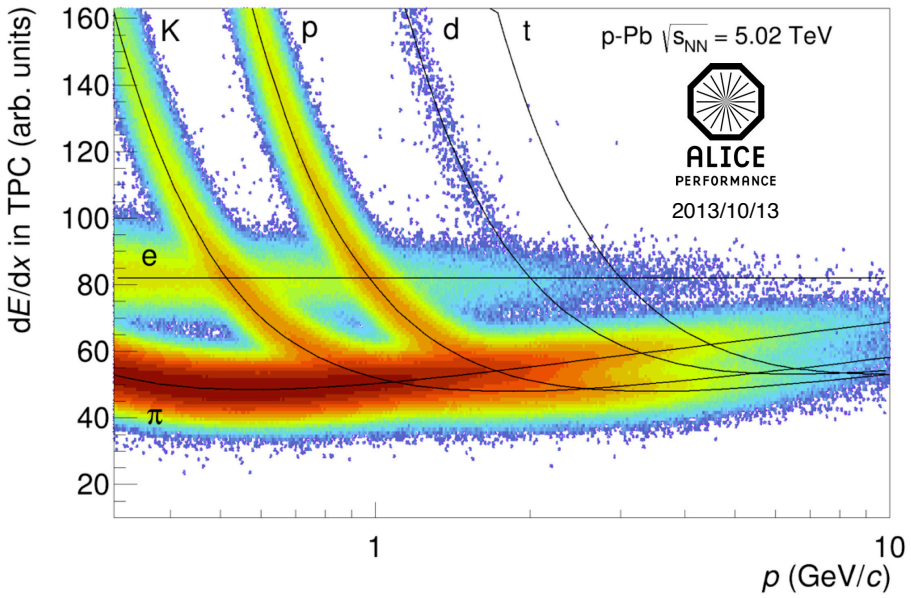

Figure 3.8: The measured energy loss (dE/dx) as a function of particle momentum in p–Pb collisions with the Time Projection Chamber. The Bethe–Bloch parameterisation for different particle masses are superimposed on the measured curves.

The TPC read-out is composed of 570,000 pads along the rφ plane. The ionisation electrons from the TPC pass through multi-wire proportional chambers (MWPC) where the signal is amplified through the creation of electron avalanches, before the final signal is captured by the read-out pads and transmitted to the front-end electronics. The wires on the end anode of the MWPCs are placed such that they form a two-dimensional grid. The segments on the end plate defined by the grid are of three

different sizes, therefore the pad areas vary from 0.3 cm^2 at inner radii to 0.9 cm^2 at outer radii. Precise spacial coordinates in the transverse plane of the trajectory of a charged particle are obtained by reconstructing the peaks of the distribution obtained by the signals in a group of adjacent pads. The conjunction of such a peak with drift time measurements for the same group of pads is called a *cluster*.

3.2.3 The V0 detector

Two arrays of scintillators are placed in the forward rapidity regions, forming the V0 system [109]. The V0C detector is placed 90 cm from the interaction point on the positive z-side. The V0A detector, on the opposite side, is located at the z= -340 cm position. Both are composed of 32 plastic scintillator tiles, which form four rings along the transverse ($r\varphi$) plane, with a radius of 50 cm each. They cover the pseudorapidity regions of 2.8> η >5.1 and -3.7< η <-1.7. The interaction of charged particles with the scintillator material releases photons, which pass through wavelength shifting fibres before they are conducted to photomultipliers via optical fibres. Measurements with the V0 detector define *Minimum Bias(M.B)* events, which are those in which at least one of the scintillator counters of V0A and of the V0C record a hit [1]

The scintillators give an identical response for different particles with different momenta and therefore, the total energy deposited in the scintillator detectors can be assumed to be proportional to the number of particles created in the event. The V0 detector thus serves as an estimator of the event multiplicity. In p–Pb collisions, the distribution of the amplitude measured in the V0A detector - the array of scintillators placed in the Pb-going side - is used to divide the data sample into seven multiplicity classes. This will be the subject of section 4.1 in the next chapter.

[1]The M.B. sample is the one that is as inclusive as possible of all events. This notion will be used in the following chapters in the context of event multiplicity, where it will represent the sample with no selection based on multiplicity.

In addition to providing trigger signals and multiplicity estimations, the V0 detector is used in order to discriminate background from beam-gas interactions, i.e. interactions of the beam with atoms from residual gas present in the beam-pipe. The V0 achieves good suppression of such events due to its time resolution better than 0.5 ns. A discrepancy is observed in the difference between the first hit in the V0C and V0A scintillators from real beam-beam events, as compared to beam-gas events. The discrimination power of this type of background is illustrated in Figure 3.9, where the correlation between the sum and the difference of signal incidences in V0A and V0C are plotted for pp collisions. The recorded events form three classes in that correlation figure, one for the real pp events and two for beam-gas background events, one for each of the two beams. [110]. In addition to placing a cut on such time correlation distributions, the V0 can be compared with the T0 collision time reference for further background subtraction.

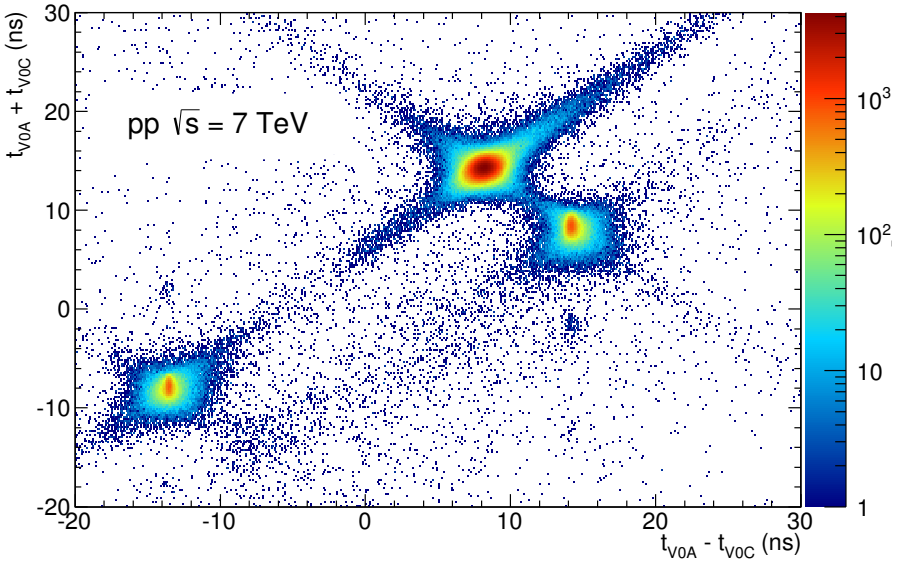

Figure 3.9: Correlation between the sum and the difference of the signal arrivals at the V0A and V0C detectors. The pp events are populated around the (8.3; 14.3)ns position.

3.3 The Central Trigger Processor

3.3.1 Operation

The Central Trigger Processor (CTP) of the ALICE experiment [3] decides and communicates to the sub-detectors to read out data, according to the conditions for the physics analysis. That information is sent simultaneously to the individual systems in several steps. As Figure 3.10 illustrates, the CTP first receives signals from triggering detectors, of which there are 11, indicating the possible occurrence of a collision. These are sent in case the data satisfies the conditions predefined in the trigger configuration for a particular run, according to the physics analysis interests. As an example, a signal might be sent by the SPD if at least one hit in the pixel layers has been observed. There are 24 L0 connections to the CTP, 24 L1, and 12 L2 inputs. Subsequently, the CTP sends out signals to a group of detectors which are to take part in the data read-out. It does so in three steps, according to the different levels of data processing by the triggering detectors, levels L0, L1 and L2. An initial L0 signal is sent out to the sub-detectors, in order to notify that a potential collision has taken place. If the triggering detectors send additional messages consistent with the detection of particles, the CTP transmits the L1 signal 6.5 μs later, a time interval which is constant for all L1 instances. Finally, the CTP emits an L2 signal after a time delay of at least 106.5 μs. This last signal indicates whether the data is to be read-out and stored as an event (L2a) or rejected (L2r). The L0, L1 and L2 signals are all transmitted via an intermediary Local Trigger Unit board (LTU), which is responsible for the communication between the CTP and the sub-detectors. No trigger signal is sent to the respective detectors if at least one of them is declared to be in the state 'busy', in which case it is incapable of processing incoming data. This may be the case when the trigger rate is too large or in case the detector has observed some error in its operation. A complete diagram of all the connections to and from the CTP is shown in Figure 3.10.

The above description defines the trigger protocol, which can be summarised as consisting of the following signals, for each instance of a potential collision of interest:

- An L0 pulse, synchronous with respect to the interaction time;
- An L1 pulse, also synchronous; a missing L1 signal after an initial L0 is interpreted as a rejection of the data;
- An L1 message (L1m), asynchronous with respect to the interaction time
- An L2a or L2r message, depending on whether the data will be read out or not; This signal is also asynchronous;

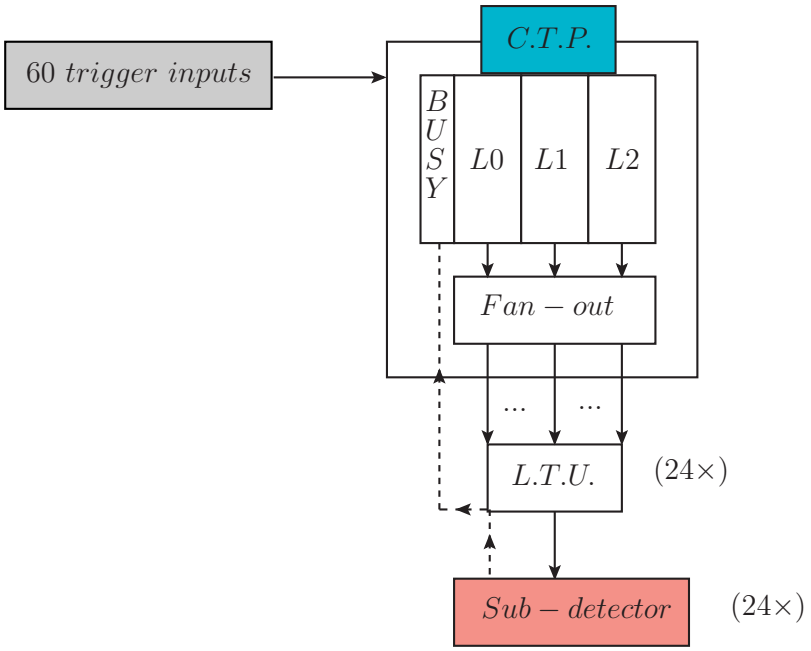

Figure 3.10: A diagram of the CTP board and its operation: The CTP receives trigger inputs from the detectors and processes them before triggering the read-out of a group of sub-detectors.

In the following parts of the CTP section more details are given on the triggering process and a project developed during the long shutdown of the LHC in 2014 and

early 2015, in preparation for the second main collision period of the LHC (Run 2) is described. The focus of that project was to perform tests to ensure the correct operation of the trigger protocol as defined above.

3.3.2 Trigger classes

Trigger inputs determine the kind of events that are to be selected for specific runs. An example of a trigger input is the aforementioned minimum bias trigger, which requires the selection of events with at least one hit in the V0A and the V0C detector (*V0AND*). In addition, decisions are made on which detectors to activate for the read-out of the data for later event reconstruction. The group of participating systems is referred to as *trigger cluster*, of which there are six possible combinations. With this choice, certain sub-detectors may not be included in the data collection process. The choice of not including a sub-detector depends on the intended physics analysis for which the data is collected. For example, forward physics analyses like the measurement of J/ψ mesons which decay into two muons may prioritise the information from the muon detector, in which case the event information from the SDD, which covers the mid-rapidity region and has the longest dead time of all ALICE systems, mainly due to the drift time of the electrons in the silicon, may not be used in the read-out, thus allowing a group of detectors to read out more often. It is possible to apply multiple inputs and clusters in parallel during a LHC run, enabling data collection by different groups of detectors. The combination of the trigger inputs and clusters define the *trigger classes*. The upgrade of the CTP from Run 1 to Run 2 of the LHC included an increase from 50 to 100 possible classes, i.e. 100 different input and cluster combinations. For each trigger, the information about which classes are active is expressed in the form of trigger patterns. These patterns consist of 100 bits, one for each of the available classes, and is either set to 1, in case that class is active or 0, in case it is not.

3.3.3 The Local Trigger Unit (LTU)

The Local Trigger Unit (LTU) is the interface board between the CTP and the sub-detector (see Figure 3.10). It can be run in two modes: *standalone* or *global*. The former is employed for the emulation of trigger signals by the LTU, while the latter mode is applied when receiving signals from the CTP. During the collection of data for physics analysis, the global mode is used. L0, L1 and L2 signals are generated, or received and transferred to the respective front-end electronics of the sub-systems. Each sub-detector has its own LTU board in the ALICE trigger chamber. The LTU triggers the read-out of the sub-detectors by sending the signals simultaneously to them.

A replica of the LTU board, and of the entire CTP system, is available in the CTP laboratory at the CERN main site, in order to work on the debugging of its firmware. The description of a test software for the LTU board, developed during the months preceding Run 2, is the subject of this section. Consistency checks were performed on whether the trigger protocol was programmed correctly onto the CTP and LTU firmware.

3.3.3.1 The LTU operation

The trigger signals are sent from the LTU to the sub-detectors via a TTC (Timing, Trigger and Control) system. The TTC system, described in [111], is composed of an emitter board (TTC-ex) and receiver chips in the front-end electronics of the ALICE read out systems (TTC-rx). In the CTP laboratory, a receiver interface testboard, the TTC-it, is used instead. As shown in Figure 3.11, the trigger information is sent to the TTC through two different cables: L0 and L1 pulses are sent through channel A, which ensures that both arrive with a constant time difference, whereas L1 and L2 messages, with details on the trigger class patterns, are carried by channel B. The arrival time of the latter messages at the detector read out system is not synchronous with respect to the interaction time, and depends on the traffic through the channel.

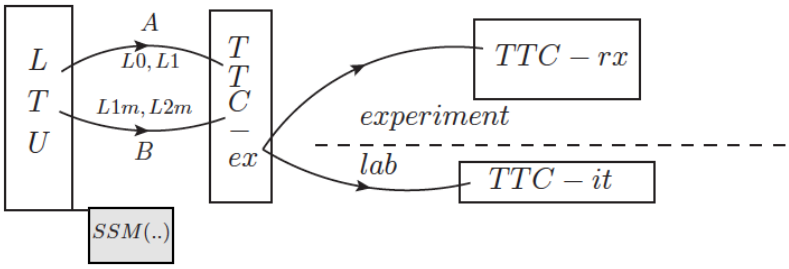

Figure 3.11: A diagram showing the LTU connection to the TTC system. TTC-ex board is connected to a TTC-rx chip of the sub-detector front-end electronics in the ALICE experiment. In the CTP laboratory, a TTC-it board imitates the sub-detector receiver.

Among other LTU information, all the signals sent via the TTC channels may be recorded onto a snapshot memory (SSM), an essential tool for the identification of problems with the LTU firmware. Data is stored in the snapshot for every single bunch crossing, one bunch crossing in the LHC corresponding to 25 ns.

3.3.3.2 Snapshot Memory

The SSM records the LTU information that is passed to the TTC channels as follows: An initial L0 pulse is recorded, which is followed by a positive L1 pulse. The time difference between a L0 and a corresponding L1 signal must be exactly 260 bunch crossings, if it is consistent with the 6.5 μs of the trigger protocol. In case the SSM records a different time interval, the protocol is not programmed correctly onto the firmware. An L1-data message (L1m) follows the pulse, which contains the trigger pattern. An L2 message completing the trigger sequence appears in the SSM with a minimum time difference of 4260 BC (106.5 μs) with respect to the L0 pulse. The SSM continues to record information for a period of around 26 ms to allow for one million bunch crossings, after which a new snapshot is taken. In order to allow the SSM to be read and saved, the firmware must stop writing. Therefore, the ends of two consecutive snapshots do not match, so that each SSM must be analysed sepa-

rately. Figure 3.12 illustrates an example of a saved SSM and its recorded information.

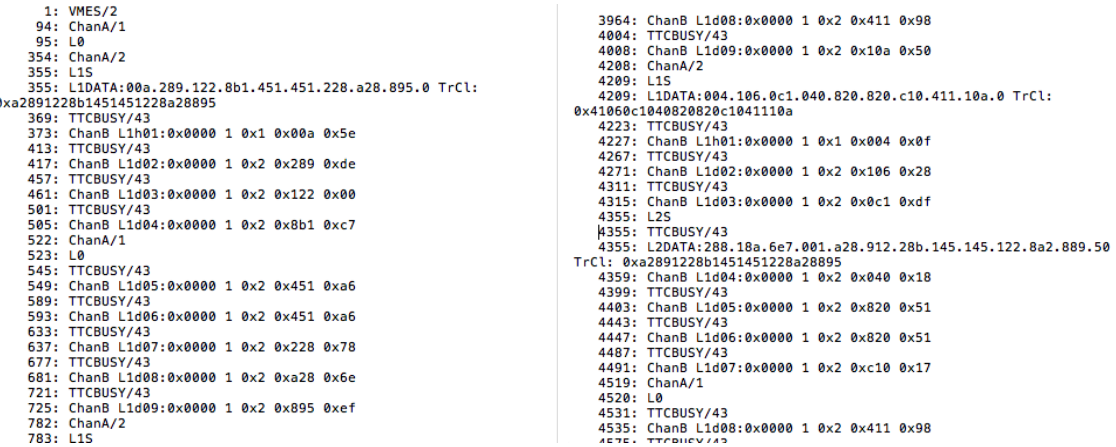

Figure 3.12: Extracts of a snapshot memory showing the first L0, L1, L1m (shown as L1DATA) and L2m (L2DATA) signals in the SSM. The left columns indicate the BCs of the recorded information.

3.3.3.3 LTU tests in the CTP laboratory

An SSM reader and analysis programme was developed in order to run tests on the LTU protocol, in particular on the timing and content of the transmitted data. Finding failures in the data sent to the TTC is important in order to pinpoint the location of a given issue with the trigger system, which may lie in the CTP or LTU firmware. In addition, this work also serves for consistency checks in situations in which the front-end electronics of a sub-detector observes an error the origin of which is not understood.

Both the standalone and global modes were used for the LTU protocol tests. In the standalone mode, the LTU works as a completely independent unit. The emulation tool programmed into its firmware simulates trigger sequences: L0, L0-L1-L2a, or L0-L1-L2r. The emulation is controlled via a software, in which a class pattern is defined and the rates for the sequences are set. In the global mode, the trigger signals

are generated earlier in the CTP, and then are sent to the LTU. Also in that case, the trigger classes to be generated are controlled via a software. The advantage of running tests in the global mode is that it permits errors to be detected that occur in the CTP, whereas tests with the standalone mode alone can only find LTU problems.

The following tests could be performed on the trigger protocol at the LTU level, both in the standalone and global mode:

- Incomplete trigger sequences, i.e. missing L2a or L2r;
- faulty L1m or L2m, e.g. incomplete or too long class patterns;
- Non-constant intervals between the L0 and L1 signals;
- Inconsistency between the class pattern extracted from L1 with that extracted from L2m
- Inconsistency between the L1(L2) class pattern and the software-assigned pattern;

In order to perform the above cross-checks, a trigger configuration is first prepared with the dedicated software. As explained above, the trigger classes and sequences to be generated by either the LTU emulator (in standalone) or the CTP (in global mode) can be chosen. Next, the software is run, the trigger signals generated, and the first SSM is recorded in the LTU board. The full analysis is run on the snapshot before another one is allowed to be recorded. The method used to perform the last item in the above list is dependent on the applied mode. In the standalone mode, exactly one class pattern can be assigned for generation. In the global mode, however, the class patterns can be made to vary for each trigger instance, allowing for a series of possible class patterns. Four different internal trigger inputs can be defined for each of the 100 classes. The consistency check thus consists of checking that either all or none of the classes, which have been attributed one same trigger input out of

the possible four, are set to unity in the obtained class pattern. This is repeated for the four trigger inputs.

The output of the analysis is a table with all identified trigger patterns, which passed all the consistency checks, and the frequency with which they were observed in the analysed SSMs. In case of the detection of errors in an SSM, the programme halts with appropriate error messages and dumps the corresponding SSM.

These cross-checks helped with the identification of firmware flaws. They are part of a global effort, which included tests of the same nature on the CTP board, and on the TTC-it board, which imitates the receiving board of a sub-detector. Together, they provided enough information to identify the faulty board of the trigger system, in situations of unsuccessful running of the CTP. The LTU analysis just described is a volatile analysis, as it is programmed in such a way that it can be applied for the CTP system in the laboratory or in the ALICE cavern, depending on the need.

Chapter 4

Selection of multi-strange hadrons in p–Pb collisions

4.1 Centrality in p-Pb collisions

The p–Pb run of the LHC that provided the data for this work is unique in the sense that, for the first time, enough collisions were collected for a study of strangeness production as a function of the geometry of the collisions to be permitted. Just like in the heavy-ion physics programme, p–Pb collisions allow the sub-division of the data into events originating from collisions of different centralities. This term has a similar geometrical meaning to that in Pb–Pb collisions [112], where it indicates how the two nuclei overlap at the moment of impact. There, it determines how much of the Pb cross-sectional area participates in the collision, ranging from fully head-on (central) collisions to interactions between the outer edges (peripheral interactions) of the nuclei. In p–Pb, more central collisions correspond to the proton hitting the Pb nucleus at its centre, while more peripheral events are the result of the proton penetrating the outer edge of the nucleus, in the approximation of a spherically shaped nucleus. The former type of collision gives rise to a production of a larger number of particles than the latter. Figure 4.1 illustrates these examples of proton–nucleus

(p–A) interactions, which are quantified by the geometrical impact parameter b, a variable indicative of the centrality defined as the transverse distance between the centre of the two interacting particles. The maximum impact parameter obtainable in p-Pb collisions is equivalent to the radius of the Pb nucleus $R_{Pb} = 6.62 \pm 0.06$ fm [113].

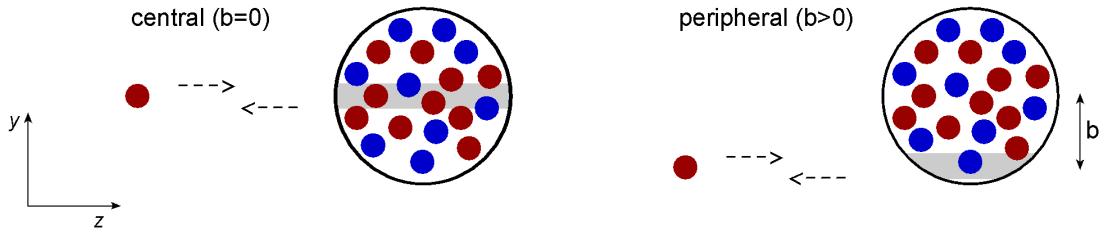

Figure 4.1: Example sketches illustrating central (left) and peripheral (right) p–A collisions. In central collisions, the incident proton interacts with a larger number of nucleons and a larger number of particles are generated into the detector. Peripheral collisions see a smaller number of N–N interactions, which results in smaller multiplicities.

4.1.1 The Glauber model

High energy nuclear collisions are often described with Monte Carlo simulations according to the purely geometric Glauber model [114], which treats p–A or A–A interactions as a superposition of individual nucleon–nucleon interactions. Its aim is to provide a description of the geometrical configuration of the collisions on a statistical basis, allowing a direct comparison relative to the simpler pp interactions. This model makes some simplifying assumptions: Nucleons are taken to follow straight trajectories and to be completely transparent to previous interactions. Therefore, the nucleon–nucleon (N–N) cross-section remains unchanged for subsequent collisions undergone by the same proton. In addition, the N–N cross-section is assumed to be the same regardless of whether it occurs in a vacuum (pp–like collision) or inside nuclear matter (p–A or A–A –like collision). In the case of p–Pb collisions, the Monte Carlo generates simulations of Pb ions composed of 208 nucleons randomly

distributed within a sphere defined by the radius of the Pb nucleus (R_{Pb}), separated by a distance no smaller than a hard sphere exclusion separation of 0.4 fm and such that they follow a density profile described by the Woods-Saxon parameterisation:

$$\rho_{Pb} = \frac{\rho_N}{1 + e^{\frac{r - R_{Pb}}{a}}} \quad , \tag{4.1}$$

where r is the radial position of a particular nucleon inside the ion, ρ_N its density and a the skin thickness of the nucleus. Collisions are simulated with randomly changing values for b and N–N interactions take place only if the transverse distance between the respective nucleons is smaller than the distance corresponding to the inelastic cross-section ($\sigma_{NN}^{inel} = 70 \pm 5mb$ [115]):

$$b_{NN} < \sqrt{\sigma_{NN}^{inel}/\pi}. \tag{4.2}$$

The number of N–N collisions (N_{coll}), and with it, the number of participating nucleons ($N_{part} = N_{coll} + 1$) are counted in the event-by-event simulation to determine their dependence on the impact parameter [115].

4.1.2 Multiplicity as an indicator of centrality

Since b cannot be measured directly experimentally, the obtained N_{coll} or N_{part} distributions have to be mapped onto a measurable quantity. In ALICE p–Pb collisions, that quantity is the V0A amplitude, which is proportional to the number of charged particles produced in the collision. This is the energy deposited in the hodoscopes of the V0 detector on the A-side (in which the Pb beam travels) of the experiment. With its high-η range, this selection avoids the central rapidity region where the actual measurements of hyperons are made. This selection is consistent with the choice made for heavy-ion collisions, in which case the amplitude measured in the scintillators of both the VZERO detectors is used. The data are divided into seven different multiplicity classes defined by different percentile ranges. Figure 4.2 demonstrates how

different bands are defined based on the multiplicity distribution. The 0-5% band encompasses the 5% most multiplicity-rich events produced in the collisions during the data run. Similarly, the 80-100% class contains the 20% lowest multiplicity events. The same figure also shows how the Glauber model can be mapped to the V0A distribution. This is done by a convolution of N_{part} and a negative binomial distribution (NBD) defined in terms of the mean V0A amplitude per participant nucleon (μ) and a dispersion parameter k. This NBD describes the probability of the contributions to the total amplitude accounted for by each N–N collision. The V0A distribution is reproduced well by the Glauber model, showing a discrepancy only for very low multiplicity events, where multiplicities lie below the mean multiplicity reached in pp data at $\sqrt{s_{\rm NN}}$ =7TeV. The extracted N_{part} parameter values from the fit range from 2.9±1.4 to 15.7±3.8 from the most peripheral to the most central multiplicity class.

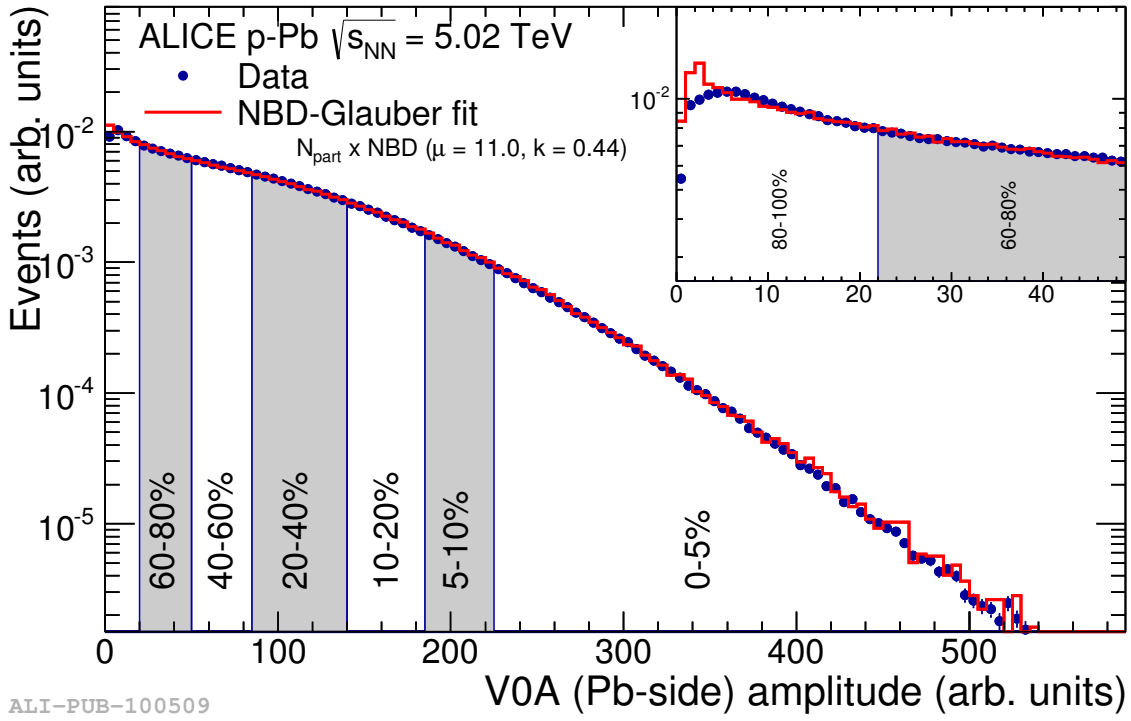

Figure 4.2: The V0A amplitude distribution measured in p–Pb collisions divided into seven multiplicity classes. The distribution is fitted with a Glauber model function [115].

4.2 Event reconstruction

The raw data from the collisions includes the information of which detector elements were activated and at what time due to the passing of charged particles. These so-called *hit* positions must be reconstructed into intelligible information for analysis, providing track trajectory coordinates, revealing their curvature, and thus allowing their momentum, energy loss and *Distance of Closest Approach* (DCA) to the primary vertex (PV) to be calculated and quantified in their corresponding physical units. Once this reconstruction is performed, it is stored in more compact *Event Summary Data* (ESD) files, on which the analysis, presented in this chapter, was performed. The track reconstruction and PV determination are carried out by a number of algorithms.

As discussed in the previous chapter, out of compact groups of signals in adjacent detector sensors (pads in the TPC), clusters are defined by the measured centre-of-gravity. Each such cluster gives a presumed position of the trajectory of the track. Meanwhile, an algorithm using only information from the more granular SPD detector makes a first estimate of the PV of the event. It does so by following track candidates inwardly towards the location of the p–Pb interaction. Next, a 'Kalman filter' algorithm [116, 117, 118] searches for track clusters at the outer TPC radii, referring to them as its 'seeds'. It works its way towards more inner TPC radii, and eventually to the ITS, by repeatedly looking for plausible space points row-for-row, each time allowing the values of the track parameters to be re-evaluated, by taking into account the energy losses and the potential material absorption in interactions with the detector. In doing these corrections, a mass for the hypothetical particle track must be assumed. The particle mass is estimated from the most likely hypothesis according to the TPC ionisation loss information in preceding clusters.

A standalone ITS algorithm is implemented to look for tracks defined within the ITS only. Another estimation of the PV is made at this stage using the information of the newly reconstructed tracks. It differs from the previous estimation, in the sense that tracks reconstructed in the TPC and (or) ITS can be used, as opposed to using the SPD only. While in most cases more tracks are available with this method, allowing for a more accurate determination of the vertex position, this approach relies on good track association between track sections found in different detectors. In this work, the latter PV is selected by default; however, in the case it could not be reconstructed due to insufficient contributing tracks - as can be the case in extremely low multiplicity events with low momentum particles - one resorts to the SPD-determined vertex.

Next, the same process of track reconstruction is repeated, this time propagating in the radially outward direction from the ITS, to the TPC, TRD TOF, PHOS and HMPID. Finally, in a last step, the tracks are refitted in the inward direction, in order to obtain more precise values for the track parameters, given the new PV. At this point, making use of the refitted tracks, an algorithm searches for secondary vertices, potentially from the weak decays of strange particles. In each detector, a χ^2 is calculated in a fit of the final track to its measured parameters, serving as a track quality indicator. For this analysis, all daughter tracks of potential multi-strange decaying particles were required to have a χ^2 per number of TPC cluster below 33 [119, 120].

4.3 Event selection

During the months of January and February in 2013, ALICE recorded 26 runs totalling over one hundred million proton–lead collisions with an integrated luminosity of $58\mu b^{-1}$ [121] at a centre-of-mass energy of 5.02 TeV. These were the first collisions between protons and heavy nuclei to ever be conducted at the LHC. The quality of these events was scrutinised by imposing a few selections, which are described in the

following sections.

4.3.1 Pile-up

Pile-up is an effect caused when multiple interactions occur within the same bunch crossing (BC). ALICE is designed to run with negligible pile-up, so it is important that its contribution is minimal in order to not interfere with the results. The likelihood of the presence of such events in a given sample increases with the collision rate, which for the p–Pb sample at hand, was 10 kHz. The removal of pile-up in the available sample was not performed at an event-by-event but at a run-by-run basis. Each of the 26 runs were individually tested for their likelihood of pile-up contamination. This was carried out by working out the average number of interactions per BC (μ) in each of the recorded runs. The number μ is related to the probability distribution *(P(n))* in terms of the number of interactions per BC n, which can be expressed according to a Poisson distribution [122]:

$$P(n,\mu) = \frac{e^{-\mu}\mu^n}{n!} \quad . \tag{4.3}$$

The μ number can be obtained by counting the number of triggers per bunch crossings in the data, which is related to $P(n > 0)$. The probability to have at least two interactions per BC - i.e. pile-up - can be expressed in terms of μ as follows:

$$P(n \geq 2,\mu) = 1 - P(0,\mu) - P(1,\mu) = 1 - (\mu + 1)e^{-\mu} \quad . \tag{4.4}$$

Figure 4.3 shows the values for μ in each of the run numbers recorded. The calculations are performed for *V0AND* triggers in the data sample, i.e. for events which showed a signal both in the V0A and the V0C detectors. Three runs were removed, which showed larger likelihood for pile-up than the rest. They correspond to 2.2% fraction of the reconstructed events in the original data sample (see Table 4.1). The remaining runs have μ values of no more than around 1%. Given that the original

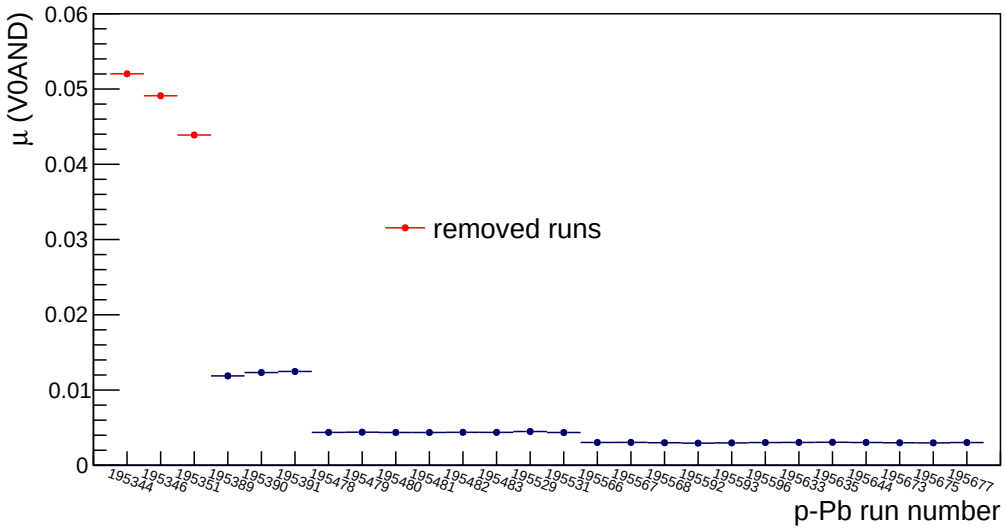

Figure 4.3: The average number of interactions per bunch crossing (μ) in the 26 respective runs among V0AND triggered events.

sample only contains events which, by definition, recorded at least one interaction, the probability for pile-up in the remainder of the sample used for analysis is smaller than $P(n \geq 2, 0.01)/P(0, 0.01)$, which equals 0.5%.

4.3.2 Trigger and Primary Vertex selection

An online trigger that requires a signal in the V0A and V0C detector (*V0AND*) was applied. The V0 detector operates with a time resolution better than 1ns. Its time measurements were checked against the collision event time obtained by the T0 system that uses a Cherenkov detection method. This ensured the removal of background events, originating from beam-gas interactions, down to negligible amounts. With this trigger, the event selection is almost exclusively composed of non-single diffractive (NSD) events. Monte Carlo studies measured an efficiency of 99.2% for the selection of NSD events [123].

In this work, the yields of multi-strange hadrons will be normalised to the number of events that correspond to the visible cross-section, in other words, the number of events that pass the offline V0 trigger. However, the selection of these baryons

is performed on the number of events that have a well-reconstructed primary vertex that follows the description of section 4.2 and which, in addition, is found to lie within the [-10;+10]cm window along the beam (z) axis. This will affect the measured hyperon rates only in the most peripheral multiplicity classes 60-80% and 80-100% where event losses from the absence of well-reconstructed PVs are observed. The reason why events pass the trigger but fail to show a PV are likely to be due to ultra-peripheral collisions, in which the protons and the lead nuclei engage in diffractive processes with the exchange of colourless pomerons or in electromagnetic interactions with the exchange of photons. Cases of missing vertices were found in 1.2% of the events in the 60-80% multiplicity class, and in 3.3% among the 20% most peripheral events. For the production rates of the multi-strange baryons in the combined sample (0-100% multiplicity class), this effect is smaller than 1%.

Table 4.1 shows the reduction of the number of events with each successive selection. The trigger and primary vertex identification cause a data loss of 1.7%, while the z-cut on the PV removes over 10% of the remaining data. Overall, around 85% of the initial data is used for analysis. The analysis chain described in detail in the following section was performed on the remaining 1.054×10^8 events.

Table 4.1: Number of events at different selection stages

Event selection stage	Number of events
Reconstructed events	1.229×10^8
after pile-up removal	1.202×10^8
passing trigger (V0AND)	1.190×10^8
with reconstructed PV	1.182×10^8
passing PV z-position cut	1.054×10^8

4.4 Selection of multi-strange baryons

Multi-strange baryons leave a characteristic signature in the detector identifiable through the topology of the two subsequent decays mediated by the weak nuclear force. The analysis described here focuses on the following decay modes:

$$\Omega^- \rightarrow \Lambda K^-(B.R.: 67.8\%) \rightarrow p\pi^- K^-(B.R.: 63.9\%) \quad , \tag{4.5}$$

$$\overline{\Omega}^+ \rightarrow \overline{\Lambda} K^+(B.R.: 67.8\%) \rightarrow \overline{p}\pi^+ K^+(B.R.: 63.9\%) \quad , \tag{4.6}$$

$$\Xi^- \rightarrow \Lambda\pi^-(B.R.: 99.9\%) \rightarrow p\pi^-\pi^-(B.R : 63.9\%) \quad , \tag{4.7}$$

$$\overline{\Xi}^+ \rightarrow \overline{\Lambda}\pi^+(B.R.: 99.9\%) \rightarrow \overline{p}\pi^+\pi^+(B.R : 63.9\%) \quad . \tag{4.8}$$

These decay processes are commonly referred to as *Cascades* and the Λ decay is known as a V^0, due to the V-shaped form the decay tracks of this neutral particle leave in the detector. The overall branching ratio (B.R.) of the Ω and Ξ cascades are 43.3% and 63.9%, respectively. Thanks to the large TPC, ALICE is well equipped to identify these types of decay. The cascade identification strategy is based on the measured values of five cascade and five V^0 topological variables, that provide information on the $\Xi^\pm$ and $\Omega^\pm$ and V^0 vertices. A set of criteria imposed on these parameters aims to select cascade candidates with identified tracks that agree with the scenario depicted in the sketch shown in Figure 4.4: a multi-strange particle produced at the primary vertex travels for some distance in the detector before producing a charged π or K track, the so-called *bachelor track*. A few centimetres away, the neutral, and therefore invisible, Λ baryon also decays, generating a pair of tracks.

Invariant mass calculations are performed for each potential multi-strange decay. In the process, the bachelor is once assumed to be a charged π and once a K. Two

invariant mass hypothesis are applied for each candidate, one under the Ξ and another under the Ω assumption. In order to reduce the memory needed for storing cascade candidates, they are only selected if both their measured masses lie within a window of 150 MeV/c^2 centred around their corresponding PDG masses, which are $M^{\Xi}_{PDG} = 1.321$ GeV/c^2 and $M^{\Omega}_{PDG} = 1.672$ GeV/c^2.

In the remaining parts of this section, a selection strategy aimed at optimising the resulting multi-strange signal is outlined.

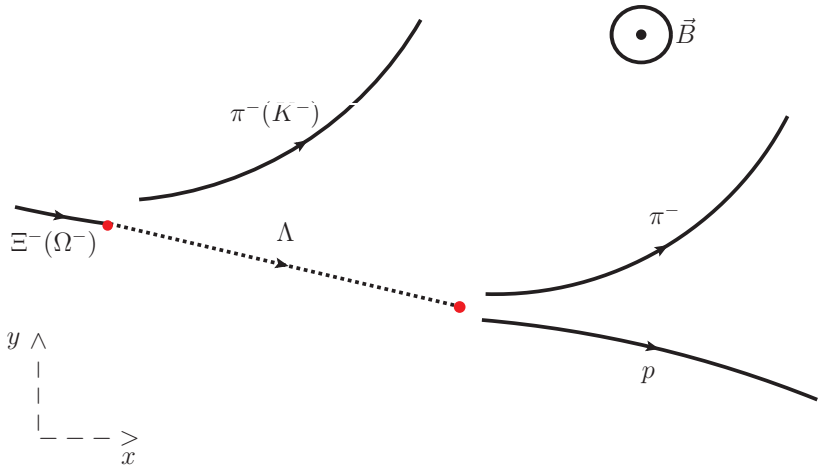

Figure 4.4: The decay of a negatively charged multi-strange baryon as seen in the transverse plane inside the detector. The solid curves show the visible tracks in the detector and the dashed line represents the invisible neutral V^0. The decay vertices of the cascade are depicted by the red points.

4.4.1 Acceptance

In p–Pb collisions, the centre-of-mass of the nucleon–nucleon collisions is shifted with respect to the laboratory frame of reference by 0.465 units of rapidity in the direction in which the proton beam travels. This is due to the fact that the same magnetic rigidity, defined as the product of the field with the cyclotron radius, is provided to both the proton and the lead ion beams. Charged nucleons are accelerated at an energy of 4 TeV, but the heavier Pb nuclei, which are composed of both protons and neutrons, acquire less energy per nucleon. Therefore, the colliding nucleons have

unequal energies at the moment of interaction. The measurements reported in this thesis were performed in the central rapidity window defined in the centre-of-mass frame within $-0.5 < y < 0$, where negative rapidity corresponds to the side of the detector into which the Pb beam travels, and within the pseudorapidity range $|\eta| < 0.8$.

4.4.2 TPC dE/dx selection

As explained in the previous chapter, the energy loss inside the TPC by charged particles allows tracks to be identified by comparing their position to the Bethe-Bloch dE/dx vs momentum relationship of $\pi^{\pm}$, (anti)protons or $K^{\pm}$. The cascade daughter tracks were allowed to deviate from that parameterisation by no more than 4σ, where σ is determined from the Gaussian width of the dE/dx curve. The background on the invariant mass of the reconstructed hyperon candidates is reduced significantly by this selection, as is shown in Figure 4.5. A background removal of a factor 2-3 is seen for the Ξ, while the Ω see a reduction of about one order of magnitude. This is due to the background of the Ω being largely dominated by the presence of Ξ candidates, given that prior to this track identification cut, there is no distinction between pion and kaon bachelor tracks. The selection based on the energy loss in the time projection chamber removes a negligible amount of real multi-strange hadrons, given the very loose 4σ cut.

4.4.3 Topological variables

In order to purify the selection of multi-strange baryons it is essential to consider the topology of their decays. The topological parameters of cascades are depicted in Figure 4.6. In order to limit the memory needs for the storage of potential candidates for multi-strange decays, initial loose thresholds had been imposed on the variables during reconstruction of the event and recording of the ESDs. In the following parts of this section, the fine-tuning of each selection cut relative to those original loose

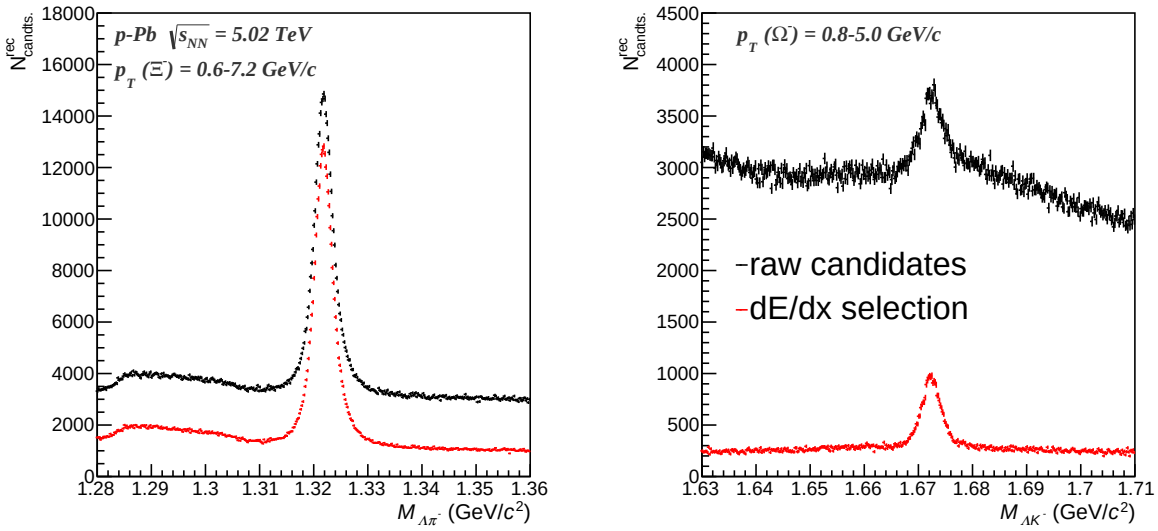

Figure 4.5: The invariant mass distribution of multi-strange baryons under the Ξ^- (left) and Ω^- mass hypothesis. The distribution after the selection according to track energy losses in the TPC is compared with the raw initial histogram.

selections, is described. It will be shown how decisions were made based on a study of the effects that potential selections may imply for the expected signal and background outcome. Use of the Minimum Bias sample - i.e. of the multiplicity-integrated sample - was made for this study, as it is reasonable to assume that in p–Pb collisions, the topology of the cascades does not depend on the event multiplicity. This assumption is based on the fact that in this collision system, event multiplicities reach at most a few tens per unit pseudorapidity, so the reconstruction of the topological parameters is not challenged by large track densities. In the following, the topological variables are described and the decisions on the values of the selection cuts to these variables are explained.

a) The radial positions of the cascade secondary vertices in the transverse plane - R_{tr} and R_{tr}^{V0}

The positions of the decay vertices are calculated from the information of the origin of the tracks (and/or the neutral Λ particle) and their respective momenta. Their location is determined by identifying the radius at which the distance of closest approach

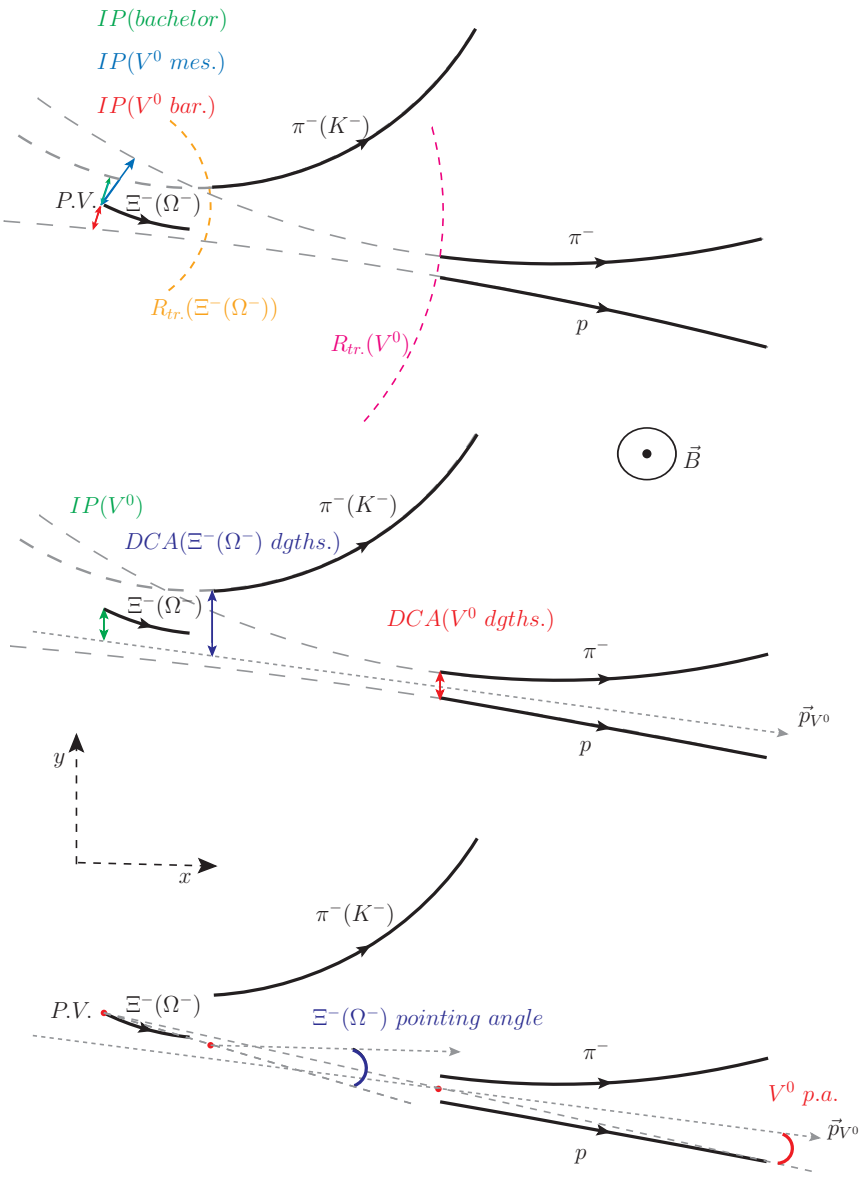

Figure 4.6: Diagrams illustrating the topological variables related to the weak decays of negatively charged multi-strange hadrons produced in the PV: decay radii and impact parameters (IP, top), DCA between tracks (middle) and the cosine of pointing angles (P.A.) of decaying particles. The solid curves show the visible tracks in the detector. The red points represent the reconstructed positions of the primary and decay vertices.

between the daughter particles originating from the decay is found. Those distances are the DCA between the bachelor and the V^0 line of flight for the presumed $\Xi(\Omega)$ decay vertex and the DCA between the V^0 daughters for the vertex of the subsequent Λ decay. The transverse radii of the secondary vertices depend on the lifetime of the Λ, $\Xi^{\pm}$ and $\Omega^{\pm}$ baryons and the p_{T} of these particles. The lower-limit thresholds on their distributions:

$$R_{tr}(\Xi^{\pm}) \geq 0.6\ cm\ ;\ R_{tr}(\Omega^{\pm}) \geq 0.5\ cm\ \ , \tag{4.9}$$

and

$$R_{tr}^{V0}(\Xi^{\pm}) \geq 1.2\ cm\ ;\ R_{tr}^{V0}(\Omega^{\pm}) \geq 1.1\ cm \tag{4.10}$$

were found to be consistent with a maximum signal significance, given by the ratio $\frac{S}{\sqrt{S+B}}$, where S stands for the signal and B the background. In order to calculate the significance, both a signal and a background distribution of the radii are needed. These are extracted from the candidates that lie in the corresponding invariant mass peak and background region, the signal distribution being obtained from a subtraction of the latter to the former. Detailed information on how the signal is defined will be provided in the section of the signal extraction in this chapter (4.5). The slightly looser restrictions in the $\Omega^{\pm}$ selection in cuts 4.9 and 4.10 are a consequence of its smaller mean lifetime ($c\tau$) of 2.461 cm compared to 4.91 cm for the charged Ξ baryons [124].

Figure 4.7 shows the distribution of the significance on the top panels as a function of the potential cut on the radii for the Ξ^- selection. In the bottom panels, it is visible that signal losses are kept well under 1% when applying either of the two cuts, while the background removal is stronger by a factor of about 3 in a multiplicity-integrated and p_{T}-integrated sample. The signal losses are well represented by the Monte Carlo, which ensures a small systematic uncertainty when performing the efficiency correction later. Information on the Monte Carlo simulations will be given in the discussion

of the selection efficiencies in section 4.5.

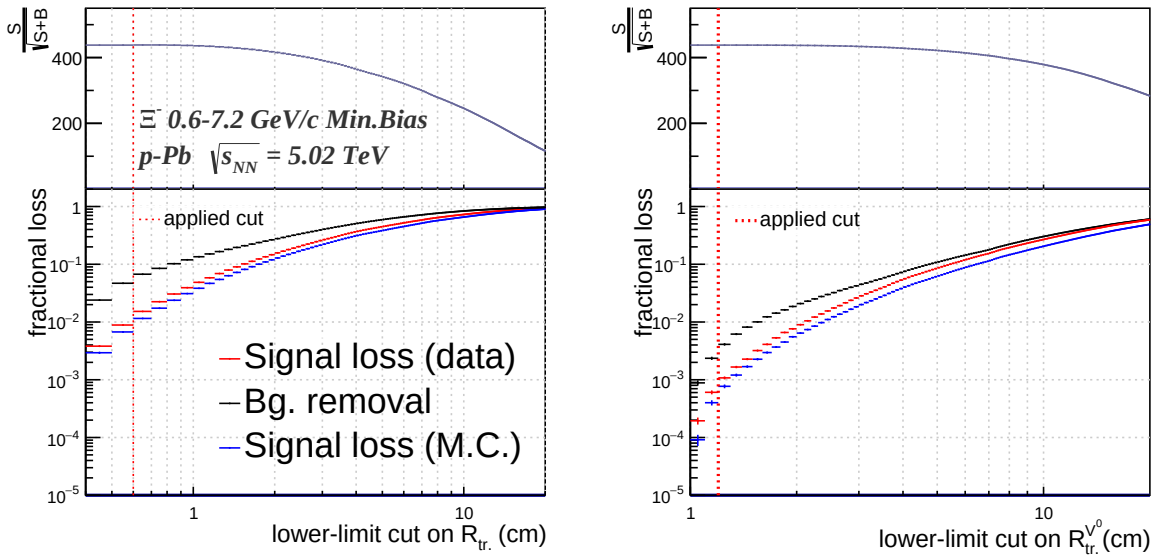

Figure 4.7: The significance (top) and the signal and background losses (bottom) as a function of possible lower-limit thresholds for the cuts on the decay radii of the Ξ^- and its Λ decay radii in multiplicity and p_{T} integrated data.

b) The impact parameter (IP) of the daughter particles

The IP of the bachelor and of the V^0 daughter tracks are sketched in the upper part of Figure 4.6. They are defined as the DCA in the transverse plane between the track and the reconstructed position of the primary vertex. The trajectory of the track is calculated down to the location of the interaction vertex as if it were a primary particle. The smaller the IP of a charged particle is, the higher is its likelihood of actually being a primary particle. In the case of a cascade, all three daughter tracks emerge at secondary vertices and therefore, lower-limit cuts are applied for their selection. While for larger cascade momenta, the tracks are placed further away from the PV causing an increase in the IP, their trajectories will be less bent, thereby reducing the value of the parameter. The two effects help shape the distributions. The following cuts were applied to the IP of the charged tracks:

$$IP_{\,bach} \geq 0.04cm \quad , \tag{4.11}$$

$$IP_{V^0-meson} \geq 0.04cm \quad , \tag{4.12}$$

$$IP_{V^0-baryon} \geq 0.03cm \quad , \tag{4.13}$$

as they are consistent with a maximum overall significance, which can be seen in Figure 4.8. A selection cut is also set to the IP of the neutral Λ, determined by the distance between its trajectory and the PV. The value of this parameter is influenced by both the decay vertex momentum resolution of the two V^0 tracks, which is why a more stringent cut can be applied:

$$IP_{V^0} \geq 0.06cm \quad . \tag{4.14}$$

As seen in Figure 4.8, the total signal losses never exceed 1%, and are well reproduced by the M.C. sample. The most discriminatory cut is the threshold applied to the IP of the bachelor track (4.11), for which a total background removal of about 5% is observed, mostly due to the rejection of wrongly identified secondary tracks found close to the PV.

c) The DCA between the V^0 daughter tracks

The distance of closest approach between the proton and pion tracks produced in the decay of the intermediate Λ baryon would be equal to zero for real Λ decays in case or perfect resolution of the trajectory of tracks. However, the finite track resolution translates into an uncertainty on the particle trajectories and momenta. Therefore the DCA between the daughter tracks is also associated with an uncertainty. Here, this parameter is expressed in units of its own uncertainty σ. An upper-limit is applied to its distribution in order to enhance the probability of selecting candidates for which the two tracks originate from the same vertex:

$$DCA(V^0\ daughters) \leq 1.5\sigma \quad . \tag{4.15}$$

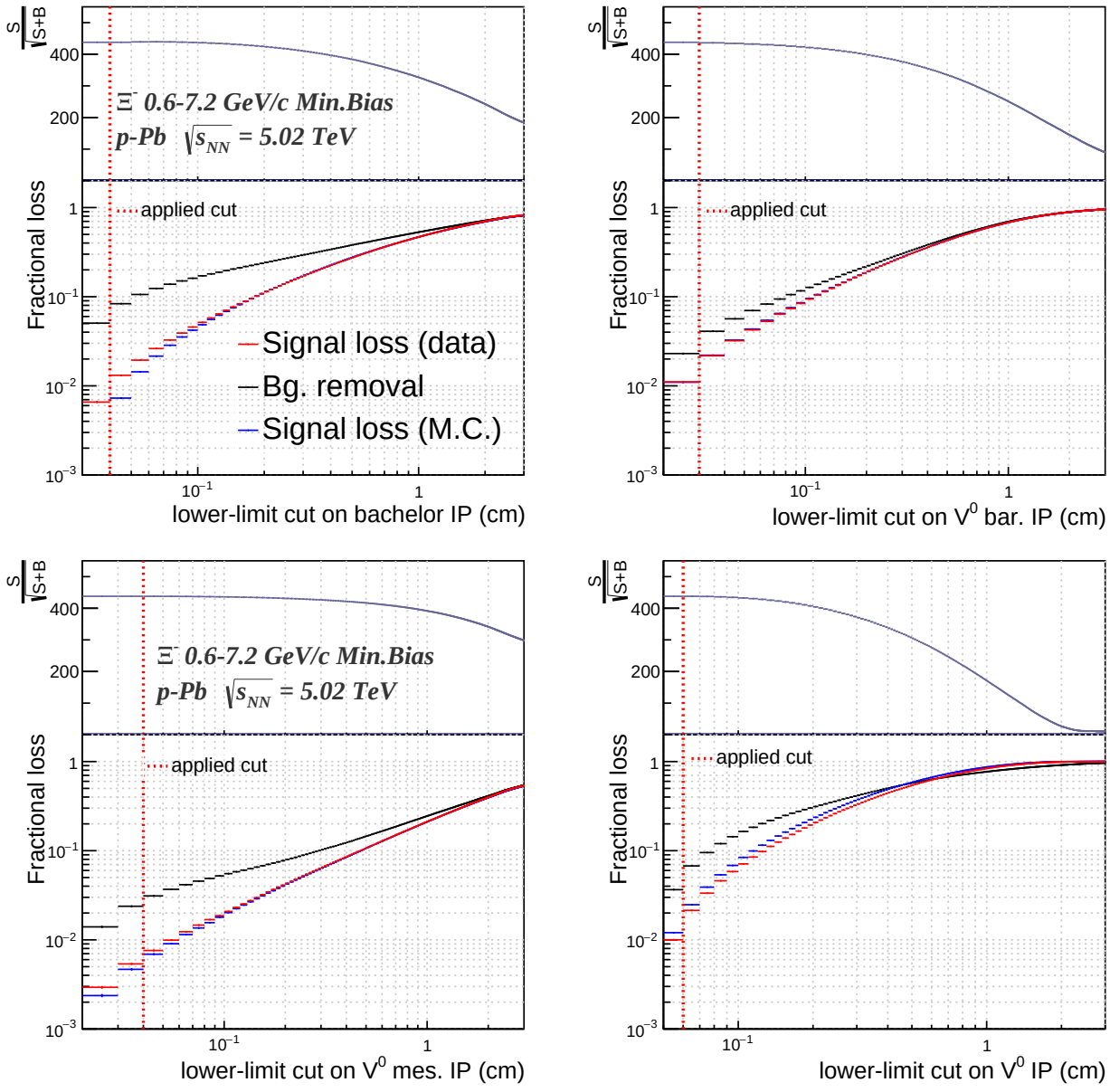

Figure 4.8: The impact parameters of the bachelor (top right), the tracks from the V^0 decay (top left for the proton and bottom right for the π), and of the neutral Λ. The figures show the significances as a function of a hypothetical cut and the signal losses in two different p_{T} intervals, as well as the background removal.

A fractional signal loss of up to 2% and a background removal of 10% follows with this restriction, as is shown for the Ξ^- particles on the left side of Figure 4.9. Monte Carlo appears to underestimate the estimation of the signal losses with respect to the data by a factor of around two at the value of the applied cut (4.15) however due to the small losses observed, the systematic effects are kept low.

d) The DCA between bachelor track and the V^0

As demonstrated in the diagram in the middle part of Figure 4.6, the vertex of the $\Xi^{\pm}$ (or $\Omega^{\pm}$) is also assigned a DCA value between the bachelor track and the line of flight of the Λ particle. The latter position is estimated by tracing back the V^0 momentum vector towards the radial position of the hypothetical hyperon decay vertex. This variable, too, should approach zero for real cascades, the deviations from it being due to the finite track resolution. To this variable, a requirement of

$$DCA(bach - V^0) \leq 1.3\ cm \tag{4.16}$$

is set, giving rise to similar signal losses to those from the DCA variable of the V^0. Similarly to the previous parameter, the value set as upper threshold on this variable also maximises the significance and has a large background suppression potential, in this case exceeding 10%. This can be seen on the right side of Figure 4.9.

e) The cosine of the pointing angles cos(P.A.) and cos$^{V^0}$(P.A.)

The pointing angle (P.A.) is defined as the angle between the line connecting the primary to the decay vertex and the reconstructed momentum vector of the decaying particle (see bottom diagram of Figure 4.6). This angle increases with the bending of the decaying particle. Since the Λ follows a straight trajectory, it does not contribute to a larger P.A. with respect to the angle of the decay of the multi-strange particle, except for a small kink its direction suffers with respect to the direction of the Ξ, at the decay vertex of the latter. The momentum resolution, however, has a dominant

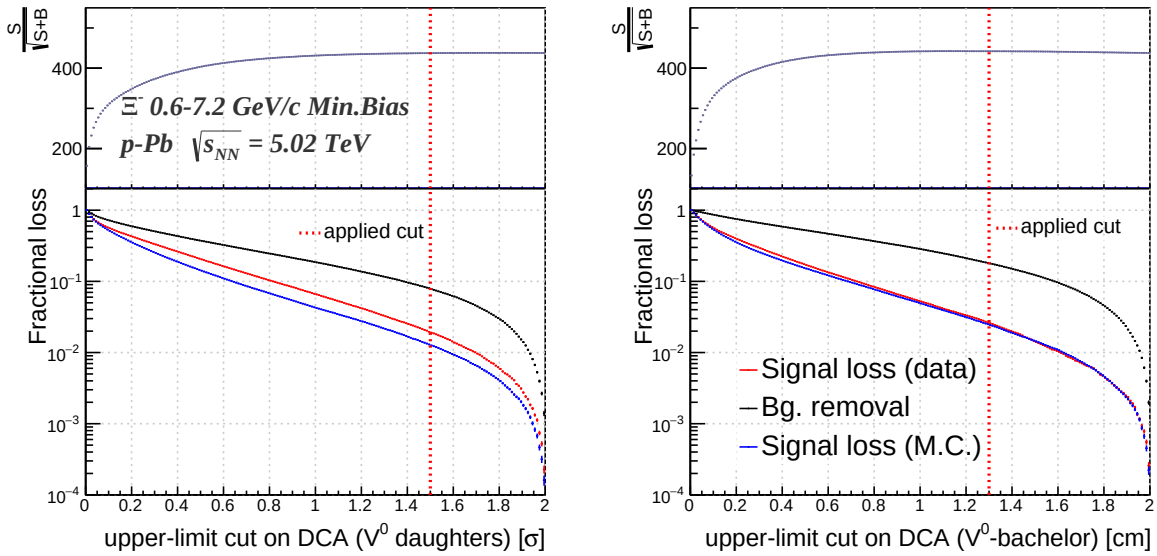

Figure 4.9: The significance (upper panel) as a function of cut threshold on the DCA of the Ξ^- daughters and the signal and background losses (lower panel) entailed with the same cut. The Monte Carlo signal losses for M.C. truth-associated candidates are also shown for comparison.

effect in the determination of this variable, and due to the addition of a third and soft track (the bachelor) in its calculation, the $\Xi^{\pm}$ ($\Omega^{\pm}$) P.A. is on average larger than that of the V^0. As a result, the V^0 distribution of the cosine of P.A. is steeper towards 1, and allows for tighter cuts:

$$cos(PA) > 0.97 \tag{4.17}$$

$$cos(PA)^{V^0} > 0.98 \quad . \tag{4.18}$$

The p_{T} -integrated significances, signal and background losses observed for the Ξ^- particle are shown in Figure 4.10 for these two variables. These variables are both largely discriminatory against background, however they are the worst reproduced by the simulated data. Therefore, care must be taken in avoiding large signal losses in order to minimise the systematic effect due to the efficiency corrections. For that reason, the cut on the cos(P.A.) is not placed at maximum significance (see left side of the figure). Overall, the total background is reduced by above 20% at the cost of

a signal reduction around 1%.

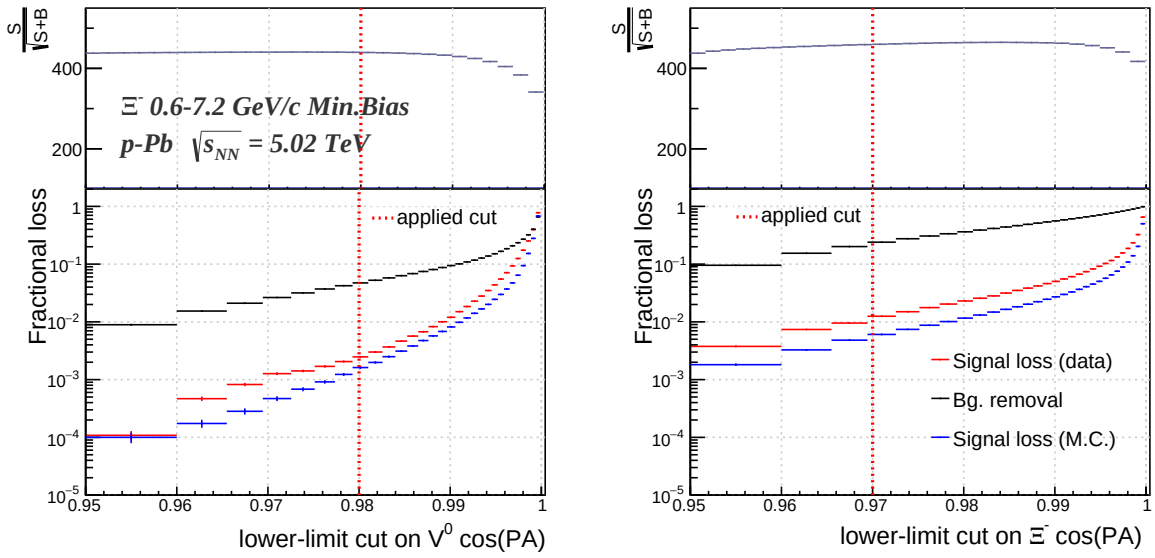

Figure 4.10: The significance (upper panel) as a function of cut threshold on the cosines of the pointing angle corresponding to each of the two weak decays that constitute a Ξ^- cascade, and the signal and background losses (lower panel) entailed with the same cut. The Monte Carlo signal losses for M.C. truth-associated candidates are also shown for comparison.

The p_{T} dependence of the topological variables

From the definition of the ten topological parameters, it is clear that all of them are momentum-dependent, both for physical reasons (decay radii) and technical reasons, due to the influence of the finite momentum resolution of the tracks. In the figures above, the decision on the cuts were placed according to the momentum-integrated sample, rather than studying different p_{T} intervals separately. Due to this choice, the latter study is necessary when determining the systematic uncertainties, in particular for those variables where the Monte Carlo estimated signal losses differ from those in the data, and will do so by different amounts according to the cascade momentum. The systematic studies are described in more detail later in section 4.7.

4.4.4 Number of TPC clusters

A minimum number of TPC clusters is imposed on each track in order to select good quality tracks. The peak on this number occurs at around 140 for both $\Xi^{\pm}$ and $\Omega^{\pm}$, while the M.C. peaks are displaced by about up to 10%, estimating a lower number of clusters than is the case for real tracks. The data and M.C. distributions are superimposed in Figure 4.11. It is due to this misrepresentation - a consequence of both an imperfect track simulation in the M.C. and of a misrepresented p_{T} distributions in the simulated data with DPMJet - that the minimum number of clusters required for the selection of cascade candidates is maintained at a very loose value of 70, thus avoiding systematic biases.

$$N_{cls}^{TPC} > 70 \quad . \tag{4.19}$$

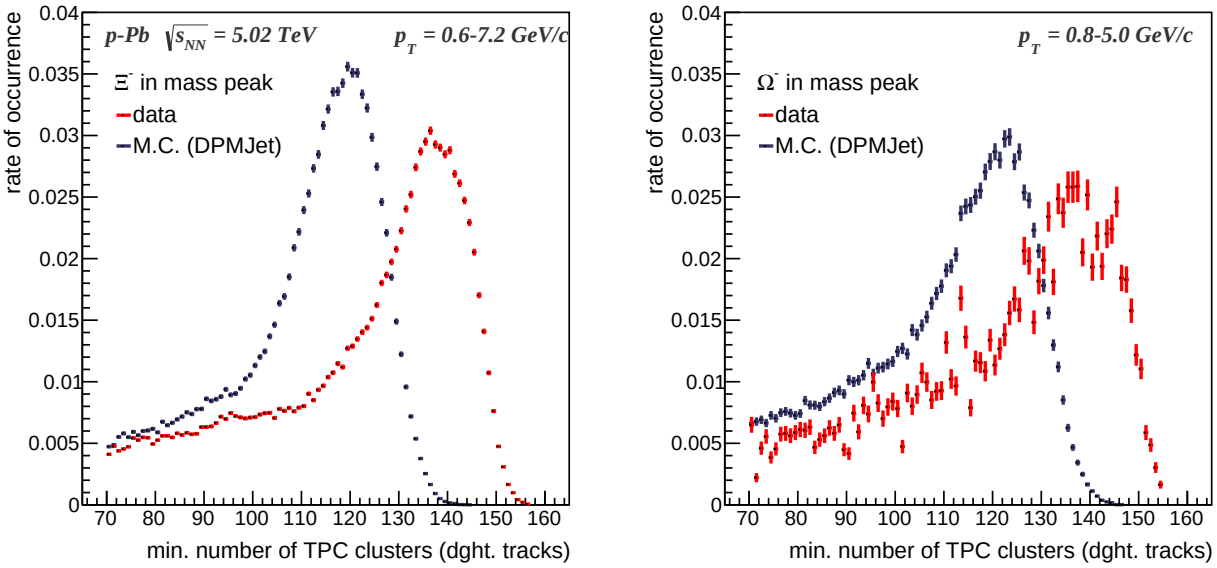

Figure 4.11: The distribution of the minimum number of TPC clusters for the daughter tracks of the Ξ^{-} (left) and Ω^{-} (right) candidates reconstructed in their respective invariant mass peak, subtracted by the curve formed by candidates from the side bands.

4.4.5 The proper lifetime

The lifetime of a decaying particle is expressed in units of length and defined as:

$$c\tau = cmL/p, \tag{4.20}$$

where m is the Particle Data Group (PDG) mass of the multi-strange baryon, L is the decay length traversed by the $\Xi^{\pm}$ or $\Omega^{\pm}$ candidate in the laboratory frame and p is the total momentum of the cascade candidate. Though the multi-strange baryons are charged, the bending of their trajectory due to the presence of a magnetic field is assumed to be negligible for this computation and thus L is measured as the distance between the decay position and the primary vertex. The mean PDG Ξ^{-} lifetime is 4.91 cm and that of the Ω is 2.46 cm. The multi-strange candidates are required to have a measured lifetime within three times their PDG mean lifetime:

$$c\tau \leq 3 \times c\tau_{PDG} \tag{4.21}$$

This cut is particularly powerful at removing low-momentum fake cascade candidates, the tracks of which were produced in interactions with the ITS detector material. This is because it removes particles that appear to have travelled further in the detector than their small momentum would allow them to, giving an implausibly high value for $c\tau$. This is clear from equation 4.20, where low p on the denominator is compensated by a small length Ł in the numerator. In Figure 4.12, the increase in the signal-to background (S/B) ratio is drawn as a function of p_{T} both for the negatively charged Ξ and Ω baryon, confirming that the gain occurs especially at low-momentum, where the increase reaches 2.5. This cut comes at the cost of a total loss of real multi-strange baryons equal to $e^{-3} \sim 5\%$, as the particle decay in a sample can be represented by an exponential decay function, with $c\tau_{PDG}$ as the decay constant.

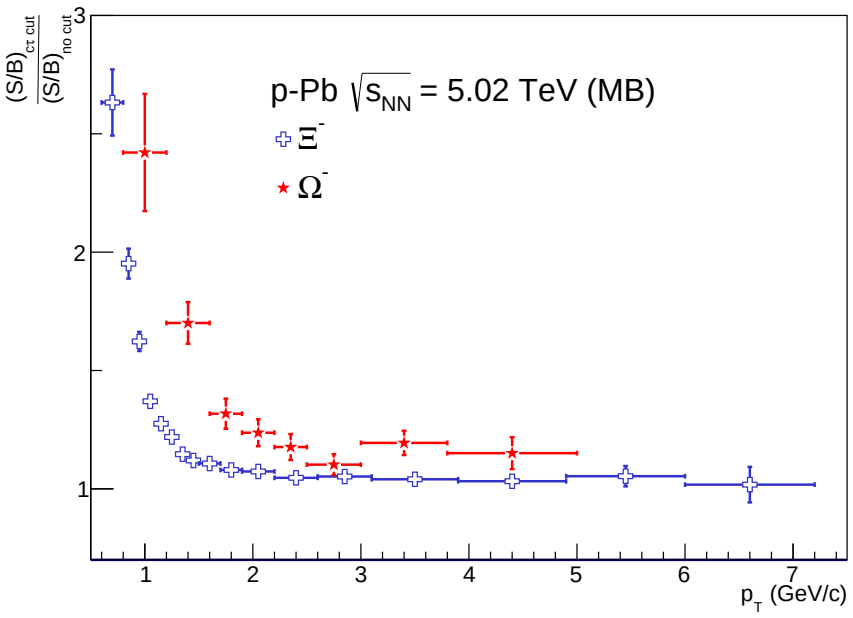

Figure 4.12: The increase in the Ξ^- and Ω^- signal to background ratios when applying the cut on the lifetime. The gain is more pronounced in the low p_{T} region.

4.4.6 Selection based on Invariant mass

Despite the invariant mass restrictions applied before storing the final sample of cascade candidates, and despite the TPC selection according to energy loss, the $\Omega^{\pm}$ selection can still be subject to contamination from $\Xi^{\pm}$ decays. As was already explained at the beginning of this section, the reconstruction of cascades is performed once under the Ξ and once under the Ω mass hypothesis. The background due to Ξ can be partially removed from the Ω selection by not allowing the Ξ-assumed invariant mass to be any closer to the PDG mass of the Ξ^- than 8 MeV/c^2:

$$|M_{\Omega}^{as\ \Xi} - M_{\Omega}^{PDG}| > 0.008\ GeV/c^2 \tag{4.22}$$

The $\Omega^{\pm}$ can also form part of the Ξ background but only to a negligible degree, given that their cross-section is smaller by an order of magnitude. This cut does not improve the extracted signal, however, it plays an important role in reducing

the background, and changing its shape. Figure 4.13 shows an overall background reduction of approximately a factor of two. After the mass cut, its shape takes a linear form in the vicinity of the peak, which is important for the signal extraction. An additional invariant mass selection cut is applied to the mass of the V^0 daughter, which removes all candidates for which that mass lies outside a window of ± 10 MeV/c^2 around the PDG mass of the Λ baryon.

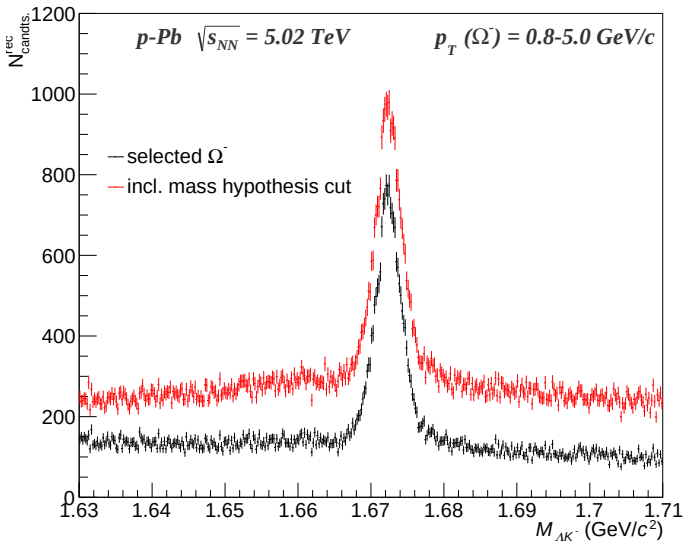

Figure 4.13: The Ω^- p_{T}-integrated invariant mass distribution in M.B. before and after the application of the mass hypothesis cut.

4.5 Signal extraction

The signal is extracted directly from the invariant mass distributions, in different p_{T} and multiplicity bins. Figure 4.14 demonstrates how mass histograms are divided into bands in the process, with the example of low-p_{T} distributions for the high multiplicity class (the 0-5% class) and a low multiplicity one (the 60-80% class). Both Ξ^- and Ω^- mass plots are shown to be fitted with a Gaussian function in the peak region. A central peak band is defined in terms of the number of σ from the Gaussian peak, in this case chosen to be within -4σ and +4σ (i.e. inside the [-4;+4]σ window).

Adjacent side-bands to the mass peak in the ranges [-8; -4]σ and [+4; +8]σ, represent the background. This choice was made to ensure that in every p_{T} interval of every spectrum, the side-bands do not overlap with the mass peak and be fully defined in the background region. The background subtraction method applied is a so-called *bin counting* approach, which consists of directly subtracting the bin entries inside the two side-bands from the total number of entries registered in the peak region. Such a method forcibly assumes that the background area under the mass peak is the same as it is in the outside regions where no signal is present. In other words, it assumes a linear background. A linear function fit to the background on both sides of the peak is shown in the four mass histograms of Figure 4.14. Although the fit was not directly used in the default signal extraction method, an approach in which the integral under that linear function represents the background was pursued in the studies of the systematic uncertainties.

4.5.1 Statistical uncertainty

The subtraction applied in the signal extraction method is performed on two non-correlated quantities: the peak counts, which contain the signal (N_s) and the background (N_b) and the sum of the entries in the adjacent background bands which also constitute the background (N_b). A Poisson uncertainty is attributed to these three counts. The statistical uncertainty on the signal is obtained through the error propagation of this subtraction and is:

$$\sigma_{stat} = \sqrt{N_s + 2N_b} \quad . \tag{4.23}$$

4.6 Signal Correction

In order to estimate the true number of multi-strange hadrons available in each p_{T} interval, it is important to correct the measured cascades signals for the *efficiency* of

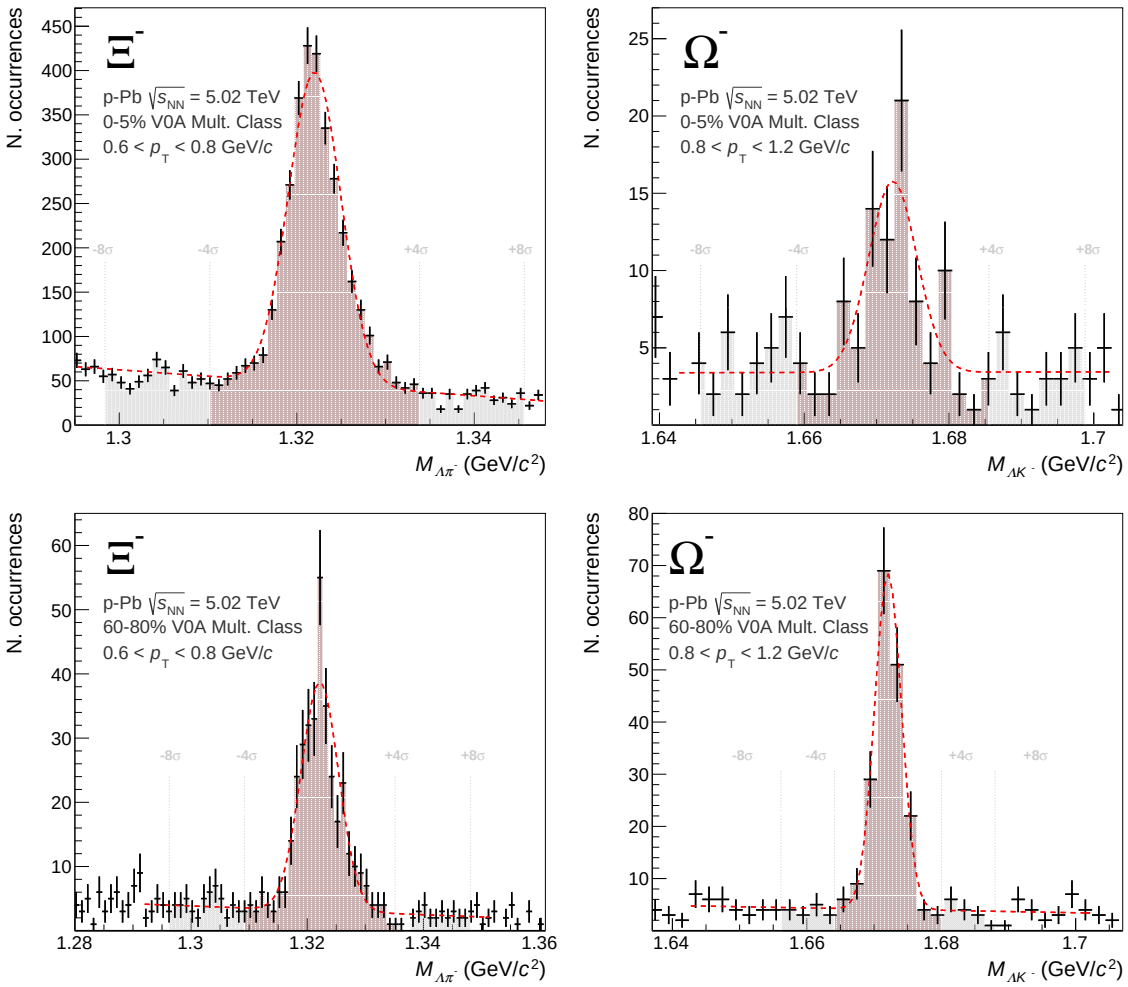

Figure 4.14: The final Ξ^-(left) and the Ω^-(right) invariant mass distributions in the 0-5% (top) and 60-80% multiplicity classes in low-p_{T} intervals. A Gaussian function (red dotted line) fits the peak. The peak and side-bands (coloured boxes) are defined by the standard deviation parameter of the Gaussian fit. In order to extract the signal, the area under the side-bands is directly subtracted from the peak region. The choice of this method is supported by a good representation of the background of a linear fit.

the selection approach described above. The *efficiency* is in fact only partially defining of the correction factors that need to be applied. The selection of cascades in data must be corrected for the efficiencies of the reconstruction and selection methods, the acceptance limits due to the geometrical constraints in which the measurements are conducted, and for the branching ratio of the decay channels that are not considered (decays of $\Xi^{\pm}$ and $\Omega^{\pm}$ other than (4.5)-(4.8)). [1]

The estimation of the efficiencies was carried out by repeating the same analysis process in simulated data as that performed in data and checking against the truth information of the generated multi-strange particles. With the DPMJet simulated data it is not straightforward to obtain similar signal to background ratios as in data. It will be shown later in the next chapter, that the DPMJet model underestimates the relative Ξ and Ω cross-sections. This plays a crucial role in the estimation of the final $\Omega^{\pm}$ signal-to-background ratio, as we know that apart from the combinatorial part, a fraction of its background is due to the presence of real $\Xi^{\pm}$ when reconstructed under the $\Omega^{\pm}$ mass hypothesis. This could result in inaccurate efficiencies if the same signal extraction method described in the previous section is applied. In order to get around this problem, only the reconstructed candidates that could be associated to true cascades were selected. This method - which is the only part where the M.C. analysis differs from the analysis in data - removes the necessity to perform any background subtraction. It is a cleaner way to arrive at the signal of multi-strange hyperons. The occasional true multi-strange hadron, the invariant mass of which was binned outside the peak band was also removed in exactly the same way as it would have been in the data. This is to remove cascades with a badly determined invariant mass, a situation which occurs with similar frequency in the data as in the M.C. The efficiency in p_{T} bin i (ϵ^i) is calculated by dividing the obtained M.C. signal by the inclusive number of actual generated multi-strange particles in the M.C. sample, within the desired rapidity interval:

$$\epsilon^i = \left. \frac{N^i_{ass.}}{N^i_{gen}} \right|_{-0.5<y<0} , \tag{4.24}$$

where $N^i_{ass.}$ is the number of both selected and associated, and N^i_{gen} the number of generated $\Xi^{\pm}$ or $\Omega^{\pm}$ in the same p_{T} bin.

[1]For conventional reasons, the correction factors to be applied to the number of measured multi-strange hadrons are here referred to as *efficiencies*.

Unlike $N^i_{ass.}$, N^i_{gen} is inclusive of all decay channels. The signal corrected for these limitations is obtained by dividing the extracted signal in data by the correction factor, i.e. N^i_s/ϵ^i, where N^i_s is the extracted signal in p_{T} bin i.

The numerator and denominator of the correction factor ϵ are two highly correlated quantities: the hadrons counted in the former are counted in the denominator, too. A binomial error:

$$\sigma_{\epsilon^i} = \frac{\sqrt{N^i_{ass.}(1-\epsilon^i)}}{N^i_{gen}} \tag{4.25}$$

is thus assigned to the efficiency ϵ.

4.6.1 Monte Carlo

The Monte Carlo data used for the estimation of the efficiencies were obtained through simulations by the DPMJet event generator [125], alongside simulations for the propagation of particles in the ALICE detector performed by GEANT–3 [126]. The DPMJet model is known to severely underestimate the multi-strange cross-sections. While the production rate of these particles is not relevant for the calculation of the efficiencies, it is preferable to have a large number of such particles present in the sample, in order to avoid the efficiencies to dominate the statistical uncertainty on the measured momentum spectra. For that reason, special specifications were applied in the simulation of the M.C. data. Four different samples were produced, one for each of the particles and anti-particles. Knowing that the generation of particles causes only a small fraction of the consumption cost compared to the reconstruction process, the latter was only pursued when an event was encountered with at least one generated multi-strange baryon. In addition, a pseudorapidity cut of $|\eta| < 1.2$ was introduced in order to reduce the production time cost further. For the Ξ baryons only, an additional transverse momentum cut of $p_T > 2.0$ GeV/c was applied. This was due to

the model mis-representation of the rate being most pronounced in the higher momentum range, as will be discussed in the next chapter (section 5.2.1). In total, 5 and 10 million such events were reconstructed with $\Xi^{\pm}$ and $\Omega^{\pm}$ respectively. The fact that the measured efficiencies did not show any deviation with respect to the default, non-enhanced productions allowed the two types to be merged into one sample for charged Ξ and another one for charged Ω particles.

4.6.2 Efficiencies

The obtained efficiencies in the Minimum Bias sample are presented in Figure 4.15. A strong rise with increasing transverse momentum is observed reaching maxima of 32% ($\Xi^{\pm}$) and 18% ($\Omega^{\pm}$) measured at 4 GeV/c. These maxima represent just slightly less than half the total amount of baryons detectable, given the branching ratios for the decay modes considered.

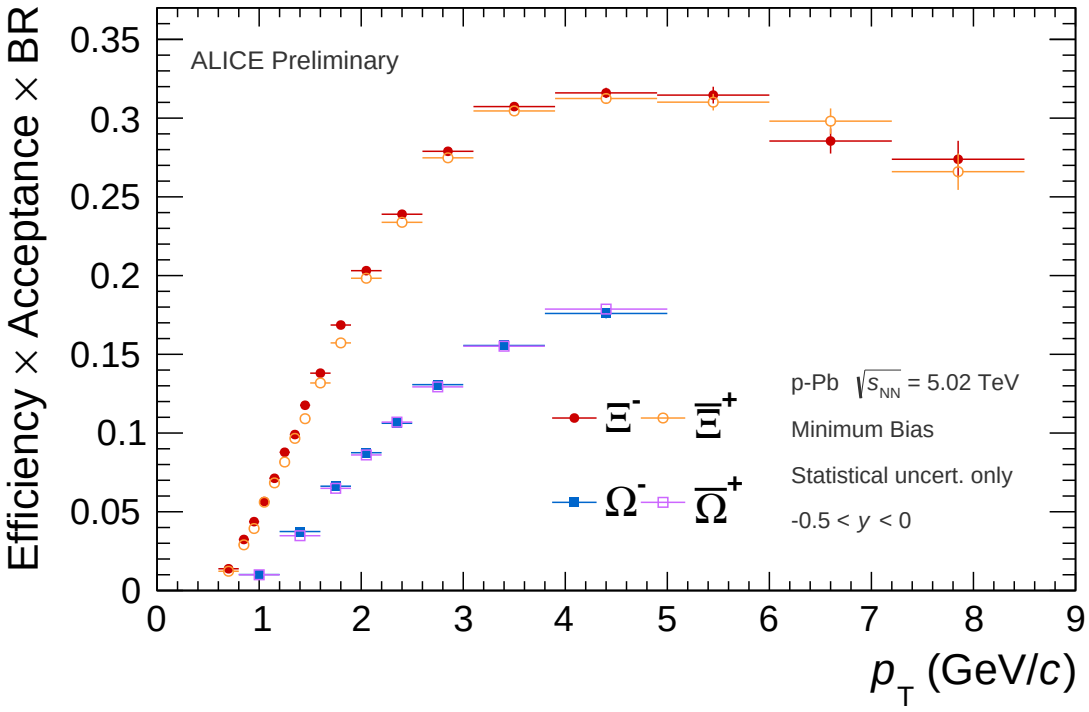

Figure 4.15: Minimum Bias efficiencies for Ξ^-, $\overline{\Xi}^+$, $\Omega^-$and $\overline{\Omega}^+$.

There is the possibility of *feed-down* in the Ξ selection, i.e. the presence of secondary $\Xi^{\pm}$ in the sample that decay from the $\Omega^- \to \Xi^-\pi$ and its charge conjugate decay. The branching ratio of this decay is only 8.6%, and the Ω/Ξ ratio is smaller than 10%. As a result, less than 1% of the selected Ξ^- could potentially have originated from feed-down processes. The selection cuts based on the topological parameters reduces their contribution. The amount that remains, is not corrected for by the efficiency as defined above. This effect is however negligible, compared to other systematic errors.

4.6.3 Dependence on Multiplicity

It is important to study whether the event multiplicity can have an effect on the efficiency to identify cascades. In cases where the charged particle multiplicities are very high, one can expect the successful reconstruction of multi-strange baryons to decrease. In p–Pb collisions, however, the changes in average multiplicity are within one order of magnitude and are well below the nominal multiplicity handling capabilities of the ALICE detector: the mid-rapidity charged particle pseudo-rapidity density is 45 ± 1 [127], but the ITS and TPC were designed to cope with up to 8000 tracks. Similarly, in very lowly populated events, the primary vertex is determined with less accuracy, which in turn affects the accuracy of the topological parameters. Although this case is a concern for a systematic error, it can affect the efficiencies, too. Figure 4.16 compares the efficiencies measured in M.B. events with those from the 0-5% and the 80-100% classes. Within the uncertainties, no multiplicity dependence is observed, and therefore efficiencies calculated with the M.B. sample were used in order to correct the measured signals in the data. This choice benefits from the larger statistics available in the sample and thus minimises the statistical uncertainty of the measurements. A 2% systematic uncertainty is applied across all multiplicity classes due to this choice, in order to cover any potential effect buried within the statistical fluctuations of the ratios in Figure 4.16.

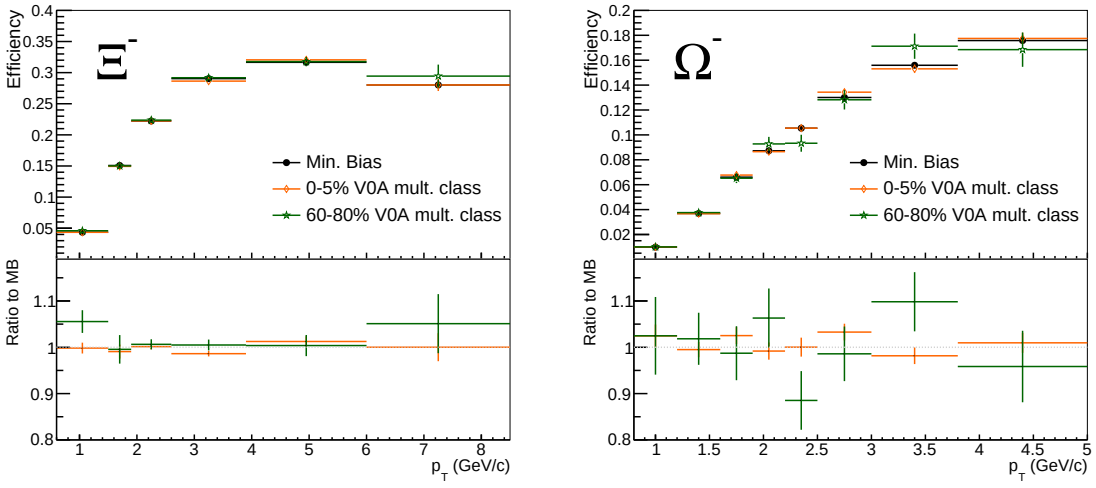

Figure 4.16: Efficiencies obtained in the 0-5% and in the 60-80% multiplicity classes compared with the M.B. efficiencies. The ratios to the M.B. efficiencies are drawn on the bottom panel.

4.7 Systematic uncertainties

As described in the preceding sections of this chapter, a series of decisions had to be taken when making the selection of multi-strange baryons. While these were mostly justified by minimising the statistical uncertainty and optimising the signal, systematic effects were introduced in the process. The Monte Carlo simulations with which the signal corrections were calculated do not provide an accurate description of the values of some topological and kinematic properties of the hyperons, nor of the detector responses to them. Due to these modelling imperfections, the choice of cuts affects the final results and it is imperative to compute by how much in order to compute the systematic uncertainties on the p_{T} spectra.

The strategy to obtain an estimate of the systematic errors in the corrected p_{T} spectra relies on exploring variations on the selection cuts, and observe the deviations in the hyperon yields. In this process, it is important to consider the different distributions of several parameters in different p_{T} ranges. The following sub-sections provide a description of the variations that were applied to the analysis settings and

the considerations that were made for low and high p_{T}.

4.7.1 Uncertainties due to selection cuts

In this section a detailed account of the estimated systematic uncertainties is given due to the various selection cuts mentioned earlier.

a) Topological selections

Table 4.2 shows the variations in the selection criteria that were applied to evaluate the systematic shifts in the bins of the p_{T} spectra. The decisions on the variations were made such that signal changes were within 10%. The whole analysis was rerun for every single cut variation, while keeping all other settings according to their default values. As has been discussed previously, the shapes of the topological variables are p_{T}-dependent, and thus different cut thresholds entail different signal losses depending on the p_{T} of the multi-strange baryon candidate. This is illustrated for the distribution of the DCA between the two V^0 daughters in Figure 4.17: identical selection cuts remove larger signal fractions at low than at large momentum and, therefore, different changes to the default selection on this variable are considered.

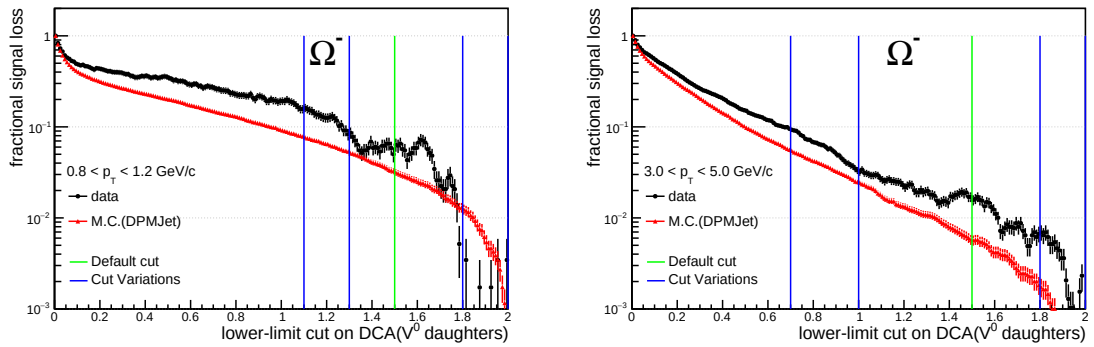

Figure 4.17: Variations considered to the cut on the DCA between the V^0 daughters for the estimation of the systematic uncertainty on the Ω^- due to this selection criterion. At high p_{T} , tighter cut variations with respect to low p_{T} are applied in order to observe similar signal losses. The variations are obtained by studying the $0.8<p_{\mathrm{T}}<1.2$ GeV/c (left) and $3.0<p_{\mathrm{T}}<5.0$ GeV/c (right) ranges separately.

The following facts about the momentum dependence of the topological parameters

were considered for the decision on the values presented in the table:

- The decay radii of the multi-strange hadrons and V^0s are distributed at larger radii for particles with higher momentum. To compensate for this, tighter cut variations are considered at high p_T such that similar signal losses with respect to low-p_T are explored.

- High momentum particles follow less curved trajectories, which is why the impact parameters of the decay products of particles with larger p_T are generally smaller. This results in steeper distributions towards zero, which allows for looser cuts to see the same signal losses as in lower momenta. In addition, for the same p_T of the mother particle, the heavier bachelor track of the $\Omega^{\pm}$ baryons ($K^{\pm}$) carries, on average, more momentum than the bachelor track of $\Xi^{\pm}$ ($\pi^{\pm}$). This was also taken into account, resulting in less severe variations in the selections based on the impact parameter of the bachelor track of the $\Omega^{\pm}$ with respect to the same parameter of the $\Xi^{\pm}$ bachelor.

- The DCA between the cascade daughters and the DCA between the V^0 daughters have better resolution at high momentum. The varied upper limit cuts are therefore tightened with respect to low-p_T.

- The cascade cos(PA) and V^0 cos(PA) distributions are flatter at small p_T due to smaller resolutions and hence show larger deviations from one. Looser selection variations were pursued at low p_T for the study of the systematic uncertainties.

Corrected spectra are extracted for every variation on the topological selection criteria. The ratio of these spectra to the default spectrum are all shown in Figures 4.18 and 4.19 for Ξ^- and Ω^- respectively. The observed deviations are in general well below 5%, with the maximum deviations occurring in the extremities of the p_T spectra. The systematic uncertainty of any p_T interval is the maximum deviation observed among the several analyses, divided by two.

Table 4.2: Topological selection variations used in systematics studies. Values in parenthesis correspond to selection settings used for the $\Omega^{\pm}$ analysis only, in those cases where those varied with respect to the $\Xi^{\pm}$.

Variable	v. loose	loose	default	tight	v. tight
				low/mid-p_{T}, high-p_{T}	low/mid-p_{T}, high-p_{T}
$R_{tr.}$	> 0.4	>0.5	$> 0.6(0.5)$ cm	$> 0.8(0.7)$, $1.5(1.0)$	$> 1.1(0.9)$, $3.25(1.7)$
$R_{tr.}^{V^0}$	> 1.0	>1.1	$> 1.2(1.1)$ cm	> 2.0, $5.0(3.5)$	> 3.0, $11.0(6.0)$
IP$_{bach.}$	-	>0.03	> 0.04 cm	> 0.1, $0.1(0.07)$	> 0.22, $0.15(0.10)$
IP $_{V^0}$	-	>0.05	> 0.06 cm	> 0.10	$> 0.17(0.20)$, 0.13
IP $_{V^0-mes.}$	> 0.02	> 0.03	> 0.04 cm	> 0.15	> 0.30, 0.34
IP $_{V^0-bar.}$	-	> 0.02	> 0.03 cm	> 0.10, 0.08	> 0.17, 0.11
DCA $_{V^0 dgths.}$	< 2.00	<1.80	$< 1.5\ \sigma$	< 1.30, 1.00	< 1.10, 0.70
DCA $_{bach.-V^0}$	< 2.00	<1.80	< 1.3 cm	< 1.20, 1.00	< 0.90, 0.80
cos(P.A.)	> 0.95	> 0.96	> 0.97	$> 0.982(0.980)$	$>0.982(0.985)$
V^0 cos(P.A.)	> 0.95	> 0.96	> 0.98	> 0.98, 0.99	$> 0.983(0.980)$, $0.9996(0.9982)$

b) Invariant mass window of V^0 daughter

The invariant mass range allowed for the Λ daughter is changed from a size of 6 MeV to 10 MeV, and the resulting small (1-2%) changes in the spectra are also shown in Figures 4.18 and 4.19.

c) Selection based on TPC energy loss

The track identification through TPC energy loss ($\mathrm{d}E/\mathrm{d}x$), as outlined in section 4.4.2 was performed with a restriction for tracks to lie within 4σ of the Bethe-Bloch curves. The systematic uncertainty due to this selection is obtained from varying this setting between 3 and 7 σ as shown in Figure 4.20 (top figures). As expected, the systematic spectrum deviations show no major systematic momentum dependence. Therefore, based on the observed scatter, p_{T} independent errors of 2% and 3% are assigned due to this selection.

d) Lifetime

The maximum threshold set for the proper lifetime of the cascade candidates had an effect on removing non-primary particles, in particular at low-p_{T}. This threshold

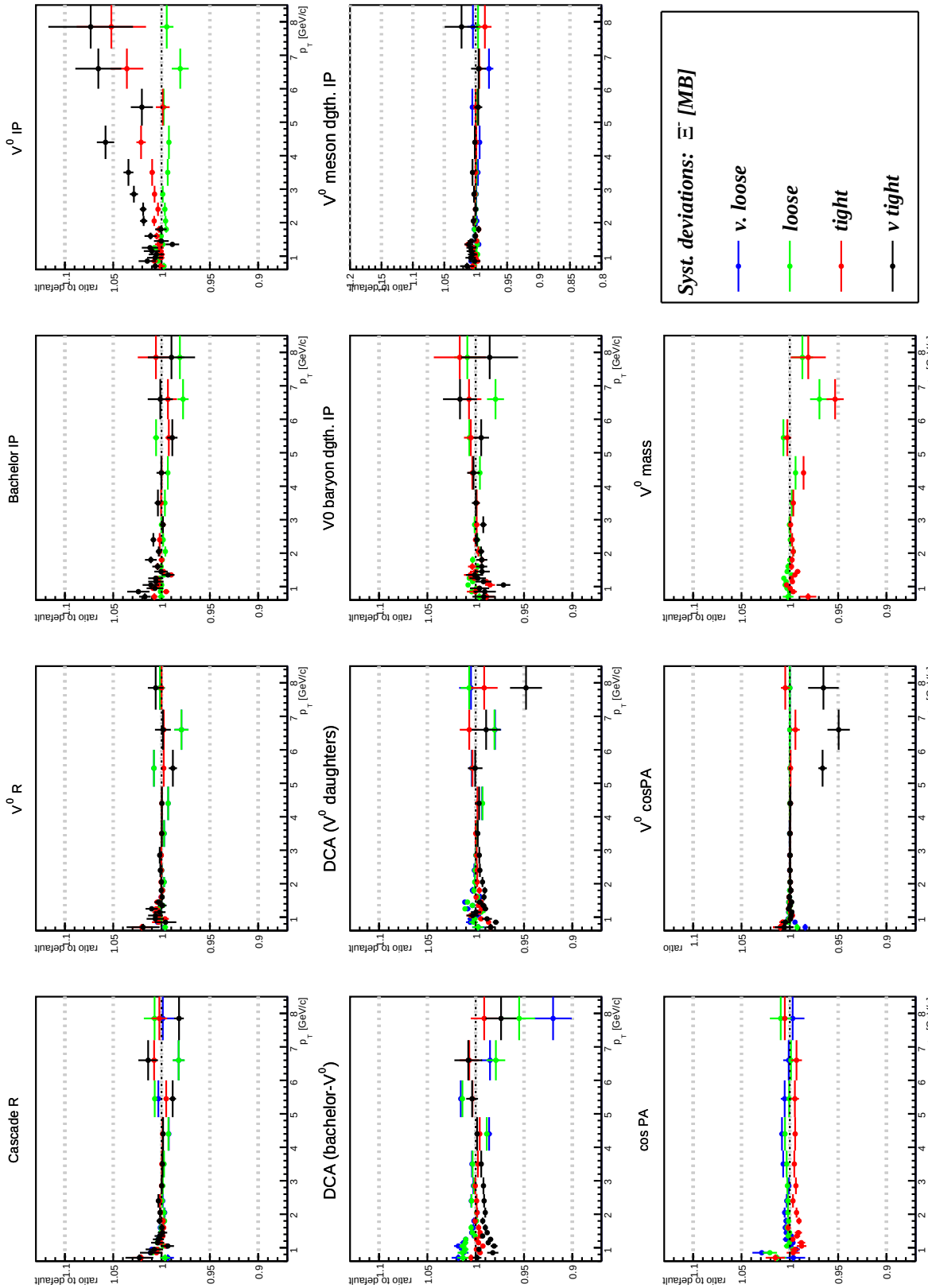

Figure 4.18: Deviations observed in the fully corrected Ξ^- spectra due to changes in the topological selection and on the V^0 mass window in the M.B. sample.

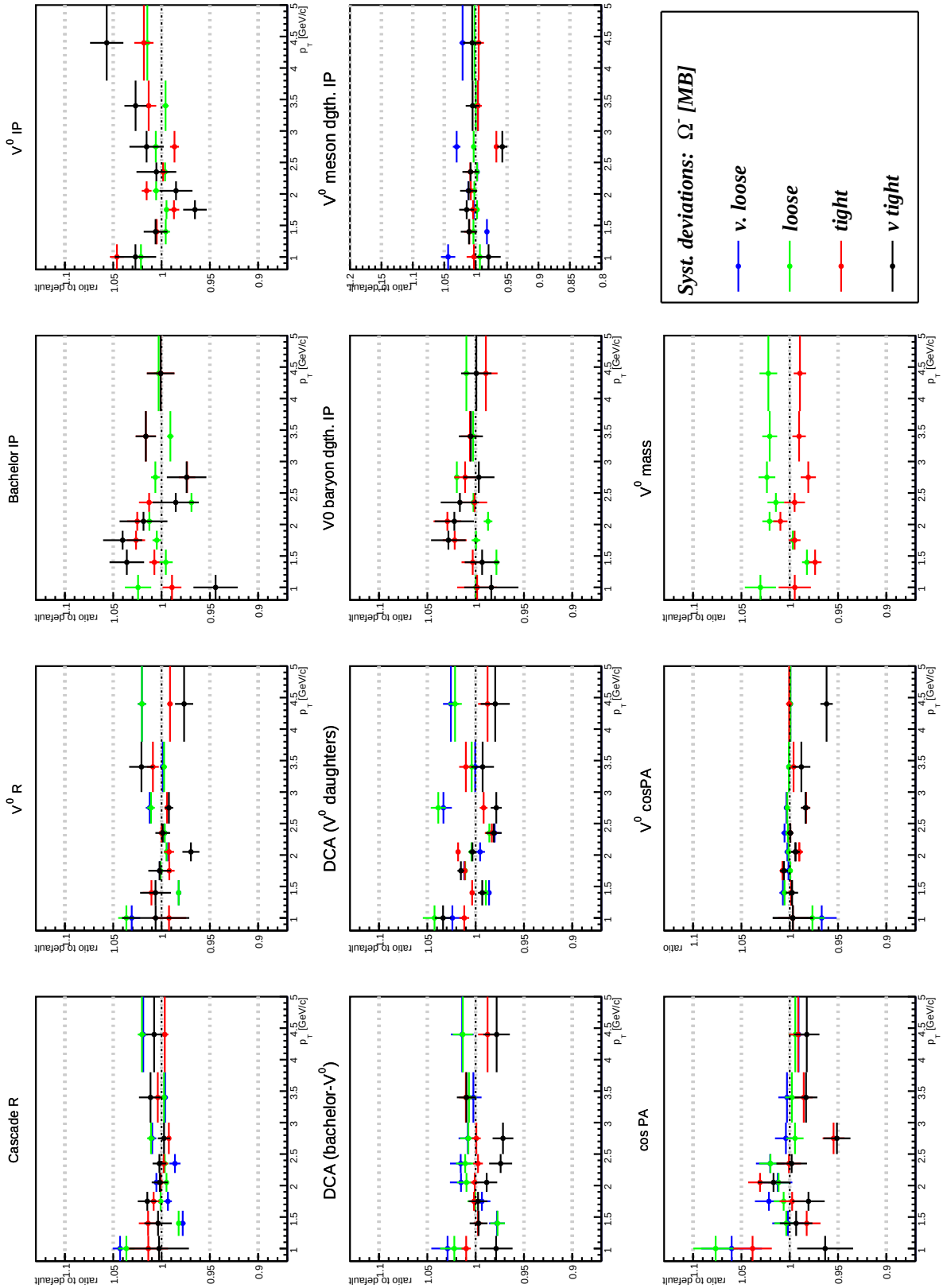

Figure 4.19: Deviations observed in the fully corrected Ω^- spectra due to changes in the topological selection and on the V^0 mass window in the M.B. sample.

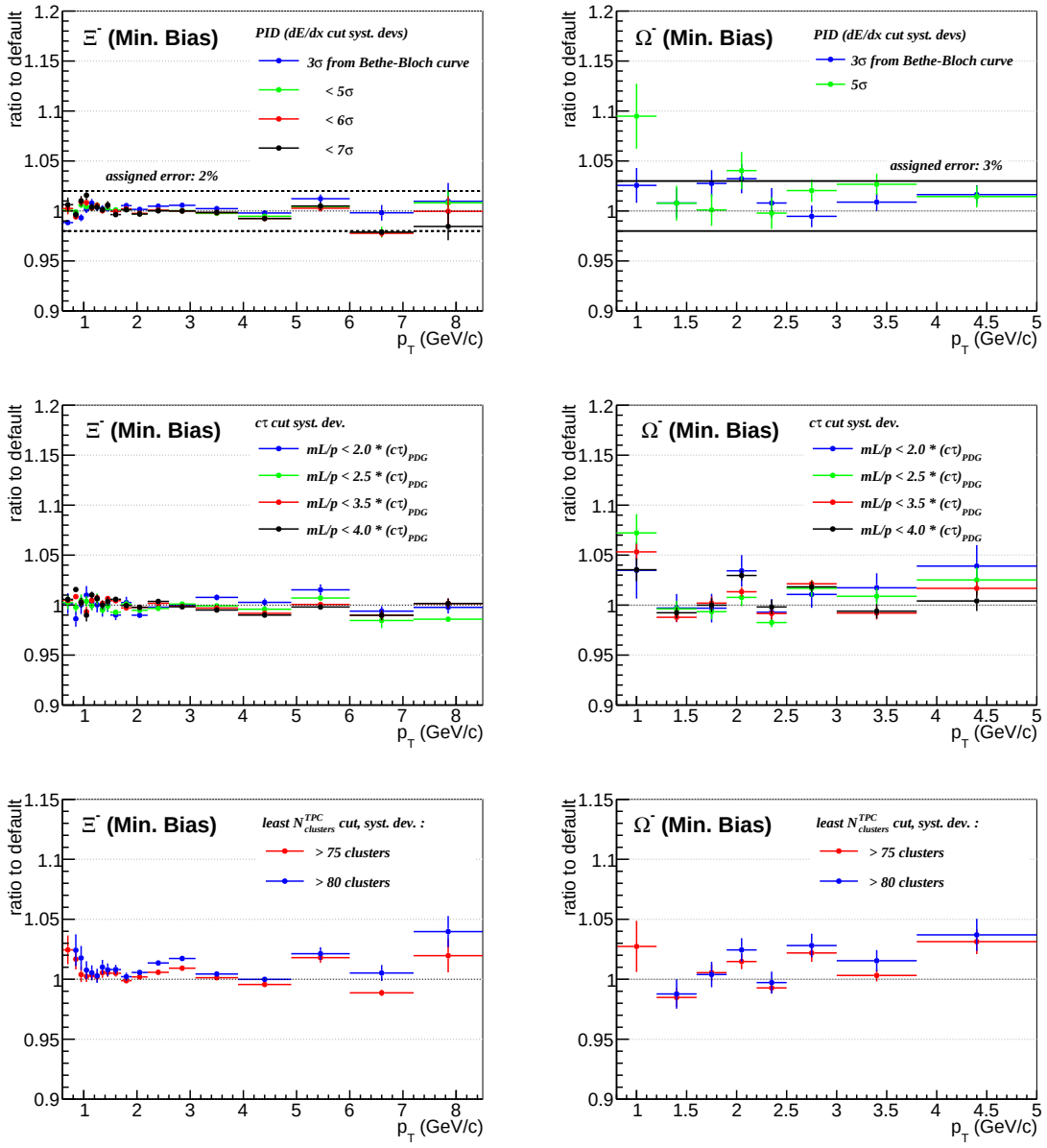

Figure 4.20: The systematic deviations in the fully corrected M.B. Ξ^- (left) and Ω^- (right) spectra with selection changes according to the energy loss of the daughter tracks in the TPC (top), the proper lifetime of the mother particle (middle) and the minimum number of clusters formed in the TPC by the daughter tracks.

is loosened to as much as $4\times c\tau_{PDG}$ and tightened to $2\times c\tau_{PDG}$. Figure 4.20 (middle figures) shows the systematic errors, which add another 2% to the overall uncertainty, with larger errors seen at low momentum.

e) Number of TPC clusters

Also in Figure 4.20 (bottom figures) the spectra ratios according to the selection of a larger minimum number of TPC clusters (75 and 80) for the cascade daughter tracks, than the default 70. Caution must be taken here not to explore very tight cuts, as it is known that Monte Carlo misrepresents their distributions. Uncertainties of 3-4% are seen at low and high momenta, whereas at mid p_{T} the deviations are smaller.

f) Mass hypothesis cut

The cut on the invariant mass for the $\Omega^{\pm}$ selection to remove cascades that are actually $\Xi^{\pm}$ was entirely removed in order to study the effect on the spectrum. The result, shown in Figure 4.21, suggests that the corrected signals suffer very low systematic variations, based on which a constant 1% uncertainty is assigned to the charged Ω spectra.

4.7.2 Uncertainties due to the signal extraction

The systematic error introduced by the extraction of the signal (see section 4.5) was calculated in two different ways: In a first examination, the spectra deviations were studied when varying the size of the peak and their adjacent background bands. This is to test any deviation from the linear behaviour of the background, which is assumed with the employed method. Peak bands were alternatively defined within [-3; 3]σ, [-3.5; 3.5]σ and [-4.5; 4.5]σ and the signal re-evaluated. Secondly, the *bin counting* approach itself was substituted for a background fitting technique. Under that procedure, the background was estimated from a linear fit to the side-bands. The latter

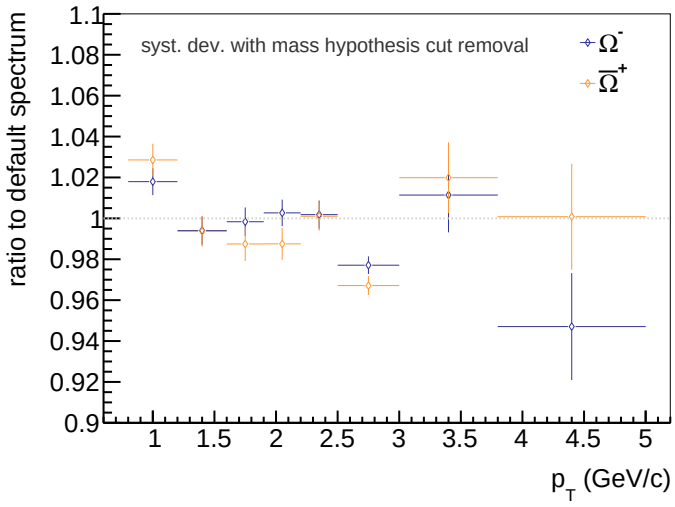

Figure 4.21: Systematic deviations to the M.B. Ω^- spectrum observed when removing the mass hypothesis cut supposed to reject Ξ particles from the selection.

method revealed a 1% uncertainty to the signal extraction, the total error of which vary with p_{T} between 2-5% as shown by the shaded box histogram of Figures 4.23 and 4.24. While these figures show the Minimum Bias errors, the signal extraction is the only source of systematic error that shows some multiplicity dependence. In higher multiplicity events, the background is larger, which can increase the risk of deviations from a linear description. To study this possibility, the signal extraction systematic errors were computed in the different multiplicity classes. However, as Figure 4.22 indicates, the multiplicity-dependence is small. The error on the 0-5% and 60-80% are shown to differ by 2% in the lowest momentum bin. When considering the sum of all the other sources of uncertainty, this will result in a change below 1% with respect to the uncertainty in M.B.

4.7.3 The total systematic uncertainties

The individual systematic uncertainties introduced above are summed up in quadrature in order to obtain the total error. The combined values for the uncertainty are shown in Figures 4.23 and 4.24 for the negatively charged hyperons. A complete breakdown of the values of the different error sources is also shown in these figures.

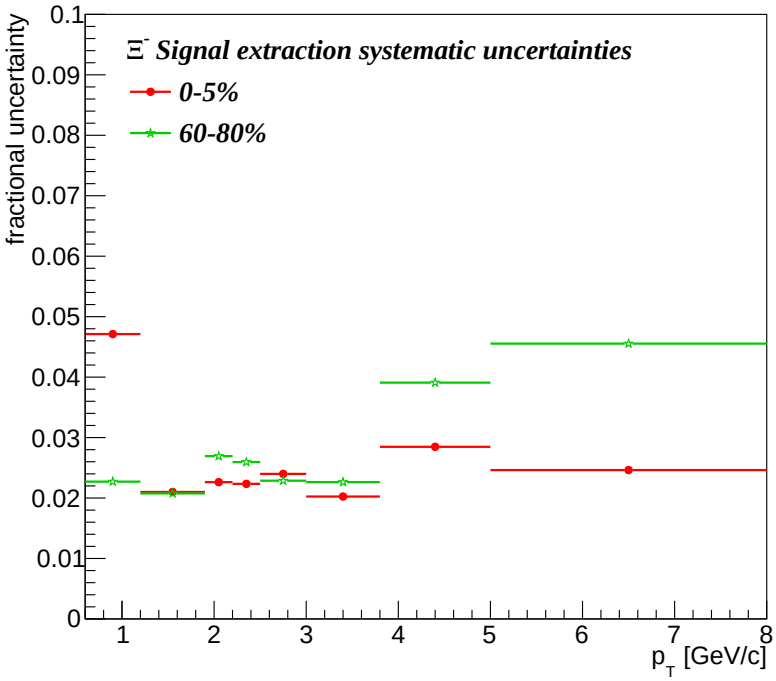

Figure 4.22: The Ξ^- systematic uncertainty due to the signal extraction method in the 0-5% and 60-80% multiplicity classes. An increase in the error by 2% in the high multiplicity bin is observed at low p_{T} . This corresponds to the bins in which the signal to background is smallest.

A constant 4% uncertainty is attributed to the amount of material crossed by the particles. This estimate is based on earlier M.C. tests in which the material budget was varied and the effect of those variations on particle spectra were studied. The signal extraction and the topological selection are the largest contributing sources of uncertainty of the analysis strategy. The systematic uncertainty for Ξ lies between 5% in the mid-p_{T} region, reaches 7% at low-p_{T} and is around 10% at large p_{T}. The $\Omega^{\pm}$ errors are a larger by a few percent, fluctuating around 8% at mid-p_{T} and reaching between 10-12% in the edges of the measured spectrum. As mentioned in section 4.6.2 an additional 2% error is added in quadrature to the systematic error for all multiplicity classes, due to the possible changes in the efficiencies as a function of multiplicity, increasing the total uncertainties by an amount smaller than 1%.

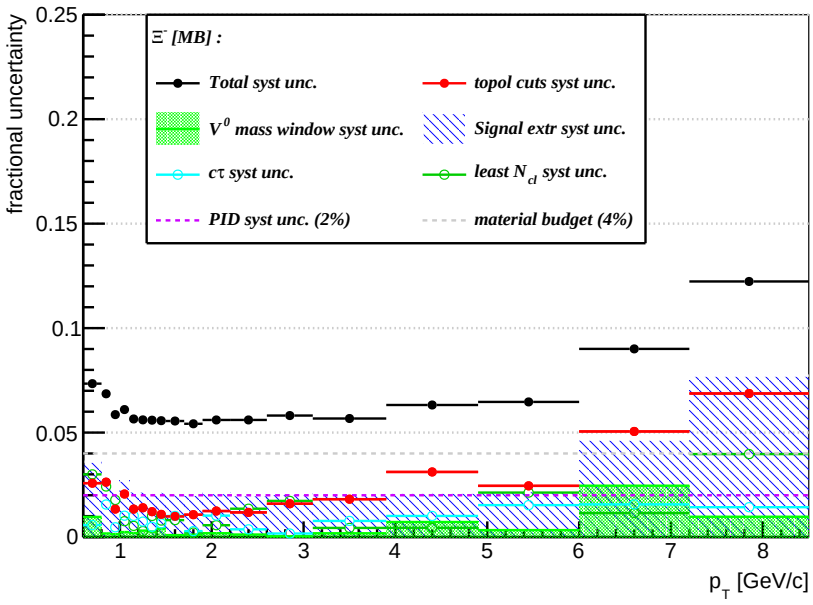

Figure 4.23: Breakdown of the total Ξ^- systematic uncertainties as a function of transverse momentum in M.B..

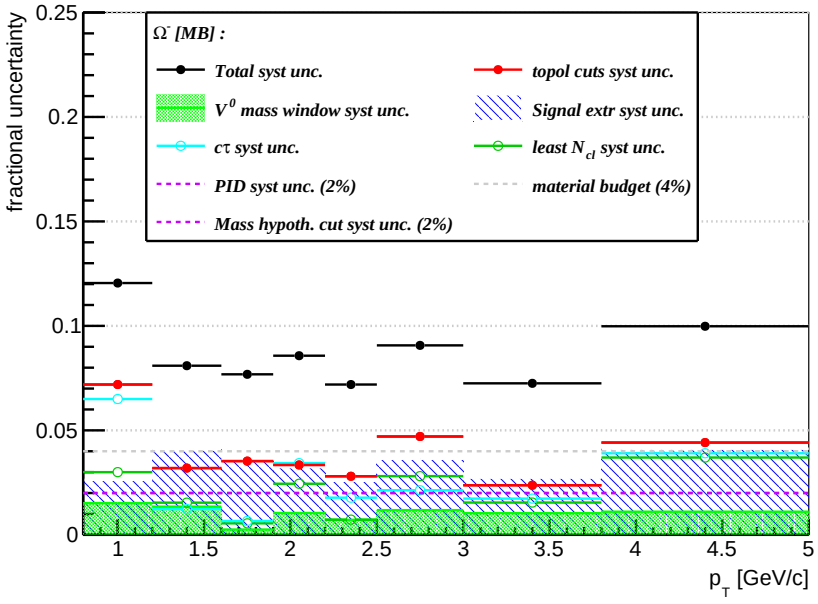

Figure 4.24: Breakdown of the total Ω^- systematic uncertainties as a function of transverse momentum in M.B..

4.7.4 Multiplicity-independent uncertainties

The systematic uncertainty in a given multiplicity class is composed of both a correlated fraction, that is common across all of the multiplicity range, and an uncorrelated proportion that is specific to that class. The fraction of the systematic uncertainty that is independent of multiplicity can be informative for studies of the measured quantities as a function of multiplicity. The presence of the uncorrelated uncertainty becomes apparent when one specific cut causes an upward shift on the yield in a given p_{T} interval and multiplicity class, while in the remaining multiplicity range, the same cut results in a reduction of the yield in that p_{T} bin. In that case, the deviation is unique to that multiplicity class. This uncertainty can be estimated from the ratio of spectra deviations with respect to the shifts seen in M.B. data, as defined by the following double ratio:

$$\sigma^{i}_{uncorr} = \frac{Y_{m}^{dev,i}}{Y_{m}^{def,i}} \Big/ \frac{Y_{MB}^{dev,i}}{Y_{MB}^{def,i}} \quad , \tag{4.26}$$

where $Y_{m}^{dev,i}$ is the measured yield in p_{T} interval i and multiplicity class m deviated from the default value $Y_{m}^{def,i}$ due to the variation of a given cut. This method works under the presumption that uncorrelated errors are small enough that they are smeared by the remaining data in the M.B. sample, such that they only appear on the numerator of σ_{uncorr}.

In estimating σ_{uncorr}, both p_{T} and multiplicity bins were merged in order to reduce statistical effects. As was seen in section 4.7.2, the systematic uncertainty due to the signal extraction was found to show some dependence on multiplicity. It is therefore also the main contributor to the total uncorrelated uncertainty, which was estimated to lie at around 2% for $\Xi^{\pm}$ and 3% for $\Omega^{\pm}$ with little variation with multiplicity class. Figure 4.25 compares the estimated uncorrelated uncertainties in three multiplicity classes for the Ξ^{-} and in two classes for the Ω^{-} hadron with the total systematic

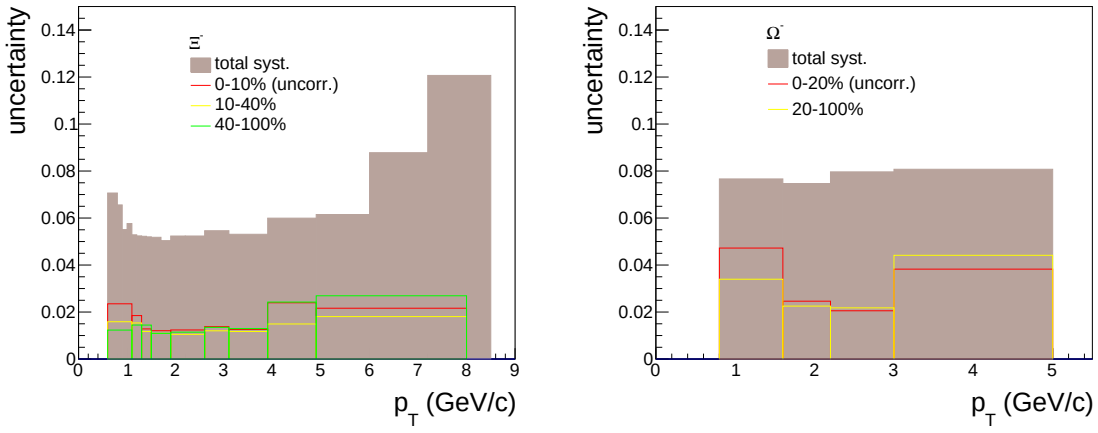

Figure 4.25: The multiplicity-uncorrelated uncertainties in comparison to the total (M.B.) systematic uncertainties for Ξ^- and Ω^-.

uncertainty. According to that figure, the uncorrelated values correspond to fractions of the total systematic uncertainties between 1/5 and 1/3 and between 1/5 and 1/2, for Ξ^- and the Ω^- respectively.

Chapter 5

Results

This chapter discusses the results obtained from the measurements of the production rates of the multi-strange particles in proton-lead collisions. It is divided into two main sections, one that describes the procedure used to obtain the yields and mean p_{T} and another dedicated to the discussion of the results. The latter takes into account measurements of other hadrons in p–Pb collisions, and gives details on comparative studies with the pp and Pb–Pb collision systems at different multiplicities. First, a comparison is made between the measured spectra and the DPMJet model, which incidentally, as mentioned in the previous chapter, has served for the production of the Monte Carlo sample with which the efficiencies of the Ξ and Ω hadrons were calculated. Then, a study of the shapes of the p_{T} spectra is conducted, which attempts to give clues with regard to the possibility of a thermodynamic expansion in p–Pb collisions. The results are analysed with regard to collective behaviour within the entire system. In addition, the reported yields relative to those of the pions will be discussed in light of the statistical hadronisation model.

5.1 Extraction of multi-strange results

5.1.1 Transverse momentum spectra

Figures 5.1, 5.2 and 5.3 show the Ξ and Ω p_{T} spectra in the multiplicity-integrated sample, and in the seven different multiplicity bins. The distributions in the seven specific multiplicity classes are shown as the average of the particle and anti-particle. This was done in order to reduce the statistical uncertainty and considering that at the energies of the analysed collisions, the measured spectra are the same within the estimated uncertainties. This can be seen, for example, in the M.B. spectra, which show that the p_{T} spectra of the negatively and positively charged multi-strange baryons are consistent within the assigned error bars in each data point. The spectra are defined as the number of particles divided by the p_{T} value at the centre of each bin, by 2π, which represents the integral over the azimuthal angle φ, by the rapidity window of 0.5 and by the number of triggered events.

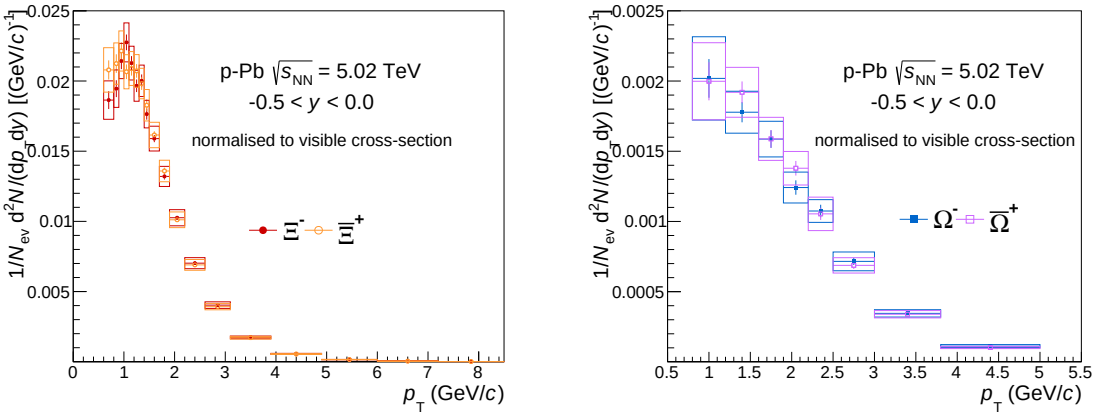

Figure 5.1: The average M.B. Ξ and Ω p_{T} spectra measured with p–Pb collisions at $\sqrt{s}$ = 5.02 TeV, normalised to the visible cross-section.

The $\Xi^{\pm}$ ($\Omega^{\pm}$) spectra, which range from 0.6-8.5 GeV/c (0.8-5.0 GeV/c), are normalised to the number of events corresponding to the visible cross-section. As mentioned in the previous chapter, these are the events that pass the *V0AND* trigger selection. There it was shown that the p_{T} spectra were extracted from the finally

selected number of events, which were obtained after the trigger and the primary vertex quality cuts. With this change in normalisation, only the 60-80% and 80-100% signals suffered alterations by a factor of 0.998 and 0.967, respectively. The M.C. reproduces this signal loss to within less than 1% in those multiplicity classes.

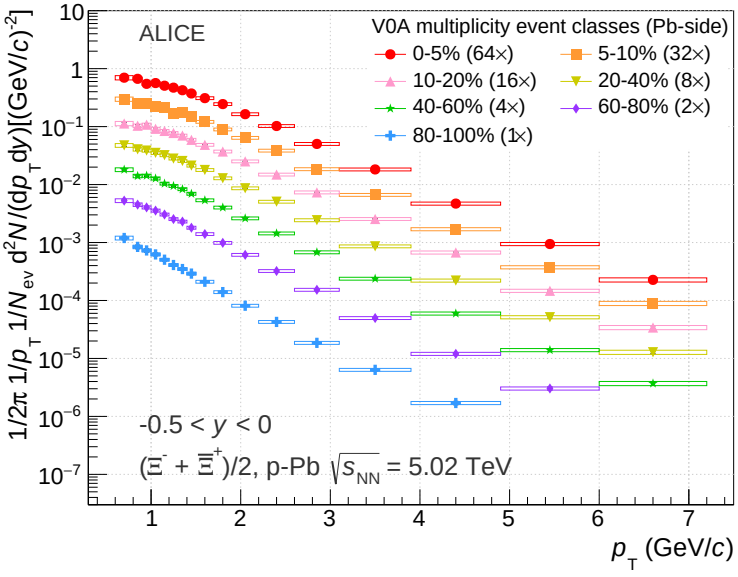

Figure 5.2: The $(\Xi^- + \bar{\Xi}^+)/2$ p_{T} distributions in seven p–Pb multiplicity classes measured in central rapidity. The spectra are normalised to the visible cross-section. The distributions are multiplied by scaling factors in order to be able to visualise all of the seven in the same figure without overlaps of the error bars.

5.1.2 Integrated Yields as a function of multiplicity

The yields of the multi-strange particles are obtained from two contributions: the sum of the $\mathrm{d}N/\mathrm{d}y$ from all measured data points, and the integral under the curve of a function in the unmeasured low and high regions of the p_{T} spectrum. The Lévy-Tsallis function, introduced in section 2.3.2.2 (equation 2.17), was used to fit the measured data points of each spectra, and thus to extrapolate the distributions to the unmeasured regions in order to extract their contributions to the total yield. This function describes the p_{T} distribution of different hadrons with four free parameters,

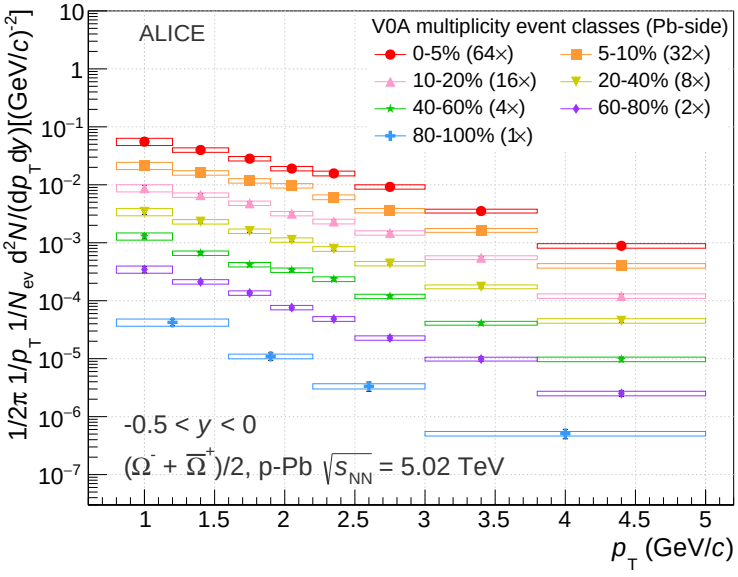

Figure 5.3: The $(\Omega^- + \bar{\Omega}^+)/2$ p_{T} distributions in seven p–Pb multiplicity classes measured in central rapidity. The spectra are normalised to the visible cross-section.

one of which is the particle mass, which can be fixed, and another the yield per unit rapidity itself. The Lévy-Tsallis function fits to the measured $(\Xi^- + \overline{\Xi}^+)/2$ and $(\Omega^- + \overline{\Omega}^+)/2$ spectra in all seven multiplicity classes are shown in Figure 5.4.

The total yields are given in Table 5.1 for the $\Xi^{\pm}$ and $\Omega^{\pm}$, where the mean charged-particle multiplicities measured in the $-0.5 < y < 0.5$ rapidity range [127] for each of these classes are also indicated. Their reduced χ^2 (χ^2/ndf) were below one in all cases indicating that they fit the observed spectra very well across the full measured p_{T} ranges. The values of the T_k and the exponent parameter (n) from the Lévy-Tsallis function are given in table 5.2. The yields obtained from the measured p_{T} region only and their fraction of the total yields can be seen in Appendix A. These fractions range from around 15% to 27% for the $\Xi^{\pm}$ and from about 19 to 40% for the $\Omega^{\pm}$ with decreasing multiplicity. It should be noted that these fits were merely used as a means to obtain the yields, and no physical interpretation is to be made of the extracted parameters. A broader discussion of radial flow in p–Pb collisions will be made in section 5.2.2, involving a simultaneous fit to several hadrons with a common

set of parameter values for the kinetic freeze-out temperature and the transverse flow velocity.

The yields indicated in the above-mentioned table are also drawn in Figure 5.5 as a function of multiplicity. In proton–lead collisions we observe an increase in the yields of multi-strange baryons relative to the charged-particle multiplicities in the event. Within one order of magnitude of charged-particle multiplicity, the multi-strange yields increase by a factor of just over ten.

Table 5.1: The mid-rapidity $\langle \mathrm{d}N_{\mathrm{ch}}/\mathrm{d}\eta \rangle$ values for each of the seven multiplicity classes and the $(\Xi^- + \overline{\Xi}^+)/2$ and $(\Omega^- + \overline{\Omega}^+)/2$ integrated yields per unit rapidity normalised to the visible cross section. The statistical uncertainty on the yields is followed by the systematic uncertainty. The multiplicity-uncorrelated errors are shown in brackets.

Event class	$\langle \mathrm{d}N_{\mathrm{ch}}/\mathrm{d}\eta \rangle$ $\lvert\eta_{\mathrm{lab}}\rvert < 0.5$	$\mathrm{dN/dy}(\Xi^- + \overline{\Xi}^+)/2 \times 10^{-1}$	$\mathrm{dN/dy}(\Omega^- + \overline{\Omega}^+)/2 \times 10^{-2}$
0–5%	45 ± 1	1.181±0.010±0.082(0.025)	1.33±0.06±0.18(0.05)
5–10%	36.2 ± 0.8	0.934±0.008±0.070(0.019)	1.10±0.04±0.15(0.05)
10–20%	30.5 ± 0.7	0.755±0.005±0.057(0.015)	0.87±0.03±0.12(0.04)
20–40%	23.2 ± 0.5	0.555±0.003±0.043(0.010)	0.60±0.03±0.08(0.03)
40–60%	16.1 ± 0.4	0.368±0.003±0.033(0.007)	0.36±0.01±0.05(0.02)
60–80%	9.8 ± 0.2	0.200±0.002±0.012(0.005)	0.21±0.01±0.03(0.01)
80–100%	4.3 ± 0.1	0.074±0.002±0.008(0.003)	0.07±0.02±0.02(0.01)

5.1.3 The Ξ and Ω mean transverse momentum

In addition to calculating the integrated yields for each particle species, it is also interesting to extract their mean transverse momenta ($\langle p_{\mathrm{T}} \rangle$). The $\langle p_{\mathrm{T}} \rangle$ in the seven multiplicity classes are shown in Table 5.3 and drawn in Figure 5.6, as the average of the measured values for particle and anti-particle. They are observed to increase with multiplicity, the rise being more pronounced for lower multiplicity classes than for the most central data points. Furthermore, these measurements also indicate

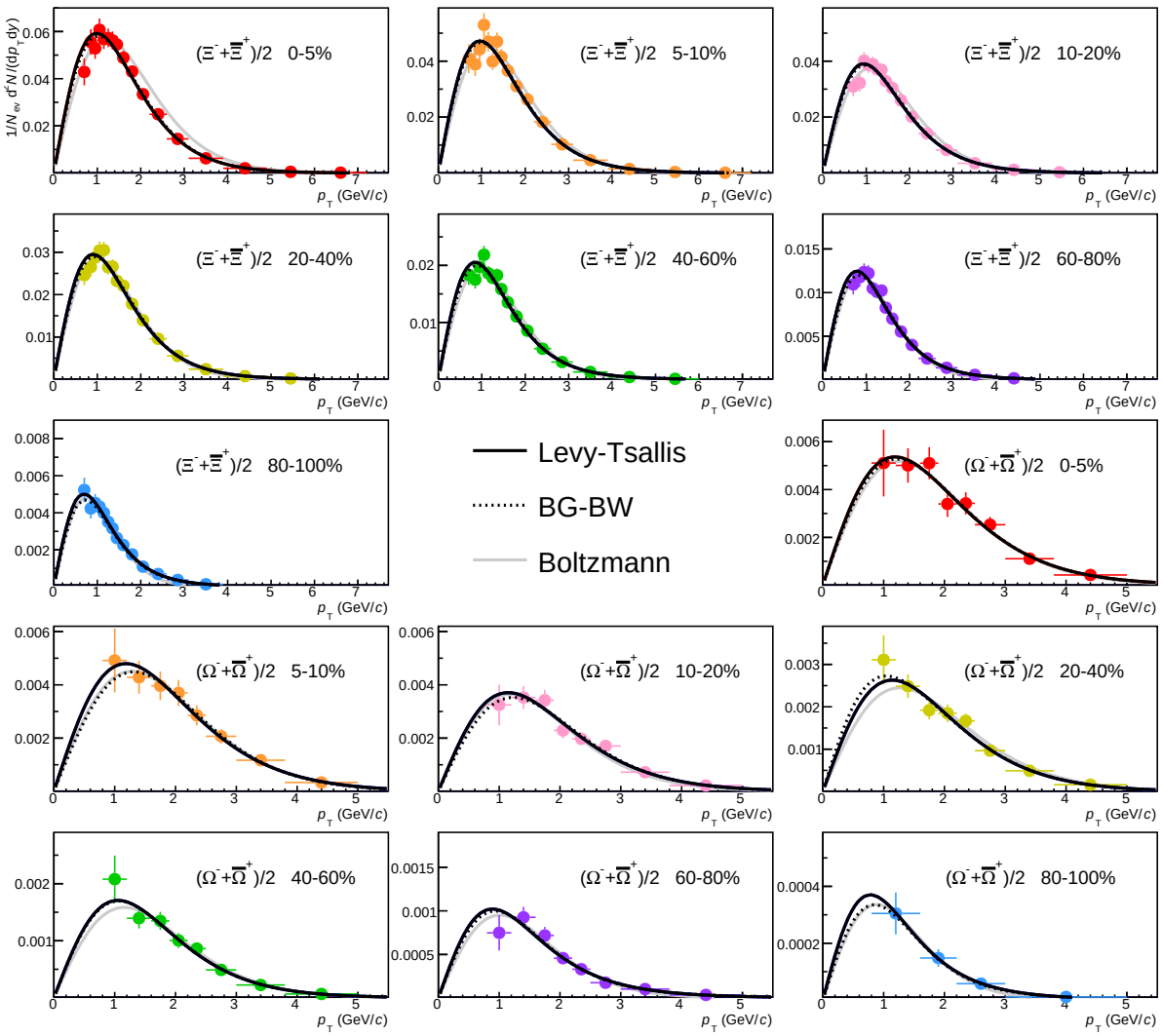

Figure 5.4: The $(\Xi^- + \overline{\Xi}^+)/2$ and $(\Omega^- + \overline{\Omega}^+)/2$ p_{T} spectra in the seven multiplicity classes in p–Pb collisions. A Lévy-Tsallis, BG-BW, and Boltzmann function is fitted to each distribution. The Lévy-Tsallis fit determines the yields for every spectrum in the non-measured spectrum regions. The other fits allow to study the variations in the yields due to a different modelling of the low-p_{T} region. The Boltzmann function was only fit to the data in the low momentum region, i.e. in the 0.6-1.5 GeV/c range for $\Xi^{\pm}$ and in the 0.8-2.2 GeV/c range for $\Omega^{\pm}$, the ranges at higher p_{T} having been extrapolated when using this function to estimate the yields.

that the transverse momentum distributions of the Ω undergo a larger shift to bigger p_{T} with increasing multiplicity than do the Ξ baryons. The observed multiplicity dependence of the $\langle p_{\mathrm{T}} \rangle$ values reveal that there is an evolution of the peak in the p_{T} distributions towards larger transverse momentum as the multiplicity of the events increases. This observation is known as *spectrum hardening*. The $\langle p_{\mathrm{T}} \rangle$ as a function

Table 5.2: The T_k and n parameter extracted from the Tsallis fits that were used in order to obtain the yields in each of the p_{T} spectra measured in p–Pb events. The χ^2 divided by the number of degrees of freedom (ndf) values are also shown.

Mult. Class	($\Xi^{\pm}$) T_k (MeV)	n	χ^2/ndf
0–5%	585 ± 19	66.1 ± 38.9	17.6/14
5–10%	553 ± 19	37.3 ± 12.6	16.6/14
10–20%	534 ± 17	29.7 ± 7.2	13.9/14
20–40%	497 ± 15	21.6 ± 3.5	10.1/14
40–60%	438 ± 14	14.8 ± 1.7	12.8/13
60–80%	379 ± 15	12.4 ± 1.4	5.8/12
80–100%	301 ± 20	8.8 ± 1.2	3.7/11

Mult. Class	($\Omega^{\pm}$) T_k (MeV)	n	χ^2/ndf
0–5%	684 ± 30	999.7 ± 711.9	3.1/5
5–10%	683 ± 28	999.9 ± 536.0	1.7/5
10–20%	649 ± 23	997.7 ± 697.3	4.1/5
20–40%	640 ± 108	352.3 ± 541.3	4.5/5
40–60%	555 ± 84	62.4 ± 17.9	3.1/5
60–80%	392 ± 71	8.7 ± 3.9	4.6/5
80–100%	306 ± 132	7.2 ± 5.5	0.02/1

of p–Pb multiplicity will be discussed for various hadrons in section 5.2.2.2.

5.1.4 Uncertainties on the yields and mean transverse momenta

The systematic uncertainties on the yields and $\langle p_{\mathrm{T}} \rangle$ have two main sources: the bin-by-bin contributions from the p_{T} spectra which were discussed in the previous chapter and summarised in Figures 4.23 and 4.24, and the uncertainty introduced by the extrapolation of the spectra in the low p_{T} region by fitting the Lévy-Tsallis function, as was discussed in the preceding section. In the following, the methods to determine the size of these two uncertainties and of the multiplicity-uncorrelated fractions on

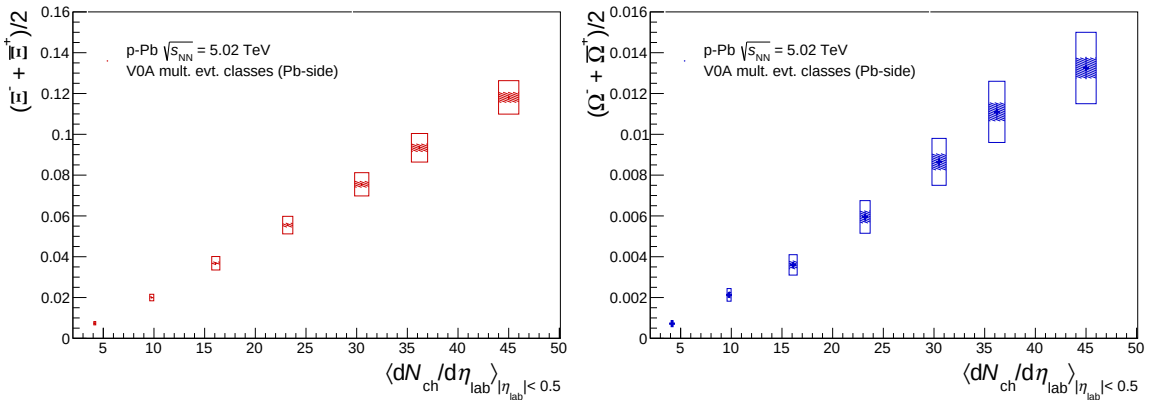

Figure 5.5: The dN/dy values for $(\Xi^- + \overline{\Xi}^+)/2$ and $(\Omega^- + \overline{\Omega}^+)/2$ in seven multiplicity classes in p–Pb collisions. The boxes show the total systematic errors, and the shaded uncertainties show the contribution from the uncorrelated fraction

them are described.

Exploring the full size of the error bands on the different p_{T} bins, the minimum and maximum values of the integrated yields were calculated. The maximum deviations on the yields contribute to the systematic uncertainties. The contribution from the estimation of the fraction of the yield made up by the low-p_{T} region that was not reached experimentally is dependent on the choice of the function used for extrapolation, as different models assume different shapes at low momentum. Both a Boltzmann-Gibbs Blast-Wave function (equation 2.13 of chapter 2), and a simple Boltzmann function

$$\frac{\mathrm{d}N}{\mathrm{d}y} = C_{norm}\ p_T\ m_T\ exp\left(-\frac{m_T}{T_k}\right) \quad , \tag{5.1}$$

where C_{norm} is the normalisation constant and $m_T = \sqrt{m^2 + (p_T)^2}$ is the transverse mass of the hadron, were also fitted to all the spectra. This allowed different fractions of the extrapolation region with respect to the total yield to be estimated. These alternative fits to all the spectra are also shown in Figure 5.4. The yield variations that were observed gave rise to uncertainties on the multi-strange yields, which range from 3-5% for $\Xi^{\pm}$ and 8-15% for $\Omega^{\pm}$ yields, the highest errors having been attributed

to the lowest multiplicity class. The larger size of the Ω errors, due to the yield extrapolation technique, is expected when considering the shorter p_{T} range that was measured for this baryon as compared to the Ξ hadron.

Estimates are also provided for the multiplicity-uncorrelated systematic uncertainties from the above two sources. To estimate the effect of the extrapolation on this uncertainty, the variations on the yield observed when fitting the spectra with the functions alternative to the Lévy-Tsallis, are compared with the deviations to the M.B. yield when using the same fit alterations. This method attempts to isolate the contributions to the total uncertainty that are not common to the whole sample but unique to a given multiplicity class. The technique is similar to the computation of the double-ratio described by equation 4.26, but in this case Y represents the fraction of the total yield that is extrapolated at low p_{T}.

The total systematic errors on the integrated yields of the Ξ baryons progressively increase from 7-10% and those of the Ω baryons from 13-23%, with increasing multiplicity. The estimated uncorrelated uncertainty varies between 0.22 and 0.48 of the total systematic error, the largest uncertainties tending to be those in lower multiplicity data, more so for the Ω^{-}. In both cases, this is due to a larger contribution to the integrated yield by the extrapolation.

The systematic uncertainties (total and uncorrelated) on the $\langle p_{\mathrm{T}} \rangle$ are obtained in a similar manner to the errors on the yields. In order to explore the maximal deviations on these measurements allowed by the point-by-point spectrum error bars, it was necessary to consider the softest and hardest p_{T} distributions. This is done by re-plotting the spectra with the peak placed at the lowest and highest possible p_{T} , by varying the values within the sizes of the error bars accorded to the measurements in each p_{T} interval. The combined systematic uncertainty on the $\langle p_{\mathrm{T}} \rangle$ varies between

2-3.5% and 3.5-5.5% for the charged Ξ and Ω baryons, respectively. An exception is the error on the $\langle p_{\mathrm{T}} \rangle$ of the Ω in the 80-100% multiplicity class, which reaches around 8%. The contributions from multiplicity-uncorrelated sources were estimated to vary between 0.30 and 0.53 of the combined systematic uncertainty.

Table 5.3: The $\langle p_{\mathrm{T}} \rangle$ of $\Xi^{\pm}$ and $\Omega^{\pm}$ in each multiplicity class with their statistical and systematic uncertainties, with the uncorrelated errors shown in parentheses after the latter. The numbers represent the average of the measured values for particles and anti-particles.

Event class	$\langle \mathrm{d}N_{\mathrm{ch}}/\mathrm{d}\eta \rangle$ $\lvert\eta_{\mathrm{lab}}\rvert < 0.5$	$\Xi^{\pm}$ $\langle p_{\mathrm{T}} \rangle$	$\Omega^{\pm}$ $\langle p_{\mathrm{T}} \rangle$
0–5%	45 ± 1	1.574 ± 0.010 ± 0.037(0.012)	1.818 ± 0.056 ± 0.076(0.025)
5–10%	36.2 ± 0.8	1.529 ± 0.009 ± 0.036(0.014)	1.829 ± 0.062 ± 0.079(0.030)
10–20%	30.5 ± 0.7	1.515 ± 0.007 ± 0.034(0.016)	1.771 ± 0.058 ± 0.082(0.038)
20–40%	23.2 ± 0.5	1.468 ± 0.006 ± 0.032(0.011)	1.668 ± 0.040 ± 0.082(0.029)
40–60%	16.1 ± 0.4	1.394 ± 0.012 ± 0.030(0.016)	1.563 ± 0.033 ± 0.067(0.035)
60–80%	9.8 ± 0.2	1.280 ± 0.009 ± 0.032(0.015)	1.544 ± 0.055 ± 0.084(0.040)
80–100%	4.3 ± 0.1	1.155 ± 0.018 ± 0.037(0.011)	1.350 ± 0.110 ± 0.106(0.048)

5.2 Discussion of results

5.2.1 Multi-strange spectra compared to DPMJet model

A model comparison of the multi-strange measurements is made with the DPMJet event generator, based on the DPM model [128], which was the source of the efficiency calculations in this analysis. The p_{T} spectra of the multi-strange particles are superimposed on the M.C. distributions in Figure 5.7 for all four particles in the M.B. sample. Ratios of the measured to the model-generated spectra are shown in the bottom panel of that figure. Not only does the model under-estimate the yields by a factor of up to 7 and 25 for $\Xi^{\pm}$ and $\Omega^{\pm}$ respectively, but the spectral shape

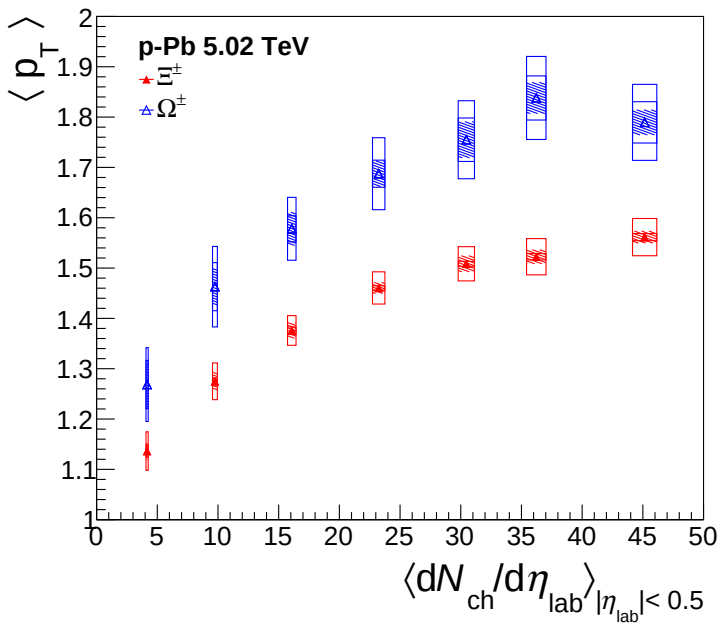

Figure 5.6: $\langle p_{\mathrm{T}} \rangle$ of the multi-strange hadrons as a function of multiplicity in p-Pb collisions.

predictions are also misrepresented, with the peak occurring at lower p_{T}.

Figure 5.8 compares the data to the Monte Carlo in all multiplicity classes. It can be seen that the degree of discrepancy varies according to multiplicity.

For the Ξ particles, at low p_{T} up to about 1.5 GeV/c, the data/model ratios do not vary. However, at larger momenta, the disagreement with the model is progressively reduced with decreasing multiplicity. For the Ω baryons, the comparisons of the individual multiplicity classes with each other are more disparate. In this case, it is the spectra in lower event multiplicity data that show the biggest disagreement with the model.

Overall, the DPMJet fails to reproduce the measured p_{T} spectra, underestimating the multi-strange yields. This misrepresentation depends on the p_{T} and on the event multiplicity.

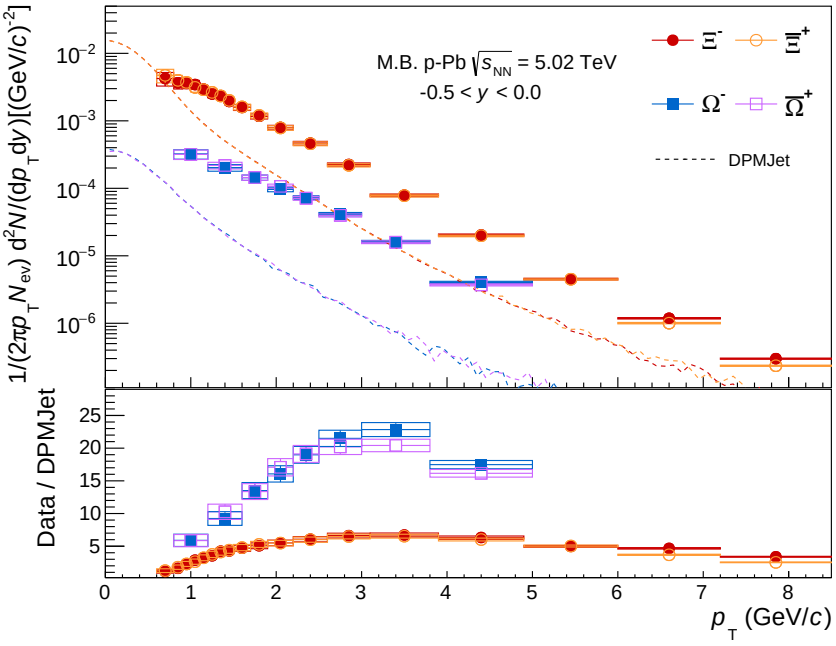

Figure 5.7: The Ξ^-, $\overline{\Xi}^+$, $\Omega^-$and $\overline{\Omega}^+$ spectra in the Minimum Bias sample at mid-rapidity, normalised to the visible cross-section. The Monte Carlo p_{T} distributions are superimposed on the top panel. The bottom panel, shows the data to model ratio of the spectra.

5.2.2 Hydrodynamic systems in p–Pb collisions

5.2.2.1 Data comparisons to Blast-Wave model

In chapter 2, the Boltzmann-Gibbs Blast-Wave (BG-BW) model was introduced. Combining Boltzmann statistics with hydrodynamics, this model describes thermally distributed particles that are boosted in the transverse direction due to an expansion undergone by the entire system they are part of. Such an outward expansion is commonly referred to as radial flow. In the preceding section of this chapter, the predicted function of this model for the p_{T} distribution was mentioned in the context of the systematic uncertainties, for which the Blast-Wave function was used to measure the integrated yields of the particles from the measured transverse momentum spectra in seven different multiplicity classes. With χ^2/ndf values below one, the model proved to fit the data very well, as far as the multi-strange baryons are concerned. Therefore

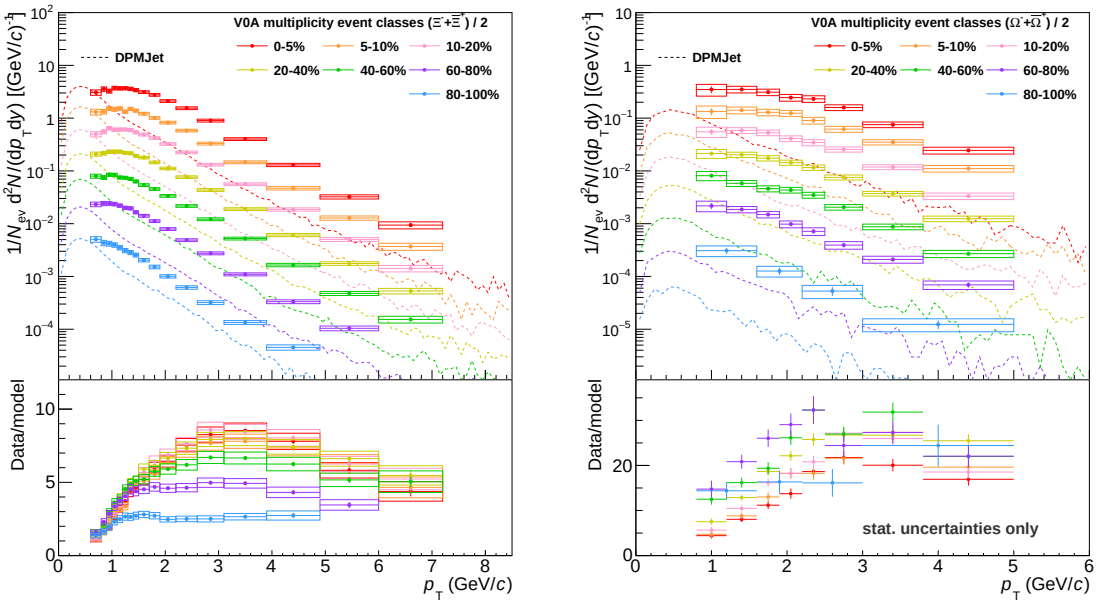

Figure 5.8: The $(\Xi^-+\bar{\Xi}^+)/2$ and $(\Omega^-+\bar{\Omega}^+)/2$ spectra in all seven multiplicity classes compared to predictions from the DPMJet Monte Carlo model. The ratio of the former to the latter are shown on the bottom panels.

it makes sense to test whether the multi-strange particles compare well with the BW model collectively with other hadrons, too.

The BG-BW model raised interest originally because it was expected to be an appropriate description for systems created under A–A collisions, given the large pressure gradients originating in the conditions of high energy density. However, in [129], using the BW model, indications of collective behaviour in pp collisions were observed for the first time at the LHC. These observations were most striking due to the fact that they only appear when specifically selecting high multiplicity events, whereas the model fails to fit the shape of the p_{T} spectra of the $\pi^{\pm}$, $K^{\pm}$ and $p(\overline{p})$ hadrons in M.B., when events from all multiplicities are included in the data. In addition, the p–Pb data recorded by ALICE, discussed in this analysis, was previously used for the measurement of the latter hadrons and the singly-strange K^0_s mesons and $\Lambda(\overline{\Lambda})$ baryons [127]. The discussion with regard to the BG-BW model in that paper shows that for high multiplicity p–Pb collisions, it is possible to describe the shapes of the

p_{T} distributions of all particles with one single set of parameters. In order to do this, the fits neglect the low-p_{T} range of the $\pi^{\pm}$ spectra in order to avoid contributions from feed-down, i.e. from the decays of heavier resonances, which affect mostly the low-momentum yields. In addition, the high-p_{T} ranges of all particle spectra were also excluded in the fit, in this case to avoid contributions from independent, non-thermalised, hard processes. Thus, the π spectra are only fitted between 0.5 and 1.0 GeV/c, the remaining particles are fitted up to 1.5 GeV/c, and the multi-strange up to 3.0 GeV/c. The successful fit (with $\chi^2/ndf = 0.27$) in the highest multiplicity data is a good indication of a common behaviour among several hadrons, as would be expected if they were subject to a global expansion with common kinetic freeze-out. Just as was the case in pp data, this observation was also only made when looking at high-multiplicity events specifically. With regard to that finding, it is interesting to investigate whether the multi-strange baryons share the good agreement with the model when setting those same parameters for kinetic freeze-out temperature and transverse expansion velocity. In other words, one attempts to answer the question whether hyperons participate in a collective radial flow with the other hadrons.

The comparisons illustrated in Figures 5.9 and 5.10 show that this is indeed the case in the 0-5% highest multiplicity events (red curves). Up to a p_{T} of around 4 GeV/c (5 GeV/c), it can be seen that the model and data stand in agreement with each other within the uncertainties of the measured $\Xi^{\pm}$ ($\Omega^{\pm}$) spectra, for a T_k of 143 MeV and an average transverse expansion velocity relative to the speed of light ($\langle\beta_T\rangle$) of 0.547 [127]. According to the Blast-Wave model, the hyperons behave as if they participated in a common hydrodynamical expansion with lighter non-strange hadrons. The same cannot be said when one repeats the comparison for lower multiplicity classes. In fact, the agreement progressively worsens with decreasing multiplicity, and the p_{T} distributions of the BG-BW model are the least comparable with the spectra in the 80-100% multiplicity class. The comparison can also be seen in the same figures.

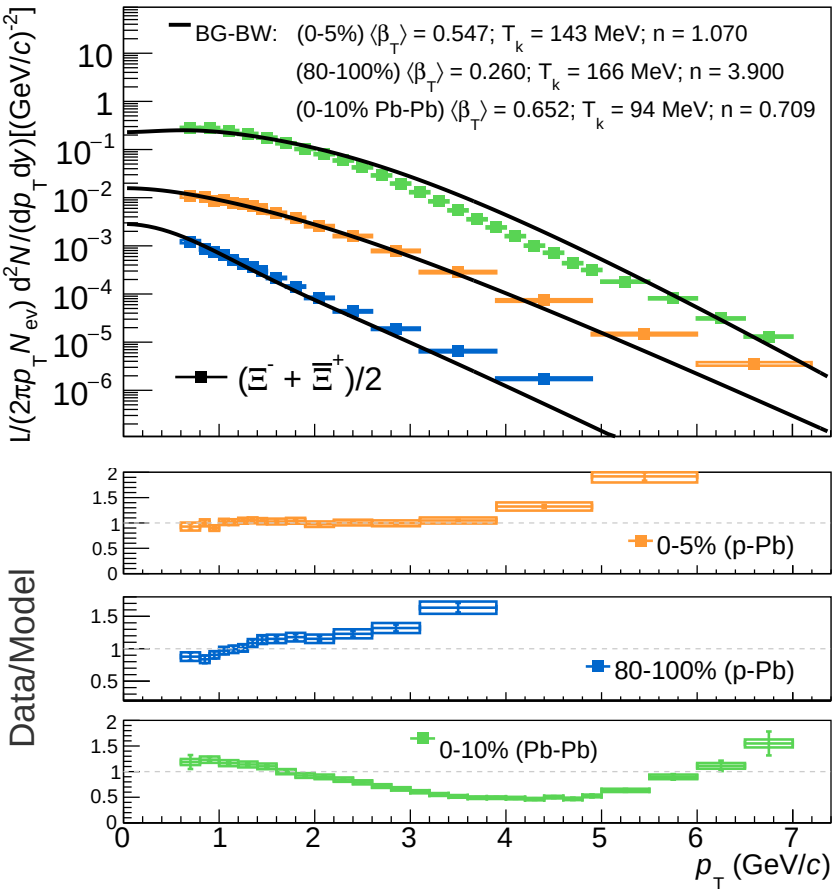

Figure 5.9: The p–Pb $(\Xi^{-}+\overline{\Xi}^{+})/2$ p_{T} spectra in the highest (0-5%) and lowest (80-100%) multiplicity classes compared with the BG-BW predicted distributions for the extracted parameters from the global fit that included the $\pi^{-}(\pi^{+})$, $\mathrm{K}^{-}(\mathrm{K}^{+})$, $p(\overline{p})$, K^{0}_{S} and $\Lambda(\overline{\Lambda})$ hadrons [127]. In addition, the same spectra in the 0-10% highest centrality band is compared to the Blast-Wave curve obtained with the parameters extracted from the successful simultaneous fit to the $\pi^{-}(\pi^{+})$, $\mathrm{K}^{-}(\mathrm{K}^{+})$, $p(\overline{p})$ hadrons [130].

Of additional interest, is the fact that the p_{T} spectra for multi-strange baryons measured in central Pb–Pb collisions [131], stand in disagreement with the same model, as is also shown in Figures 5.9 and 5.10. The Blast-Wave functions used for that comparison are obtained by using the parameters extracted from successful global fits to the lighter hadrons. Those successful Blast-Wave fits to Pb–Pb data are reported in [130]. They were performed to the 0.5-1.0 GeV/c, 0.2-1.5 GeV/c and 0.3-3 GeV/c p_{T} ranges of the π, K and p, respectively. These BG-BW curves predict harder

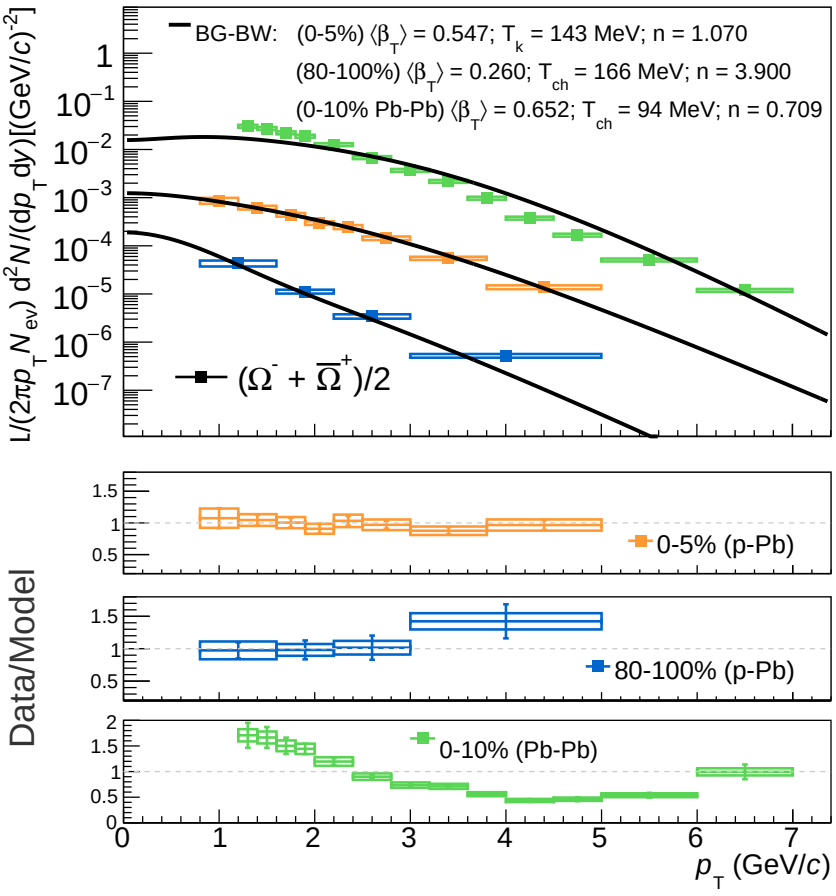

Figure 5.10: The p–Pb $(\Omega^{-}+\overline{\Xi}^{+})/2$ p_{T} spectra in high and low multiplicity classes, and in the Pb–Pb most central Pb–Pb class, compared to the BG-BW predictions as in Figure 5.9.

p_{T} distributions for the masses of the multi-strange hadrons than is observed in the measured spectra. The peaks of the spectra in the model occur at larger p_{T} values than they do in the data. A possible explanation for this observation involves the duration of the hadronic phase. This is the phase between the moment of hadronisation and kinematic freeze-out - when all hadrons have stopped interacting and exchanging momentum. If this phase lasts for a sufficient amount of time, distinct hadrons will decouple at different times, in contrast to an instantaneous hadronic phase described by a sudden common freeze-out, and therefore common temperature, for all particles in the system. It could be argued that the hadronic phase is finite in Pb–Pb collisions, so that different particles decouple at different temperatures, once they

no longer interact with the system. It has been suggested that due to their smaller hadronic cross-sections, multi-strange hadrons would decouple earlier from the system, at a hotter temperature, with respect to the lighter particles that experience radial flow for longer, a scenario which would be consistent with the observations in the data. This has been argued, for instance, by calculations from the relativistic quantum molecular dynamics (RQMD), a microscopic model for the description of heavy-ion collisions[132]. It is a possible explanation for why the $\Xi^{\pm}$ and $\Omega^{\pm}$ distributions are less boosted towards higher momenta than the radial flow model predictions.

A possible hint for the different durations of the hadronic phase in different collisions, are the extracted values of the kinetic freeze-out temperature from the Blast-Wave fits. As Figures 5.9 and 5.10 show, a value of 143 MeV was obtained from the global fit in high multiplicity p–Pb data, whereas a smaller temperature, of 94 MeV describes the data in central Pb–Pb data. As the hadronisation temperature is universal for all collisions, this is consistent with the hadronic system in Pb–Pb collisions being longer-lived, and as a result experiencing more cooling before kinetic freeze-out takes place.

5.2.2.2 Mass ordering

One of the consequences of radial flow is the mass dependence of the transverse boosts experienced by the particles. As the pressure gradients provide equal velocity to all particles, heavier particles are pushed to higher momenta than lighter particles. Figure 5.11 shows the $\langle p_{\mathrm{T}} \rangle$ evolution as a function of multiplicity in p–Pb collisions for nine different hadrons measured with ALICE in that colliding system. These include the multi-strange hadrons discussed in this thesis and published in [2] and the ϕ and $K^{\star^0}$ resonances [133]. While a mass hierarchy is observed for $\pi^{\pm}$, $K^{\pm}$, $p(\overline{p})$, K^0_S, $\Lambda(\overline{\Lambda})$, $\Xi^{\pm}$ and $\Omega^{\pm}$, it is with the resonances that the radial flow picture fails to adequately represent the data. The $\langle p_{\mathrm{T}} \rangle$ values of the ϕ meson lie above those of the

Λ, despite their PDG mass being smaller (1.02 GeV/c^2 compared to 1.12 GeV/c^2). In addition, the $\langle p_{\mathrm{T}} \rangle$ of the $K^{\star 0}$ should not lie above the proton values (0.892 GeV/c^2 versus 0.931 GeV/c^2), if radial flow were the only mechanism affecting the transverse momenta of all the particles in the p–Pb system.

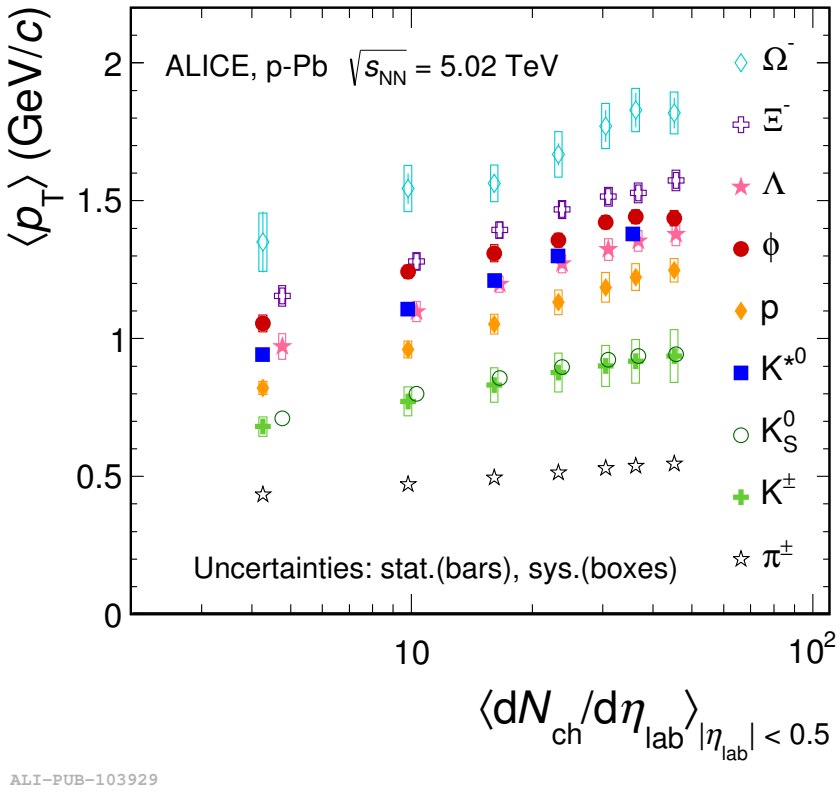

Figure 5.11: The $\langle p_{\mathrm{T}} \rangle$ of 9 mesons and baryons measured in p–Pb collisions at mid-rapidity with the ALICE experiment, including the $K^{\star 0}$ and ϕ resonances [133].

5.2.3 Hyperon to Pion Ratios

5.2.3.1 Experimental observation

Having established that the yields of the hyperons increase as a function of the event multiplicity, the first question that follows is how this increase compares to the measured increase in the yields of non-strange hadrons. A reasonable particle choice to normalise the multi-strange yields to is the mostly abundant charged π meson. The ratio of strange particles to particles containing the lighter u and d quarks can show

whether the observed increase in strangeness is the consequence of an enhancement mechanism that is shared between all particles, or whether there would be an effect affecting strangeness in particular. Since hyperons and $\pi^{\pm}$ were measured using the same data in a consistent experimental set-up, it is possible to calculate the hyperon-to-pion ratios as a function of multiplicity. These ratios are plotted in the plots of Figure 5.12, where the same measurements made in M.B. pp data and in five Pb–Pb centrality classes are also shown. From an experimental point of view, the following remarks can be made from observations of the data in the figure:

- The hyperon-to-pion ratios in p–Pb collisions show an increase with charged-particle multiplicity consistent with a logarithmic scaling. The p–Pb results are represented by the blue data in the intermediate region between pp and Pb–Pb data. From the lowest to the highest multiplicity class, the values of the Ξ/π and Ω/π ratios increase by approximately 60% and 100%, respectively.

- The largest multiplicity dependence in the yield ratios occurs in the multiplicity range of the p–Pb data. This is the case, despite the p–Pb charged particle multiplicity varying by a factor of ten only. The hyperon-to-pion ratios of all three colliding systems are drawn on the same figures, including the M.B. pp data points at centre-of-mass energies of 0.9 [134][135] and 7 TeV [136][137] (black data points), as well as the centrality dependent Pb–Pb yield ratios, which range from a mid-rapidity mean charged particle multiplicity of 50 to 1200 (red data points). The five Pb–Pb measurements correspond to the 0-10%, 10-20%, 20-40%, 40-60% and 60-80% centrality classes [131].

- The low-multiplicity particle ratios in p–Pb are consistent with the measurements in pp data, and the high-multiplicity ratios are comparable with the obtained values in central Pb–Pb collisions. The superposition of all three colliding systems in the figures shows a (mostly) continuous evolution of the ratios from one system to another. The Ξ/π ratios in the highest multiplicity bins of

p–Pb and Pb–Pb are consistent with each other within their measured uncertainties. The same does not hold for the Ω/π ratio, which in p–Pb reaches the values of the suppressed ratio in less central Pb–Pb collisions with respect to more central interactions.

5.2.3.2 Comparison to the Statistical Hadronisation Model

The Grand-Canonical limit for chemical equilibrium

The surprising results presented above, showing similar hyperon-to-pion ratios in high-multiplicity p–Pb events to the ratios in Pb–Pb collisions, open the question of the possibility of the formation of a de-confined state of matter in smaller collision systems, which was originally suggested by Bjorken as discussed in chapter 2 (see section 2.4). While it is not possible to ascertain the presence of a Quark-Gluon Plasma, it is worthwhile to look for common features with Pb–Pb data with regard to the Statistical Hadronisation Model. Introduced in chapter 2 (see section 2.3.1), this theoretical model describes a system in which hadrons are in thermal equilibrium. The relative abundances of the particles in equilibrium depend on the size of the system, the chemical potential and the temperature. For a system in which strangeness is fully equilibrated with the rest of the system, the strangeness undersaturation factor, γ_S, which was introduced in section 2.3.1, is equal to one. Grand canonical equilibrium values for the particle ratios are predicted by the model for such a system.
In Figure 5.12, the grand canonical limits are shown by the two green horizontal lines, which were obtained from two different implementations of the thermal model. The fits were performed on the yields of the $\pi^{\pm}$, $K^{\pm}$, $p(\overline{p})$, K^0_S, $\Lambda(\overline{\Lambda})$, $\Xi^{\pm}$ and $\Omega^{\pm}$ hadrons, the deuteron (d), and the $K*^0$ and ϕ resonances.

A strangeness canonical (S.C.) implementation of the thermal model was applied with the THERMUS package [138] for the 0-5% multiplicity class. This approach treats strangeness according to the canonical equations (see eq.2.10-2.10), while non-strange

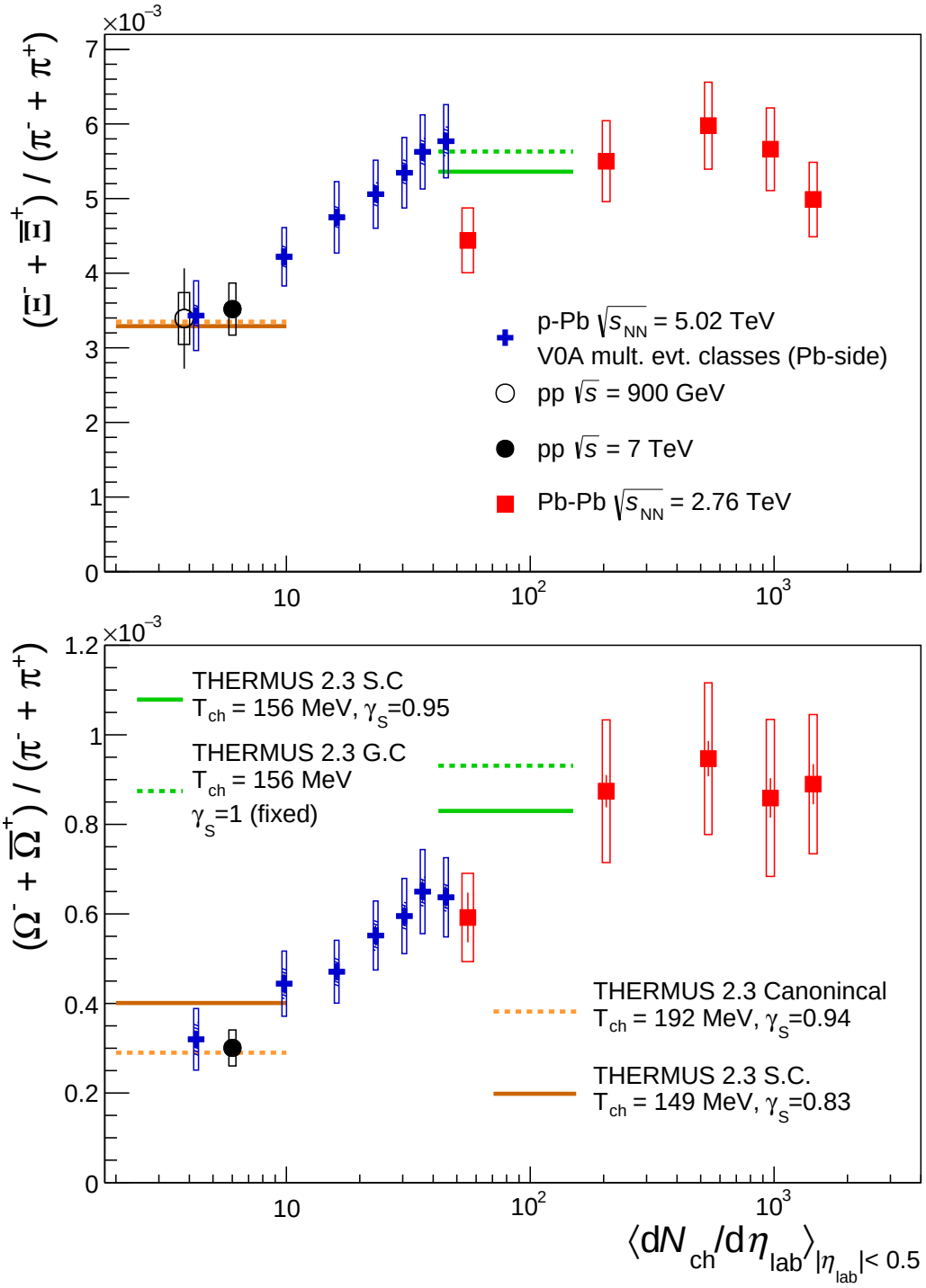

Figure 5.12: The Ξ/π and Ω/π ratios as a function of $\mathrm{d}N_{\mathrm{ch}}/\mathrm{d}\eta$ in all three collision systems compared to the predictions from the Statistical Hadronisation Model. In the low-multiplicity limit, particle ratio predictions with the parameters extracted from fits to the 80-100% multiplicity class in p–Pb data, using the fully canonical and the strangeness canonical approach (see text). Similarly, at the high-multiplicity end, values are given for the grand-canonical limit, extracted, this time, from fits to the results in the most central Pb–Pb collisions (see text).

particles (with up and down quarks) are dealt with according to the grand canonical partition function (see eq.2.8). In this model, a distinction is made between the canonical radius R_c (also called correlation radius), within which strangeness must be conserved exactly, according to the local conservation rules of the canonical equations, and the radius of the full system, within which the baryon quantum number B and the electric charge Q are conserved on average. The following parameters and reduced χ^2 values characterise the fit:

T_{ch} = 156±2 MeV; R = 3.29±0.10 fm; R_c = 10.04±2.97 fm; γ_S = 0.95±0.03; χ^2/ndf = 36.3/6 .

In addition, a grand canonical (G.C.) fit to the same data, in which γ_S was fixed to unity, gave extracted values of:

T_{ch} = 156±2 MeV; R = 3.22±0.10 fm; χ^2/ndf = 37.5/8 .

For these parameter values, the two fits give similar particle ratio values, shown by the green horizontal lines in Figure 5.12. While they agree with the Ξ/π values at high multiplicity, they lie above the measured Ω/π ratio. A larger disagreement between data and model for the Ω/π ratio is observed with the grand canonical approach. Both fits give high χ^2/ndf values which are 6.0 for the S.C. and 4.7 for the G.C. model. More details on the results of these two thermal model fits and comparisons of the extracted yields with the measured values are shown in Appendix B.

Canonical fits to low-multiplicity data

At the other end of the multiplicity range are the low-multiplicity results, where the lowest hyperon-to-pion ratios were measured and which are comparable to those found in the analysis of pp collisions. Two different approaches of the SHM were used to provide predictions for the Ξ/π and Ω/π ratios based on fits to the results in the 80-100% p–Pb multiplicity class. The fit included all particles mentioned above that were used for the fits in the high multiplicity data. First, a canonical fit was

performed. The extracted values for these parameters and the reduced χ^2 of this fit were:

$$T_{ch} = 192\pm2 \text{ MeV; } R = 1.08\pm0.03 \text{ fm; } \gamma_S = 0.94\pm0.02; \chi^2/ndf = 195.5/7$$

Secondly, a Strangeness Canonical (S.C.) fit was attempted using the same data:

$$T_{ch} = 149\pm1 \text{ MeV; } R_c = 12.9\pm3.1 \text{ fm; } R = 1.77\pm0.05 \text{ fm; } \gamma_S = 0.83\pm0.02;$$

$$\chi^2/ndf = 43.2/6$$

The hyperon-to-pion ratios extracted from these two fits are also shown in Figure 5.12, by two horizontal lines on the low-multiplicity end. The theoretical lines are in agreement with the measurements of the multi-strange yields at low multiplicity, although the χ^2/ndf of 7.2 (for the S.C. fit) and 27.9 (for the canonical fit) do not suggest a good description of the overall system by the SHM.
Just as for the fits to the high multiplicity data discussed above, Appendix B also provides a full data-model comparison on various hadronic yields. The next section describes an attempt to describe the full range of p–Pb measurements with just one varying parameter: the size of the system.

Strangeness canonical suppression

The decrease in the hyperon-to-pion yield ratios with decreasing event multiplicity measured in p–Pb collisions is now compared to the canonical suppression interpretation of the SHM. Under this approach, applicable to small systems such as those produced in pp or p–A interactions, strangeness production is dependent on the available phase-space. The calculations can thus make predictions on the relative integrated yields of hadrons depending on the size of the system formed. The volume-dependence of the hyperon-to-pion ratios can be studied using THERMUS. Figure 5.13 compares such calculations for Λ/π, Ξ/π and Ω/π ratios with the data from three collision systems. The model curves were obtained by using the strangeness

canonical implementation.

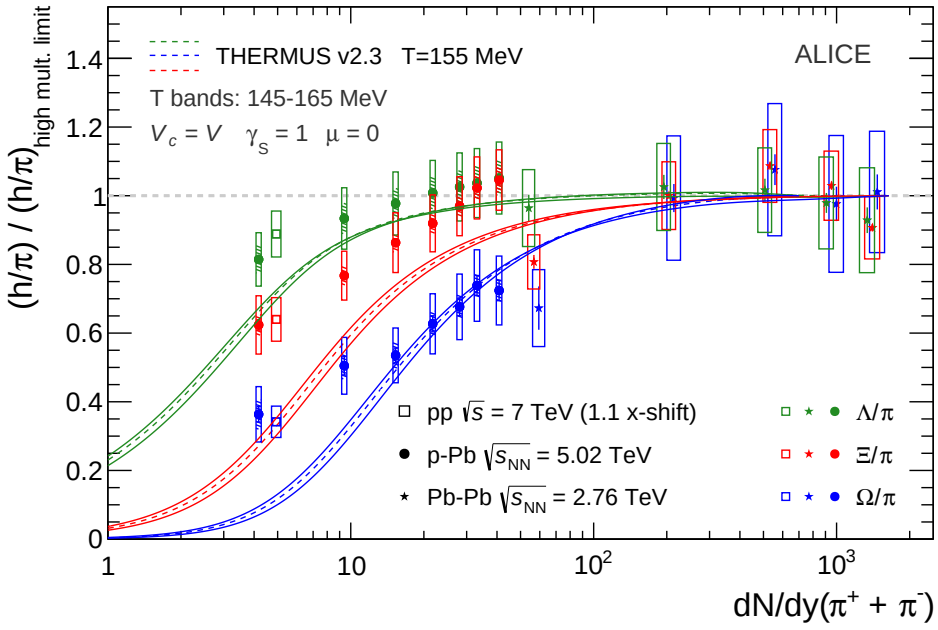

Figure 5.13: Hyperon-to-pion ratios as a function of pion multiplicity with strangeness canonical THERMUS curves superimposed, for which only the volume varies along the x-axis [2].

In order to study the dependence of strangeness production with the volume, it is necessary to fix all other parameters. In this exercise, all parameters were set to the values they assume in the grand canonical limit. Thus, the strangeness undersaturation factor γ_s is fixed to unity. The canonical volume is set to the size of the full system, $V_C = V$, an assumption which holds true when strangeness is fully equilibrated with the rest of the system. The chemical freeze-out temperature is set to T_{ch} = 155 MeV, according to the value extracted from the fit to the results in the central Pb–Pb class [139]. In p–Pb data, the same fits give similar values for this parameter across the whole multiplicity range, with T_{ch} varying between 150 MeV and 160 MeV (see Appendix B). In this exercise, a variation of ±10 MeV is applied to the temperature in order to see the dependence of the suppression on this parameter. The chemical potential μ, as defined in equation 2.9, is fixed to zero. This is a good

assumption at central rapidity for LHC energies, where the baryon/antibaryon ratio tends to one. In summary, the G.C. limits are assumed in the limit of very high multiplicity, and the suppression with respect to the G.C. equilibrium values with decreasing volume are studied. The volume is swept from a radius of 12 fm down to zero.

In Figure 5.13, the data and the model are normalised to their respective grand canonical limits. In the data this limit was obtained from a fit with a constant function to the results in the 0-60% most central events in heavy-ion collisions, which are the four measurements with highest multiplicity made in Pb–Pb collisions. The chemical equilibrium limit obtained from the model is given by calculating the yield ratios with the largest possible volume size. The hyperon-to-pion ratios are plotted as a function of the corresponding pion multiplicity (the sum of the π^- and π^+ yields), which are obtained from the calculations and are known to vary linearly with the radius of the volume in the model.
It can be seen in the figure that the strangeness suppression based on the shrinking of the system size, as calculated with THERMUS, qualitatively reproduces the behaviour of the measured hyperon-to-pion ratios with decreasing multiplicity. Quantitatively however, the suppression described by the theoretical curves is stronger, which is due to the fact that the G.C. assumptions are applied across the whole volume range. The chemical freeze-out temperature appears not to be very influential on the shape of the curves.

The multiplicity dependence of the S.C model was also studied with all the above-mentioned parameters set free. Fits were performed to each of the seven p–Pb multiplicity classes, which are the subject of the second part of Appendix B, where the evolution of the extracted parameters with multiplicity class is shown.

5.2.4 Comparison to other hadrons

Having discussed the increase in the production rate of the hyperons with respect to the pions, it is important to put this in context with other hadrons, the yields of which were measured using the same data from p–Pb collisions. Figure 5.14 adds the p/π and the ϕ/π measurements to the same ratios involving the three strange baryons. The ratios are normalised to their values in M.B. pp data in order to observe the relative increases with multiplicity. The production rate of the proton is shown to follow that of the pion across the multiplicity range. In fact, the production of both particles increases at the same rate with increasing event multiplicity [127]. The hidden strange ϕ resonance, however, appears to follow a slightly bigger increase relative to the charged π mesons than the Λ baryons. The canonical suppression would be similar to the non-strange proton, which has similar mass, however it would increase according to γ_S in the same way as the Ξ, which also has two strange valence quarks. An increase of the ϕ/π ratio intermediate between these two hadrons, as observed in the figure, is therefore qualitatively consistent with the SHM.

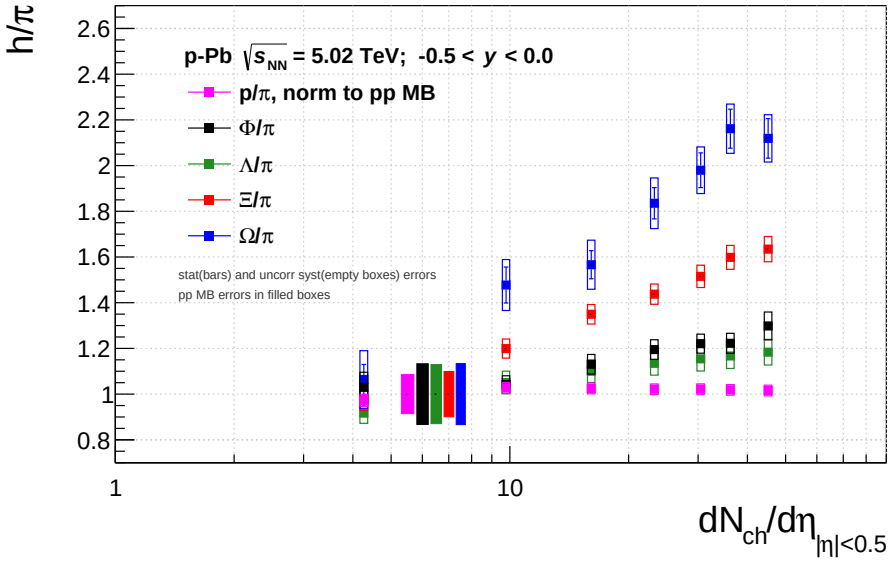

Figure 5.14: Hadron over pion ratios as a function of $\mathrm{d}N_{\mathrm{ch}}/\mathrm{d}\eta$ in p–Pb collisions at 5.02 TeV

Chapter 6

Summary and further discussion

The previous chapter reported on the shapes of the p_{T} of the multi-strange baryons in p–Pb collisions and their yields as a function of multiplicity. $\Xi^{\pm}$ and $\Omega^{\pm}$ were shown to agree well with the Blast-Wave model in high multiplicity events, in conjunction with lighter hadrons. This provides indications for collectivity in p–Pb systems. The yields of these hyperons were shown to follow a sharp increase as a function of multiplicity. Thermal model (SHM) fits were performed on various hadronic yields. At low multiplicity, the canonical model stands in agreement with the hyperon-to-pion ratios within the experimental uncertainties. At high multiplicity, a grand canonical fit shows a discrepancy between the data and model for the Ω/π ratio. In addition, it was shown that the rise in the hyperon-to-pion ratios can be qualitatively reproduced with a description that applies the canonical equations for strangeness, and in which the size of the system is the only variable.

Recently, the multi-strange baryons have been measured as a function of multiplicity also in pp collisions at a centre-of-mass energy of $\sqrt{s} = 7$ TeV. The multiplicity range overlaps with the p–Pb range, ranging from around three to 20 charged particles at central rapidity. In these measurements, presented in Figure 6.1, both the Ξ/π and Ω/π are in strong agreement with the p–Pb results. These ratios follow the same increase trend as those measured in p–Pb.

The p–Pb results suggest that the formation of Quark-Gluon Plasmas in collisions other than between heavy-ion, is possible. QGPs may be formed but fail to be large enough - and therefore sufficiently long-lived - for strangeness production to equilibrate with the system. This may be why the Ω/π ratio in high multiplicity p–Pb data only approaches rather than reach the ratio of central Pb–Pb collisions. Particles with a smaller strangeness quantum number would reach saturation earlier, as supported by the Ξ/π observation at high multiplicity. The measurements in pp data also support this argument. The larger deviation from the central Pb–Pb measurements in pp with respect to p–Pb can be interpreted as the formation of even smaller, shorter-lived systems in the former collisions.

These results are also important to test models, alternative to QGP formation, with respect to strangeness production. Some hadronisation models introduce mechanisms that may reproduce the yields of strange particles in pp and p–Pb data. One such mechanism, which could be at the origin of collective behaviour and of enhancement of strange particles [141], is the effect of colour reconnection [142] based on the Lund hadronisation model [94]. In this model, quarks and gluons are pictured as being linked by strings. As the latter stretch and break, hadrons are created as a result of the string fragmentation. Under the colour reconnection mechanism, a quark dipole, linked by a string, may connect to another string nearby. String junctions can form, which increase the colour field, causing an enhancement of baryons upon hadronisation, to the detriment of the meson production. PYTHIA [143] is an event simulator and generator which uses an implementation of colour reconnection. However, as seen in Figure 6.1, this mechanism does not appear to describe the strangeness enhancement effect observed in pp collisions, but instead predicts flat hyperon-to-pion ratios as a function of multiplicity.

A different model is that of the formation of colour 'ropes', as a result of the fusion

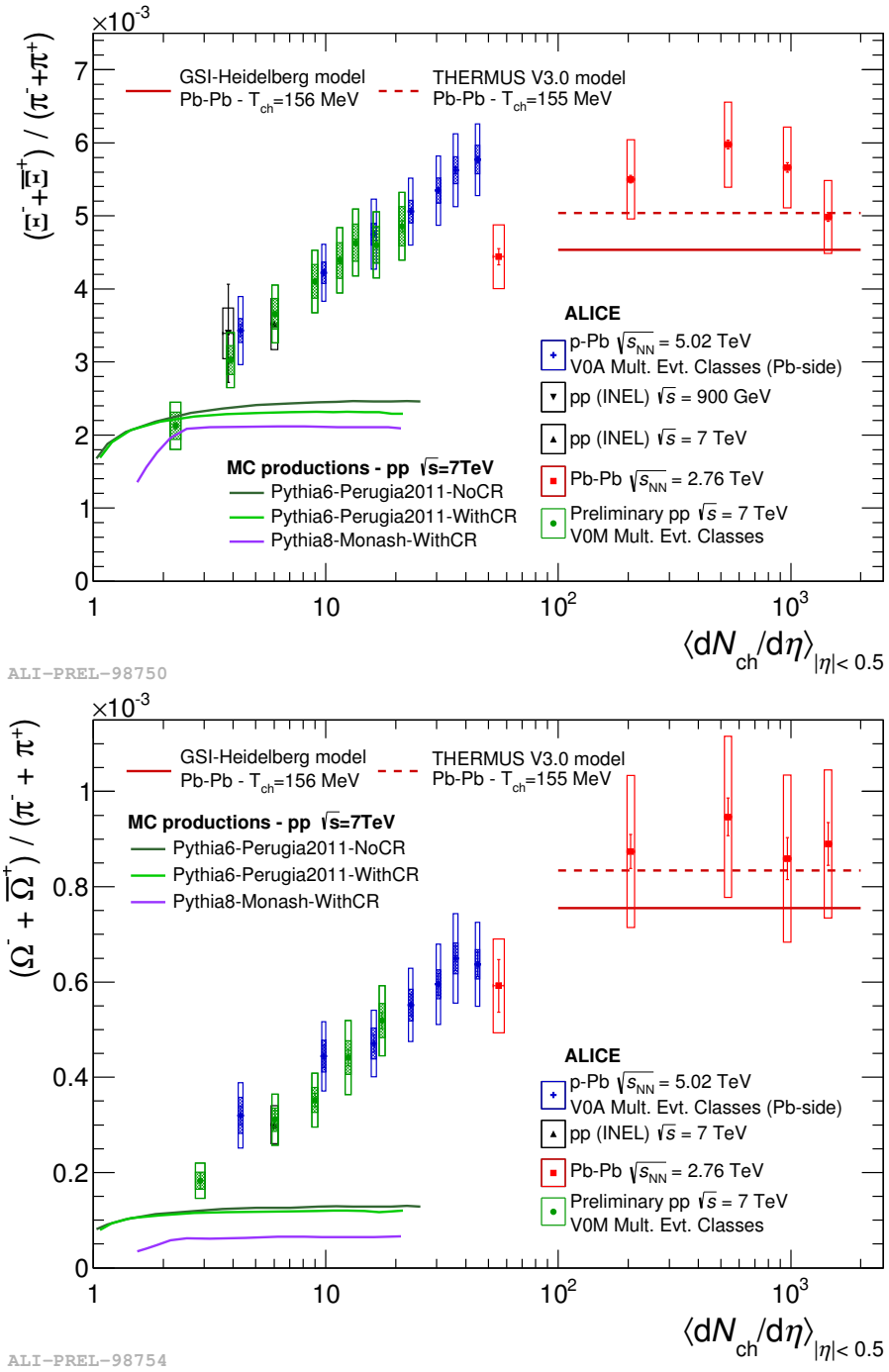

Figure 6.1: The Ξ/π and Ω/π ratios in pp, p–Pb and Pb–Pb as a function with multiplicity as measured with the ALICE experiment. Pythia model calculations for pp collisions with different implementations are included in the Figure, showing no strangeness enhancement [140] .

of several strings. Ropes are characterised by a larger string tension, which is translated to an increased energy release during the fragmentation of the rope, i.e. during

hadronisation. This model, implemented for instance in the DIPSY event generator [144, 142], predicts the enhancement of strangeness production, and would therefore be of interest for future comparisons with the data.

The EPOS model [145, 146, 147] attempts to model the entire evolution of high energy collisions, by using a microscopic description for the partonic phase and the later individual hadronic interactions. The interactions between partons in nucleon–nucleon collisions create 'ladders' of partonic interactions, forming quasi-longitudinal colour fields referred to as 'flux tubes', which are essentially strings. Such tubes disintegrate by emitting quark-antiquark pairs. A core-corona approach is taken to describe a central core with a large number of string and a peripheral region with smaller string density. The two regions are separated by a threshold density. The core forms a group of locally thermalised clusters, which hadronise according to statistical physics. Multi-parton scatterings (MPI) in pp collisions are described as forming several flux tubes. The densities in such collisions can be high enough such that the largest fractions of particles originate from the core. Radial flow effects can thus be reproduced by the EPOS model [145], which provides a motivation to test this model with the multiplicity dependence of the pp and p–Pb spectral shapes and yields of hadrons.

In summary, according to Figure 6.1, the hyperon-to-pion ratios appears to follow a smooth trend towards saturation as a function of multiplicity, regardless of whether the collision system is pp, p–Pb or Pb–Pb, which represents an interesting scenario from an experimental and theoretical point of view. Future data taking runs at the LHC will allow the multiplicity ranges to be expanded in every collision system. It will be interesting to investigate what values the hyperon-to-pion ratios take when the pp (p–Pb) multiplicity range overlaps with the Pb–Pb. The data will confirm whether the apparent limit at high event multiplicity persists, and whether that limit is eventually

reached in pp (p–Pb) collisions. These future measurements are expected to improve our understanding of hadronic physics, in particular of strangeness production, and the possibility of Quark-Gluon Plasma formation in small collision systems.

Appendix A

Yields of multi-strange baryons in measured p_{T} range

Table A.1: The $(\Xi^- + \overline{\Xi}^+)/2$ and $(\Omega^- + \overline{\Omega}^+)/2$ yields determined by the data only and their statistical and systematic uncertainties. The fractions f of the total yields accounted by the data are also shown.

Event class	dN/dy$(\Xi^-+\overline{\Xi}^+)/2$ $\times 10^{-1}$ $\lvert\eta_{\mathrm{lab}}\rvert < 0.5$	f	dN/dy$(\Omega^-+\overline{\Omega}^+)/2$ $\times 10^{-2}$	f
0–5%	1.039±0.009±0.067	0.88	1.09±0.05±0.13	0.82
5–10%	0.814±0.007±0.055	0.87	0.88±0.03±0.10	0.80
10–20%	0.657±0.004±0.045	0.87	0.71±0.02±0.08	0.82
20–40%	0.472±0.003±0.033	0.85	0.45±0.02±0.05	0.76
40–60%	0.305±0.002±0.025	0.83	0.28±0.01±0.03	0.77
60–80%	0.158±0.002±0.010	0.79	0.15±0.01±0.02	0.70
80–100%	0.055±0.001±0.005	0.75	0.05±0.01±0.01	0.65

Appendix B

Thermal model fits

B.1 Fits to low and high multiplicity data

In this appendix, details of the thermal model fits, concerning the discussion of section 5.2.3.2 are provided. Figures B.1 to B.4 are related to the model comparisons of Figure 5.12. The yields of various hadrons are compared to the experimental values. The fits in the 0-5% multiplicity class were obtained with the Strangeness Canonical (Figures B.3) and Grand Canonical (Figure B.4) implementations in THERMUS. In the 80-100% multiplicity class, also two fits were conducted, one with the fully canonical (Figure B.1) and another with the S.C. (Figure B.1) formulae. The G.C. fit to the high multiplicity data was performed with the strangeness undersaturation factor fixed to 1, while in the remaining three fits this parameter was kept free.

The data and model values disagree within 2σ for all hadrons in the fits to the 0-5% multiplicity class, where σ represents the size of the experimental uncertainty of the particular hadron. In the 80-100% class, the disagreement is stronger, lying within 3σ for the S.C fit. The fully canonical model suggests yield values that deviate from the data even further, in particular for the ϕ meson. Consequently, the extracted γ_S factor appears too close to unity.

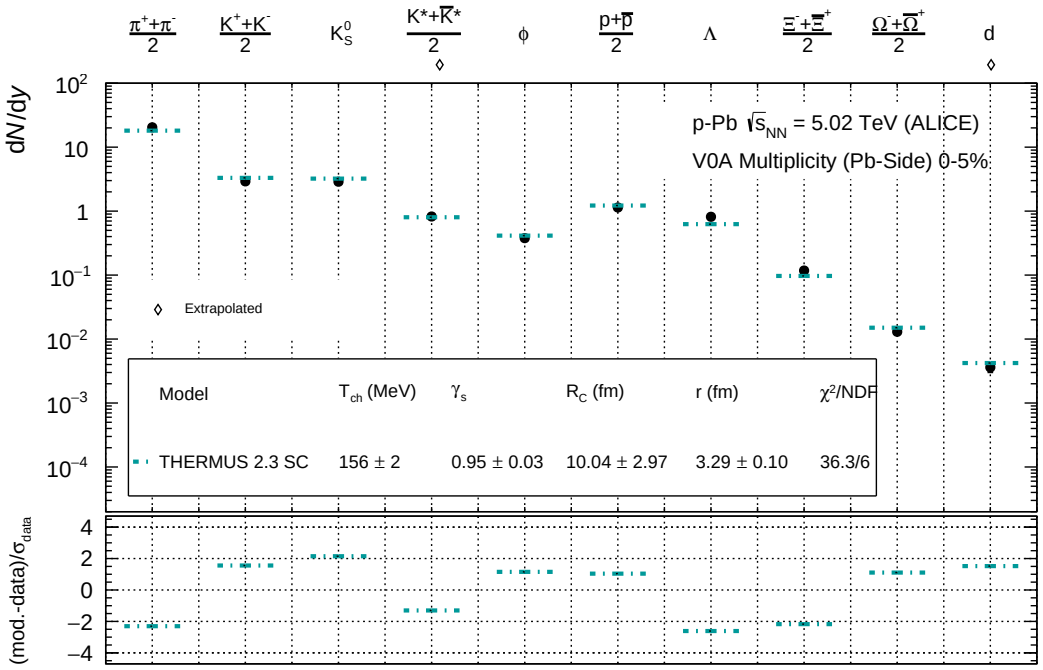

Figure B.1: Particle yields from the S.C. THERMUS fit to the data of the 0-5% multiplicity class compared to the experimental values. The bottom panel shows the difference between the model and data yields, normalised to the experimental uncertainties on the individual yields.

B.2 Strangeness Canonical fits versus multiplicity

The parameters for all p–Pb multiplicity classes extracted from thermal model fits with the Strangeness Canonical implementation are shown in Figure B.5. For these fits, all parameters were kept free. The figure shows the evolution of γ_S, R, R_c and T as a function of multiplicity. The obtained χ^2/ndf values are also plotted in the bottom panel.

The freeze-out temperature does not vary significantly with multiplicity, taking values between 150 and 160 MeV. The radius of the system is observed to increase with multiplicity. The γ_S factor rises smoothly as a function of multiplicity and approaches unity for the 0-5% data.

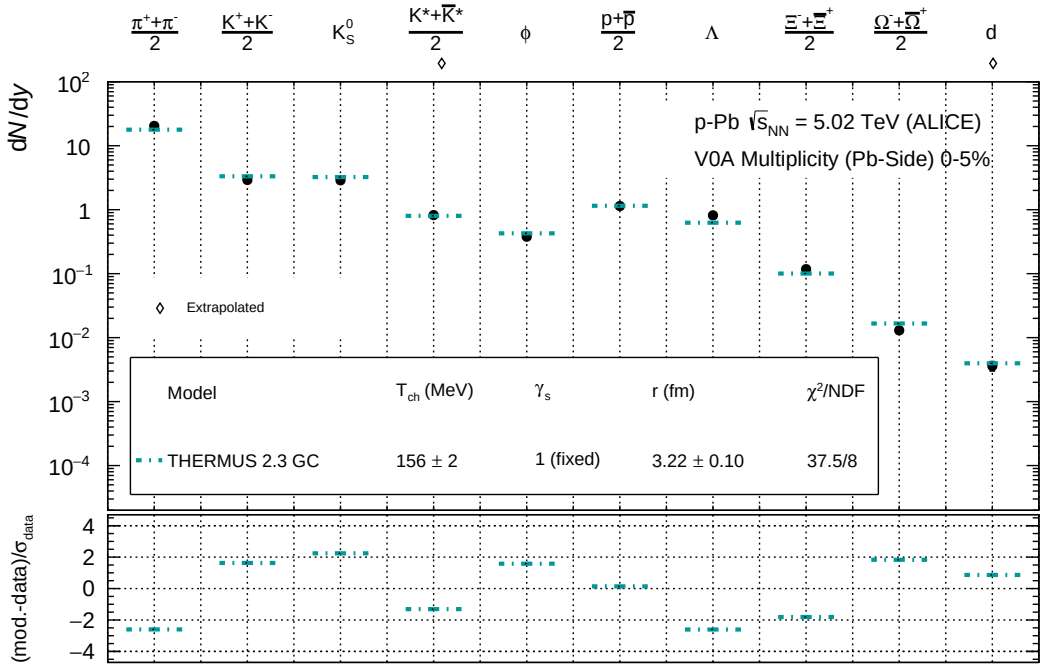

Figure B.2: Particle yields from the G.C. THERMUS fit to the data of the 0-5% multiplicity class compared to the experimental values, with γ_S=1.

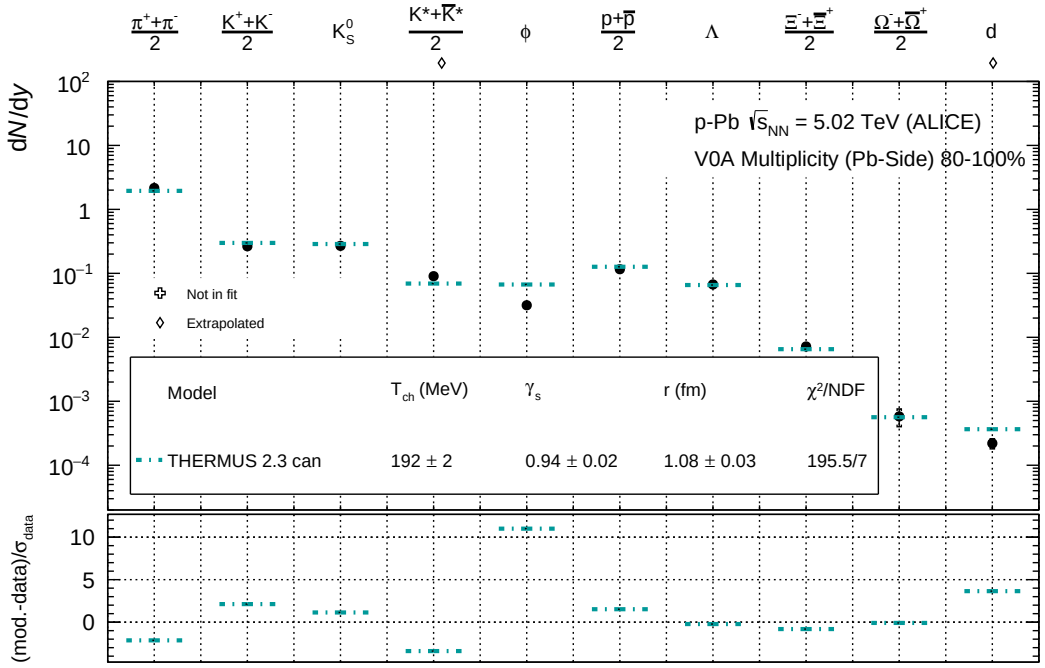

Figure B.3: Particle yields from the fully canonical THERMUS fit to the data of the 80-100% multiplicity class compared to the experimental values.

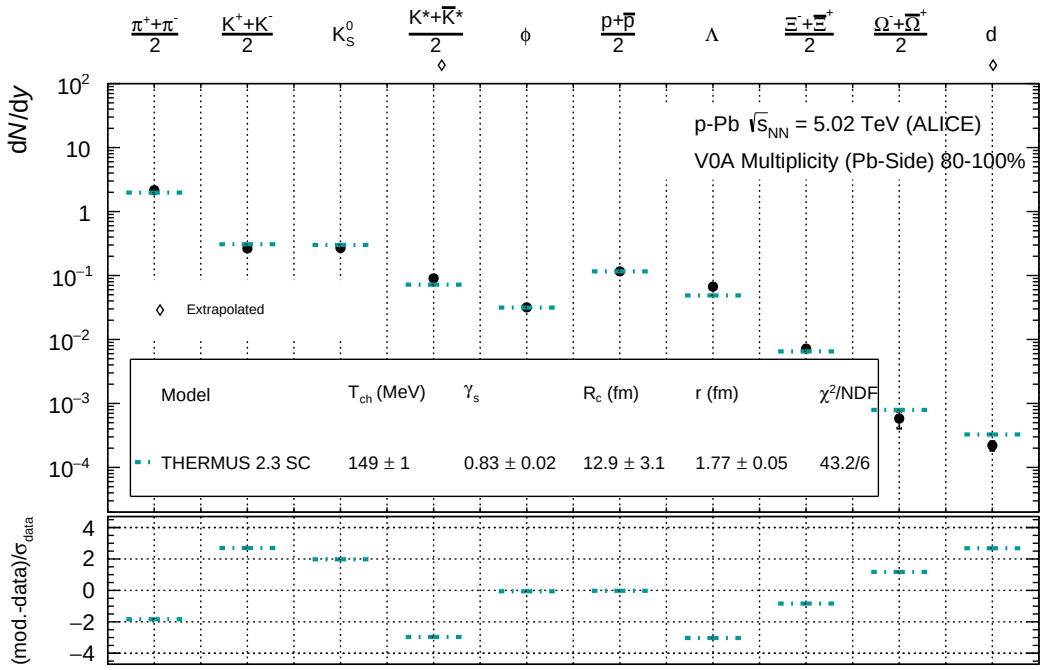

Figure B.4: Particle yields from the S.C. THERMUS fit to the data of the 80-100% multiplicity class compared to the experimental values.

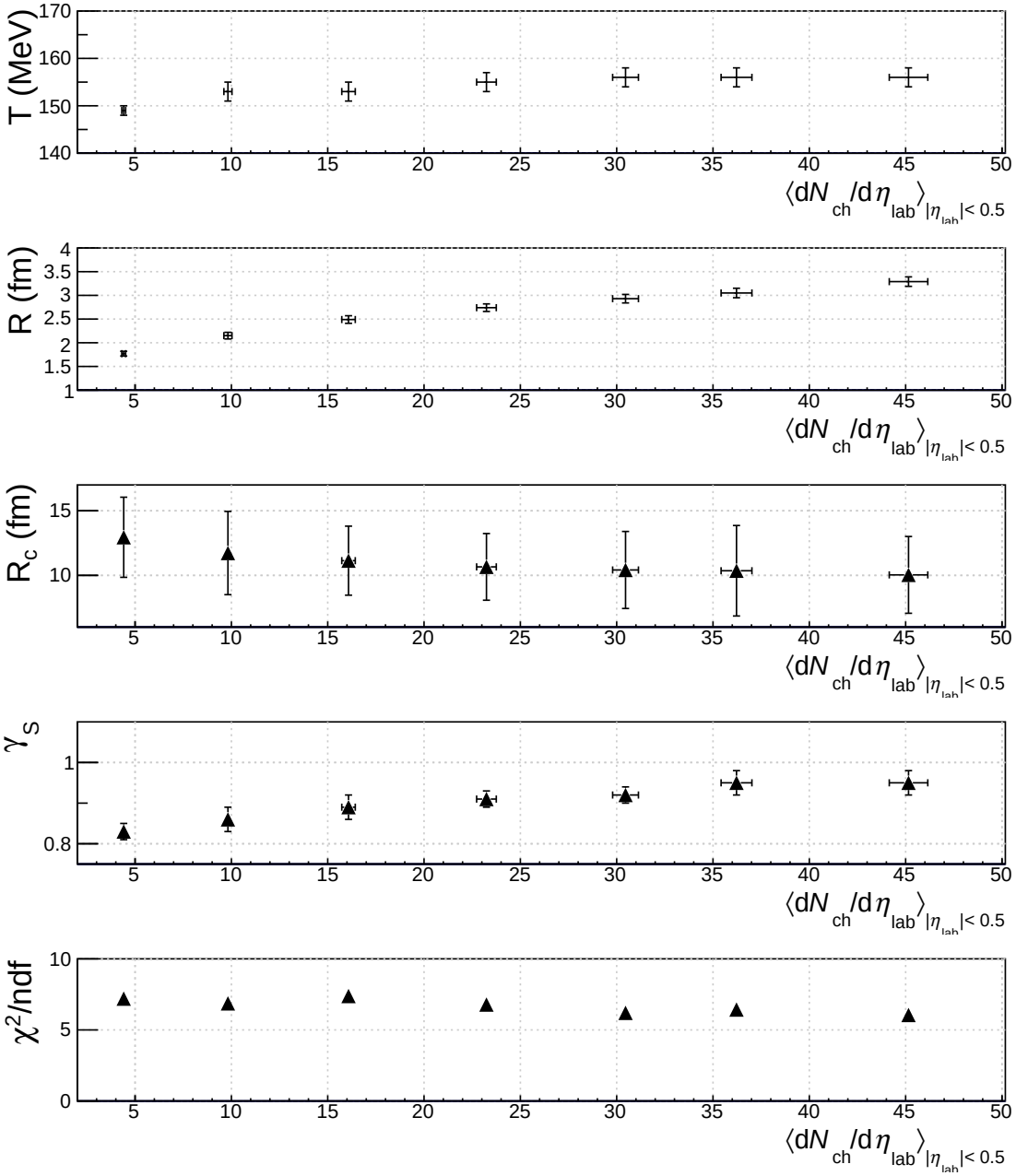

Figure B.5: Fit parameters and χ^2/ndf as a function of multiplicity from S.C. fits performed with THERMUS .

Appendix C

Multi-strange baryon production in p–Pb collisions at $\sqrt{s_{\mathrm{NN}}} = 5.02$ TeV

Physics Letters B, Volume 758, 10 July 2016, Pages 389–401 [2]

Physics Letters B 758 (2016) 389–401

Contents lists available at ScienceDirect

Physics Letters B

www.elsevier.com/locate/physletb

Multi-strange baryon production in p–Pb collisions at $\sqrt{s_{\rm NN}} = 5.02$ TeV

ALICE Collaboration *

ARTICLE INFO

Article history:
Received 16 January 2016
Received in revised form 10 May 2016
Accepted 10 May 2016
Available online 12 May 2016
Editor: L. Rolandi

ABSTRACT

The multi-strange baryon yields in Pb–Pb collisions have been shown to exhibit an enhancement relative to pp reactions. In this work, Ξ and Ω production rates have been measured with the ALICE experiment as a function of transverse momentum, $p_{\rm T}$, in p–Pb collisions at a centre-of-mass energy of $\sqrt{s_{\rm NN}} = 5.02$ TeV. The results cover the kinematic ranges 0.6 GeV/c < $p_{\rm T}$ < 7.2 GeV/c and 0.8 GeV/c < $p_{\rm T}$ < 5 GeV/c, for Ξ and Ω respectively, in the common rapidity interval $-0.5 < y_{\rm CMS} < 0$. Multi-strange baryons have been identified by reconstructing their weak decays into charged particles. The $p_{\rm T}$ spectra are analysed as a function of event charged-particle multiplicity, which in p–Pb collisions ranges over one order of magnitude and lies between those observed in pp and Pb–Pb collisions. The measured $p_{\rm T}$ distributions are compared to the expectations from a Blast-Wave model. The parameters which describe the production of lighter hadron species also describe the hyperon spectra in high multiplicity p–Pb collisions. The yield of hyperons relative to charged pions is studied and compared with results from pp and Pb–Pb collisions. A continuous increase in the yield ratios as a function of multiplicity is observed in p–Pb data, the values of which range from those measured in minimum bias pp to the ones in Pb–Pb collisions. A statistical model qualitatively describes this multiplicity dependence using a canonical suppression mechanism, in which the small volume causes a relative reduction of hadron production dependent on the strangeness content of the hyperon.

1. Introduction

Collisions of heavy nuclei at ultra-relativistic energies allow the study of a deconfined state of matter, the Quark–Gluon Plasma, in which the degrees of freedom are partonic, rather than hadronic. The role of strange hadron yields in searching for this state was pointed out at an early stage [1]. It was subsequently found that in high energy nucleus–nucleus (A–A) collisions at the Super Proton Synchrotron (SPS), the Relativistic Heavy Ion Collider (RHIC) and the Large Hadron Collider (LHC) the abundances of strange and multi-strange baryons are compatible with those from thermal statistical model calculations [2–10].

In smaller collision systems at the same centre-of-mass energies, in particular proton–proton (pp) collisions, the relative abundance of multi-strange baryons is lower with respect to A–A collisions, whether normalised to participant nucleons or produced particles (pions or charged hadrons). This led to the interpretation that strangeness enhancement is observed in A–A collisions. Attempts to explain this phenomenon include the application of a canonical formalism in the statistical model, replacing the grand canonical approach, in which the requirement to conserve the strangeness quantum number when producing (multi-)strange baryons in small systems is imposed [11]. This means that strange hadrons are produced with a lower relative abundance in small systems, an effect known as canonical suppression. Such a theoretical framework has been used to make predictions for LHC energies [12]. Further complications in the interpretation arise when the produced system, although small, is formed in peripheral A–A collisions where the particle production may not be from a contiguous volume due to core-corona effects [13,14]. Evidence for this effect was seen at RHIC where a canonical suppression calculation based on the estimated number of participant nucleons could not successfully reproduce the data [15]. A cleaner way to investigate canonical suppression effects is provided by proton–nucleus (p–A) collisions.

Proton–nucleus collisions provide an opportunity to study the $p_{\rm T}$-dependence of the particle spectra created in a system with a different, more compact, initial geometry than A–A collisions where a similar number of charged particles are produced. Studying this dependence is important in determining the applicability of hydrodynamics [16] which has been successful in describing the particle spectra in A–A collisions [17–19].

At the LHC the combination of the rise in particle production per nucleon–nucleon collision with increasing $\sqrt{s}$ and a dedicated p–Pb data-taking period have enabled the ALICE experiment to

* *E-mail address:* alice-publications@cern.ch.

http://dx.doi.org/10.1016/j.physletb.2016.05.027

collect a large sample of $\Xi^{\pm}$ and $\Omega^{\pm}$. In this Letter, we set out the methods for these studies, present the results obtained and discuss how they fit into a theoretical picture.

2. Sample and data analysis

The results presented in this Letter were obtained from a sample of the data collected with the ALICE detector [20] during the LHC p–Pb run at $\sqrt{s_{\rm NN}} = 5.02$ TeV in the beginning of 2013. The two scintillator arrays V0A (direction of Pb beam), and V0C (direction of p beam), covering pseudo-rapidity ranges of $2.8 < \eta < 5.1$ and $-3.7 < \eta < -1.7$, respectively, served both as triggering detectors and for determining the event multiplicity class [21]. The tracking of particles in the central barrel, covering $|\eta| < 0.9$, takes place in the Inner Tracking System (ITS), which consists of the two innermost silicon pixel layers, surrounded by two silicon drift and two silicon strip layers, all placed within a radius of 43 cm, and the Time Projection Chamber (TPC), a large cylindrical drift chamber filled with a Ne–CO_2 gas mixture [20]. Measurements of the energy loss by charged particles in the gas allow particles to be identified with this detector.

A trigger requiring a coincidence within less than 1 ns in the V0 detectors selected around 100 million events, which are mainly non-single diffractive (NSD) events and contain a negligible contribution from single diffractive (SD) and electromagnetic (EM) processes [22]. A dedicated radiator-quartz detector (T0) provided a measurement of the event time of the collisions. The V0 and T0 time resolutions allowed discrimination of beam–beam interactions from background events in the interaction region. Further background suppression was applied in the offline analysis using time information from the neutron Zero Degree Calorimeter on the Pb-going side. Primary vertices (PVs) were selected if their position along the beam axis was reconstructed within 10 cm of the geometrical centre of the detector. In Monte Carlo (MC) studies an efficiency of 99.2% for this trigger was obtained, while the joint trigger and primary vertex reconstruction efficiency lies at 97.8% [22]. The estimated mean number of interactions per bunch crossing was below 1% in the sample chosen for this analysis.

The analysed events were divided into seven multiplicity percentile classes according to the total number of particles measured in the forward V0A detector. The efficiency-corrected mean number of charged primary particles per unit rapidity ($\langle {\rm d}N_{\rm ch}/{\rm d}\eta \rangle$) within $-0.5 < \eta < 0.5$ in the laboratory reference frame for each of these multiplicity bins were published in [23].

Due to the asymmetric energies of the proton and lead ion beams, a consequence of the 2-in-1 magnet design of the LHC, the nucleon–nucleon centre-of-mass system is shifted by 0.465 units of rapidity in the direction of the proton beam with respect to the laboratory frame. The measurements reported in this Letter were performed in the central rapidity window defined in the centre-of-mass frame within $-0.5 < y < 0$, where negative rapidity corresponds to the side of the detector into which the Pb beam travels.

The identification of multi-strange baryons was based on the topology of their weak decays through the reconstruction of the tracks left behind by the decay products, referred to as the daughter particles. The daughters of the $\Xi^- \to \Lambda\pi^-$ (BR: 99.9%), $\Omega^- \to \Lambda K^-$ (BR: 67.8%) and the subsequent $\Lambda \to p\pi^-$ (BR: 63.9%) weak decays [24], as well as the corresponding decays of the $\overline{\Xi}^+$ and $\overline{\Omega}^+$, were reconstructed by combining track information from the TPC and the ITS [25]. Proton, anti-proton and charged π and K tracks were identified in the TPC via their measured energy deposition, which was compared with a mass-dependent parameterisation of ionisation loss in the TPC gas as a function of momentum [26]. All daughter candidates were required to lie within 4σ of their characteristic Bethe–Bloch energy loss curve. Multi-strange candidates were selected through the geometrical association of the V^0 component (Λ or $\bar{\Lambda}$ decay) to a further secondary, 'bachelor' track (identified as $\pi^{\pm}$ or $\rm K^{\pm}$). In this process, several geometrical variables were measured for each candidate, and criteria were set on them in order to purify the selected sample: numerical values for the selection cuts applied are reported in Table 1. These selections are similar to those in the pp measurements [25], a consequence of the low multiplicities present in the detector in the p–Pb collisions. As a result the correction factors for the efficiency are also similar. In addition to the settings on topological variables, a cut has been applied on the V^0 invariant mass window of ± 8 MeV/c^2 from the nominal Λ mass [24]. Further restrictions were set on the proper lifetime of the $\Xi^{\pm}$ and $\Omega^{\pm}$. By requiring this variable to be less than 3 times the mean decay length (4.91 cm and 2.46 cm, respectively), we discarded low-momentum secondary particles and false multi-strange candidates, the daughter tracks of which originated from interactions with detector material.

Table 1
The parameters for V^0 (Λ and $\bar{\Lambda}$) and cascades ($\Xi^{\pm}$ and $\Omega^{\pm}$) selection criteria. Where a criterion for $\Xi^{\pm}$ and $\Omega^{\pm}$ finding differs, the value for the $\Omega^{\pm}$ case is in parentheses. DCA represents "distance of closest approach," PV the primary vertex, θ is the angle between the momentum vector of the reconstructed V^0 or cascade, and the displacement vector between the decay and primary vertices. The curvature of the cascade particle's trajectory is neglected.

V^0 finding criteria	
DCA: $h^{\pm}$ to PV	> 0.04 (0.03) cm
DCA: h^- to h^+	< 1.5 standard deviations
Λ mass ($m_{\rm V0}$)	$1.108 < m_{\rm V0} < 1.124$ GeV/c^2
Fiducial volume ($R_{\rm 2D}$)	$R_{\rm 2D} > 1.1$ (1.2) cm
V^0 pointing angle	$\cos\theta_{\rm V0} > 0.97$
Cascade finding criteria	
Proper decay length	$< 3\times$ mean decay length
DCA: $\pi^{\pm}$ ($K^{\pm}$) to PV	> 0.04 cm
DCA: V^0 to PV	> 0.06 cm
DCA: $\pi^{\pm}$ ($K^{\pm}$) to V^0	< 1.3 cm
Fiducial volume ($R_{\rm 2D}$)	$R_{\rm 2D} > 0.5(0.6)$ cm
Cascade pointing angle	$\cos\theta_{\rm casc} > 0.97$

The invariant mass of the Ξ and Ω hyperons was calculated by assuming the known masses [24] of the Λ and of the bachelor track. The mass was reconstructed twice for each cascade candidate, once assuming the bachelor to be a π and once a K. This allowed the removal of an important fraction of the Ω background, which contained a large contribution from the Ξ candidates that pass the Ω selection criteria. Most of these false Ω were removed discarding all candidates that could be reconstructed as Ξ with a mass within 10 MeV/c^2 of the known mass [24] of the Ξ baryon. Fig. 1 shows the invariant mass distributions for the Ξ^- and Ω^- hadrons in well populated $p_{\rm T}$ bins for the lowest and highest multiplicity classes.

For the signal extraction, a peak region was defined within 4σ of the mean of a Gaussian invariant mass peak for every measured $p_{\rm T}$ interval. Adjacent background bands, covering an equal combined mass interval as the peak region, were defined on both sides of that central region. This is illustrated in Fig. 1 with the shaded bands on either side of the peak. The number of bin entries inside the side-bands was subtracted from the number of candidates within the peak region, assuming the background to be linear across the mass range considered.

The $p_{\rm T}$ distributions were corrected for detector acceptance and reconstruction efficiencies. These were estimated with the use of DPMJet [27] simulated Monte Carlo (MC) events, which were propagated through the detector with GEANT3 [28].

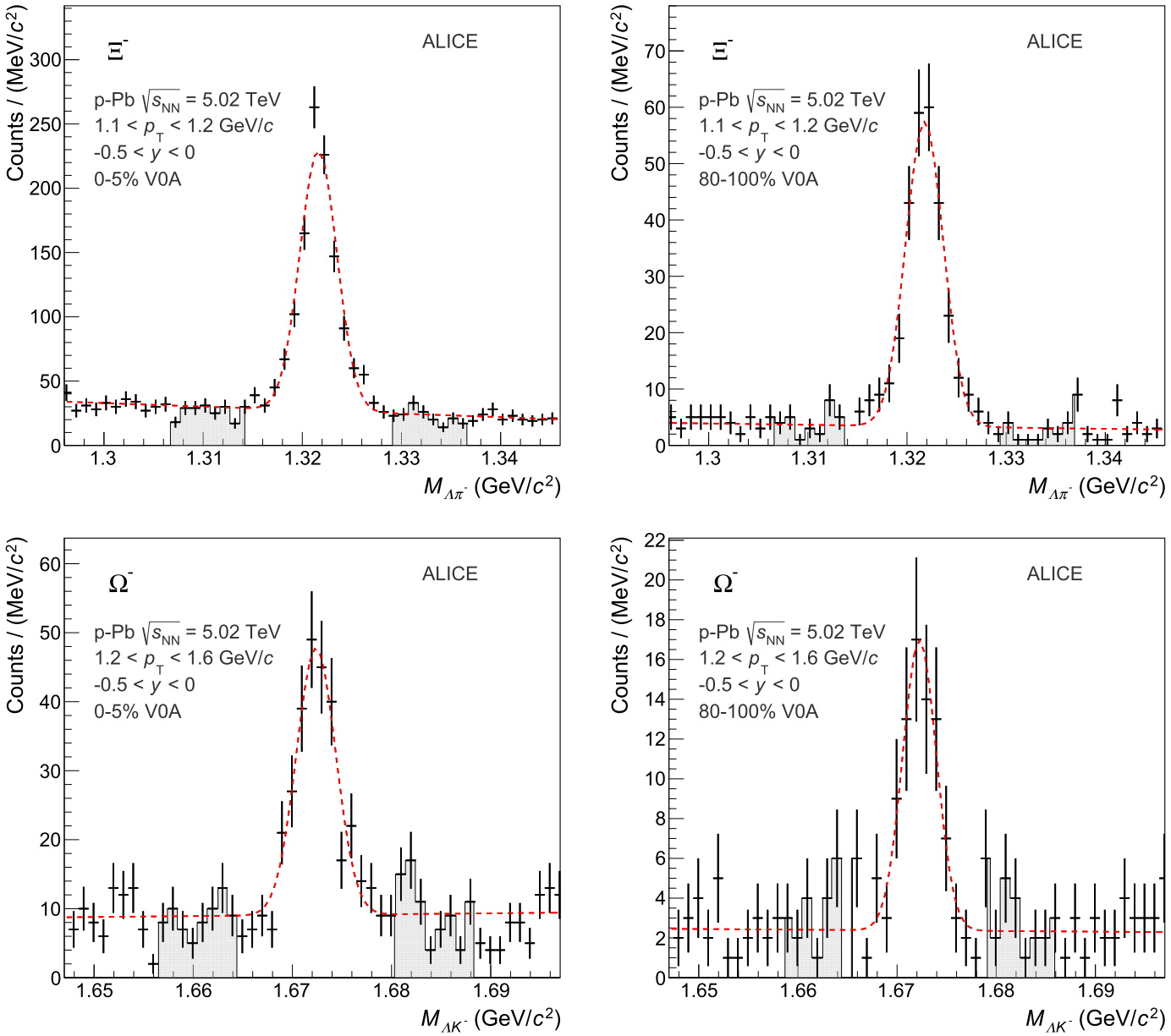

Fig. 1. Invariant mass distributions of the Ξ^- and Ω^- in the 1.1–1.2 GeV/c and 1.2–1.6 GeV/c p_{T} bins respectively, fitted with a Gaussian peak and linear background (dashed red curves). The distributions for highest (left) and lowest (right) multiplicity classes are shown. The fits only serve to illustrate the peak position with respect to which the bands were defined and the linear background assumption for the applied signal extraction method.

2.1. Systematic uncertainties

Systematic uncertainties due to the choice of selection criteria were examined separately in each p_{T} interval of the measured spectra. Individual settings were loosened and tightened, in order to measure changes in the signal loss correction. For the Ξ hyperons, the signal extraction accounts for an uncertainty of around 2% but reaches 5% at low-p_{T} and in high multiplicity events, while for the Ω, uncertainties of 3–5% were measured. The uncertainty due to the topological selections is around 2(3)% for the main p_{T} region, and up to 3(5)% at low momentum for $\Xi(\Omega)$. The constraint on the V^0 mass window contributes to the total uncertainty with around 0.5(1)% and both the TPC tracking and identification cuts with 2(3)%. The proper decay length cut gives another 3(5)% uncertainty at low p_{T}. A 4% error was added due to the material budget, and for the $\Omega^{\pm}$ only, an additional 3% due to the mass hypothesis cut. All these individual error contributions, which are listed in Table 2, are added in quadrature. Apart from the low momentum region, no p_{T} dependence is observed in the total uncertainty. The total systematic error lies between 5–6(8)% across the whole spectrum, reaching up to 8(14)% in the lowest p_{T} bins for the $\Xi(\Omega)$ baryons.

The fraction of the systematic error that is uncorrelated across multiplicity was calculated by using the same method applied in [23], in which spectra deviations in specific multiplicity classes were compared to those observed in the integrated data sample. The choice of the topological parameter values and the applied signal extraction method generates the dominant contribution to the uncorrelated uncertainties across multiplicity. These uncertainties were measured to be within 2% in the case of the Ξ and 3% in the case of the Ω, which constitutes a fraction that lies between 20 and 40% of the total systematic uncertainties.

Table 2
Contributions to the total systematic uncertainties for the $\Xi^{\pm}$ and $\Omega^{\pm}$ spectra measurements. The values in brackets indicate the maximum uncertainties measured for low-p_{T} cascades (see text).

Source	$\Xi^{\pm}$	$\Omega^{\pm}$
Material budget	4%	4%
Competing mass hypothesis	–	3%
Topological variables	2–3(5)%	3–5%
Signal extraction	2(5)%	3(5)%
Particle identification	2%	3%
Track selection	2%	3%
Proper decay length	1(3)%	2(5)%
V^0 mass window	0.5%	1%

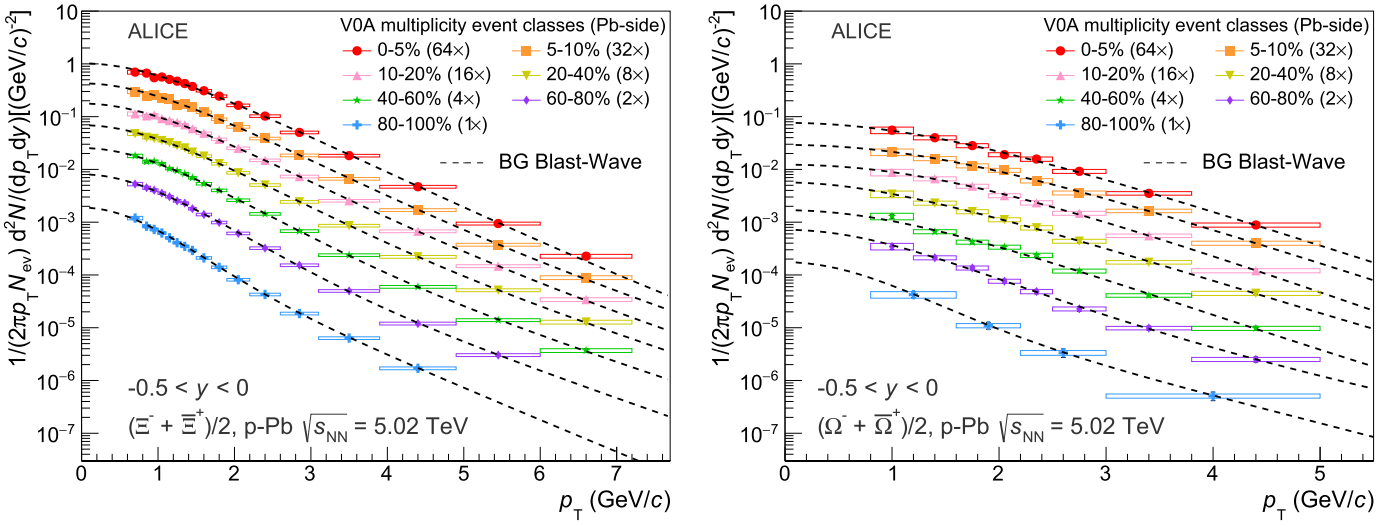

Fig. 2. (Colour online.) Invariant p_{T}-differential yields of $(\Xi^- + \overline{\Xi}^+)/2$ and $(\Omega^- + \overline{\Omega}^+)/2$ in different multiplicity classes. Data have been scaled by successive factors of 2 for better visibility. Statistical (bars), full systematic (boxes) and uncorrelated across multiplicity (transparent boxes) uncertainties are plotted. The dashed curves represent Blast-Wave fits to each individual distribution.

3. Results

3.1. Transverse momentum spectra

The p_{T} distributions of Ξ^-, $\overline{\Xi}^+$, Ω^- and $\overline{\Omega}^+$ in $-0.5 < y < 0$ are shown in Fig. 2 for different multiplicity intervals, as defined in [23]. Since antiparticle and particle spectra are identical within uncertainties, the average of the two is shown. The spectra exhibit a progressive flattening with increasing multiplicity, which is qualitatively reminiscent of what is observed in Pb–Pb collisions [10].

The calculation of p_{T}-integrated yields can be performed by using data in the measured region and a parametrisation-based extrapolation elsewhere. The Boltzmann–Gibbs Blast-Wave (BG–BW) model [16] gives a good description of each p_{T} spectrum and has been used as a tool for this extrapolation. Other alternatives, such as the Levy–Tsallis [29] and Boltzmann distributions, were used for estimating the systematic uncertainty due to the extrapolation.

The extrapolation in the unmeasured $\Xi^{\pm}$ ($\Omega^{\pm}$) low-p_{T} region grows progressively with decreasing multiplicity, from around 16%(19%) of the total yield in the 0–5% multiplicity class to around 27%(40%) in the 80–100% class. The systematic uncertainty assigned to the yield due to the extrapolation technique is 2.8%(7.8%) for high multiplicities and rises to 5.2%(14.5%) in the case where the fraction of the extrapolated yield is highest.

3.2. Comparison to Blast-Wave model

In order to investigate whether the observed spectral shapes are consistent with a system that exhibits hydrodynamical radial expansion, the measured distributions have been further studied in the context of the BG–BW model [16]. This model assumes a locally thermalised medium that expands collectively with a common velocity field and then undergoes an instantaneous freeze-out. In this framework, a simultaneous fit to identified particle spectra allows for the determination of common freeze-out parameters. These can be used to predict the p_{T} distribution for other particle species in a collective expansion picture. It should be noted that such a simultaneous fit differs from the individual fits mentioned in the previous section and used only for extrapolating the spectra.

The Ξ^-, $\overline{\Xi}^+$, Ω^- and $\overline{\Omega}^+$ p_{T} spectra in the 0–5% and 80–100% multiplicity classes are compared to predictions from the BG–BW model with parameters acquired from a simultaneous fit to $\pi^{\pm}$, $\mathrm{K}^{\pm}$, $\mathrm{p}(\overline{\mathrm{p}})$ and $\Lambda(\bar{\Lambda})$ in Fig. 3 [23]. The model describes the measured shapes within uncertainties up to a p_{T} of approximately 4 GeV/c for Ξ and 5 GeV/c for Ω in the highest multiplicity class. This indicates that multi-strange hadrons also follow a common motion with the lighter hadrons and is suggestive of the presence of radial flow in p–Pb collisions. However, it is worth noting that some final state effects could also modify the spectra in a similar manner to radial flow. For example, PYTHIA [30] implements the colour reconnection mechanism, which fuses strings originating from independent parton interactions, leading to fewer but more energetic hadrons, which has been shown to mimic radial flow [31].

Applying the same technique to results from the lower multiplicity classes reveals that the agreement of the data with the

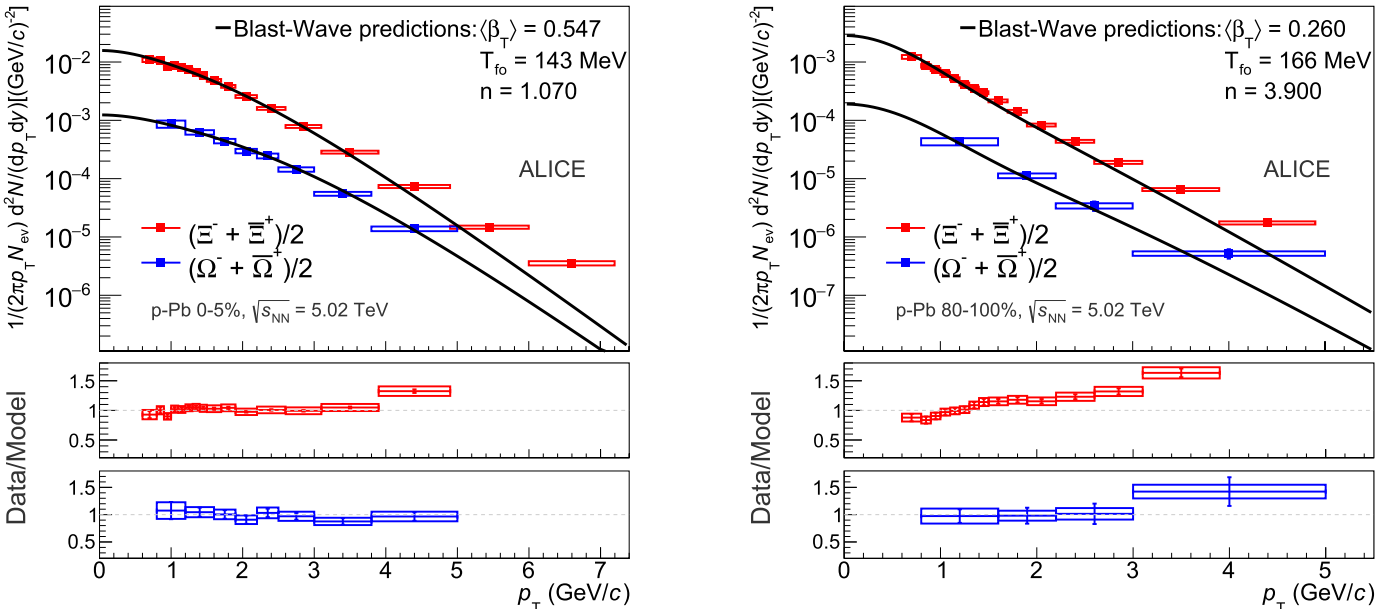

Fig. 3. (Colour online.) $(\Xi^- + \overline{\Xi}^+)/2$ and $(\Omega^- + \overline{\Omega}^+)/2$ p_{T} spectra in the 0–5% (left) and 80–100% (right) multiplicity classes compared to predictions from the BG–BW model (upper panels) with the ratios on a linear scale (lower panels). The parameters are based on simultaneous fits to lighter hadrons [23]. See text for details.

Table 3
The mid-rapidity $\langle \mathrm{d}N_{\mathrm{ch}}/\mathrm{d}\eta \rangle$ values for each of the 7 multiplicity classes and the $\Xi^- + \overline{\Xi}^+$ and $\Omega^- + \overline{\Omega}^+$ integrated yields per unit rapidity normalised to the visible cross section. The statistical uncertainty on the yields is followed by the systematic uncertainty.

Event class	$\langle \mathrm{d}N_{\mathrm{ch}}/\mathrm{d}\eta \rangle$ $\lvert\eta_{\mathrm{lab}}\rvert < 0.5$	$\mathrm{dN/dy}(\Xi^- + \overline{\Xi}^+)$	$\mathrm{dN/dy}(\Omega^- + \overline{\Omega}^+)$
0–5%	45 ± 1	$0.2354 \pm 0.0020 \pm 0.0161$	$0.0260 \pm 0.0011 \pm 0.0034$
5–10%	36.2 ± 0.8	$0.1861 \pm 0.0016 \pm 0.0138$	$0.0215 \pm 0.0008 \pm 0.0029$
10–20%	30.5 ± 0.7	$0.1500 \pm 0.0010 \pm 0.0112$	$0.0167 \pm 0.0006 \pm 0.0022$
20–40%	23.2 ± 0.5	$0.1100 \pm 0.0006 \pm 0.0085$	$0.0120 \pm 0.0005 \pm 0.0016$
40–60%	16.1 ± 0.4	$0.0726 \pm 0.0006 \pm 0.0065$	$0.0072 \pm 0.0003 \pm 0.0010$
60–80%	9.8 ± 0.24	$0.0398 \pm 0.0004 \pm 0.0031$	$0.0042 \pm 0.0002 \pm 0.0006$
80–100%	4.3 ± 0.1	$0.0143 \pm 0.0003 \pm 0.0015$	$0.0013 \pm 0.0003 \pm 0.0003$

Blast-Wave predictions become progressively worse. The comparison between lowest and highest multiplicity cases can be seen in Fig. 3, where their respective ratios to the model predictions are shown in the lower panels. These observations indicate that common kinetic freeze-out conditions are able to better describe the spectra in high multiplicity p–Pb collisions.

The multi-strange baryon spectra in central Pb–Pb collisions [10] have also been investigated in a common freeze-out scenario [17,18] and similar studies were performed for Au–Au collisions [19]. In contrast to high multiplicity p–Pb collisions, where all stable and long-lived hadron spectra are compatible with a single set of kinetic freeze-out conditions (the temperature $\mathrm{T_{fo}}$ and the mean transverse flow velocity $\langle \beta_{\mathrm{T}} \rangle$), multi-strange particles in central heavy-ion collisions seem to experience less transverse flow and may freeze out earlier in the evolution of the system when compared to most of the other hadrons.

3.3. Hyperon to pion ratios

The measured integrated yields in the seven multiplicity classes are given in Table 3. To study the relative production of strangeness and compare it with results in pp and Pb–Pb collisions, the yield ratios to pions were calculated as a function of charged particle multiplicity. Both the $(\Xi^- + \overline{\Xi}^+)/(\pi^+ + \pi^-)$ and $(\Omega^- + \overline{\Omega}^+)/(\pi^+ + \pi^-)$ ratios are observed to increase as a function of multiplicity, as seen in Fig. 4. The relative increase is more pronounced for the Ω^- and $\overline{\Omega}^+$ than for Ξ^- and $\overline{\Xi}^+$, being approximately 100% for the former and 60% for the latter. These relative increases are larger than the 30% increase observed for the Λ/π ratio [23], indicating that strangeness content may control the rate of increase with multiplicity.

These ratios are further compared to measurements performed in the pp [25,34] and Pb–Pb [10] collision systems. The $(\Xi^- + \overline{\Xi}^+)/(\pi^+ + \pi^-)$ ratio for the highest p–Pb multiplicity is compatible with the Pb–Pb measurements in the Pb–Pb 0–60% centrality range and the $(\Omega^- + \overline{\Omega}^+)/(\pi^+ + \pi^-)$ reaches a value slightly below its Pb–Pb equivalent in this centrality range, although the error bars still overlap. It is also noteworthy that the values obtained for the p–Pb 80–100% multiplicity event class are similar to the ones measured in minimum bias pp collisions.

Finally, the hyperon to pion ratios can also be compared with the values in the Grand Canonical (GC) limit obtained from global fits to Pb–Pb data. Two different implementations of the thermal model are shown in Fig. 4, where the dashed lines represent the values from the THERMUS 2.3 model [36] and the solid lines represent predictions from the GSI-Heidelberg model [35]. Both models provide values that are consistent with the most central Pb–Pb measurements.

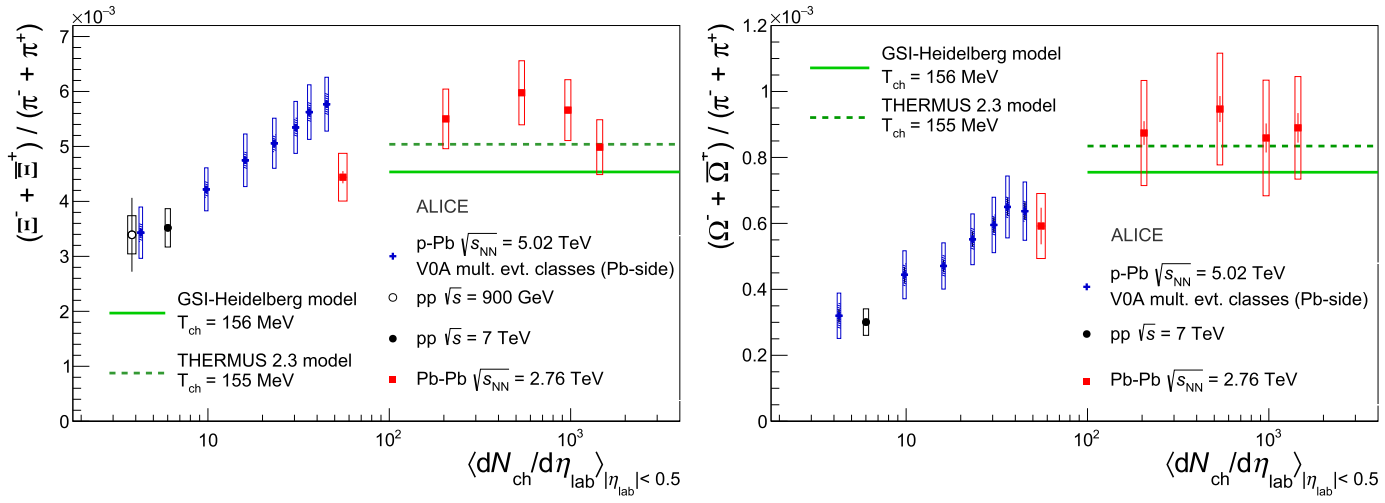

Fig. 4. (Colour online.) $(\Xi^- + \overline{\Xi}^+)/(\pi^+ + \pi^-)$ (left) and $(\Omega^- + \overline{\Omega}^+)/(\pi^+ + \pi^-)$ (right) ratios as a function of $\langle dN_{ch}/d\eta \rangle$ for all three colliding systems. The ratios for the seven multiplicity classes in p–Pb data lie between the Minimum Bias pp ($\sqrt{s} = 900$ GeV [32,33] and $\sqrt{s} = 7$ TeV [25,34]) and peripheral Pb–Pb results. The Pb–Pb points [10] represent, from left to right, the 60–80%, 40–60%, 20–40% and 10–20% and 0–10% centrality classes. The chemical equilibrium predictions by the GSI-Heidelberg [35] and the THERMUS 2.3 [36] models are represented by the horizontal lines.

In small multiplicity environments such as those produced in p–Pb collisions, a grand canonical statistical description may not be appropriate. Instead, local conservation laws might play an important role. The evolution of hyperon to pion ratios in terms of the event multiplicity can be calculated with a Strangeness Canonical (SC) model implemented in THERMUS [36]. This model applies a local conservation law to the strangeness quantum number within a correlation volume V_c while treating the baryon and charge quantum numbers grand-canonically within the fireball volume V. This implies a decrease of the strangeness yields with respect to the pion yields with a shrinking system size. To model this canonical suppression effect as a function of pion rapidity density, yield calculations were repeated for varying system sizes. Strangeness conservation was imposed within the size of the fireball ($V_c = V$), and the strangeness saturation parameter γ_S was fixed to 1, thus changes in the hadron to pion ratios were due to the variations of the restraints on the system size only. The chemical potentials (μ) of the conserved strangeness, baryon and electric charge quantum numbers were set to zero. The obtained suppression curves for Λ, Ξ and Ω are shown in Fig. 5 for a temperature of 155 MeV, the value extracted from a GC global fit to high multiplicity Pb–Pb data, with a variation of ± 10 MeV (solid lines). Both the data and model points were normalised to the high multiplicity limit. For the data, this limit is the mean hyperon to pion ratio in the 0–60% most central Pb–Pb events, whereas for the model it corresponds to the GC limit. The theoretical curves for strangeness suppression computed with THERMUS are in qualitative agreement with the effect observed in the data.

4. Conclusions

In summary, a measurement of the p_T spectra of Ξ^-, $\overline{\Xi}^+$, Ω^- and $\overline{\Omega}^+$ for seven multiplicity classes in p–Pb collisions at $\sqrt{s_{NN}} = 5.02$ TeV at the LHC has been presented. These measurements represent an important contribution to the understanding of strangeness production, as hyperon production rates are now measured at LHC energies over a large range in charged–particle multiplicity, from pp to central Pb–Pb collisions.

The multi-strange baryon spectra exhibit a progressive flattening with increasing multiplicity suggesting the presence of radial flow. A comparison with the Boltzmann–Gibbs Blast-Wave model indicates a common kinetic freeze-out with lighter hadrons in the highest multiplicity p–Pb collisions. This is in contrast to higher multiplicity heavy-ion collisions where there is an indication for an earlier freeze-out of these particles.

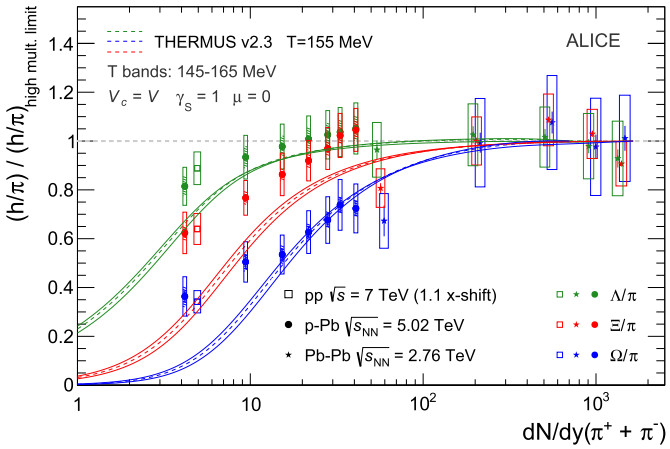

Fig. 5. (Colour online.) Hyperon to pion ratios as a function of pion yields for pp, p–Pb and Pb–Pb colliding systems compared to the THERMUS [36] strangeness suppression model prediction, in which only the system size is varied. The h/π are the ratios of the particle and antiparticle sums, except for the $2\Lambda/(\pi^- + \pi^+)$ data points in pp [33], p–Pb [23] and Pb–Pb [37]. All values are normalised to the high multiplicity limit, which is given by the mean of the 0–60% highest multiplicity Pb–Pb measurements for the data and by the GC limit for the model.

For the first time, the lifting of strangeness suppression with system size has been observed with measurements in a single collision system. Hyperon to pion ratios are shown to increase with multiplicity in p–Pb collisions from the values measured in pp to those observed in Pb–Pb. The rate of increase is more pronounced for particles with higher strangeness content. Comparing these results to the trends observed in statistical hadronisation models that conserve strangeness across the created system indicates that the behaviour is qualitatively consistent with the lifting of canonical suppression with increasing multiplicity.

Acknowledgements

The ALICE Collaboration would like to thank all its engineers and technicians for their invaluable contributions to the construction of the experiment and the CERN accelerator teams for the outstanding performance of the LHC complex. The ALICE Collaboration gratefully acknowledges the resources and support provided by all Grid centres and the Worldwide LHC Computing Grid (WLCG) collaboration. The ALICE Collaboration acknowledges the following funding agencies for their support in building and running the ALICE detector: State Committee of Science, World Federation of Scientists (WFS) and Swiss Fonds Kidagan, Armenia; Conselho Nacional de Desenvolvimento Científico e Tecnológico (CNPq), Financiadora de Estudos e Projetos (FINEP), Fundação de Amparo à Pesquisa do Estado de São Paulo (FAPESP); National Natural Science Foundation of China (NSFC), the Chinese Ministry of Education (CMOE) and the Ministry of Science and Technology of China (MSTC); Ministry of Education and Youth of the Czech Republic; Danish Natural Science Research Council, the Carlsberg Foundation and the Danish National Research Foundation; The European Research Council under the European Community's Seventh Framework Programme; Helsinki Institute of Physics and the Academy of Finland; French CNRS-IN2P3, the 'Region Pays de Loire', 'Region Alsace', 'Region Auvergne' and CEA, France; German Bundesministerium fur Bildung, Wissenschaft, Forschung und Technologie (BMBF) and the Helmholtz Association; General Secretariat for Research and Technology, Ministry of Development, Greece; National Research, Development and Innovation Office (NKFIH), Hungary; Department of Atomic Energy and Department of Science and Technology of the Government of India; Istituto Nazionale di Fisica Nucleare (INFN) and Centro Fermi – Museo Storico della Fisica e Centro Studi e Ricerche "Enrico Fermi", Italy; Japan Society for the Promotion of Science (JSPS) KAKENHI and MEXT, Japan; Joint Institute for Nuclear Research, Dubna; National Research Foundation of Korea (NRF); Consejo Nacional de Cienca y Tecnologia (CONACYT), Direccion General de Asuntos del Personal Academico (DGAPA), México, Amerique Latine Formation academique – European Commission (ALFA-EC) and the EPLANET Program (European Particle Physics Latin American Network); Stichting voor Fundamenteel Onderzoek der Materie (FOM) and the Nederlandse Organisatie voor Wetenschappelijk Onderzoek (NWO), Netherlands; Research Council of Norway (NFR); National Science Centre, Poland; Ministry of National Education/Institute for Atomic Physics and National Council of Scientific Research in Higher Education (CNCSI–UEFISCDI), Romania; Ministry of Education and Science of Russian Federation, Russian Academy of Sciences, Russian Federal Agency of Atomic Energy, Russian Federal Agency for Science and Innovation and The Russian Foundation for Basic Research; Ministry of Education of Slovakia; Department of Science and Technology, Republic of South Africa, South Africa; Centro de Investigaciones Energeticas, Medioambientales y Tecnologicas (CIEMAT), E-Infrastructure shared between Europe and Latin America (EELA), Ministerio de Economía y Competitividad (MINECO) of Spain, Xunta de Galicia (Consellería de Educación), Centro de Aplicaciones Tecnológicas y Desarrollo Nuclear (CEADEN), Cubaenergía, Cuba, and IAEA (International Atomic Energy Agency); Swedish Research Council (VR) and Knut & Alice Wallenberg Foundation (KAW); Ukraine Ministry of Education and Science; United Kingdom Science and Technology Facilities Council (STFC); The United States Department of Energy, the United States National Science Foundation, the State of Texas, and the State of Ohio; Ministry of Science, Education and Sports of Croatia and Unity through Knowledge Fund, Croatia; Council of Scientific and Industrial Research (CSIR), New Delhi, India; Pontificia Universidad Católica del Perú.

References

[1] J. Rafelski, B. Müller, Strangeness production in the quark–gluon plasma, Phys. Rev. Lett. 48 (1982) 1066–1069, http://link.aps.org/doi/10.1103/PhysRevLett.48.1066, Phys. Rev. Lett. 56 (1986) 2334 (Erratum).

[2] WA97 Collaboration, E. Andersen, et al., Enhancement of central Λ, Ξ and Ω yields in Pb–Pb collisions at 158 A GeV/c, Phys. Lett. B 433 (1998) 209–216, http://www.sciencedirect.com/science/article/pii/S0370269398006893.

[3] WA97 Collaboration, E. Andersen, et al., Strangeness enhancement at mid-rapidity in Pb–Pb collisions at 158 A GeV/c, Phys. Lett. B 449 (1999) 401–406, http://www.sciencedirect.com/science/article/pii/S0370269399001409.

[4] NA49 Collaboration, S. Afanasiev, et al., Ξ^- and $\overline{\Xi}^+$ production in central Pb+Pb collisions at 158 GeV/c per nucleon, Phys. Lett. B 538 (2002) 275–281, http://www.sciencedirect.com/science/article/pii/S0370269302019706.

[5] NA57 Collaboration, F. Antinori, et al., Energy dependence of hyperon production in nucleus–nucleus collisions at SPS, Phys. Lett. B 595 (2004) 68–74, http://www.sciencedirect.com/science/article/pii/S0370269304007725.

[6] NA49 Collaboration, T. Anticic, et al., Λ and $\overline{\Lambda}$ production in central Pb–Pb collisions at 40, 80, and 158A GeV, Phys. Rev. Lett. 93 (2004) 022302, http://link.aps.org/doi/10.1103/PhysRevLett.93.022302.

[7] STAR Collaboration, J. Adams, et al., Multistrange baryon production in Au–Au collisions at $\sqrt{s_{NN}} = 130$ GeV, Phys. Rev. Lett. 92 (2004) 182301, http://link.aps.org/doi/10.1103/PhysRevLett.92.182301.

[8] STAR Collaboration, J. Adams, et al., Scaling properties of hyperon production in Au + Au collisions at $\sqrt{s_{NN}} = 200$ GeV, Phys. Rev. Lett. 98 (2007) 062301, http://link.aps.org/doi/10.1103/PhysRevLett.98.062301.

[9] STAR Collaboration, B.I. Abelev, et al., Enhanced strange baryon production in Au+Au collisions compared to $p+p$ at $\sqrt{s_{NN}} = 200$ GeV, Phys. Rev. C 77 (2008) 044908, http://link.aps.org/doi/10.1103/PhysRevC.77.044908.

[10] ALICE Collaboration, B. Abelev, et al., Multi-strange baryon production at mid-rapidity in Pb–Pb collisions at $\sqrt{s_{NN}} = 2.76$ TeV, Phys. Lett. B 728 (2014) 216–227, http://www.sciencedirect.com/science/article/pii/S0370269313009544.

[11] K. Redlich, A. Tounsi, Strangeness enhancement and energy dependence in heavy ion collisions, Eur. Phys. J. C 24 (2002) 589–594, http://link.springer.com/article/10.1007/s10052-002-0983-1.

[12] I. Kraus, J. Cleymans, H. Oeschler, K. Redlich, Particle production in p–p collisions and predictions for $\sqrt{s} = 14$ TeV at the CERN Large Hadron Collider (LHC), Phys. Rev. C 79 (2009) 014901, http://link.aps.org/doi/10.1103/PhysRevC.79.014901.

[13] F. Becattini, J. Manninen, Strangeness production from SPS to LHC, J. Phys. G, Nucl. Part. Phys. 35 (2008) 104013, http://stacks.iop.org/0954-3899/35/i=10/a=104013.

[14] J. Aichelin, K. Werner, Centrality dependence of strangeness enhancement in ultrarelativistic heavy ion collisions: a core-corona effect, Phys. Rev. C 79 (2009) 064907, arXiv:0810.4465 [nucl-th], http://link.aps.org/doi/10.1103/PhysRevC.79.064907, Phys. Rev. C 81 (2010) 029902 (Erratum).

[15] STAR Collaboration, G. Agakishiev, et al., Strangeness enhancement in Cu–Cu and Au–Au collisions at $\sqrt{s_{NN}} = 200$ GeV, Phys. Rev. Lett. 108 (2012) 072301, http://link.aps.org/doi/10.1103/PhysRevLett.108.072301.

[16] E. Schnedermann, J. Sollfrank, U.W. Heinz, Thermal phenomenology of hadrons from 200A GeV S+S collisions, Phys. Rev. C 48 (1993) 2462–2475, arXiv:nucl-th/9307020, http://link.aps.org/doi/10.1103/PhysRevC.48.2462.

[17] V. Begun, W. Florkowski, M. Rybczynski, Transverse-momentum spectra of strange particles produced in Pb + Pb collisions at $\sqrt{s_{NN}} = 2.76$ TeV in the chemical nonequilibrium model, Phys. Rev. C 90 (2014) 054912, http://link.aps.org/doi/10.1103/PhysRevC.90.054912.

[18] I. Melo, B. Tomasik, Blast wave fits with resonances to p_t spectra from nuclear collisions at the LHC, in: 15th International Conference on Strangeness in Quark Matter (SQM 2015) Dubna, Moscow region, Russia, July 6–11, 2015, 2015, arXiv:1509.05383 [nucl-th].

[19] STAR Collaboration, J. Adams, et al., Experimental and theoretical challenges in the search for the quark–gluon plasma: the STAR Collaboration's critical assessment of the evidence from RHIC collisions, Nucl. Phys. A 757 (2005) 102–183, arXiv:nucl-ex/0501009, http://www.sciencedirect.com/science/article/pii/S0375947405005294.

[20] ALICE Collaboration, The ALICE experiment at the CERN LHC, J. Instrum. 3 (2008) S08002, http://stacks.iop.org/1748-0221/3/i=08/a=S08002.

[21] ALICE Collaboration, Performance of the ALICE VZERO system, J. Instrum. 8 (2013) P10016, http://stacks.iop.org/1748-0221/8/i=10/a=P10016.

[22] ALICE Collaboration, B. Abelev, et al., Pseudorapidity density of charged particles in p + Pb collisions at $\sqrt{s_{NN}} = 5.02$ TeV, Phys. Rev. Lett. 110 (2013) 032301, http://link.aps.org/doi/10.1103/PhysRevLett.110.032301.

[23] ALICE Collaboration, J. Adam, et al., Multiplicity dependence of pion, kaon, proton and lambda production in p–Pb collisions at $\sqrt{s_{NN}} = 5.02$ TeV, Phys. Lett. B 728 (2014) 25–38, http://www.sciencedirect.com/science/article/pii/S0370269313009234.

[24] K.A. Olive, et al., Particle data group, Chin. Phys. C 38 (2014) 090001, http://stacks.iop.org/1674-1137/38/i=9/a=090001.
[25] ALICE Collaboration, B. Abelev, et al., Multi-strange baryon production in pp collisions at $\sqrt{s} = 7$ TeV with ALICE, Phys. Lett. B 712 (2012) 309–318, http://www.sciencedirect.com/science/article/pii/S037026931200528X.
[26] ALICE Collaboration, Performance of the ALICE experiment at the CERN LHC, Int. J. Mod. Phys. A 29 (2014) 1430044, http://www.worldscientific.com/doi/abs/10.1142/S0217751X14300440.
[27] S. Roesler, R. Engel, J. Ranft, The Monte Carlo event generator DPMJET-III, in: A. Kling, F. Barão, M. Nakagawa, L. Távora, P. Vaz (Eds.), Advanced Monte Carlo for Radiation Physics, Particle Transport Simulation and Applications, Springer, Berlin, Heidelberg, 2001, pp. 1033–1038, arXiv:hep-ph/0012252.
[28] R. Brun, F. Bruyant, F. Carminati, S. Giani, M. Maire, A. McPherson, G. Patrick, L. Urban, Geant detector description and simulation tool, CERN Program Library Long Writeup (1994).
[29] C. Tsallis, Possible generalization of Boltzmann–Gibbs statistics, J. Stat. Phys. 52 (1988) 479–487.
[30] T. Sjostrand, S. Mrenna, P.Z. Skands, PYTHIA 6.4 physics and manual, J. High Energy Phys. 05 (2006) 026, arXiv:hep-ph/0603175.
[31] A. Ortiz Velasquez, P. Christiansen, E. Cuautle Flores, I.A. Maldonado Cervantes, G. Paić, Color reconnection and flowlike patterns in *pp* collisions, Phys. Rev. Lett. 111 (2013) 042001, http://link.aps.org/doi/10.1103/PhysRevLett.111.042001.
[32] ALICE Collaboration, K. Aamodt, et al., Production of pions, kaons and protons in pp collisions at $\sqrt{s} = 900$ GeV with ALICE at the LHC, Eur. Phys. J. C 71 (2011) 1655, http://dx.doi.org/10.1140/epjc/s10052-011-1655-9.
[33] ALICE Collaboration, K. Aamodt, et al., Strange particle production in proton–proton collisions at $\sqrt{s} = 0.9$ TeV with ALICE at the LHC, Eur. Phys. J. C 71 (2011) 1594, http://dx.doi.org/10.1140/epjc/s10052-011-1594-5.
[34] ALICE Collaboration, J. Adam, et al., Measurement of pion, kaon and proton production in proton–proton collisions at $\sqrt{s} = 7$ TeV, Eur. Phys. J. C 75 (2015) 226, http://dx.doi.org/10.1140/epjc/s10052-015-3422-9.
[35] A. Andronic, P. Braun-Munzinger, J. Stachel, Thermal hadron production in relativistic nuclear collisions: the hadron mass spectrum, the horn, and the QCD phase transition, Phys. Lett. B 673 (2009) 142–145, http://www.sciencedirect.com/science/article/pii/S0370269309001609.
[36] S. Wheaton, J. Cleymans, M. Hauer, THERMUS — a thermal model package for ROOT, Comput. Phys. Commun. 180 (2009) 84–106, http://www.sciencedirect.com/science/article/pii/S0010465508002750.
[37] ALICE Collaboration, B.B. Abelev, et al., K^0_S and Λ production in Pb–Pb collisions at $\sqrt{s_{NN}} = 2.76$ TeV, Phys. Rev. Lett. 111 (2013) 222301, arXiv:1307.5530 [nucl-ex].

ALICE Collaboration

J. Adam [40], D. Adamová [84], M.M. Aggarwal [88], G. Aglieri Rinella [36], M. Agnello [110], N. Agrawal [48], Z. Ahammed [132], S. Ahmad [19], S.U. Ahn [68], S. Aiola [136], A. Akindinov [58], S.N. Alam [132], D. Aleksandrov [80], B. Alessandro [110], D. Alexandre [101], R. Alfaro Molina [64], A. Alici [12,104], A. Alkin [3], J.R.M. Almaraz [119], J. Alme [38], T. Alt [43], S. Altinpinar [18], I. Altsybeev [131], C. Alves Garcia Prado [120], C. Andrei [78], A. Andronic [97], V. Anguelov [94], J. Anielski [54], T. Antičić [98], F. Antinori [107], P. Antonioli [104], L. Aphecetche [113], H. Appelshäuser [53], S. Arcelli [28], R. Arnaldi [110], O.W. Arnold [37,93], I.C. Arsene [22], M. Arslandok [53], B. Audurier [113], A. Augustinus [36], R. Averbeck [97], M.D. Azmi [19], A. Badalà [106], Y.W. Baek [67], S. Bagnasco [110], R. Bailhache [53], R. Bala [91], S. Balasubramanian [136], A. Baldisseri [15], R.C. Baral [61], A.M. Barbano [27], R. Barbera [29], F. Barile [33], G.G. Barnaföldi [135], L.S. Barnby [101], V. Barret [70], P. Bartalini [7], K. Barth [36], J. Bartke [117], E. Bartsch [53], M. Basile [28], N. Bastid [70], S. Basu [132], B. Bathen [54], G. Batigne [113], A. Batista Camejo [70], B. Batyunya [66], P.C. Batzing [22], I.G. Bearden [81], H. Beck [53], C. Bedda [110], N.K. Behera [50], I. Belikov [55], F. Bellini [28], H. Bello Martinez [2], R. Bellwied [122], R. Belmont [134], E. Belmont-Moreno [64], V. Belyaev [75], P. Benacek [84], G. Bencedi [135], S. Beole [27], I. Berceanu [78], A. Bercuci [78], Y. Berdnikov [86], D. Berenyi [135], R.A. Bertens [57], D. Berzano [36], L. Betev [36], A. Bhasin [91], I.R. Bhat [91], A.K. Bhati [88], B. Bhattacharjee [45], J. Bhom [128], L. Bianchi [122], N. Bianchi [72], C. Bianchin [134,57], J. Bielčík [40], J. Bielčíková [84], A. Bilandzic [81,37,93], G. Biro [135], R. Biswas [4], S. Biswas [79], S. Bjelogrlic [57], J.T. Blair [118], D. Blau [80], C. Blume [53], F. Bock [74,94], A. Bogdanov [75], H. Bøggild [81], L. Boldizsár [135], M. Bombara [41], J. Book [53], H. Borel [15], A. Borissov [96], M. Borri [83,124], F. Bossú [65], E. Botta [27], C. Bourjau [81], P. Braun-Munzinger [97], M. Bregant [120], T. Breitner [52], T.A. Broker [53], T.A. Browning [95], M. Broz [40], E.J. Brucken [46], E. Bruna [110], G.E. Bruno [33], D. Budnikov [99], H. Buesching [53], S. Bufalino [36,27], P. Buncic [36], O. Busch [94,128], Z. Buthelezi [65], J.B. Butt [16], J.T. Buxton [20], D. Caffarri [36], X. Cai [7], H. Caines [136], L. Calero Diaz [72], A. Caliva [57], E. Calvo Villar [102], P. Camerini [26], F. Carena [36], W. Carena [36], F. Carnesecchi [28], J. Castillo Castellanos [15], A.J. Castro [125], E.A.R. Casula [25], C. Ceballos Sanchez [9], P. Cerello [110], J. Cerkala [115], B. Chang [123], S. Chapeland [36], M. Chartier [124], J.L. Charvet [15], S. Chattopadhyay [132], S. Chattopadhyay [100], A. Chauvin [93,37], V. Chelnokov [3], M. Cherney [87], C. Cheshkov [130], B. Cheynis [130], V. Chibante Barroso [36], D.D. Chinellato [121], S. Cho [50], P. Chochula [36], K. Choi [96], M. Chojnacki [81], S. Choudhury [132], P. Christakoglou [82], C.H. Christensen [81], P. Christiansen [34], T. Chujo [128], S.U. Chung [96], C. Cicalo [105], L. Cifarelli [12,28], F. Cindolo [104], J. Cleymans [90], F. Colamaria [33], D. Colella [59,36], A. Collu [74,25], M. Colocci [28], G. Conesa Balbastre [71], Z. Conesa del Valle [51], M.E. Connors [136,ii], J.G. Contreras [40], T.M. Cormier [85], Y. Corrales Morales [110], I. Cortés Maldonado [2], P. Cortese [32], M.R. Cosentino [120], F. Costa [36], P. Crochet [70], R. Cruz Albino [11], E. Cuautle [63], L. Cunqueiro [54,36], T. Dahms [93,37], A. Dainese [107], A. Danu [62], D. Das [100], I. Das [100,51], S. Das [4], A. Dash [121,79], S. Dash [48], S. De [120], A. De Caro [12,31], G. de Cataldo [103], C. de Conti [120], J. de Cuveland [43], A. De Falco [25], D. De Gruttola [12,31], N. De Marco [110], S. De Pasquale [31], A. Deisting [97,94], A. Deloff [77], E. Dénes [135,i], C. Deplano [82], P. Dhankher [48], D. Di Bari [33], A. Di Mauro [36], P. Di Nezza [72], M.A. Diaz Corchero [10], T. Dietel [90], P. Dillenseger [53], R. Divià [36], Ø. Djuvsland [18], A. Dobrin [57,82],

D. Domenicis Gimenez [120], B. Dönigus [53], O. Dordic [22], T. Drozhzhova [53], A.K. Dubey [132], A. Dubla [57], L. Ducroux [130], P. Dupieux [70], R.J. Ehlers [136], D. Elia [103], E. Endress [102], H. Engel [52], E. Epple [136], B. Erazmus [113], I. Erdemir [53], F. Erhardt [129], B. Espagnon [51], M. Estienne [113], S. Esumi [128], J. Eum [96], D. Evans [101], S. Evdokimov [111], G. Eyyubova [40], L. Fabbietti [93,37], D. Fabris [107], J. Faivre [71], A. Fantoni [72], M. Fasel [74], L. Feldkamp [54], A. Feliciello [110], G. Feofilov [131], J. Ferencei [84], A. Fernández Téllez [2], E.G. Ferreiro [17], A. Ferretti [27], A. Festanti [30], V.J.G. Feuillard [15,70], J. Figiel [117], M.A.S. Figueredo [124,120], S. Filchagin [99], D. Finogeev [56], F.M. Fionda [25], E.M. Fiore [33], M.G. Fleck [94], M. Floris [36], S. Foertsch [65], P. Foka [97], S. Fokin [80], E. Fragiacomo [109], A. Francescon [36,30], U. Frankenfeld [97], G.G. Fronze [27], U. Fuchs [36], C. Furget [71], A. Furs [56], M. Fusco Girard [31], J.J. Gaardhøje [81], M. Gagliardi [27], A.M. Gago [102], M. Gallio [27], D.R. Gangadharan [74], P. Ganoti [89], C. Gao [7], C. Garabatos [97], E. Garcia-Solis [13], C. Gargiulo [36], P. Gasik [93,37], E.F. Gauger [118], M. Germain [113], A. Gheata [36], M. Gheata [36,62], P. Ghosh [132], S.K. Ghosh [4], P. Gianotti [72], P. Giubellino [110,36], P. Giubilato [30], E. Gladysz-Dziadus [117], P. Glässel [94], D.M. Goméz Coral [64], A. Gomez Ramirez [52], V. Gonzalez [10], P. González-Zamora [10], S. Gorbunov [43], L. Görlich [117], S. Gotovac [116], V. Grabski [64], O.A. Grachov [136], L.K. Graczykowski [133], K.L. Graham [101], A. Grelli [57], A. Grigoras [36], C. Grigoras [36], V. Grigoriev [75], A. Grigoryan [1], S. Grigoryan [66], B. Grinyov [3], N. Grion [109], J.M. Gronefeld [97], J.F. Grosse-Oetringhaus [36], J.-Y. Grossiord [130], R. Grosso [97], F. Guber [56], R. Guernane [71], B. Guerzoni [28], K. Gulbrandsen [81], T. Gunji [127], A. Gupta [91], R. Gupta [91], R. Haake [54], Ø. Haaland [18], C. Hadjidakis [51], M. Haiduc [62], H. Hamagaki [127], G. Hamar [135], J.C. Hamon [55], J.W. Harris [136], A. Harton [13], D. Hatzifotiadou [104], S. Hayashi [127], S.T. Heckel [53], H. Helstrup [38], A. Herghelegiu [78], G. Herrera Corral [11], B.A. Hess [35], K.F. Hetland [38], H. Hillemanns [36], B. Hippolyte [55], D. Horak [40], R. Hosokawa [128], P. Hristov [36], M. Huang [18], T.J. Humanic [20], N. Hussain [45], T. Hussain [19], D. Hutter [43], D.S. Hwang [21], R. Ilkaev [99], M. Inaba [128], E. Incani [25], M. Ippolitov [75,80], M. Irfan [19], M. Ivanov [97], V. Ivanov [86], V. Izucheev [111], N. Jacazio [28], P.M. Jacobs [74], M.B. Jadhav [48], S. Jadlovska [115], J. Jadlovsky [115,59], C. Jahnke [120], M.J. Jakubowska [133], H.J. Jang [68], M.A. Janik [133], P.H.S.Y. Jayarathna [122], C. Jena [30], S. Jena [122], R.T. Jimenez Bustamante [97], P.G. Jones [101], H. Jung [44], A. Jusko [101], P. Kalinak [59], A. Kalweit [36], J. Kamin [53], J.H. Kang [137], V. Kaplin [75], S. Kar [132], A. Karasu Uysal [69], O. Karavichev [56], T. Karavicheva [56], L. Karayan [97,94], E. Karpechev [56], U. Kebschull [52], R. Keidel [138], D.L.D. Keijdener [57], M. Keil [36], M. Mohisin Khan [19,iii], P. Khan [100], S.A. Khan [132], A. Khanzadeev [86], Y. Kharlov [111], B. Kileng [38], D.W. Kim [44], D.J. Kim [123], D. Kim [137], H. Kim [137], J.S. Kim [44], M. Kim [44], M. Kim [137], S. Kim [21], T. Kim [137], S. Kirsch [43], I. Kisel [43], S. Kiselev [58], A. Kisiel [133], G. Kiss [135], J.L. Klay [6], C. Klein [53], J. Klein [36], C. Klein-Bösing [54], S. Klewin [94], A. Kluge [36], M.L. Knichel [94], A.G. Knospe [118], C. Kobdaj [114], M. Kofarago [36], T. Kollegger [97], A. Kolojvari [131], V. Kondratiev [131], N. Kondratyeva [75], E. Kondratyuk [111], A. Konevskikh [56], M. Kopcik [115], M. Kour [91], C. Kouzinopoulos [36], O. Kovalenko [77], V. Kovalenko [131], M. Kowalski [117], G. Koyithatta Meethaleveedu [48], I. Králik [59], A. Kravčáková [41], M. Kretz [43], M. Krivda [59,101], F. Krizek [84], E. Kryshen [86,36], M. Krzewicki [43], A.M. Kubera [20], V. Kučera [84], C. Kuhn [55], P.G. Kuijer [82], A. Kumar [91], J. Kumar [48], L. Kumar [88], S. Kumar [48], P. Kurashvili [77], A. Kurepin [56], A.B. Kurepin [56], A. Kuryakin [99], M.J. Kweon [50], Y. Kwon [137], S.L. La Pointe [110], P. La Rocca [29], P. Ladron de Guevara [11], C. Lagana Fernandes [120], I. Lakomov [36], R. Langoy [42], C. Lara [52], A. Lardeux [15], A. Lattuca [27], E. Laudi [36], R. Lea [26], L. Leardini [94], G.R. Lee [101], S. Lee [137], F. Lehas [82], R.C. Lemmon [83], V. Lenti [103], E. Leogrande [57], I. León Monzón [119], H. León Vargas [64], M. Leoncino [27], P. Lévai [135], S. Li [7,70], X. Li [14], J. Lien [42], R. Lietava [101], S. Lindal [22], V. Lindenstruth [43], C. Lippmann [97], M.A. Lisa [20], H.M. Ljunggren [34], D.F. Lodato [57], P.I. Loenne [18], V. Loginov [75], C. Loizides [74], X. Lopez [70], E. López Torres [9], A. Lowe [135], P. Luettig [53], M. Lunardon [30], G. Luparello [26], T.H. Lutz [136], A. Maevskaya [56], M. Mager [36], S. Mahajan [91], S.M. Mahmood [22], A. Maire [55], R.D. Majka [136], M. Malaev [86], I. Maldonado Cervantes [63], L. Malinina [66,iv], D. Mal'Kevich [58], P. Malzacher [97], A. Mamonov [99], V. Manko [80], F. Manso [70], V. Manzari [36,103], M. Marchisone [65,126,27], J. Mareš [60], G.V. Margagliotti [26], A. Margotti [104], J. Margutti [57], A. Marín [97], C. Markert [118], M. Marquard [53], N.A. Martin [97], J. Martin Blanco [113], P. Martinengo [36], M.I. Martínez [2], G. Martínez García [113], M. Martinez Pedreira [36], A. Mas [120], S. Masciocchi [97], M. Masera [27], A. Masoni [105], L. Massacrier [113], A. Mastroserio [33], A. Matyja [117], C. Mayer [36,117], J. Mazer [125], M.A. Mazzoni [108], D. Mcdonald [122], F. Meddi [24], Y. Melikyan [75], A. Menchaca-Rocha [64], E. Meninno [31], J. Mercado Pérez [94], M. Meres [39], Y. Miake [128], M.M. Mieskolainen [46], K. Mikhaylov [66,58], L. Milano [74,36], J. Milosevic [22], L.M. Minervini [103,23], A. Mischke [57], A.N. Mishra [49], D. Miśkowiec [97], J. Mitra [132], C.M. Mitu [62],

N. Mohammadi [57], B. Mohanty [79,132], L. Molnar [55,113], L. Montaño Zetina [11], E. Montes [10], D.A. Moreira De Godoy [54,113], L.A.P. Moreno [2], S. Moretto [30], A. Morreale [113], A. Morsch [36], V. Muccifora [72], E. Mudnic [116], D. Mühlheim [54], S. Muhuri [132], M. Mukherjee [132], J.D. Mulligan [136], M.G. Munhoz [120], R.H. Munzer [93,37], H. Murakami [127], S. Murray [65], L. Musa [36], J. Musinsky [59], B. Naik [48], R. Nair [77], B.K. Nandi [48], R. Nania [104], E. Nappi [103], M.U. Naru [16], H. Natal da Luz [120], C. Nattrass [125], S.R. Navarro [2], K. Nayak [79], R. Nayak [48], T.K. Nayak [132], S. Nazarenko [99], A. Nedosekin [58], L. Nellen [63], F. Ng [122], M. Nicassio [97], M. Niculescu [62], J. Niedziela [36], B.S. Nielsen [81], S. Nikolaev [80], S. Nikulin [80], V. Nikulin [86], F. Noferini [104,12], P. Nomokonov [66], G. Nooren [57], J.C.C. Noris [2], J. Norman [124], A. Nyanin [80], J. Nystrand [18], H. Oeschler [94], S. Oh [136], S.K. Oh [67], A. Ohlson [36], A. Okatan [69], T. Okubo [47], L. Olah [135], J. Oleniacz [133], A.C. Oliveira Da Silva [120], M.H. Oliver [136], J. Onderwaater [97], C. Oppedisano [110], R. Orava [46], A. Ortiz Velasquez [63], A. Oskarsson [34], J. Otwinowski [117], K. Oyama [94,76], M. Ozdemir [53], Y. Pachmayer [94], P. Pagano [31], G. Paić [63], S.K. Pal [132], J. Pan [134], A.K. Pandey [48], P. Papcun [115], V. Papikyan [1], G.S. Pappalardo [106], P. Pareek [49], W.J. Park [97], S. Parmar [88], A. Passfeld [54], V. Paticchio [103], R.N. Patra [132], B. Paul [100], H. Pei [7], T. Peitzmann [57], H. Pereira Da Costa [15], D. Peresunko [80,75], C.E. Pérez Lara [82], E. Perez Lezama [53], V. Peskov [53], Y. Pestov [5], V. Petráček [40], V. Petrov [111], M. Petrovici [78], C. Petta [29], S. Piano [109], M. Pikna [39], P. Pillot [113], L.O.D.L. Pimentel [81], O. Pinazza [36,104], L. Pinsky [122], D.B. Piyarathna [122], M. Płoskoń [74], M. Planinic [129], J. Pluta [133], S. Pochybova [135], P.L.M. Podesta-Lerma [119], M.G. Poghosyan [85,87], B. Polichtchouk [111], N. Poljak [129], W. Poonsawat [114], A. Pop [78], S. Porteboeuf-Houssais [70], J. Porter [74], J. Pospisil [84], S.K. Prasad [4], R. Preghenella [104,36], F. Prino [110], C.A. Pruneau [134], I. Pshenichnov [56], M. Puccio [27], G. Puddu [25], P. Pujahari [134], V. Punin [99], J. Putschke [134], H. Qvigstad [22], A. Rachevski [109], S. Raha [4], S. Rajput [91], J. Rak [123], A. Rakotozafindrabe [15], L. Ramello [32], F. Rami [55], R. Raniwala [92], S. Raniwala [92], S.S. Räsänen [46], B.T. Rascanu [53], D. Rathee [88], K.F. Read [125,85], K. Redlich [77], R.J. Reed [134], A. Rehman [18], P. Reichelt [53], F. Reidt [94,36], X. Ren [7], R. Renfordt [53], A.R. Reolon [72], A. Reshetin [56], J.-P. Revol [12], K. Reygers [94], V. Riabov [86], R.A. Ricci [73], T. Richert [34], M. Richter [22], P. Riedler [36], W. Riegler [36], F. Riggi [29], C. Ristea [62], E. Rocco [57], M. Rodríguez Cahuantzi [2,11], A. Rodriguez Manso [82], K. Røed [22], E. Rogochaya [66], D. Rohr [43], D. Röhrich [18], R. Romita [124], F. Ronchetti [72,36], L. Ronflette [113], P. Rosnet [70], A. Rossi [30,36], F. Roukoutakis [89], A. Roy [49], C. Roy [55], P. Roy [100], A.J. Rubio Montero [10], R. Rui [26], R. Russo [27], E. Ryabinkin [80], Y. Ryabov [86], A. Rybicki [117], S. Sadovsky [111], K. Šafařík [36], B. Sahlmuller [53], P. Sahoo [49], R. Sahoo [49], S. Sahoo [61], P.K. Sahu [61], J. Saini [132], S. Sakai [72], M.A. Saleh [134], J. Salzwedel [20], S. Sambyal [91], V. Samsonov [86], L. Šándor [59], A. Sandoval [64], M. Sano [128], D. Sarkar [132], P. Sarma [45], E. Scapparone [104], F. Scarlassara [30], C. Schiaua [78], R. Schicker [94], C. Schmidt [97], H.R. Schmidt [35], S. Schuchmann [53], J. Schukraft [36], M. Schulc [40], T. Schuster [136], Y. Schutz [36,113], K. Schwarz [97], K. Schweda [97], G. Scioli [28], E. Scomparin [110], R. Scott [125], M. Šefčík [41], J.E. Seger [87], Y. Sekiguchi [127], D. Sekihata [47], I. Selyuzhenkov [97], K. Senosi [65], S. Senyukov [3,36], E. Serradilla [10,64], A. Sevcenco [62], A. Shabanov [56], A. Shabetai [113], O. Shadura [3], R. Shahoyan [36], A. Shangaraev [111], A. Sharma [91], M. Sharma [91], M. Sharma [91], N. Sharma [125], K. Shigaki [47], K. Shtejer [9,27], Y. Sibiriak [80], S. Siddhanta [105], K.M. Sielewicz [36], T. Siemiarczuk [77], D. Silvermyr [34], C. Silvestre [71], G. Simatovic [129], G. Simonetti [36], R. Singaraju [132], R. Singh [79], S. Singha [132,79], V. Singhal [132], B.C. Sinha [132], T. Sinha [100], B. Sitar [39], M. Sitta [32], T.B. Skaali [22], M. Slupecki [123], N. Smirnov [136], R.J.M. Snellings [57], T.W. Snellman [123], C. Søgaard [34], J. Song [96], M. Song [137], Z. Song [7], F. Soramel [30], S. Sorensen [125], R.D. de Souza [121], F. Sozzi [97], M. Spacek [40], E. Spiriti [72], I. Sputowska [117], M. Spyropoulou-Stassinaki [89], J. Stachel [94], I. Stan [62], P. Stankus [85], G. Stefanek [77], E. Stenlund [34], G. Steyn [65], J.H. Stiller [94], D. Stocco [113], P. Strmen [39], A.A.P. Suaide [120], T. Sugitate [47], C. Suire [51], M. Suleymanov [16], M. Suljic [26,i], R. Sultanov [58], M. Šumbera [84], A. Szabo [39], A. Szanto de Toledo [120,i], I. Szarka [39], A. Szczepankiewicz [36], M. Szymanski [133], U. Tabassam [16], J. Takahashi [121], G.J. Tambave [18], N. Tanaka [128], M.A. Tangaro [33], M. Tarhini [51], M. Tariq [19], M.G. Tarzila [78], A. Tauro [36], G. Tejeda Muñoz [2], A. Telesca [36], K. Terasaki [127], C. Terrevoli [30], B. Teyssier [130], J. Thäder [74], D. Thomas [118], R. Tieulent [130], A.R. Timmins [122], A. Toia [53], S. Trogolo [27], G. Trombetta [33], V. Trubnikov [3], W.H. Trzaska [123], T. Tsuji [127], A. Tumkin [99], R. Turrisi [107], T.S. Tveter [22], K. Ullaland [18], A. Uras [130], G.L. Usai [25], A. Utrobicic [129], M. Vajzer [84], M. Vala [59], L. Valencia Palomo [70], S. Vallero [27], J. Van Der Maarel [57], J.W. Van Hoorne [36], M. van Leeuwen [57], T. Vanat [84], P. Vande Vyvre [36], D. Varga [135], A. Vargas [2], M. Vargyas [123], R. Varma [48], M. Vasileiou [89], A. Vasiliev [80], A. Vauthier [71], V. Vechernin [131], A.M. Veen [57], M. Veldhoen [57], A. Velure [18],

M. Venaruzzo [73], E. Vercellin [27], S. Vergara Limón [2], R. Vernet [8], M. Verweij [134], L. Vickovic [116], G. Viesti [30,i], J. Viinikainen [123], Z. Vilakazi [126], O. Villalobos Baillie [101], A. Villatoro Tello [2], A. Vinogradov [80], L. Vinogradov [131], Y. Vinogradov [99,i], T. Virgili [31], V. Vislavicius [34], Y.P. Viyogi [132], A. Vodopyanov [66], M.A. Völkl [94], K. Voloshin [58], S.A. Voloshin [134], G. Volpe [135], B. von Haller [36], I. Vorobyev [37,93], D. Vranic [97,36], J. Vrláková [41], B. Vulpescu [70], B. Wagner [18], J. Wagner [97], H. Wang [57], M. Wang [7,113], D. Watanabe [128], Y. Watanabe [127], M. Weber [36,112], S.G. Weber [97], D.F. Weiser [94], J.P. Wessels [54], U. Westerhoff [54], A.M. Whitehead [90], J. Wiechula [35], J. Wikne [22], M. Wilde [54], G. Wilk [77], J. Wilkinson [94], M.C.S. Williams [104], B. Windelband [94], M. Winn [94], C.G. Yaldo [134], H. Yang [57], P. Yang [7], S. Yano [47], C. Yasar [69], Z. Yin [7], H. Yokoyama [128], I.-K. Yoo [96], J.H. Yoon [50], V. Yurchenko [3], I. Yushmanov [80], A. Zaborowska [133], V. Zaccolo [81], A. Zaman [16], C. Zampolli [104], H.J.C. Zanoli [120], S. Zaporozhets [66], N. Zardoshti [101], A. Zarochentsev [131], P. Závada [60], N. Zaviyalov [99], H. Zbroszczyk [133], I.S. Zgura [62], M. Zhalov [86], H. Zhang [18], X. Zhang [74], Y. Zhang [7], C. Zhang [57], Z. Zhang [7], C. Zhao [22], N. Zhigareva [58], D. Zhou [7], Y. Zhou [81], Z. Zhou [18], H. Zhu [18], J. Zhu [113,7], A. Zichichi [28,12], A. Zimmermann [94], M.B. Zimmermann [54,36], G. Zinovjev [3], M. Zyzak [43]

[1] *A.I. Alikhanyan National Science Laboratory (Yerevan Physics Institute) Foundation, Yerevan, Armenia*
[2] *Benemérita Universidad Autónoma de Puebla, Puebla, Mexico*
[3] *Bogolyubov Institute for Theoretical Physics, Kiev, Ukraine*
[4] *Bose Institute, Department of Physics and Centre for Astroparticle Physics and Space Science (CAPSS), Kolkata, India*
[5] *Budker Institute for Nuclear Physics, Novosibirsk, Russia*
[6] *California Polytechnic State University, San Luis Obispo, CA, United States*
[7] *Central China Normal University, Wuhan, China*
[8] *Centre de Calcul de l'IN2P3, Villeurbanne, France*
[9] *Centro de Aplicaciones Tecnológicas y Desarrollo Nuclear (CEADEN), Havana, Cuba*
[10] *Centro de Investigaciones Energéticas Medioambientales y Tecnológicas (CIEMAT), Madrid, Spain*
[11] *Centro de Investigación y de Estudios Avanzados (CINVESTAV), Mexico City and Mérida, Mexico*
[12] *Centro Fermi – Museo Storico della Fisica e Centro Studi e Ricerche "Enrico Fermi", Rome, Italy*
[13] *Chicago State University, Chicago, IL, USA*
[14] *China Institute of Atomic Energy, Beijing, China*
[15] *Commissariat à l'Energie Atomique, IRFU, Saclay, France*
[16] *COMSATS Institute of Information Technology (CIIT), Islamabad, Pakistan*
[17] *Departamento de Física de Partículas and IGFAE, Universidad de Santiago de Compostela, Santiago de Compostela, Spain*
[18] *Department of Physics and Technology, University of Bergen, Bergen, Norway*
[19] *Department of Physics, Aligarh Muslim University, Aligarh, India*
[20] *Department of Physics, Ohio State University, Columbus, OH, United States*
[21] *Department of Physics, Sejong University, Seoul, South Korea*
[22] *Department of Physics, University of Oslo, Oslo, Norway*
[23] *Dipartimento di Elettrotecnica ed Elettronica del Politecnico, Bari, Italy*
[24] *Dipartimento di Fisica dell'Università 'La Sapienza' and Sezione INFN, Rome, Italy*
[25] *Dipartimento di Fisica dell'Università and Sezione INFN, Cagliari, Italy*
[26] *Dipartimento di Fisica dell'Università and Sezione INFN, Trieste, Italy*
[27] *Dipartimento di Fisica dell'Università and Sezione INFN, Turin, Italy*
[28] *Dipartimento di Fisica e Astronomia dell'Università and Sezione INFN, Bologna, Italy*
[29] *Dipartimento di Fisica e Astronomia dell'Università and Sezione INFN, Catania, Italy*
[30] *Dipartimento di Fisica e Astronomia dell'Università and Sezione INFN, Padova, Italy*
[31] *Dipartimento di Fisica 'E.R. Caianiello' dell'Università and Gruppo Collegato INFN, Salerno, Italy*
[32] *Dipartimento di Scienze e Innovazione Tecnologica dell'Università del Piemonte Orientale and Gruppo Collegato INFN, Alessandria, Italy*
[33] *Dipartimento Interateneo di Fisica 'M. Merlin' and Sezione INFN, Bari, Italy*
[34] *Division of Experimental High Energy Physics, University of Lund, Lund, Sweden*
[35] *Eberhard Karls Universität Tübingen, Tübingen, Germany*
[36] *European Organization for Nuclear Research (CERN), Geneva, Switzerland*
[37] *Excellence Cluster Universe, Technische Universität München, Munich, Germany*
[38] *Faculty of Engineering, Bergen University College, Bergen, Norway*
[39] *Faculty of Mathematics, Physics and Informatics, Comenius University, Bratislava, Slovakia*
[40] *Faculty of Nuclear Sciences and Physical Engineering, Czech Technical University in Prague, Prague, Czech Republic*
[41] *Faculty of Science, P.J. Šafárik University, Košice, Slovakia*
[42] *Faculty of Technology, Buskerud and Vestfold University College, Vestfold, Norway*
[43] *Frankfurt Institute for Advanced Studies, Johann Wolfgang Goethe-Universität Frankfurt, Frankfurt, Germany*
[44] *Gangneung-Wonju National University, Gangneung, South Korea*
[45] *Gauhati University, Department of Physics, Guwahati, India*
[46] *Helsinki Institute of Physics (HIP), Helsinki, Finland*
[47] *Hiroshima University, Hiroshima, Japan*
[48] *Indian Institute of Technology Bombay (IIT), Mumbai, India*
[49] *Indian Institute of Technology Indore, Indore (IITI), India*
[50] *Inha University, Incheon, South Korea*
[51] *Institut de Physique Nucléaire d'Orsay (IPNO), Université Paris-Sud, CNRS-IN2P3, Orsay, France*
[52] *Institut für Informatik, Johann Wolfgang Goethe-Universität Frankfurt, Frankfurt, Germany*
[53] *Institut für Kernphysik, Johann Wolfgang Goethe-Universität Frankfurt, Frankfurt, Germany*
[54] *Institut für Kernphysik, Westfälische Wilhelms-Universität Münster, Münster, Germany*
[55] *Institut Pluridisciplinaire Hubert Curien (IPHC), Université de Strasbourg, CNRS-IN2P3, Strasbourg, France*
[56] *Institute for Nuclear Research, Academy of Sciences, Moscow, Russia*
[57] *Institute for Subatomic Physics of Utrecht University, Utrecht, Netherlands*

[58] Institute for Theoretical and Experimental Physics, Moscow, Russia
[59] Institute of Experimental Physics, Slovak Academy of Sciences, Košice, Slovakia
[60] Institute of Physics, Academy of Sciences of the Czech Republic, Prague, Czech Republic
[61] Institute of Physics, Bhubaneswar, India
[62] Institute of Space Science (ISS), Bucharest, Romania
[63] Instituto de Ciencias Nucleares, Universidad Nacional Autónoma de México, Mexico City, Mexico
[64] Instituto de Física, Universidad Nacional Autónoma de México, Mexico City, Mexico
[65] iThemba LABS, National Research Foundation, Somerset West, South Africa
[66] Joint Institute for Nuclear Research (JINR), Dubna, Russia
[67] Konkuk University, Seoul, South Korea
[68] Korea Institute of Science and Technology Information, Daejeon, South Korea
[69] KTO Karatay University, Konya, Turkey
[70] Laboratoire de Physique Corpusculaire (LPC), Clermont Université, Université Blaise Pascal, CNRS-IN2P3, Clermont-Ferrand, France
[71] Laboratoire de Physique Subatomique et de Cosmologie, Université Grenoble-Alpes, CNRS-IN2P3, Grenoble, France
[72] Laboratori Nazionali di Frascati, INFN, Frascati, Italy
[73] Laboratori Nazionali di Legnaro, INFN, Legnaro, Italy
[74] Lawrence Berkeley National Laboratory, Berkeley, CA, United States
[75] Moscow Engineering Physics Institute, Moscow, Russia
[76] Nagasaki Institute of Applied Science, Nagasaki, Japan
[77] National Centre for Nuclear Studies, Warsaw, Poland
[78] National Institute for Physics and Nuclear Engineering, Bucharest, Romania
[79] National Institute of Science Education and Research, Bhubaneswar, India
[80] National Research Centre Kurchatov Institute, Moscow, Russia
[81] Niels Bohr Institute, University of Copenhagen, Copenhagen, Denmark
[82] Nikhef, Nationaal instituut voor subatomaire fysica, Amsterdam, Netherlands
[83] Nuclear Physics Group, STFC Daresbury Laboratory, Daresbury, United Kingdom
[84] Nuclear Physics Institute, Academy of Sciences of the Czech Republic, Řež u Prahy, Czech Republic
[85] Oak Ridge National Laboratory, Oak Ridge, TN, United States
[86] Petersburg Nuclear Physics Institute, Gatchina, Russia
[87] Physics Department, Creighton University, Omaha, NE, United States
[88] Physics Department, Panjab University, Chandigarh, India
[89] Physics Department, University of Athens, Athens, Greece
[90] Physics Department, University of Cape Town, Cape Town, South Africa
[91] Physics Department, University of Jammu, Jammu, India
[92] Physics Department, University of Rajasthan, Jaipur, India
[93] Physik Department, Technische Universität München, Munich, Germany
[94] Physikalisches Institut, Ruprecht-Karls-Universität Heidelberg, Heidelberg, Germany
[95] Purdue University, West Lafayette, IN, United States
[96] Pusan National University, Pusan, South Korea
[97] Research Division and ExtreMe Matter Institute EMMI, GSI Helmholtzzentrum für Schwerionenforschung, Darmstadt, Germany
[98] Rudjer Bošković Institute, Zagreb, Croatia
[99] Russian Federal Nuclear Center (VNIIEF), Sarov, Russia
[100] Saha Institute of Nuclear Physics, Kolkata, India
[101] School of Physics and Astronomy, University of Birmingham, Birmingham, United Kingdom
[102] Sección Física, Departamento de Ciencias, Pontificia Universidad Católica del Perú, Lima, Peru
[103] Sezione INFN, Bari, Italy
[104] Sezione INFN, Bologna, Italy
[105] Sezione INFN, Cagliari, Italy
[106] Sezione INFN, Catania, Italy
[107] Sezione INFN, Padova, Italy
[108] Sezione INFN, Rome, Italy
[109] Sezione INFN, Trieste, Italy
[110] Sezione INFN, Turin, Italy
[111] SSC IHEP of NRC Kurchatov institute, Protvino, Russia
[112] Stefan Meyer Institut für Subatomare Physik (SMI), Vienna, Austria
[113] SUBATECH, Ecole des Mines de Nantes, Université de Nantes, CNRS-IN2P3, Nantes, France
[114] Suranaree University of Technology, Nakhon Ratchasima, Thailand
[115] Technical University of Košice, Košice, Slovakia
[116] Technical University of Split FESB, Split, Croatia
[117] The Henryk Niewodniczanski Institute of Nuclear Physics, Polish Academy of Sciences, Cracow, Poland
[118] The University of Texas at Austin, Physics Department, Austin, TX, USA
[119] Universidad Autónoma de Sinaloa, Culiacán, Mexico
[120] Universidade de São Paulo (USP), São Paulo, Brazil
[121] Universidade Estadual de Campinas (UNICAMP), Campinas, Brazil
[122] University of Houston, Houston, TX, United States
[123] University of Jyväskylä, Jyväskylä, Finland
[124] University of Liverpool, Liverpool, United Kingdom
[125] University of Tennessee, Knoxville, TN, United States
[126] University of the Witwatersrand, Johannesburg, South Africa
[127] University of Tokyo, Tokyo, Japan
[128] University of Tsukuba, Tsukuba, Japan
[129] University of Zagreb, Zagreb, Croatia
[130] Université de Lyon, Université Lyon 1, CNRS/IN2P3, IPN-Lyon, Villeurbanne, France
[131] V. Fock Institute for Physics, St. Petersburg State University, St. Petersburg, Russia
[132] Variable Energy Cyclotron Centre, Kolkata, India
[133] Warsaw University of Technology, Warsaw, Poland
[134] Wayne State University, Detroit, MI, United States
[135] Wigner Research Centre for Physics, Hungarian Academy of Sciences, Budapest, Hungary
[136] Yale University, New Haven, CT, United States

[137] *Yonsei University, Seoul, South Korea*
[138] *Zentrum für Technologietransfer und Telekommunikation (ZTT), Fachhochschule Worms, Worms, Germany*

[i] Deceased.
[ii] Also at: Georgia State University, Atlanta, Georgia, United States.
[iii] Also at: Department of Applied Physics, Aligarh Muslim University, Aligarh, India.
[iv] Also at: M.V. Lomonosov Moscow State University, D.V. Skobeltsyn Institute of Nuclear Physics, Moscow, Russia.

Bibliography

[1] Didier Alexandre. Multi-strange baryon production in pp, pPb and PbPb collisions measured with ALICE at the LHC. *Nucl. Phys.*, A931:1093–1097, 2014.

[2] Jaroslav Adam et al. Multi-strange baryon production in p-Pb collisions at $\sqrt{s_{\mathbf{NN}}} = 5.02$ TeV. *Phys. Lett.*, B758:389–401, 2016.

[3] K. Aamodt et al. The ALICE experiment at the CERN LHC. *JINST*, 3:S08002, 2008.

[4] Lyndon Evans and Philip Bryant. LHC Machine. *JINST*, 3:S08001, 2008.

[5] CERN Press Release. New State of Matter created at CERN, 2000. `http://press-archive.web.cern.ch/press-archive/PressReleases/Releases2000/PR01.00EQuarkGluonMatter.html`.

[6] John C. Collins and M. J. Perry. Superdense Matter: Neutrons Or Asymptotically Free Quarks? *Phys. Rev. Lett.*, 34:1353, 1975.

[7] Murray Gell-Mann. A Schematic Model of Baryons and Mesons. *Phys.Lett.*, 8:214–215, 1964.

[8] Murray Gell-Mann. A Schematic Model of Baryons and Mesons. *Phys.Lett.*, 8:214–215, 1964.

[9] I.S. Hughes. *Elementary particles*. Cambridge, 1972.

[10] O. W. Greenberg. Spin and Unitary Spin Independence in a Paraquark Model of Baryons and Mesons. *Phys. Rev. Lett.*, 13:598–602, 1964.

[11] L. Montanet et al. Review of particle properties. Particle Data Group. *Phys. Rev.*, D50:1173–1823, 1994.

[12] Raymond Brock et al. Handbook of perturbative QCD: Version 1.0. *Rev. Mod. Phys.*, 67:157–248, 1995.

[13] S. Bethke. Determination of the QCD coupling α_s. *J. Phys.*, G26:R27, 2000.

[14] S. Chatrchyan et al. The CMS experiment at the CERN LHC. *JINST*, 3:S08004, 2008.

[15] Vardan Khachatryan et al. Measurement of the inclusive 3-jet production differential cross section in protonproton collisions at 7 TeV and determination of the strong coupling constant in the TeV range. *Eur. Phys. J.*, C75(5):186, 2015.

[16] Shaw G. Martin B.R. *Particle Physics*. John Wiley and Sons Ltd, third edition edition, 2008.

[17] Helmut Satz. Colour deconfinement and quarkonium binding. *J. Phys.*, G32:R25, 2006.

[18] F. Karsch and E. Laermann. Thermodynamics and in medium hadron properties from lattice QCD. 2003.

[19] Ulrich W. Heinz. Concepts of heavy ion physics. In *2003 CERN-CLAF School of High-Energy Physics, San Miguel Regla, Mexico, 1-14 June 2003*, pages 165–238, 2004. http://doc.cern.ch/yellowrep/CERN-2004-001.

[20] J. Engels, F. Karsch, H. Satz, and I. Montvay. High Temperature SU(2) Gluon Matter on the Lattice. *Phys. Lett.*, B101:89, 1981. [,293(1980)].

[21] Frithjof Karsch. Lattice results on QCD thermodynamics. *Nucl. Phys.*, A698:199–208, 2002.

[22] R. Sekhar Chivukula. The Origin of mass in QCD. *eConf*, C040802:L010, 2004.

[23] Frithjof Karsch. Deconfinement and chiral symmetry restoration. In *Strong and electroweak matter '98. Proceedings, Conference, SEWM'98, Copenhagen, Denmark, December 2-5, 1998*, 1998. `http://alice.cern.ch/format/showfull?sysnb=0307866`.

[24] Helen Caines. What's interesting about strangeness production?: An Overview of recent results. *J. Phys.*, G31:S101–S118, 2005.

[25] Johann Rafelski and Berndt Muller. Strangeness Production in the Quark - Gluon Plasma. *Phys. Rev. Lett.*, 48:1066, 1982. [Erratum: Phys. Rev. Lett.56,2334(1986)].

[26] *Olive, K.A.* et al. *(Particle Data Group), Chinese Physics C**38**, 090001 (2014).*

[27] Martin Lavelle and David McMullan. Constituent quarks from QCD. *Phys. Rept.*, 279:1–65, 1997.

[28] Josef Sollfrank and Ulrich W. Heinz. The Role of strangeness in ultrarelativistic nuclear collisions. 1995.

[29] Jan Rafelski. Strangeness and Quark–Gluon Plasma. *Acta Phys. Polon.*, B43:829, 2012.

[30] A. Andrighetto et al. Enhancement of strange and multi-strange hyperons and anti-hyperons in S S and S W interactions at 200-GeV/c. *J. Phys.*, G25:209–216, 1999.

[31] E. Andersen et al. Enhancement of central Lambda, Xi and Omega yields in Pb - Pb collisions at 158 A GeV/c. *Phys. Lett.*, B433:209–216, 1998.

[32] E. Andersen et al. Strangeness enhancement at mid-rapidity in Pb Pb collisions at 158 A GeV/c. *Phys. Lett.*, B449:401–406, 1999.

[33] T. Anticic et al. Lambda and anti-Lambda production in central Pb - Pb collisions at 40 A GeV, 80 A GeV and 158 A GeV. *Phys. Rev. Lett.*, 93:022302, 2004.

[34] S. V. Afanasiev et al. Cascade and anti-Cascade+ production in central Pb + Pb collisions at 158 GeV/c per nucleon. *Phys. Lett.*, B538:275–281, 2002.

[35] B. I. Abelev et al. Enhanced strange baryon production in Au + Au collisions compared to p + p at $\sqrt{s_{NN}} = 200$ GeV. *Phys. Rev.*, C77:044908, 2008.

[36] Serguei Chatrchyan et al. Centrality dependence of dihadron correlations and azimuthal anisotropy harmonics in PbPb collisions at $\sqrt{s_{NN}} = 2.76$ TeV. *Eur. Phys. J.*, C72:2012, 2012.

[37] Georges Aad et al. Measurement of the azimuthal anisotropy for charged particle production in $\sqrt{s_{NN}} = 2.76$ TeV lead-lead collisions with the ATLAS detector. *Phys. Rev.*, C86:014907, 2012.

[38] S. Voloshin and Y. Zhang. Flow study in relativistic nuclear collisions by Fourier expansion of Azimuthal particle distributions. *Z. Phys.*, C70:665–672, 1996.

[39] Betty Bezverkhny Abelev et al. Elliptic flow of identified hadrons in Pb-Pb collisions at $\sqrt{s_{\rm NN}} = 2.76$ TeV. *JHEP*, 06:190, 2015.

[40] R. Baier, Yuri L. Dokshitzer, Alfred H. Mueller, S. Peigne, and D. Schiff. Radiative energy loss and p(T) broadening of high-energy partons in nuclei. *Nucl. Phys.*, B484:265–282, 1997.

[41] K. Aamodt et al. Suppression of Charged Particle Production at Large Transverse Momentum in Central Pb-Pb Collisions at $\sqrt{s_{NN}} = 2.76$ TeV. *Phys. Lett.*, B696:30–39, 2011.

[42] Georges Aad et al. Observation of a Centrality-Dependent Dijet Asymmetry in Lead-Lead Collisions at $\sqrt{s_{NN}} = 2.77$ TeV with the ATLAS Detector at the LHC. *Phys. Rev. Lett.*, 105:252303, 2010.

[43] Serguei Chatrchyan et al. Jet momentum dependence of jet quenching in PbPb collisions at $\sqrt{s_{NN}} = 2.76$ TeV. *Phys. Lett.*, B712:176–197, 2012.

[44] Serguei Chatrchyan et al. Observation and studies of jet quenching in PbPb collisions at nucleon-nucleon center-of-mass energy = 2.76 TeV. *Phys. Rev.*, C84:024906, 2011.

[45] K. Aamodt et al. Particle-yield modification in jet-like azimuthal di-hadron correlations in Pb-Pb collisions at $\sqrt{s_{NN}} = 2.76$ TeV. *Phys. Rev. Lett.*, 108:092301, 2012.

[46] T. Matsui and H. Satz. J/ψ Suppression by Quark-Gluon Plasma Formation. *Phys. Lett.*, B178:416, 1986.

[47] Robert L. Thews, Martin Schroedter, and Johann Rafelski. Enhanced J/ψ production in deconfined quark matter. *Phys. Rev.*, C63:054905, 2001.

[48] Betty Bezverkhny Abelev et al. Centrality, rapidity and transverse momentum dependence of J/ψ suppression in Pb-Pb collisions at $\sqrt{s_{\rm NN}}$=2.76 TeV. *Phys. Lett.*, B734:314–327, 2014.

[49] A. Adare et al. J/ψ Production vs Centrality, Transverse Momentum, and Rapidity in Au+Au Collisions at $\sqrt{s_{NN}} = 200$ GeV. *Phys. Rev. Lett.*, 98:232301, 2007.

[50] M. C. Abreu et al. Transverse momentum distributions of J / psi, psi-prime, Drell-Yan and continuum dimuons produced in Pb Pb interactions at the SPS. *Phys. Lett.*, B499:85–96, 2001.

[51] A. Adare et al. J/psi Production in $\sqrt{s_{NN}}$ = 200-GeV Cu+Cu Collisions. *Phys. Rev. Lett.*, 101:122301, 2008.

[52] Jaroslav Adam et al. Differential studies of inclusive J/ψ and ψ(2S) production at forward rapidity in Pb-Pb collisions at $\sqrt{s_{\mathbf{NN}}}$ = 2.76 TeV. 2015.

[53] Jaroslav Adam et al. Direct photon production in Pb-Pb collisions at $\sqrt{s_{NN}}$ = 2.76 TeV. *Phys. Lett.*, B754:235–248, 2016.

[54] A. Adare et al. Centrality dependence of low-momentum direct-photon production in Au+Au collisions at $\sqrt{s_{NN}}$ = 200 GeV. *Phys. Rev.*, C91(6):064904, 2015.

[55] Betty Bezverkhny Abelev et al. $K^*(892)^0$ and (1020) production in Pb-Pb collisions at $\sqrt{sNN}$ = 2.76 TeV. *Phys. Rev.*, C91:024609, 2015.

[56] F. Becattini. An Introduction to the Statistical Hadronization Model. In *International School on Quark-Gluon Plasma and Heavy Ion Collisions: past, present, future Villa Gualino, Torino, Italy, December 8-14, 2008*, 2009. http://inspirehep.net/record/811687/files/arXiv:0901.3643.pdf.

[57] Francesco Becattini. What is the meaning of the statistical hadronization model? *J. Phys. Conf. Ser.*, 5:175–188, 2005. [,175(2004)].

[58] A. Keranen and F. Becattini. Chemical factors in canonical statistical models for relativistic heavy ion collisions. *Phys. Rev.*, C65:044901, 2002. [Erratum: Phys. Rev.C68,059901(2003)].

[59] Peter Braun-Munzinger, Krzysztof Redlich, and Johanna Stachel. Particle production in heavy ion collisions. 2003.

[60] Enrico Fermi. High-energy nuclear events. *Prog. Theor. Phys.*, 5:570–583, 1950.

[61] R. Hagedorn. Statistical thermodynamics of strong interactions at high-energies. *Nuovo Cim. Suppl.*, 3:147–186, 1965.

[62] J. Stachel, A. Andronic, P. Braun-Munzinger, and K. Redlich. Confronting LHC data with the statistical hadronization model. *J. Phys. Conf. Ser.*, 509:012019, 2014.

[63] P. Braun-Munzinger, J. Stachel, J. P. Wessels, and N. Xu. Thermal equilibration and expansion in nucleus-nucleus collisions at the AGS. *Phys. Lett.*, B344:43–48, 1995.

[64] J. Cleymans, D. Elliott, H. Satz, and R. L. Thews. Thermal hadron production in Si - Au collisions. *Z. Phys.*, C74:319–324, 1997.

[65] P. Braun-Munzinger, I. Heppe, and J. Stachel. Chemical equilibration in Pb + Pb collisions at the SPS. *Phys. Lett.*, B465:15–20, 1999.

[66] Ralf Rapp and Edward V. Shuryak. Resolving the anti-baryon production puzzle in high-energy heavy ion collisions. *Phys. Rev. Lett.*, 86:2980–2983, 2001.

[67] F. Becattini, J. Manninen, and M. Gazdzicki. Energy and system size dependence of chemical freeze-out in relativistic nuclear collisions. *Phys. Rev.*, C73:044905, 2006.

[68] P. Braun-Munzinger, D. Magestro, K. Redlich, and J. Stachel. Hadron production in Au - Au collisions at RHIC. *Phys. Lett.*, B518:41–46, 2001.

[69] A. Andronic, P. Braun-Munzinger, and J. Stachel. Hadron production in central nucleus-nucleus collisions at chemical freeze-out. *Nucl. Phys.*, A772:167–199, 2006.

[70] F. Becattini, P. Castorina, J. Manninen, and H. Satz. The Thermal Production of Strange and Non-Strange Hadrons in e+ e- Collisions. *Eur. Phys. J.*, C56:493–510, 2008.

[71] A. Andronic, F. Beutler, P. Braun-Munzinger, K. Redlich, and J. Stachel. Thermal description of hadron production in e+e- collisions revisited. *Phys. Lett.*, B675:312–318, 2009.

[72] A. Andronic, P. Braun-Munzinger, and J. Stachel. Thermal hadron production in relativistic nuclear collisions: The Hadron mass spectrum, the horn, and the QCD phase transition. *Phys. Lett.*, B673:142–145, 2009. [Erratum: Phys. Lett.B678,516(2009)].

[73] F. Becattini, M. Gazdzicki, A. Keranen, J. Manninen, and R. Stock. Chemical equilibrium in nucleus nucleus collisions at relativistic energies. *Phys. Rev.*, C69:024905, 2004.

[74] F. Becattini and J. Manninen. Centrality dependence of strangeness production in heavy-ion collisions as a geometrical effect of core-corona superposition. *Phys. Lett.*, B673:19–23, 2009.

[75] G. Agakishiev et al. Strangeness Enhancement in Cu+Cu and Au+Au Collisions at $\sqrt{s_{NN}} = 200$ GeV. *Phys. Rev. Lett.*, 108:072301, 2012.

[76] B. I. Abelev et al. Measurements of phi meson production in relativistic heavy-ion collisions at RHIC. *Phys. Rev.*, C79:064903, 2009.

[77] J. Adams et al. Scaling Properties of Hyperon Production in Au+Au Collisions at $\sqrt{s_{NN}} = 200$ GeV. *Phys. Rev. Lett.*, 98:062301, 2007.

[78] Betty Bezverkhny Abelev et al. $K^*(892)^0$ and (1020) production in Pb-Pb collisions at $\sqrt{s_{NN}}$=2.76 TeV. *Phys. Rev.*, C91(2):024609, 2015.

[79] J. Aichelin and K. Werner. Centrality Dependence of Strangeness Enhancement in Ultrarelativistic Heavy Ion Collisions: A Core-Corona Effect. *Phys. Rev.*, C79:064907, 2009. [Erratum: Phys. Rev.C81,029902(2010)].

[80] Ekkard Schnedermann, Josef Sollfrank, and Ulrich W. Heinz. Thermal phenomenology of hadrons from 200-A/GeV S+S collisions. *Phys. Rev.*, C48:2462–2475, 1993.

[81] Constantino Tsallis. Possible Generalization of Boltzmann-Gibbs Statistics. *J. Statist. Phys.*, 52:479–487, 1988.

[82] Fred Cooper and Graham Frye. Comment on the Single Particle Distribution in the Hydrodynamic and Statistical Thermodynamic Models of Multiparticle Production. *Phys. Rev.*, D10:186, 1974.

[83] J. Adams et al. Multistrange baryon production in Au-Au collisions at $\sqrt{s_{NN}}$ = 130 GeV. *Phys. Rev. Lett.*, 92:182301, 2004.

[84] John Adams et al. Experimental and theoretical challenges in the search for the quark gluon plasma: The STAR Collaboration's critical assessment of the evidence from RHIC collisions. *Nucl. Phys.*, A757:102–183, 2005.

[85] Betty Abelev et al. Pion, Kaon, and Proton Production in Central Pb–Pb Collisions at $\sqrt{s_{NN}} = 2.76$ TeV. *Phys. Rev. Lett.*, 109:252301, 2012.

[86] J. D. Bjorken. Highly Relativistic Nucleus-Nucleus Collisions: The Central Rapidity Region. *Phys. Rev.*, D27:140–151, 1983.

[87] J. D. Bjorken. Energy Loss of Energetic Partons in Quark-Gluon Plasma: Possible Extinction of High p_T Jets in Hadron-Hadron Collisions. 1982.

[88] Vardan Khachatryan et al. Observation of Long-Range Near-Side Angular Correlations in Proton-Proton Collisions at the LHC. *JHEP*, 09:091, 2010.

[89] Betty Abelev et al. Long-range angular correlations on the near and away side in p-Pb collisions at $\sqrt{s_{NN}} = 5.02$ TeV. *Phys. Lett.*, B719:29–41, 2013.

[90] Georges Aad et al. Observation of Associated Near-Side and Away-Side Long-Range Correlations in $\sqrt{s_{NN}}$=5.02TeV Proton-Lead Collisions with the ATLAS Detector. *Phys. Rev. Lett.*, 110(18):182302, 2013.

[91] Betty Bezverkhny Abelev et al. Multiplicity Dependence of Pion, Kaon, Proton and Lambda Production in p-Pb Collisions at $\sqrt{s_{NN}} = 5.02$ TeV. *Phys. Lett.*, B728:25–38, 2014.

[92] Edward Shuryak and Ismail Zahed. High-multiplicity pp and pA collisions: Hydrodynamics at its edge. *Phys. Rev.*, C88(4):044915, 2013.

[93] Betty Bezverkhny Abelev et al. Measurement of prompt D-meson production in $p - Pb$ collisions at $\sqrt{s_{NN}} = 5.02$ TeV. *Phys. Rev. Lett.*, 113(23):232301, 2014.

[94] Bo Andersson, G. Gustafson, G. Ingelman, and T. Sjostrand. Parton Fragmentation and String Dynamics. *Phys. Rept.*, 97:31–145, 1983.

[95] G. Aad et al. The ATLAS Experiment at the CERN Large Hadron Collider. *JINST*, 3:S08003, 2008.

[96] A. Augusto Alves, Jr. et al. The LHCb Detector at the LHC. *JINST*, 3:S08005, 2008.

[97] Christiane Lefèvre. *The CERN accelerator complex*, Dec 2008.

[98] Lhc programme coordination web pages, 2013. `http://lpc.web.cern.ch/lpc/`.

[99] G. Dellacasa et al. ALICE technical design report of the inner tracking system (ITS). 1999.

[100] F. Meddi. The ALICE silicon pixel detector (SPD). *Nucl. Instrum. Meth.*, A465:40–45, 2000.

[101] The ALICE Collaboration webpage. The Silicon Pixel Detector (SPD), 2008. http://aliceinfo.cern.ch/Public/en/Chapter2/Chap2_SPD.html.

[102] D. Nouais et al. The Alice silicon drift detector system. *Nucl. Instrum. Meth.*, A501:119–125, 2001.

[103] A. Rashevsky et al. Characteristics of the ALICE silicon drift detector. *Nucl. Instrum. Meth.*, A461:133–138, 2001.

[104] B. Alessandro et al. Charge collection in the Silicon Drift Detectors of the ALICE experiment. *JINST*, 5:P02008, 2010.

[105] Giacomo Contin. The ALICE Silicon Strip Detector performance during the first LHC data taking. *Conf. Proc.*, C100901:257–260, 2010.

[106] G. Dellacasa et al. ALICE: Technical design report of the time projection chamber. 2000.

[107] Christian Lippmann. Particle identification. *Nucl. Instrum. Meth.*, A666:148–172, 2012.

[108] H. Bethe. Theory of the Passage of Fast Corpuscular Rays Through Matter. *Annalen Phys.*, 5:325–400, 1930. [Annalen Phys.397,325(1930)].

[109] P Cortese et al. ALICE technical design report on forward detectors: FMD, T0 and V0. 2004.

[110] Betty Bezverkhny Abelev et al. Performance of the ALICE Experiment at the CERN LHC. *Int. J. Mod. Phys.*, A29:1430044, 2014.

[111] D. et al Evans. The ALICE Trigger System. *CERN Document Server*, 2009.

[112] Betty Abelev et al. Centrality determination of Pb-Pb collisions at $\sqrt{s_{NN}} =$ 2.76 TeV with ALICE. *Phys. Rev.*, C88(4):044909, 2013.

[113] H. De Vries, C. W. De Jager, and C. De Vries. Nuclear charge and magnetization density distribution parameters from elastic electron scattering. *Atom. Data Nucl. Data Tabl.*, 36:495–536, 1987.

[114] Michael L. Miller, Klaus Reygers, Stephen J. Sanders, and Peter Steinberg. Glauber modeling in high energy nuclear collisions. *Ann. Rev. Nucl. Part. Sci.*, 57:205–243, 2007.

[115] Jaroslav Adam et al. Centrality dependence of particle production in p-Pb collisions at $\sqrt{s_{\rm NN}}$= 5.02 TeV. *Phys. Rev.*, C91(6):064905, 2015.

[116] Pierre Billoir. Track Fitting With Multiple Scattering: A New Method. *Nucl. Instrum. Meth.*, A225:352–366, 1984.

[117] Pierre Billoir, R. Fruhwirth, and M. Regler. TRACK ELEMENT MERGING STRATEGY AND VERTEX FITTING IN COMPLEX MODULAR DETECTORS. *Nucl. Instrum. Meth.*, A241:115–131, 1985.

[118] R. Fruhwirth. Application of Kalman filtering to track and vertex fitting. *Nucl. Instrum. Meth.*, A262:444–450, 1987.

[119] Iouri Belikov. Event reconstruction and particle identification in the ALICE experiment at the LHC. *EPJ Web Conf.*, 70:00029, 2014.

[120] The ALICE Collaboration ALICE offline pages. Thealice offline bible, 2008. `http://aliweb.cern.ch/secure/Offline/sites/aliweb.cern.ch.Offline/files/uploads/OfflineBible.pdf`.

[121] Betty Bezverkhny Abelev et al. Measurement of visible cross sections in proton-lead collisions at $\sqrt{s_{\rm NN}}$ = 5.02 TeV in van der Meer scans with the ALICE detector. *JINST*, 9(11):P11003, 2014.

[122] Plamen Petrov. *Strangeness enhancement in high multiplicity proton-proton collisions at $\sqrt{s}$ = 7 TeV with the ALICE detector at the LHC*. PhD thesis, University of Birmingham, 2013. Chapter 4.

[123] Betty Abelev et al. Pseudorapidity density of charged particles in p + Pb collisions at $\sqrt{s_{NN}} = 5.02$ TeV. *Phys. Rev. Lett.*, 110(3):032301, 2013.

[124] K. A. Olive et al. Review of Particle Physics. *Chin. Phys.*, C38:090001, 2014.

[125] S. Roesler, R. Engel, and J. Ranft. The Monte Carlo event generator DPMJET-III. In Andreas Kling, FernandoJ.C. Baräo, Masayuki Nakagawa, Luis Távora, and Pedro Vaz, editors, *Advanced Monte Carlo for Radiation Physics, Particle Transport Simulation and Applications*, pages 1033–1038. Springer Berlin Heidelberg, 2001.

[126] Rene Brun, Federico Carminati, and Simone Giani. GEANT Detector Description and Simulation Tool. 1994.

[127] J. Adam et al. Multiplicity dependence of pion, kaon, proton and lambda production in p-Pb collisions at $\sqrt{s_{NN}} = 5.02$ TeV. *Physics Letters B*, 728:25–38, 2014. `http://www.sciencedirect.com/science/article/pii/S0370269313009234`.

[128] J. Ranft. New features in DPMJET version II.5. 1999.

[129] Premomoy Ghosh, Sanjib Muhuri, Jajati K. Nayak, and Raghava Varma. Indication of transverse radial flow in high-multiplicity protonproton collisions at the Large Hadron Collider. *J. Phys.*, G41:035106, 2014.

[130] Betty Abelev et al. Centrality dependence of π, K, p production in Pb-Pb collisions at $\sqrt{s_{NN}} = 2.76$ TeV. *Phys. Rev.*, C88:044910, 2013.

[131] Betty Bezverkhny Abelev et al. Multi-strange baryon production at mid-rapidity in Pb-Pb collisions at $\sqrt{s_{NN}} = 2.76$ TeV. *Phys. Lett.*, B728:216–227, 2014. [Erratum: Phys. Lett.B734,409(2014)].

[132] H. van Hecke, H. Sorge, and N. Xu. Evidence of early multistrange hadron freezeout in high-energy nuclear collisions. *Phys. Rev. Lett.*, 81:5764–5767, 1998.

[133] Jaroslav Adam et al. Production of $K^*(892)^0$ and $\phi(1020)$ in p-Pb collisions at $\sqrt{s_{\rm NN}} = 5.02$ TeV. 2016.

[134] K. Aamodt et al. Strange particle production in proton-proton collisions at sqrt(s) = 0.9 TeV with ALICE at the LHC. *Eur. Phys. J.*, C71:1594, 2011.

[135] K. Aamodt et al. Production of pions, kaons and protons in *pp* collisions at $\sqrt{s} = 900$ GeV with ALICE at the LHC. *Eur. Phys. J.*, C71:1655, 2011.

[136] Betty Abelev et al. Multi-strange baryon production in *pp* collisions at $\sqrt{s} = 7$ TeV with ALICE. *Phys. Lett.*, B712:309–318, 2012.

[137] Jaroslav Adam et al. Measurement of pion, kaon and proton production in protonproton collisions at $\sqrt{s} = 7$ TeV. *Eur. Phys. J.*, C75(5):226, 2015.

[138] S. Wheaton, J. Cleymans, and M. Hauer. THERMUS — a thermal model package for ROOT. *Computer Physics Communications*, 180:84 – 106, 2009.

[139] Michele Floris. Hadron yields and the phase diagram of strongly interacting matter. *Nucl. Phys.*, A931:103–112, 2014.

[140] Livio Bianchi. Strangeness production as a function of charged particle multiplicity in proton-proton collisions. 2016.

[141] Antonio Ortiz Velasquez, Peter Christiansen, Eleazar Cuautle Flores, Ivonne Maldonado Cervantes, and Guy Paic. Color Reconnection and Flowlike Patterns in *pp* Collisions. *Phys. Rev. Lett.*, 111(4):042001, 2013.

[142] Christian Bierlich and Jesper Roy Christiansen. Effects of color reconnection on hadron flavor observables. *Phys. Rev.*, D92(9):094010, 2015.

[143] Torbjorn Sjostrand, Stephen Mrenna, and Peter Z. Skands. A Brief Introduction to PYTHIA 8.1. *Comput. Phys. Commun.*, 178:852–867, 2008.

[144] Christoffer Flensburg, Gosta Gustafson, and Leif Lonnblad. Inclusive and Exclusive Observables from Dipoles in High Energy Collisions. *JHEP*, 08:103, 2011.

[145] T. Pierog, Iu. Karpenko, J. M. Katzy, E. Yatsenko, and K. Werner. EPOS LHC: Test of collective hadronization with data measured at the CERN Large Hadron Collider. *Phys. Rev.*, C92(3):034906, 2015.

[146] K. Werner, Iu. Karpenko, M. Bleicher, T. Pierog, and S. Porteboeuf-Houssais. Jets, Bulk Matter, and their Interaction in Heavy Ion Collisions at Several TeV. *Phys. Rev.*, C85:064907, 2012.

[147] H. J. Drescher, M. Hladik, S. Ostapchenko, T. Pierog, and K. Werner. Parton based Gribov-Regge theory. *Phys. Rept.*, 350:93–289, 2001.